

UNCLASSIFIED

AD NUMBER
ADB006844
NEW LIMITATION CHANGE
TO Approved for public release, distribution unlimited
FROM Distribution authorized to U.S. Gov't. agencies only; Test and Evaluation; Jun 1975. Other requests shall be referred to Director, Defense Nuclear Agency, Washington, DC 20305.
AUTHORITY
DNA ltr, 17 Aug 1979

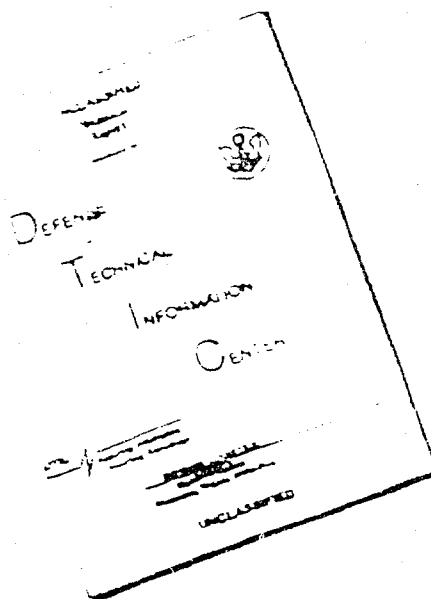
THIS PAGE IS UNCLASSIFIED

THIS REPORT HAS BEEN DELIMITED
AND CLEARED FOR PUBLIC RELEASE
UNDER DOD DIRECTIVE 5200.20 AND
NO RESTRICTIONS ARE IMPOSED UPON
ITS USE AND DISCLOSURE.

DISTRIBUTION STATEMENT A

APPROVED FOR PUBLIC RELEASE;
DISTRIBUTION UNLIMITED.

DISCLAIMER NOTICE



THIS DOCUMENT IS BEST
QUALITY AVAILABLE. THE COPY
FURNISHED TO DTIC CONTAINED
A SIGNIFICANT NUMBER OF
PAGES WHICH DO NOT
REPRODUCE LEGIBLY.

REPRODUCED FROM
BEST AVAILABLE COPY

DNA 3537F

NUMERICAL ANALYSIS OF DNA EARTH PENETRATOR EXPERIMENT AT DRES

**California Research and Technology, Inc.
6269 Varrel Avenue, Suite 200
Woodland Hills, California 91364**

18 June 1975

Final Report for Period 22 April 1974—10 October 1974

CONTRACT No. DNA 001-74-C-0222

Distribution limited to U.S. Government agencies
only (Test and Evaluation) 5 November 1974.
Other requests for this document must be
referred to the Director, Defense Nuclear Agency,
Washington, D.C. 20305.

D D C
RECEIVED
OCT 6 1975
RECEIVED
C

**THIS WORK SPONSORED BY THE DEFENSE NUCLEAR AGENCY
UNDER SUBTASK L35IAXSX338-03.**

**Prepared for
Director
DEFENSE NUCLEAR AGENCY
Washington, D. C. 20305**



Destroy this report when it is no longer
needed. Do not return to sender.

UNCLASSIFIED

SECURITY CLASSIFICATION OF THIS PAGE (When Data Entered)

REPORT DOCUMENTATION PAGE		READ INSTRUCTIONS BEFORE COMPLETING FORM
1. REPORT NUMBER DNA 3537F	2. GOVT ACCESSION NO.	3. RECIPIENT'S CATALOG NUMBER
4. TITLE (and Subtitle) NUMERICAL ANALYSIS OF DNA EARTH PENETRATOR EXPERIMENT AT DRES		5. TYPE OF REPORT & PERIOD COVERED Final Report for Period 22 Apr 74-10 Oct 74
7. AUTHOR(s) M. H. Wagner K. N. Kreyenhagen W. S. Goerke		6. PERFORMING ORG. REPORT NUMBER CRT 2050-2
8. PERFORMING ORGANIZATION NAME AND ADDRESS California Research & Technology, Inc. 6269 Variel Avenue, Suite 200 Woodland Hills, California 91364		9. CONTRACT OR GRANT NUMBER(s) DNA 001-74-C-0222
11. CONTROLLING OFFICE NAME AND ADDRESS Director Defense Nuclear Agency Washington, D.C. 20305		10. PROGRAM ELEMENT, PROJECT, TASK AREA & WORK UNIT NUMBERS NWET Subtask L35IAXSX338-03
14. MONITORING AGENCY NAME & ADDRESS (if different from Controlling Office)		12. REPORT DATE 18 June 1975
		13. NUMBER OF PAGES 170
		15. SECURITY CLASS. (of this report) UNCLASSIFIED
		16. DECLASSIFICATION/DOWNGRADING SCHEDULE
16. DISTRIBUTION STATEMENT (of this Report) Distribution limited to U.S. Government agencies only (Test and Evaluation) 5 November 1974. Other requests for this document must be referred to the Director, Defense Nuclear Agency, Washington, D.C. 20305.		
17. DISTRIBUTION STATEMENT (of the abstract entered in Block 20, if different from Report)		
18. SUPPLEMENTARY NOTES This work sponsored by the Defense Nuclear Agency under Subtask L35IAXSX338-03.		
19. KEY WORDS (Continue on reverse side if necessary and identify by block number) Penetration Terradynamics Numerical Solutions Soil Mechanics		
20. ABSTRACT (Continue on reverse side if necessary and identify by block number) A finite difference Lagrangian code calculation of the firing of an earth penetrator into a soft soil site has been carried out. The penetrator was a 400-lb, 6.5-in. diameter steel projectile with an initial velocity of 500 ft/sec. The field tests were conducted in July 1974 at the DRES Site in Canada. The penetrator was treated as a rigid body in the code solution. A four-layer idealization of the target site was used. The calculated decel- erations were approximately 110 g's, 125 g's, and 45 - 50 g's in the first		

DD FORM 1473

1 JAN 73

EDITION OF 1 NOV 65 IS OBSOLETE

UNCLASSIFIED

SECURITY CLASSIFICATION OF THIS PAGE (When Data Entered)

UNCLASSIFIED

SECURITY CLASSIFICATION OF THIS PAGE(When Data Entered)

20. ABSTRACT (Continued)

three layers. Frictional forces at the penetrator/soil interface were responsible for a major part of these decelerations. (The calculation was not carried into the fourth layer.) Experimentally-observed decelerations were somewhat smaller than the calculated values, but the general agreement between calculation and experiment was good. It is concluded that finite difference code solutions can provide useful information about earth penetrators, particularly for those portions of penetration events where loads and decelerations are changing rapidly.

UNCLASSIFIED

SECURITY CLASSIFICATION OF THIS PAGE(When Data Entered)

PREFACE

This report describes a finite difference code calculation of an earth penetrator experiment conducted in July 1974 at the DRES site in Canada. The work was carried out within a short time schedule in an effort to provide a pre-shot calculation. The principal investigators at California Research & Technology were M. H. Wagner and K. N. Kreyonhagen. W. S. Goerke performed the computer programming and code development work. C. C. Fulton and L. A. DeAngelo provided valuable assistance in formulation of the material models and data reduction, and in the computer production runs, respectively.

The site profile and material properties were provided by J. G. Jackson, Jr., U. S. Army Engineer, Waterways Experiment Station.

The Project Officer was Major T. D. Stong, SPSS, Defense Nuclear Agency.

TABLE OF CONTENTS

	<u>Page</u>
SECTION I INTRODUCTION AND SUMMARY	5
1.1 BACKGROUND AND APPROACH	5
1.2 SUMMARY OF RESULTS	7
1.3 CONCLUSIONS	12
SECTION II DNA PENETRATOR PROBLEM DESCRIPTION	14
2.1 PENETRATOR	14
2.2 TARGET MEDIA	14
2.3 FRICTION ALONG PENETRATOR-TARGET SOIL INTERFACE	19
SECTION III COMPUTATIONAL METHOD	21
3.1 BASIC GRID DESIGN	21
3.2 "ROLLING GRID"	23
3.3 PRE-DEFORMED GRID AND LOCAL REZONING	24
3.4 GRID DECOUPLING	25
3.5 VOID OPENING AND CLOSING.	25
3.6 "LEAPFROGGING".	28
SECTION IV NUMERICAL RESULTS AND EXPERIMENTAL COMPARISONS	30
4.1 PENETRATOR DYNAMICS	30
4.2 PENETRATOR-SOIL INTERACTIONS AND SOIL RESPONSE	38
4.2.1 Field Plots	38
4.2.2 Friction	38
4.2.3 Pressures and Stresses in Target near Penetrator Nose	44
4.3 COMPARISONS WITH EXPERIMENTS	48
SECTION V PROBLEM AREAS	55
SECTION VI INTERNAL STRESS RESPONSE OF PENETRATOR	58

TABLE OF CONTENTS (Continued)

	<u>Page</u>
REFERENCES	62
APPENDIX A MATERIAL MODELS	63
A.1 LAYER 1	63
A.2 LAYER 2	67
A.3 LAYER 3	76
A.4 LAYER 4	87
APPENDIX B DISTORTION, VELOCITY, AND PRINCIPAL STRESS FIELD PLOTS	97
APPENDIX C FRICTION STRESSES, TARGET DYNAMICS NEAR PENETRATOR NOSE, AND ENERGY PARTIONING	117
APPENDIX D TIME HISTORIES OF STRESS, VELOCITY, AND DISPLACEMENT OF TARGET STATIONS	127

SECTION I

INTRODUCTION AND SUMMARY

1.1 BACKGROUND AND APPROACH

For some applications of both nuclear and high explosive systems, it is desirable to have the weapon penetrate into an earth target before exploding. Ample demonstrations have been made which show that substantial penetrations are achievable, at least in soft media, using high velocity penetrators (e.g., Ref. 1).

The objective of the present study was to examine the current capabilities of finite difference codes to predict and analyze earth penetrator events. This was done by calculating a specific penetration event, which will be referred to herein as the DNA earth penetrator experiment. The calculation was performed during June and July 1974. Specific information sought from the calculation was the deceleration, velocity, and displacement histories for the penetrator, the surface loading history on the penetrator, and a description of the earth target response.

The DNA earth penetrator experiment was performed in July 1974 by Sandia Laboratories, Albuquerque.² This experiment consisted of a series of field tests conducted at the Watching Hill Blast Range of Defense Research Establishment Suffield (DRES), Alberta, Canada. The tests involved vertical firings of instrumented penetrators at 500 ft/sec into the ground. The penetrators were steel cylinders with ogival noses, weighing about 400 lbs, with a total length of about five feet and a diameter of 6.5 inches.

The earth target media at the test site is comparatively uniform to the depths of interest, consisting of layered glacial lake deposits. Using extensive soil test data previously gathered in the general area,³ recommended properties for a four-layer idealized site profile were prepared by the Waterways Experiment Station (WES). This information was used to develop the material models for the code calculation. The sketch below indicates the general conditions for modeling the DNA earth penetrator experiment.

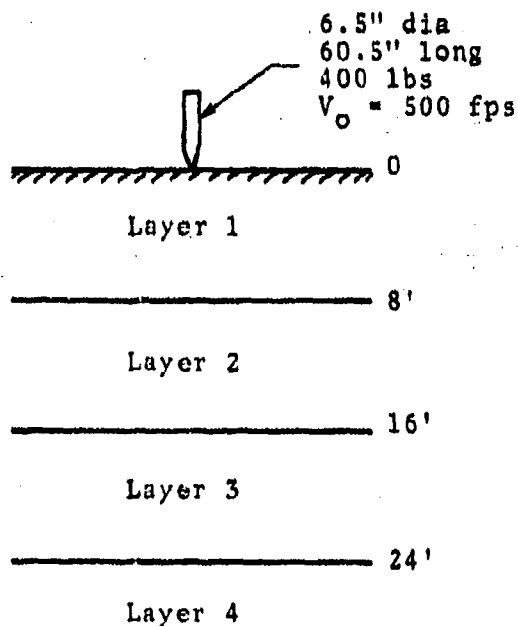


Figure 1. Calculational Model of DNA Earth Penetrator Experiment

The calculation described in this report was made with the WAVE-L code, a two-dimensional Lagrangian finite difference technique based on the HEMP method.⁴ The penetrator was represented as a rigid body, which is a realistic approximation when the penetrator deformations are entirely elastic.

In addition to the code analysis performed by CRT which is described herein, separate calculations of the same event were performed by Sandia Laboratories, Albuquerque⁵ and by Physics International.⁶

1.2 SUMMARY OF RESULTS

Figure 2 shows the calculated axial force and deceleration of the penetrator vs depth. The penetrator problem was integrated completely through Layer 1. After an initial buildup (as the nose was entering the soil), quasi-steady state conditions were established and the penetrator deceleration remained fairly constant at about 110 g's. This increased to about 125 g's after the nose had fully entered Layer 2.

Figure 3 shows the Lagrangian grid with the penetrator tip at 200 cm depth (6.6 ft), when it was completely in Layer 1. Soil separates from the penetrator about 15 inches back from the nose tip. Large frictional forces along the penetrator-soil surface cause severe distortion of the cells adjacent to the penetrator. Periodic local rezoning of the grid was required in this region.

To avoid the time-consuming and largely uninformative integration through Layer 2, the solution was stopped after the nose had fully entered Layer 2, and restarted when the

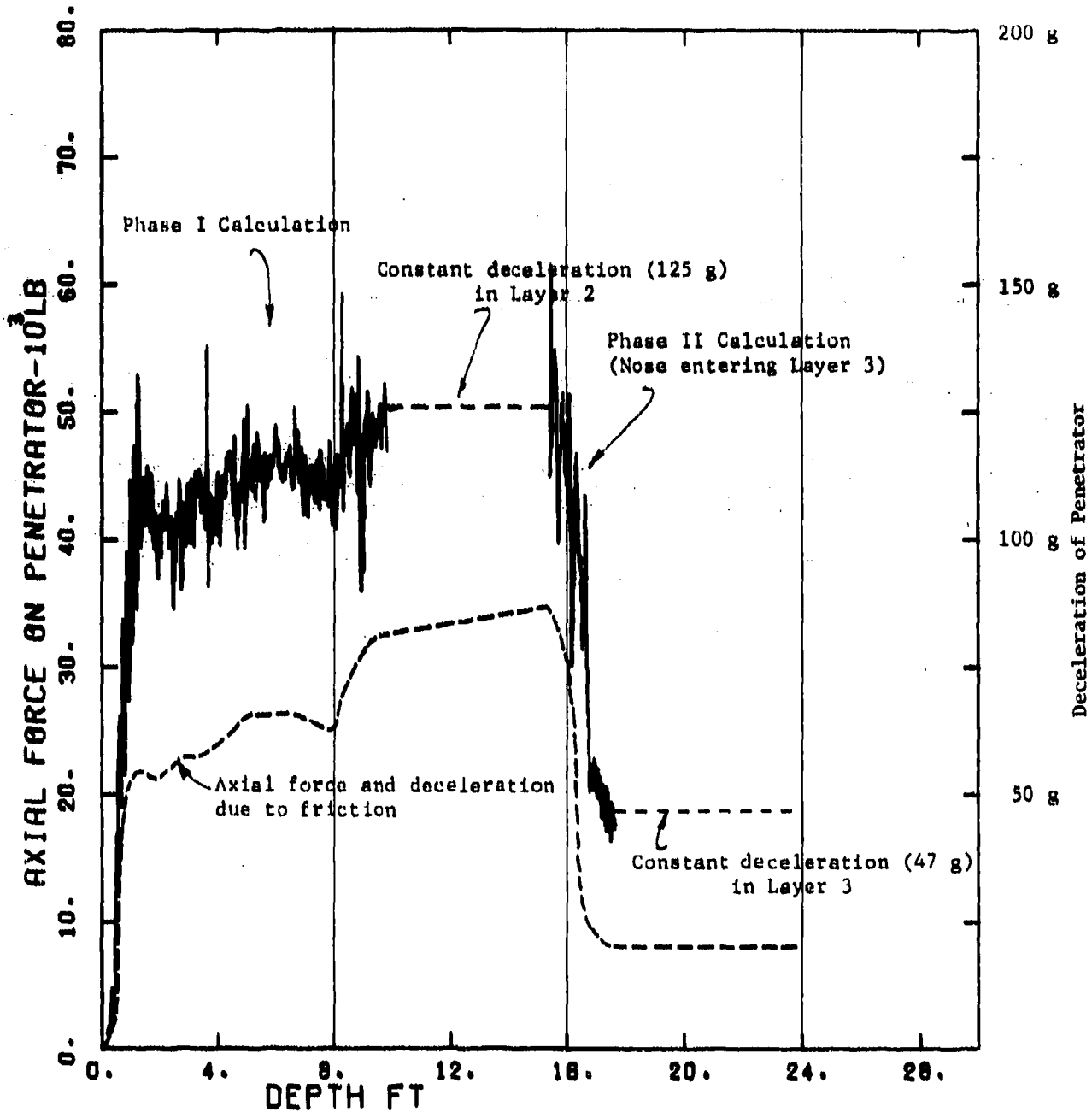


Figure 2. Axial Force on Penetrator (showing total axial force and frictional component) and Deceleration of Penetrator vs Depth

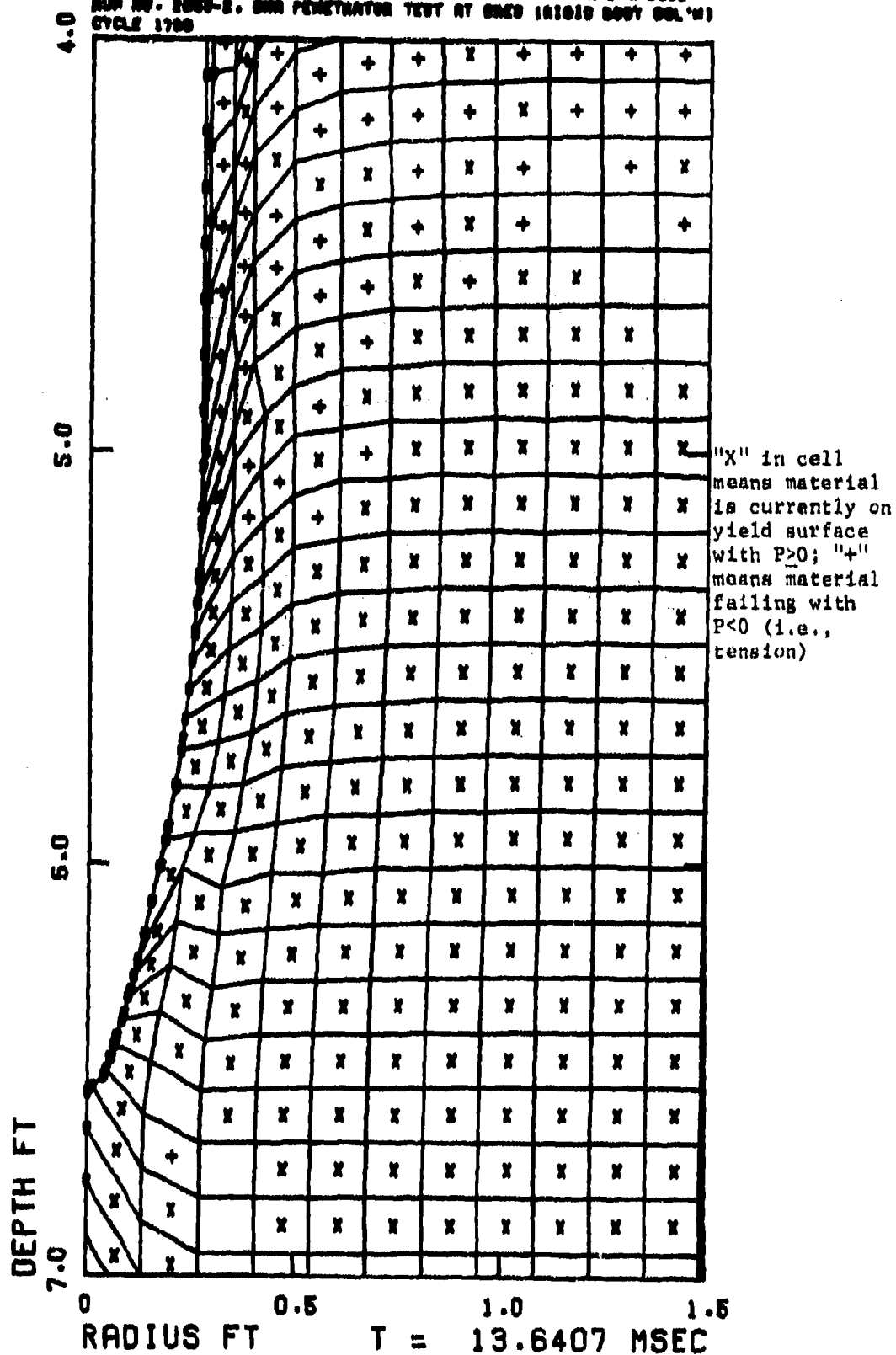


Figure 3. Grid Configuration with Penetrator at 200 cm Depth

nose reached Layer 3. The penetrator velocity was reduced to reflect a constant 125-g deceleration through Layer 2.

As the penetrator entered Layer 3, the deceleration dropped sharply, reaching 45-50 g's after the nose was fully embedded in Layer 3. Assuming the deceleration would remain constant at 47 g's in Layer 3, it was estimated that the penetrator would reach Layer 4 (at 24 ft depth) at 59.5 msec, and with a velocity of 330 ft/sec, or 101 m/sec. The solution was not extended into Layer 4 due to time constraints.

As is seen in Figure 2, friction was responsible for approximately half of the total deceleration in the calculation in all three layers.

Figure 4 shows a comparison of the calculated deceleration history with preliminary experimental results. The large excursions and the absence of obvious demarcations between layers in the experimental results once again confirm the difficulty of using idealized soil profiles to represent actual geologic conditions. The somewhat high level of deceleration predicted by the calculation in each layer suggests that excessive friction was specified in the model. Despite these problems, the agreement shown in Figure 4 is regarded as very good for an initial demonstration problem.

The basic zoning for the calculations used 4 cells per penetrator diameter. The computer time (exclusive of bad runs, check problems, and edits) was about 12 hours on the Univac 1108.

CALIFORNIA RESEARCH AND TECHNOLOGY, INC.
RUN NO. 2050-2. DWA PENETRATOR TEST AT DRES (RIGID BODY SOL'N)

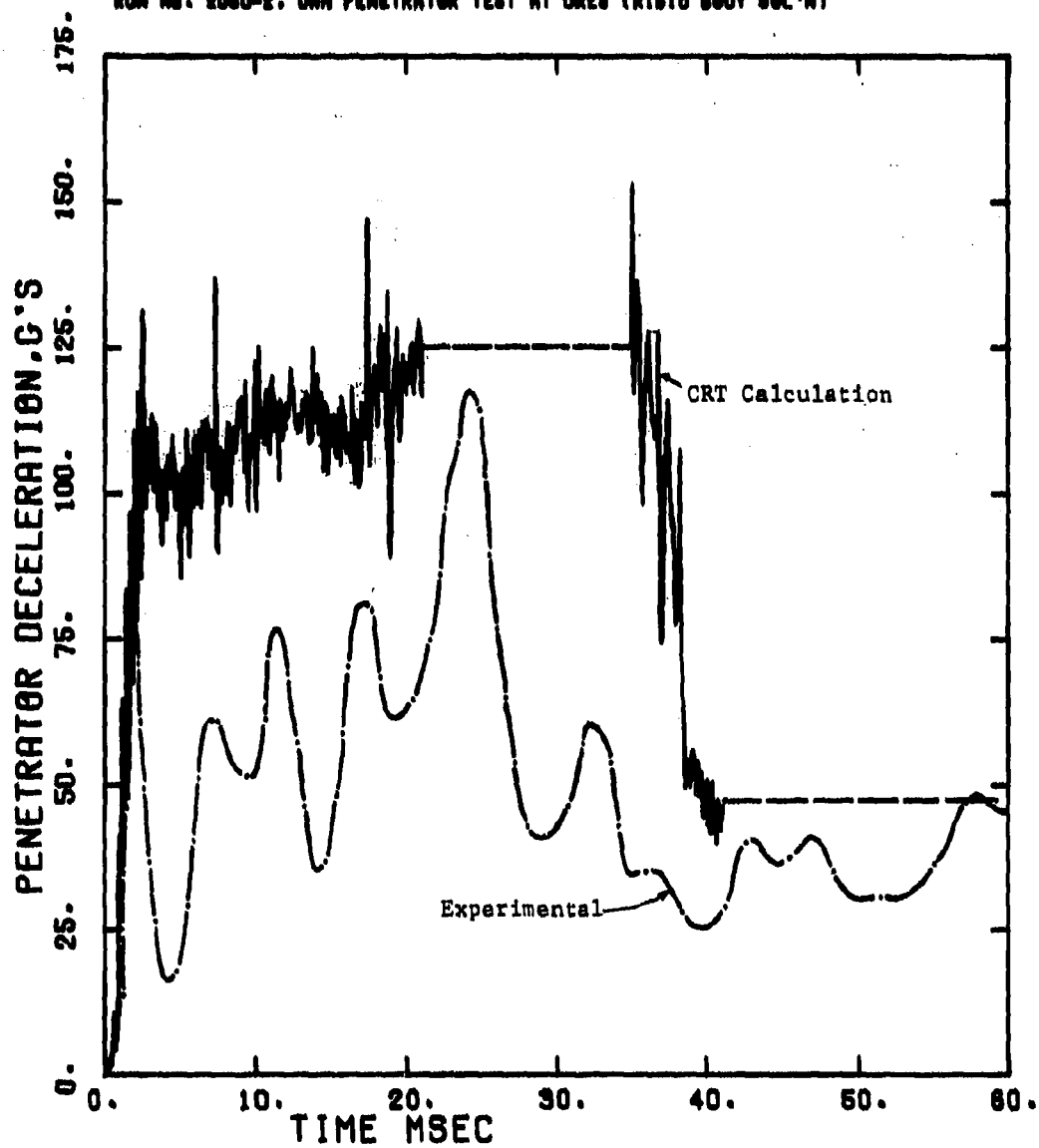


Figure 4. Comparison of Computed and Experimental Time Histories of Penetrator Deceleration

1.3 CONCLUSIONS

The Lagrangian finite difference calculation of the DNA penetrator problem produced generally good agreement with experimental acceleration records. This indicates that the WAVE-L code can provide useful information regarding important aspects of rigid-body penetration into earth targets. Results obtained from another program⁷ indicate that WAVE-L can also be used to determine stresses and accelerations *within* earth penetrators. Thus, finite difference codes can be applied to:

- o Studying phenomenology of penetration in different earth media types
- o Examining the effects of variations in target property, penetrator design, and impact parameters upon the penetration processes
- o Establishing the design environment (stresses and accelerations) within an earth penetrator in representative types of targets and under different impact conditions.

Problems undeniably exist in the application of finite difference codes to earth penetrator analyses. However, with reasonable assurance, some of these can be overcome with modest additional effort. The others, we argue, can be avoided by recognizing the objective of the numerical solutions.

In the former category, the needs for realistic characterization of friction, for efficient correction of grid distortion, and for establishment of zoning criteria for reasonably accurate solutions should all yield to currently planned work.

The more difficult problems have to do with long computer running times and with persistent geologic uncertainties.

Long running times are involved in attempting to solve complete deep penetration problems, and/or in predicting depths of penetration in soft targets. In such problems, however, major portions of the penetration may involve phenomena which change only slowly with time. It is not necessary or fruitful to analyze such quasi-steady state problems with a finite difference code. Rather, such codes should be reserved for analyzing those portions of penetration events where loading on the penetrator is most severe or is changing rapidly (e.g., while the penetrator nose is entering the surface, or while it is passing between different geologic layers, or perhaps just before it comes to rest).

Some geologic uncertainties will always exist, even when extensive subsurface surveys are possible. However, such uncertainties are generally troublesome only when one is attempting to validate a predictive method by comparing it with a test at a specific site. Exact knowledge of real target properties is unattainable, nor is such knowledge needed for the primary code applications listed at the beginning of this section.

SECTION II

DNA PENETRATOR PROBLEM DESCRIPTION

The overall problem conditions for the numerical solution are shown in Figure 5.

2.1 PENETRATOR

The penetrator was a steel cylinder, with an ogival nose section and a small 45° conical tip, as indicated in the insert in Figure 5. For this code solution, the penetrator was treated as a rigid body. This assumption is reasonable for analyses of penetration dynamics, inasmuch as the penetrator undergoes only small, elastic deformations which do not significantly interact with the penetration processes in the target. Separate analyses, either finite difference or finite element, can be performed to determine the stress environment within the projectile, as is illustrated in Section VI of this report.

2.2 TARGET MEDIA

The target media were modeled to correspond with the Watching Hill site at DRES, Alberta, Canada. The soil profile was idealized by WES into four distinct layers. Data from soil property measurements by WES were used as the basis for constructing the models for each layer.

The basic properties used for the four layers are listed in Table 1. Comparative uniaxial strain load-unload paths for each layer are shown in Figure 6. The failure surfaces for each layer are compared in Figure 7.

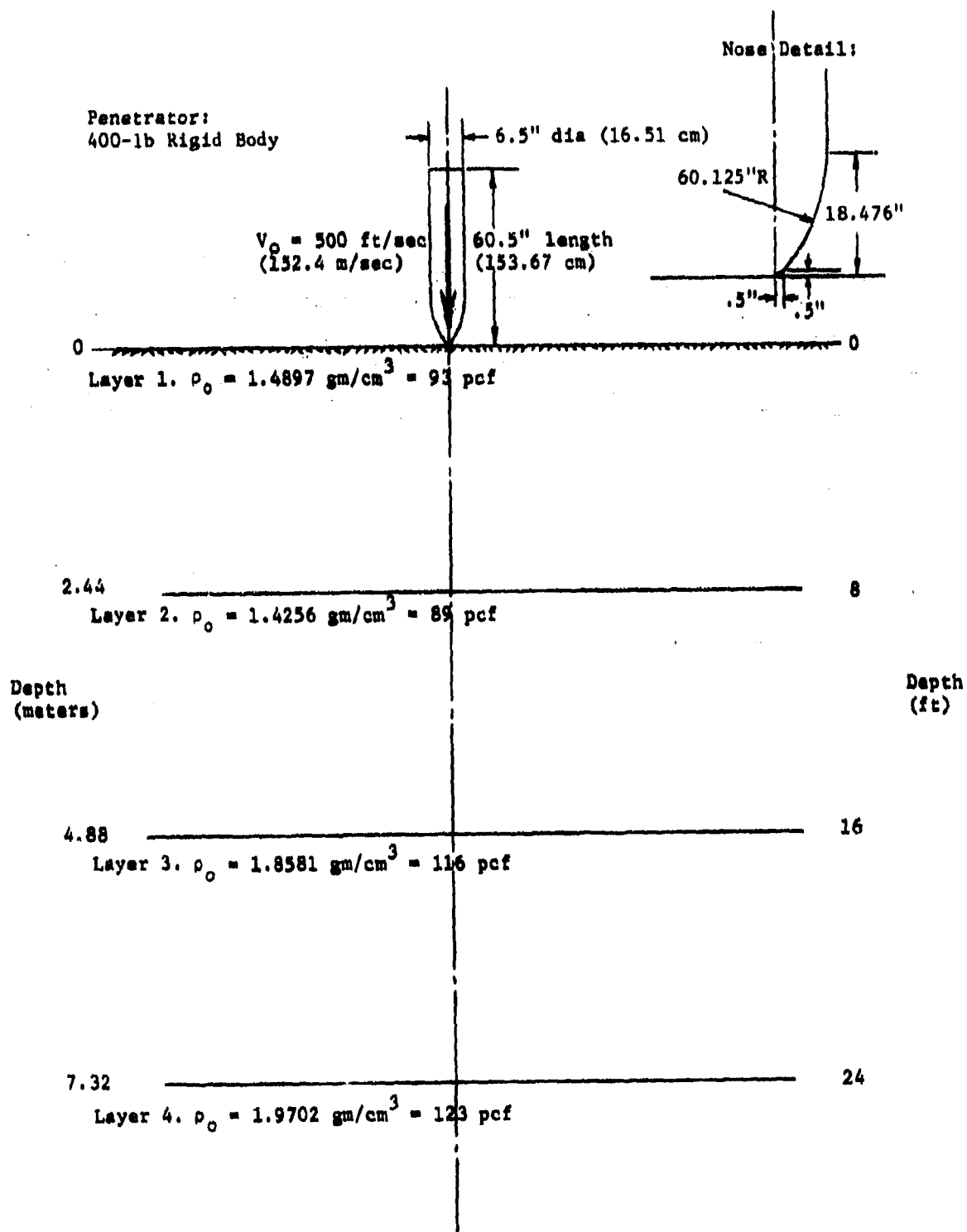


Figure 5. Problem Conditions for CRT Rigid Body
Solution of DNA Earth Penetrator Experiment

TABLE 1. SUMMARY OF TARGET MEDIA PROPERTIES

Property	Layer 1 0-8 ft	Layer 2 8-16 ft	Layer 3 16-24 ft	Layer 4 >24 ft
Density, ρ_o , gm/cm ³ lbs/ft ³	1.4897 93	1.4256 89	1.8581 116	1.9702 123
Air Fraction, V_a	37%	40%	12%	~0%
Initial value of:				
Young's modulus, E_o , psi	17173	5926	3115	2679
Shear modulus, G_o , psi	6869	2469	1154	8946
Bulk modulus, K_o , psi	11448	3292	3462	148807
Poisson's ratio, ν_o	.25	.2	.35	.497
Dilatational wave velocity c_o , fps	1013	585	447	2377
Failure surface at $P = 1000$ psi, Y , psi	540	1130	225	50
Mises limit, $Y_{max} = \sqrt{3J'_2}$, psi	750	2906	269	50

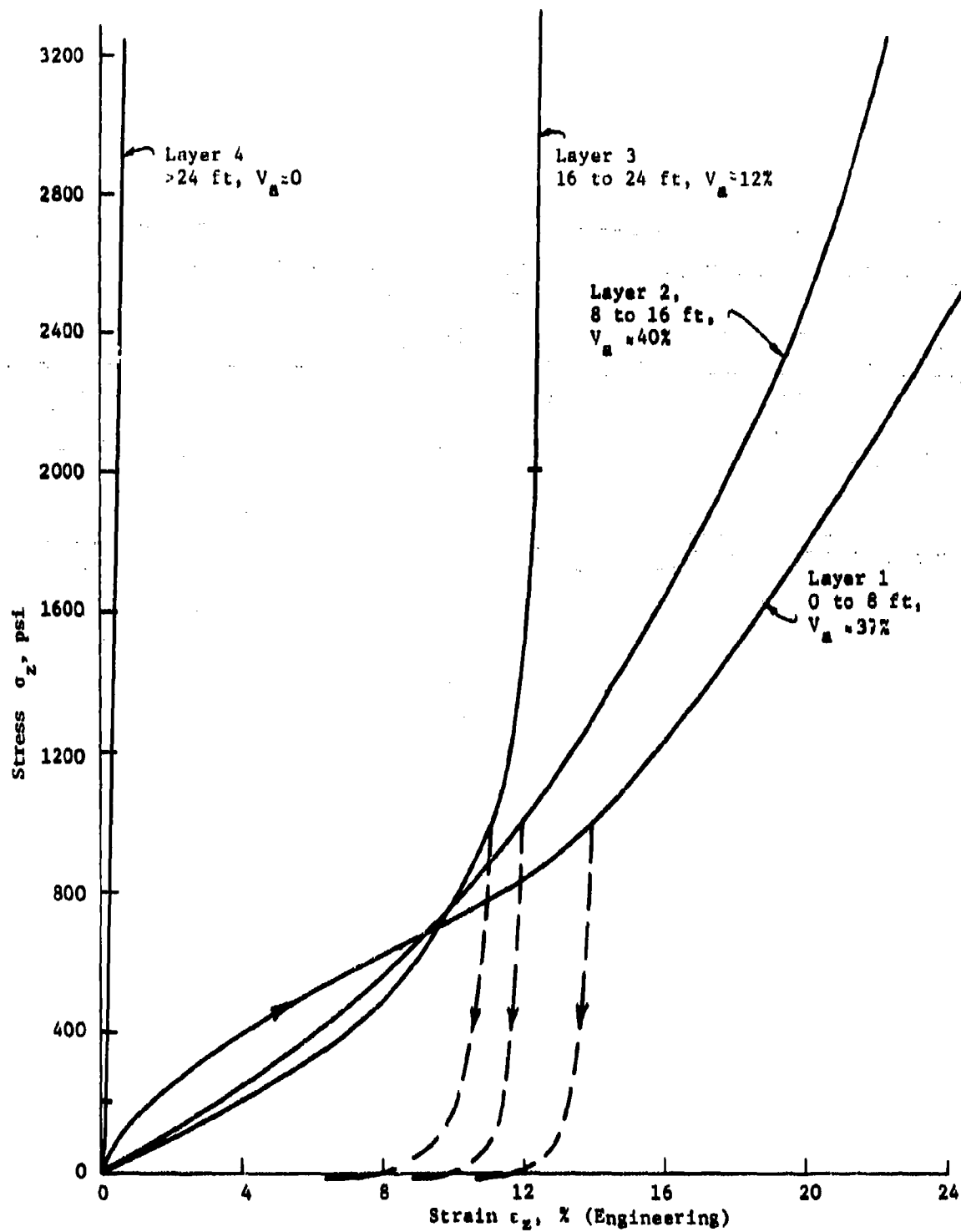


Figure 6. Uniaxial Strain Relations for DNA Penetrator Test Site, DRES, Canada

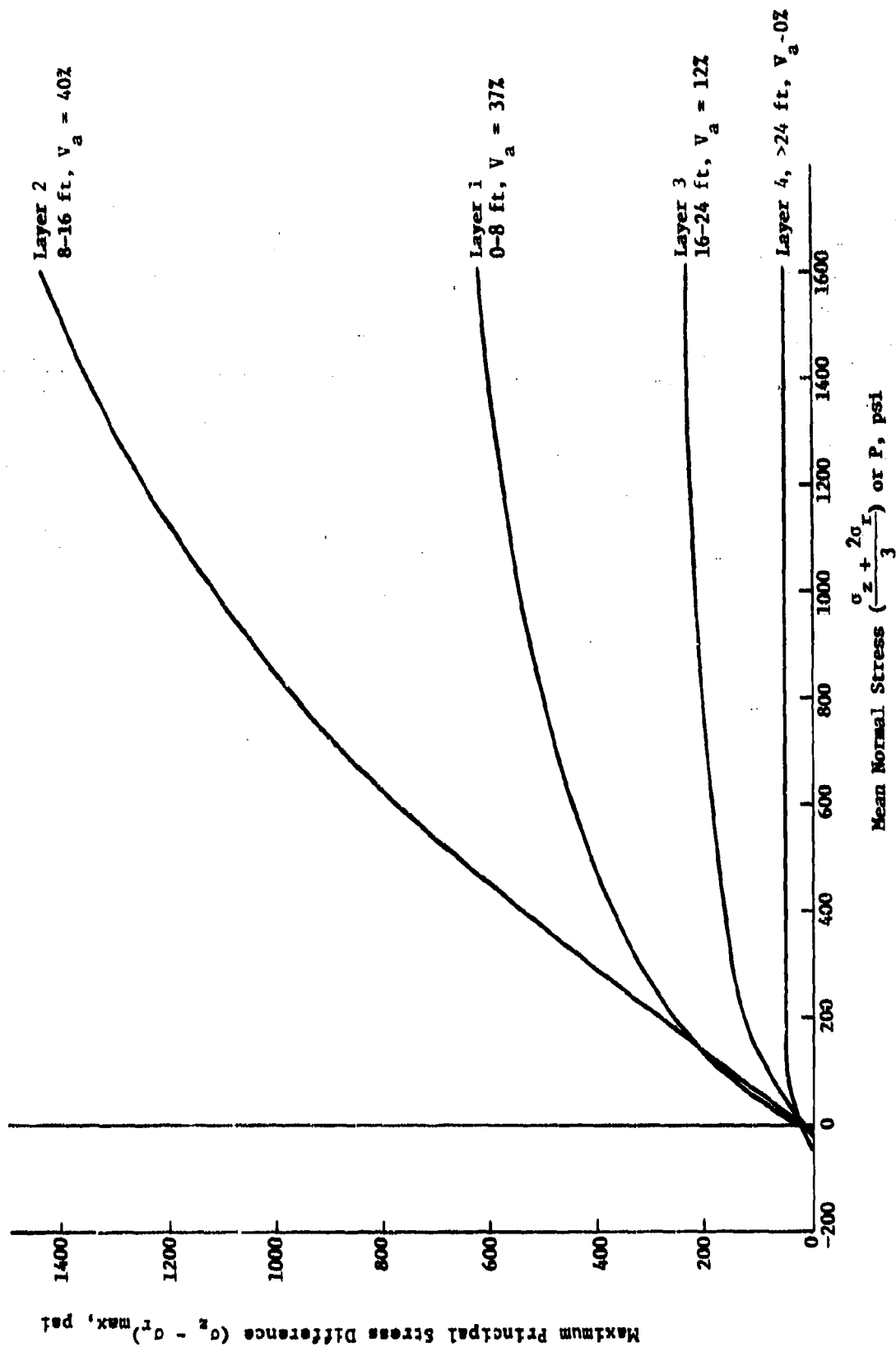


Figure 7. Shear Failure Surfaces for DMA Penetrator Test Site at IRRS

Layer 4 is considered to be water saturated, with a water content of ~30%, accounting for its low shear strength.

For all layers, a hysteretic, elastic-ideally plastic model with a non-associated flow rule (Prandtl-Reuss) was formulated. In loading, the bulk and shear moduli are functions of volumetric strain ($\mu = \rho/\rho_0$). In unloading, the bulk modulus is a function of maximum volumetric strain (μ_{\max}) or maximum pressure (P_{\max}). The unloading shear modulus is constant in Layers 1, 2, and 3. In Layer 4, the unloading shear modulus is dependent on the unloading bulk modulus. Variable failure surfaces, where the yield condition is a function of the pressure, were employed.

Detailed descriptions of the material models are contained in Appendix A.

2.3 FRICTION ALONG PENETRATOR-TARGET SOIL INTERFACE

A general friction rule was formulated and programmed into the code that includes frictional stresses in the equations of motions of both sides of the sliding interface. The code can readily accept any friction rule. For this problem, a simple friction rule was used to compute the applied shear stress on the soil-penetrator interface; i.e.,

$$\tau = .6 \frac{Y(\sigma_n)}{\sqrt{3}}$$

where Y is the yield surface equation of the medium and σ_n is the stress component normal to the penetrator surface. The yield surface equations for each layer are given in Appendix A. Selection of the .6 coefficient was

based partially on discussions with WES. This friction rule produced relatively large frictional stresses, which accounted for 40-65% of the total decelerating force in the first three layers.

Time constraints did not permit the use of a more sophisticated friction model for this calculation. Additional work is underway which accounts for limitations due to the internal friction in the soil and the effects of failure. Guidance from experiments measuring frictional parameters under conditions which are relevant to earth penetrators is also needed.

SECTION III

COMPUTATIONAL METHOD

The WAVE-L code was employed for this calculation. WAVE-L is a two-dimensional code which solves the equations of motions for elastic-plastic bodies by means of a finite difference Lagrangian technique. The mathematical formulation is basically the same as that described by Wilkins.⁴ Lagrangian cells are normally attached at the lattice points. In order to allow penetration of the projectile through the computational grid, a decoupling criteria was used along the axis of symmetry in the soil medium. A sliding interface, in conjunction with a friction model, was used between the rigid body and the soil. A lithostatic field in the soil was generated by prescribing initially compressed soil states.

3.1 BASIC GRID DESIGN

The rigid contour of the penetrator periphery, including the conical tip, was resolved with a total of 44 lattice points. The spacing in the vertical direction began with .5 in. at the tip, gradually increasing to 1.625 in. along the ogival section, and continuing at a uniform 1.625 in. to the rear of the projectile.

The computational grid in the soil was divided into two principal regions, as shown in Figure 8. From the axis of symmetry out to 19.5 in. radius, all cells were initially uniform, with $\Delta r_0 = \Delta z_0 = 1.625$ in. (Thus there are initially 4 cells per penetrator diameter.) Beyond 19.5 in. radius, Δr_0 increases in 10% steps. The grid

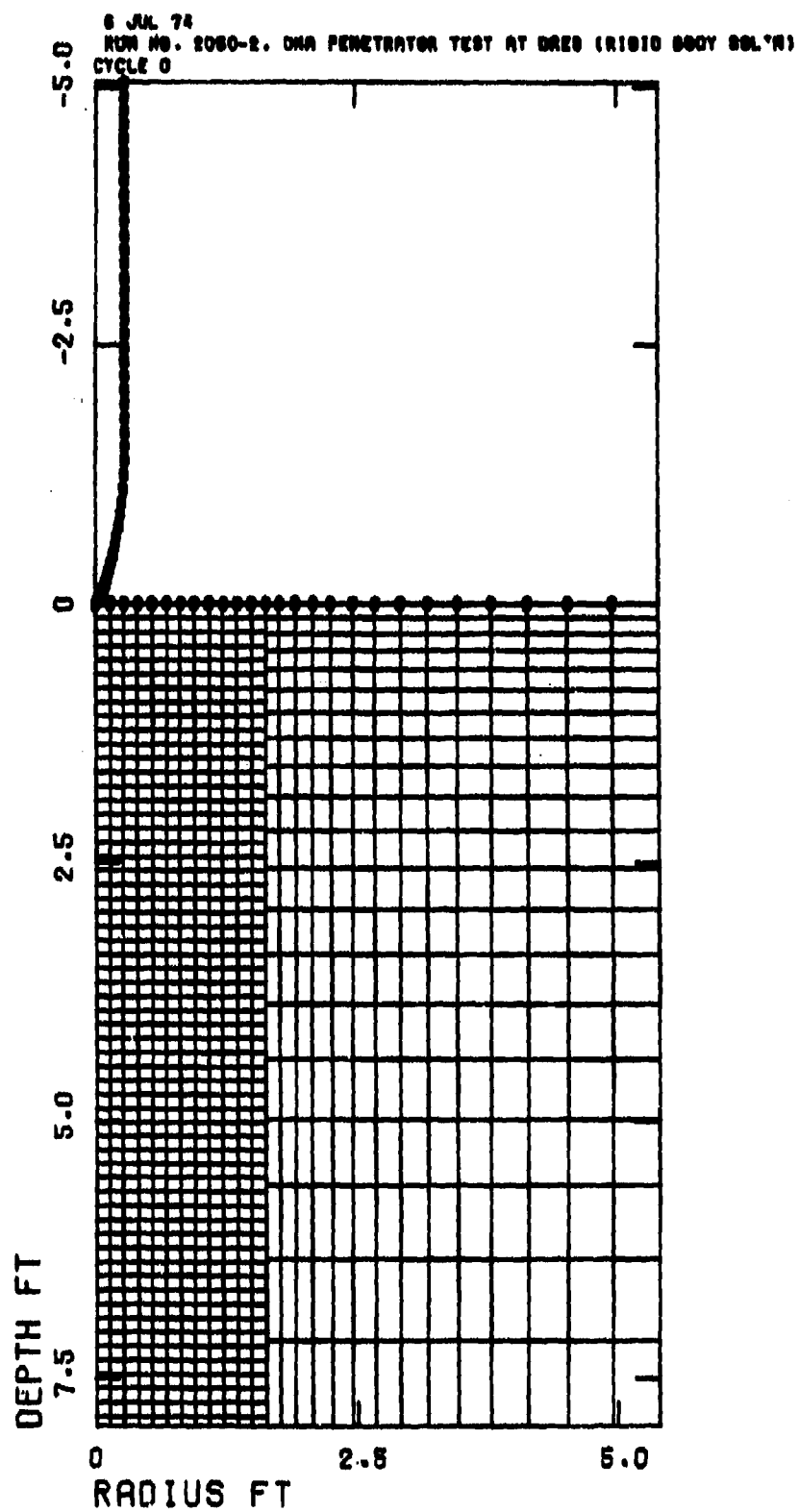


Figure 8. Initial Grid Configuration for Code Solution

extended to a radius of 7.1 ft (beyond the field of view in the figure). In this outer region, Δz_0 also increases (with increasing depth) in 10% steps until it reaches a maximum value of $10\Delta z_0$. This design for the outer region conserves computational cells, without significantly degrading the solution.

A slide line was specified that runs along the axis in the soil and along the penetrator contour. As the penetrator impinges into the target, this dual line defines the penetrator-soil interface and allows slippage and/or separation to occur. Another slide line is required along the boundary between the two grid regions. This line is needed to accommodate the differing alignment of the grids on both sides, but no substantial slippage occurs.

3.2 "ROLLING GRID"

If the initial computational grid is required to cover the entire target region which is involved in the complete penetration event, the grid will involve an extraordinary number of cells in order to achieve reasonable spatial resolution. The alternative is a smaller number of large cells (if the coarse resolution is acceptable). In either event, the efficiency of a solution of an event (such as a deep penetration) where the action is predominantly in one direction can be substantially increased by deleting cells after the "action" has passed, and adding new cells in the region where activity has not yet started. This was done in the current solution by deleting rows of cells in the target material behind the penetrator (where the material was judged to have little or no effect on the continuing solution) and simultaneously adding rows of cells in the as-yet

inactive region ahead of the penetrator. This technique conserves computational cells and thus increases the available spatial resolution which is attainable with a given number of cells in a problem. Thirty-two vertical grid lines and a maximum of 106 horizontal grid lines were used. The number of computational cells in the problem at any one time ranged from 1300 to 1800.

3.3 PRE-DEFORMED GRID AND LOCAL REZONING

During penetration, the cells in the soil near the penetrator become severely distorted. This distortion occurs for two main reasons: (1) cells from near the axis are squeezed as they are pushed outward in the flow around the penetrator nose, and (2) where large frictional stresses are present along the sliding interface, cells are distorted by the shear. While such distortion appears physically consistent with the frictional rule and the penetration dynamics, it causes computational inaccuracies and reduces the integration time step.

To correct extreme distortion, local rezones were periodically performed during the course of the integration. In a local rezone, the computational grid in the distorted region is repositioned so as to give more regular cell shapes. A comprehensive rezone processor is used for this purpose that correctly redistributes the cell variables among the new cells.

To increase the time interval between local rezones, a special grid was designed, in which cells in the first two columns near the axis are canted upward. As the penetrator reaches these cells, frictional forces deform the

cells downward. The pre-deformation is a geometric convenience only, and does not affect the stress field which is generated in any important way. Figures 9 and 10 show the grid before and after a local rezone. Note in Figure 9 that the pre-deformed cells ahead of the penetrator become "bent down" as they drag along the penetrator surface.

3.4 GRID DECOUPLING

The sliding interface formulation in WAVE-L includes the capability for dynamically decoupling or unlocking the grid points as a prescribed decoupling or failure criterion is met. Decoupled grid points can slide along the interface and also separate (forming a void). In a penetration problem, decoupling permits the cells initially attached to the axis to flow around the advancing nose shape. In this calculation, decoupling occurred when the generalized plastic strain reached 1%. Generalized plastic strain is a measure of the cumulative plastic deformation an element undergoes, and is defined⁸ as

$$\bar{\epsilon}^P = \int \left(\frac{2}{3} d\epsilon_{ij}^P d\epsilon_{ij}^P \right)^{1/2} .$$

$d\bar{\epsilon}^P$ is always ≥ 0 , thus $\bar{\epsilon}^P$ monotonically increases as any type of plastic strain is experienced.

3.5 VOID OPENING AND CLOSING

During high-velocity penetration, the soil flows around the nose and typically separates from the penetrator before reaching the tangency point. This separation and the resultant void opening are critical factors in the

8 OCT 74 CALIFORNIA RESEARCH AND TECHNOLOGY WAVE-L CODE
 RUN NO. 2050-2, DWA PENETRATOR TEST AT DRES (RIGID BODY SOL'N)
 CYCLE 1034

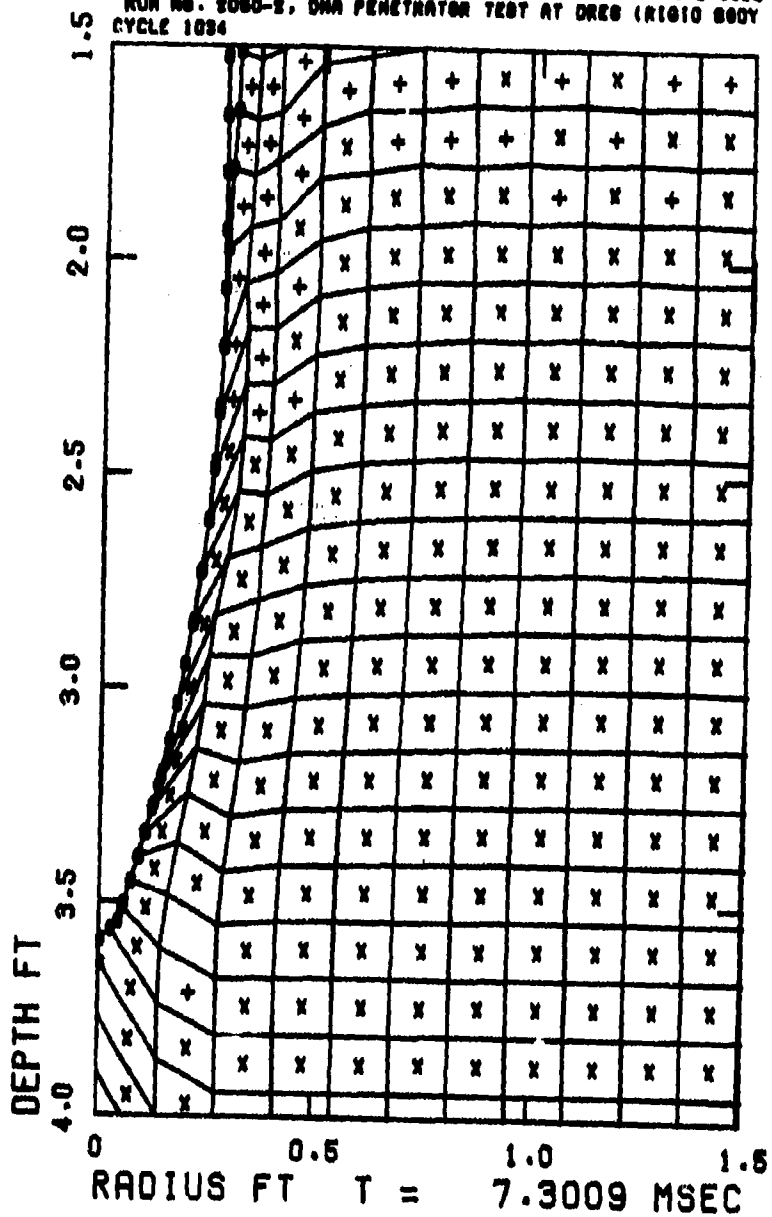


Figure 9. Grid Configuration before Local Rezone

9 OCT 74 CALIFORNIA RESEARCH AND TECHNOLOGY WAVE-L CODE
 RUN NO. 2050-2, ONA PENETRATOR TEST AT ORES (RIGID BODY SOL'N)
 CYCLE 1094

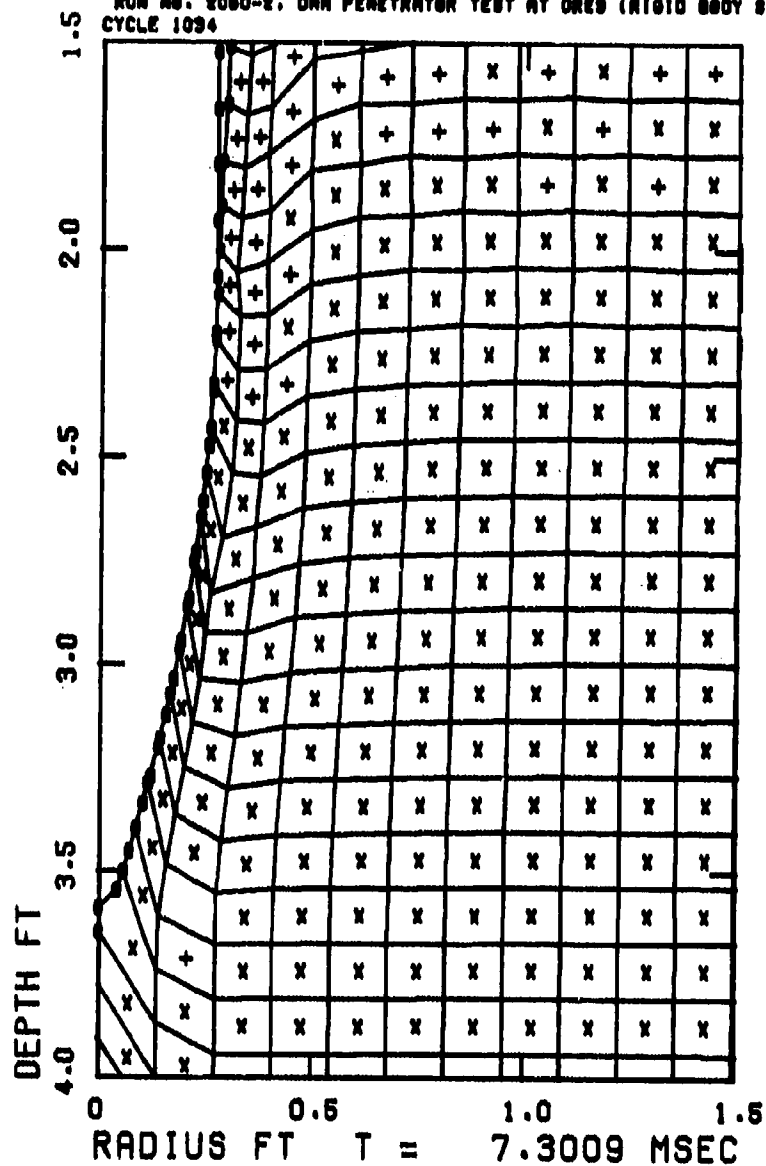


Figure 10. Grid Configuration after Local Rezone

calculations, since they determine the effective contact area over which frictional forces are applied. In this calculation, separation of a soil point could occur when the stress normal to the penetrator was no longer compressive; i.e., $\sigma_n < 0$. When this criterion is met, the point is moved as a free surface point. (The soil point may subsequently collide with the penetrator, in which case it again becomes attached to the penetrator. Closing of the void presumably occurs during the terminal stages of penetration.)

3.6 "LEAPFROGGING"

During the penetration of Layer 1, it was observed that the deceleration remained at a relatively constant level following the burial of the penetrator nose. This should be the case, so long as the penetrator velocity is not drastically changed and if the contact area of the nose with the soil remains about the same. Since no important new information is gained by integrating out the complete penetration of a layer, it was decided to skip ahead after the penetrator nose had become fully immersed in a layer. To accomplish this, the solution is stopped after the deceleration level in a layer has been established. It is restarted (with an appropriately reduced velocity) with the nose a short distance from the next layer. This technique is illustrated in Figure 11.

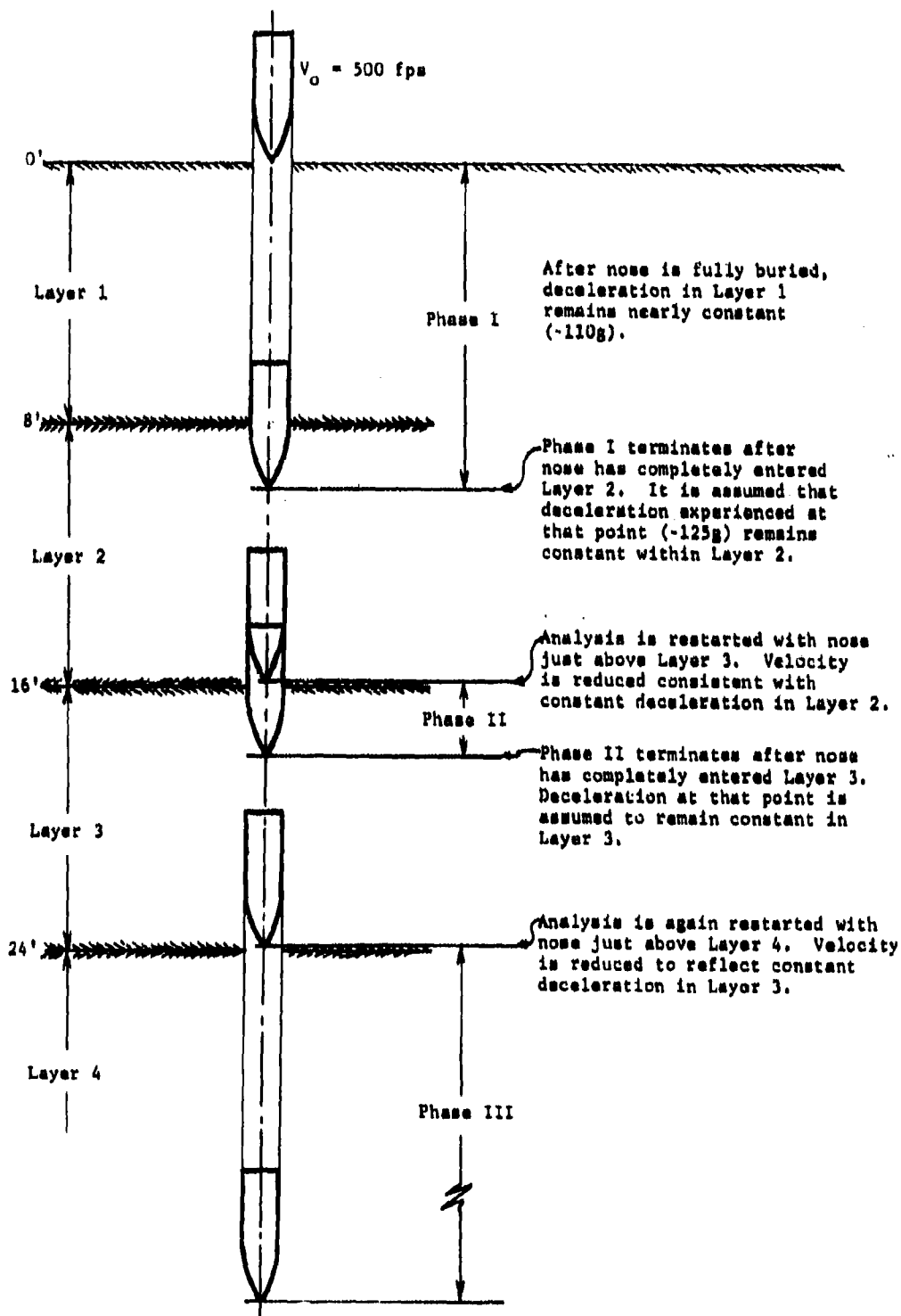


Figure 11. Illustration of "Leapfrog" Technique for Computing Deep Penetration

SECTION IV

NUMERICAL RESULTS AND EXPERIMENTAL COMPARISONS

4.1 PENETRATOR DYNAMICS

The penetration was numerically integrated completely through Layer 1, and into Layer 2 to a depth of 300 cm, or 9.8 ft. (This is identified as Phase I in Figure 11.) Figure 12 shows the computational grid at the end of Phase I. (Badly distorted cells have been deleted from the inside of the hole behind the penetrator. These cells no longer affect the penetration, and their removal improves computational efficiency.)

Figure 13 shows the axial force on the penetrator and the penetrator deceleration vs depth. The deceleration climbed sharply as the penetrator nose first entered the soil, reaching a level of about 110 g's where it remained fairly constant during the remainder of Layer 1. As the penetrator entered Layer 2, the deceleration increased somewhat, reaching about 125 g's. Based on the experience in Layer 1, it was assumed that the deceleration would continue at 125 g's in Layer 2. This assumption forms the basis for the "leapfrogging" approach described in Section 3.5, by which the time-consuming and largely uninteresting integration of the quasi-steady state penetration within a geologic layer is bypassed. Phase I of the calculation was thus stopped with the penetrator at 300 cm (9.8 ft) depth. This is 56 cm into Layer 2. Its velocity, V_{If} , at this time was 131 m/sec (430 ft/sec).

"x" in cell means material is currently on yield surface with $P \geq 0$;
 "+" means material failing with $P < 0$.

25 JUL 74 CALIFORNIA RESEARCH AND TECHNOLOGY MATH-L CODE
 RM 100, 1000-9, ONE PENETRATOR TEST AT ONE (1010 000 00, 1)
 CYCLE 0007

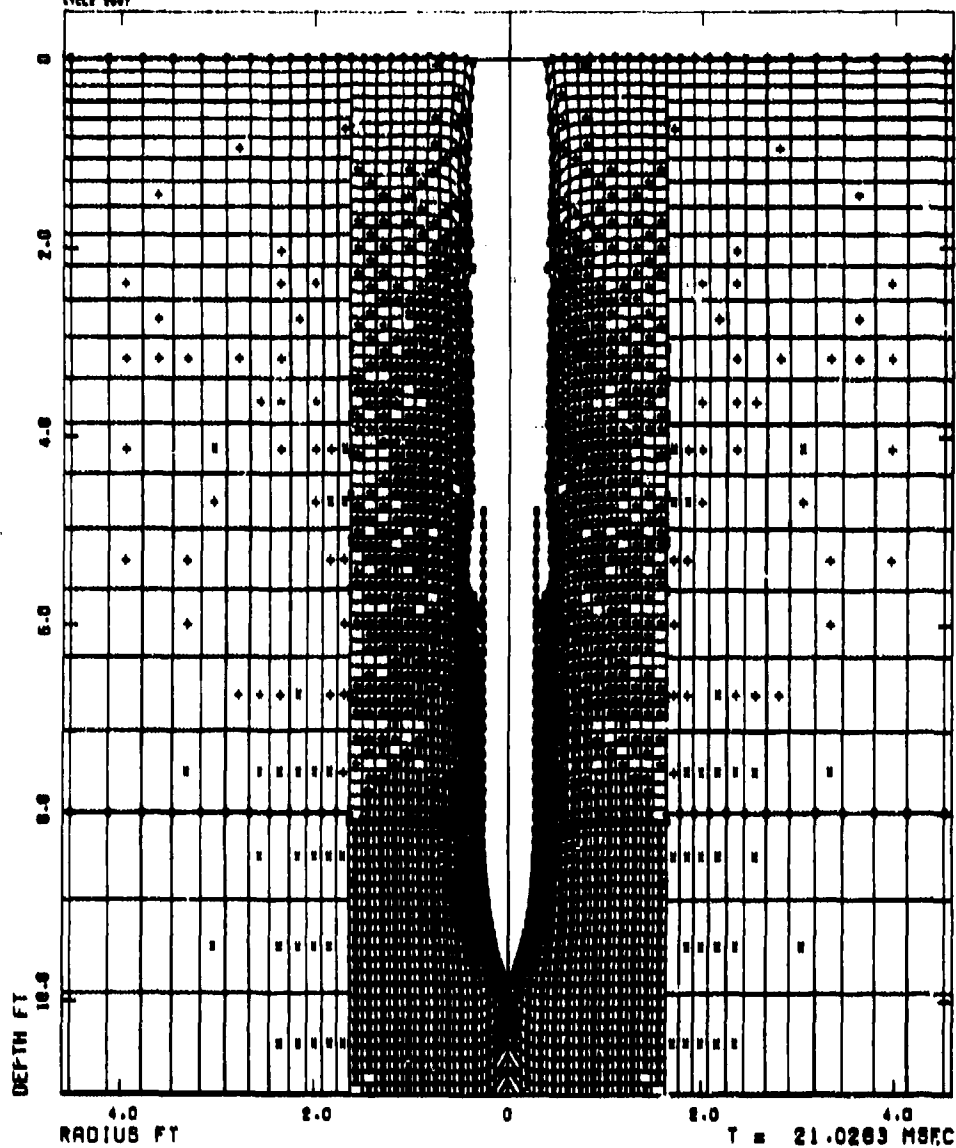


Figure 12. Grid Configuration at End of Phase I of the Solution, Penetrator at 300 cm Depth

JUL 74

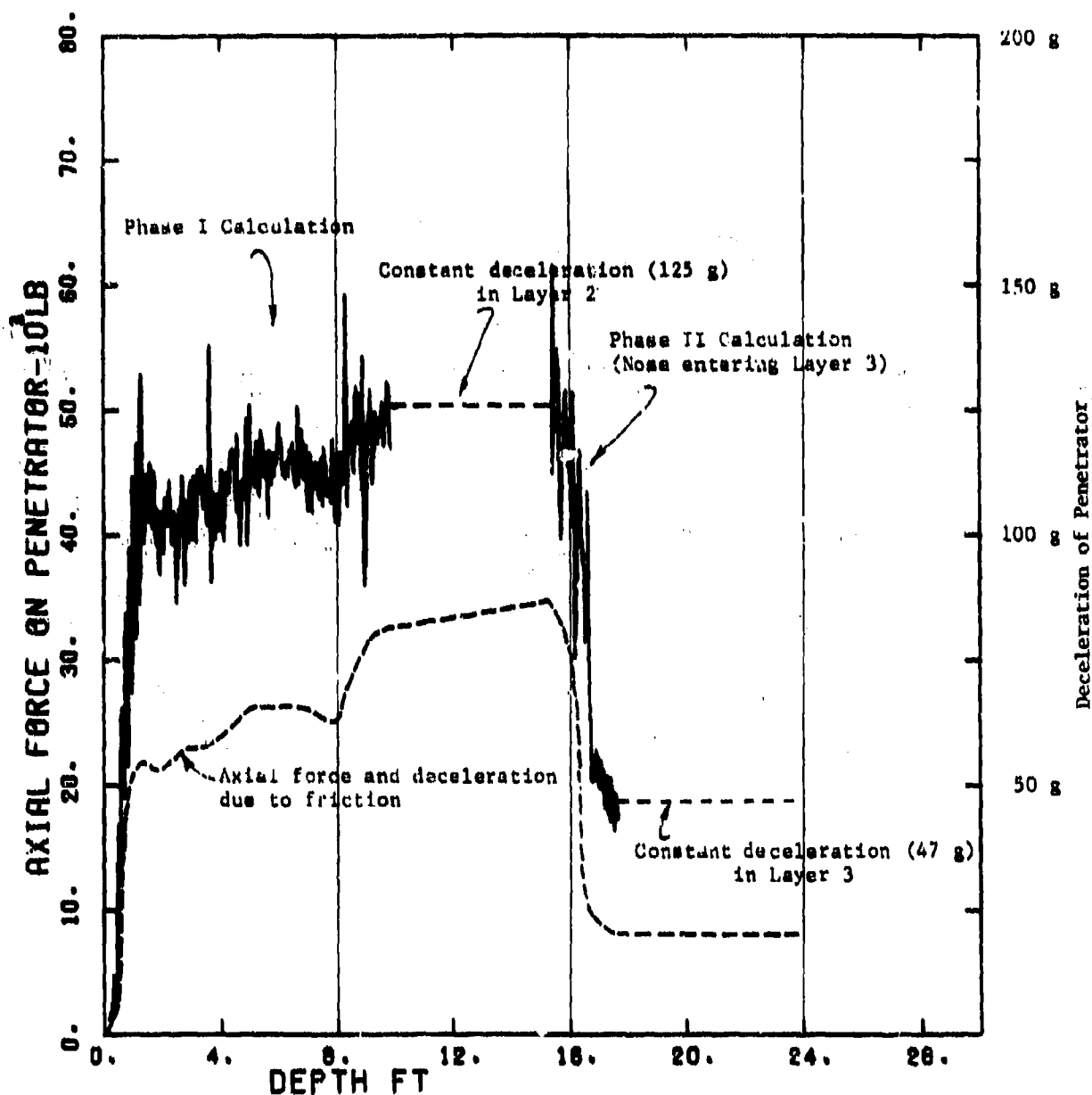


Figure 13. Axial Force on Penetrator (showing total axial force and frictional component) and Deceleration of Penetrator vs Depth

To start Phase II of the calculation, the penetrator depth was set at 469 cm, or 15.4 ft, and it was given an initial velocity, V_{II_i} , of 114 m/sec, or 374 ft/sec. (This was determined by applying 125-g deceleration to V_{I_f} , the final velocity at the end of Phase I.) The initial particle velocities in the soil field around the penetrator for Phase II were set by reducing the field velocities at the end of Phase I by the ratio $V_{II_i}/V_{I_f} = .87$. This gives a reasonable estimate of the field velocities, and inaccuracies are quickly corrected as the integration continues.

Using these starting conditions, the Phase II integration was carried out as the penetrator nose moved from Layer 2 into Layer 3, to a depth of 536 cm, or 17.6 ft. As is seen in Figure 13, the deceleration dropped sharply as the penetrator entered Layer 3, reaching a level of 45-50 g's. Again assuming that this level would remain fairly constant within Layer 3, and using a value of 47 g's, it is estimated that the penetrator reaches Layer 4, or a depth of 24 ft, at 59.5 msec and with a velocity of 101 m/sec, or 330 ft/sec. The leapfrogging approach could have been used to start a Phase III calculation (covering penetrator entry into Layer 4), but time constraints precluded further integration of the problem.

Figure 14 shows the penetrator velocity vs depth. Figure 15 shows the depth of penetration vs time. Figures 16 and 17 show the axial force, deceleration, and velocity vs time.

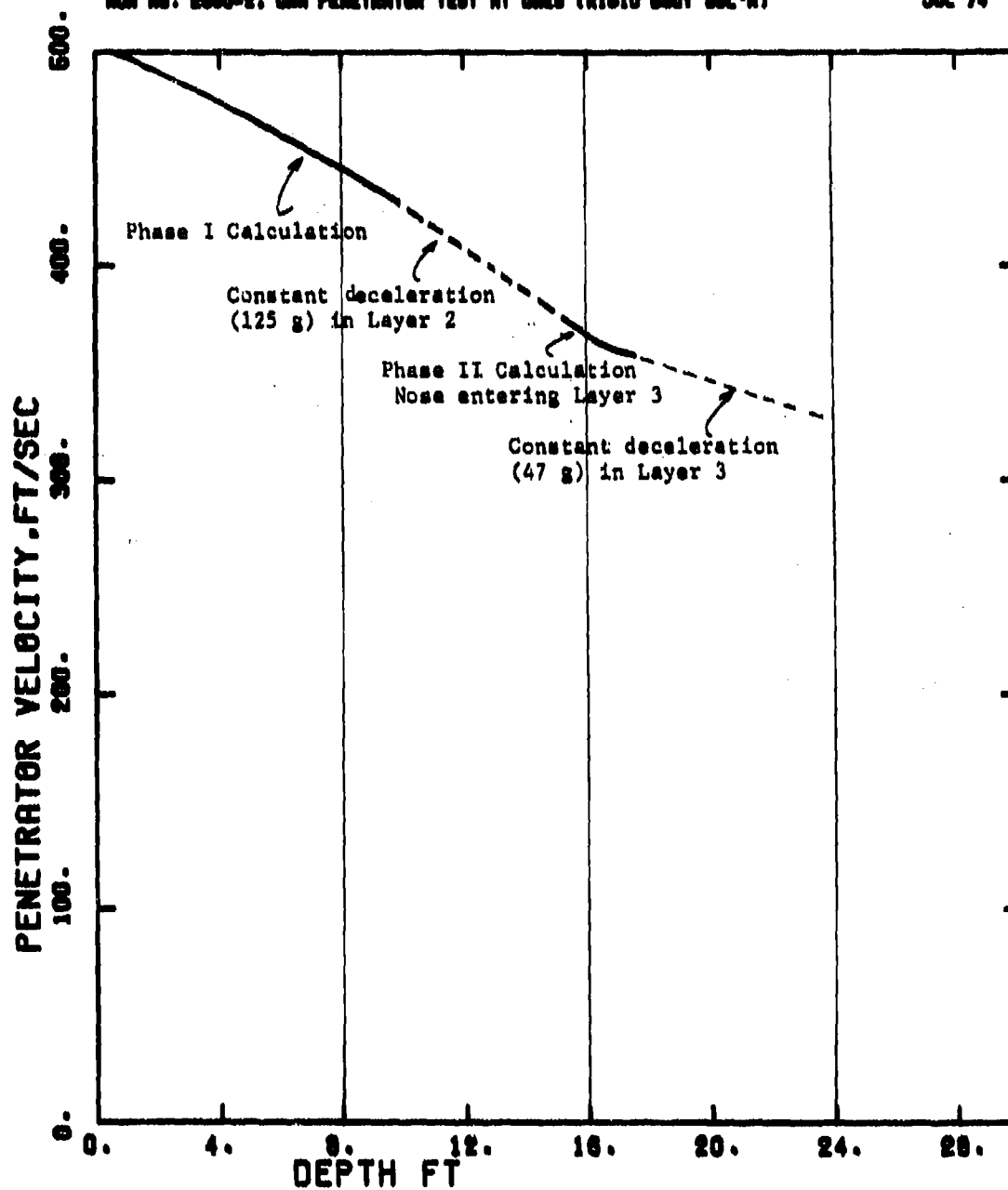


Figure 14. Penetrator Velocity vs Depth

JUL 74

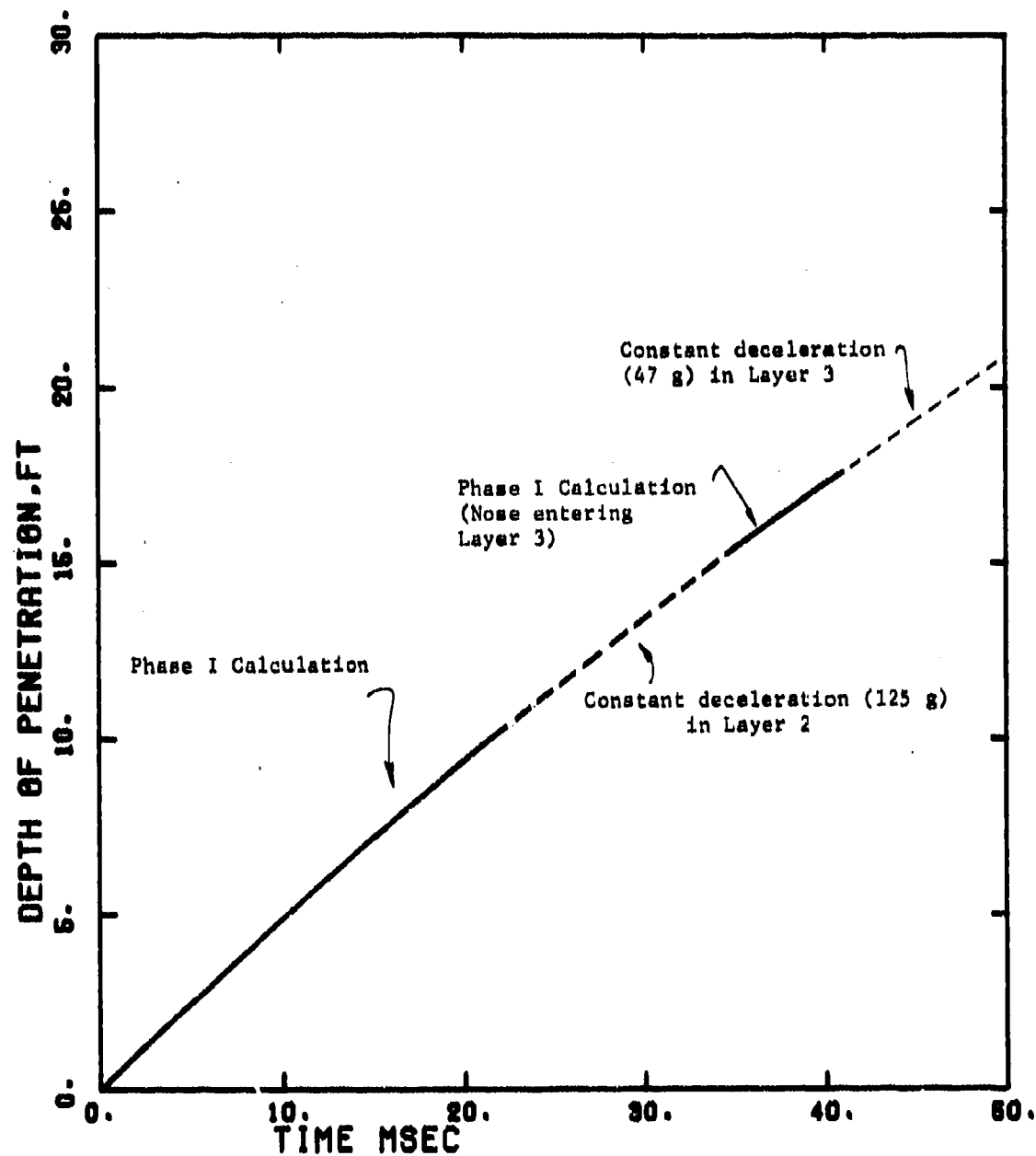


Figure 15. Depth of Penetration vs Time

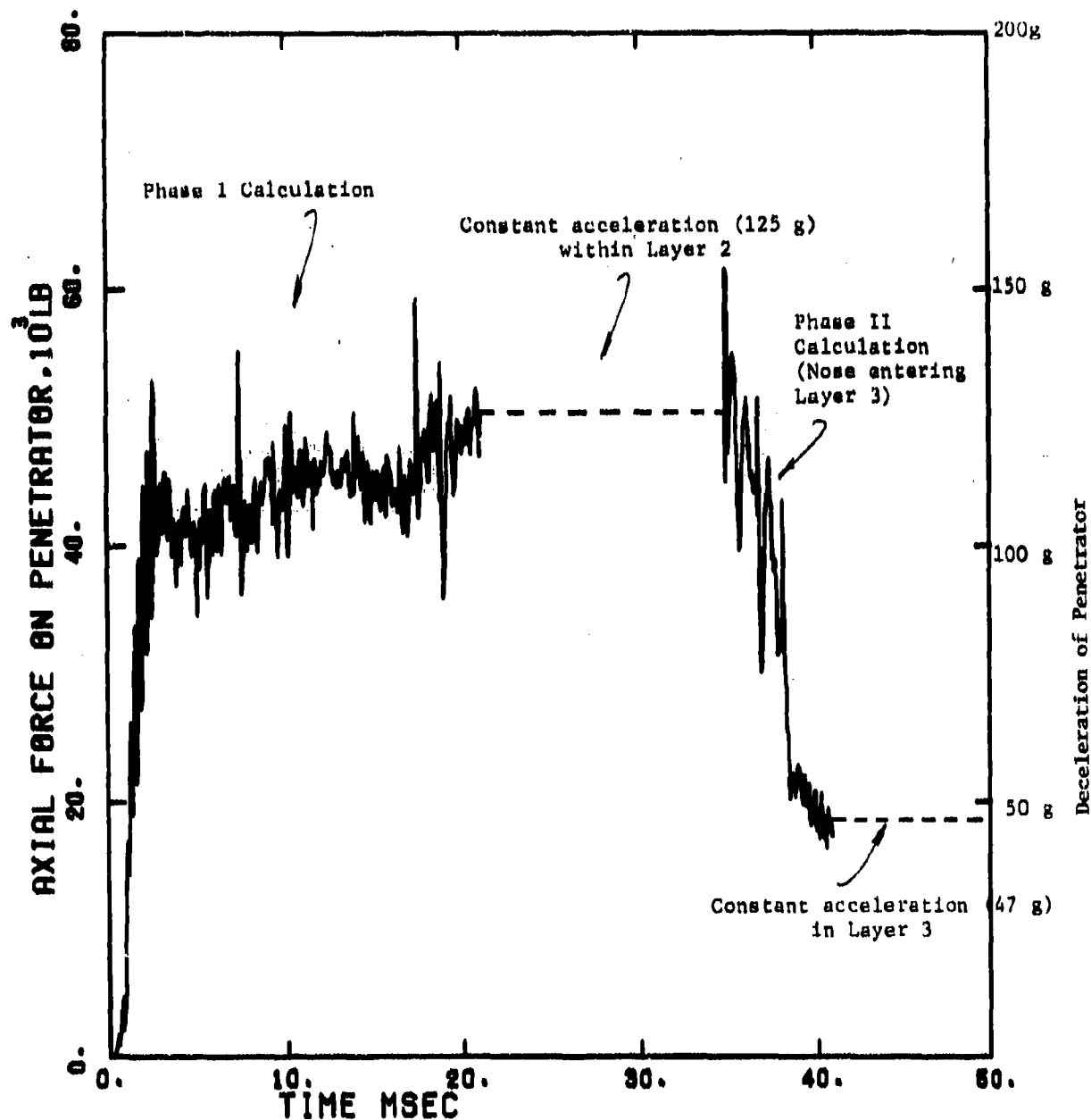


Figure 16. Total Axial Force on Penetrator and Deceleration of Penetrator vs Time

JUL 74

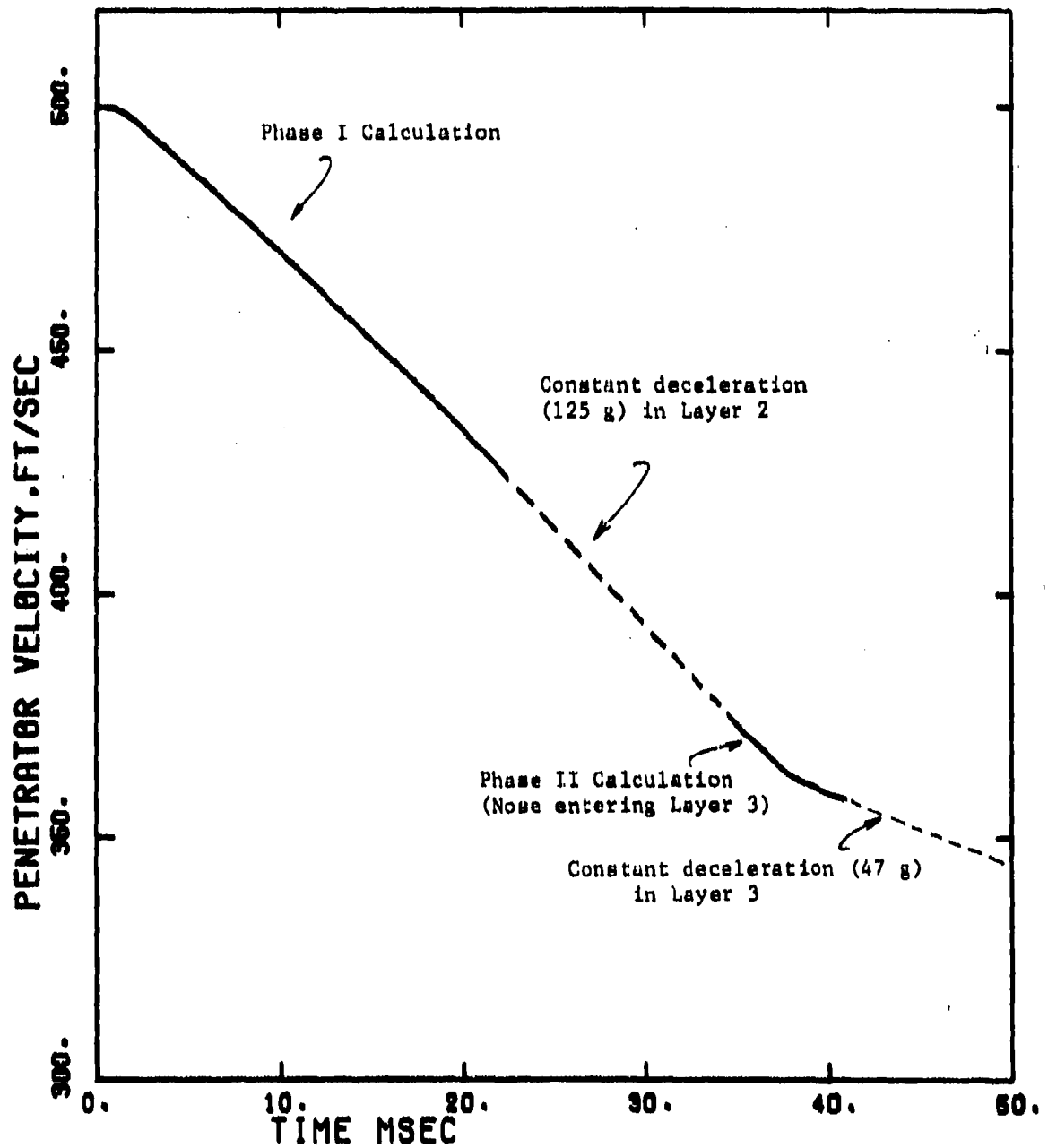


Figure 17. Penetrator Velocity vs Time

4.2 PENETRATOR-SOIL INTERACTIONS AND SOIL RESPONSE

4.2.1 Field Plots

Appendix B contains a series of field plots of the computational grid, particle velocities, and principal stresses in the soil target medium around the penetrator. These plots are for penetrator depths of 10 cm, 40 cm, 200 cm, 280 cm, and 528 cm.

4.2.2 Friction

In addition to the total axial force on the penetrator and its deceleration, Figure 13 shows the axial force and deceleration due to friction on the penetrator-soil interface. Figure 18 shows the frictional force as a percentage of the total axial force on the penetrator. It is seen that the friction rule used in this calculation was responsible for a 40-60 percent of the penetrator deceleration in all the layers considered.

Figure 19 shows the loading distribution along the penetrator nose in terms of the normal and tangential (frictional) stresses. This plot is made with the nose at 200 cm (6.6 ft), entirely within Layer 1. (Loading distributions for other depths are given in Appendix C.) The normal stress, σ_n , falls sharply with increasing distance from the nose, dropping to zero at about 38 cm, or 15 in. However, frictional stress, τ , remains fairly level along the nose. This is because τ is limited in the friction rule by the yield surface. The yield surface for Layer 1 is fairly flat, as seen in Figure 7.

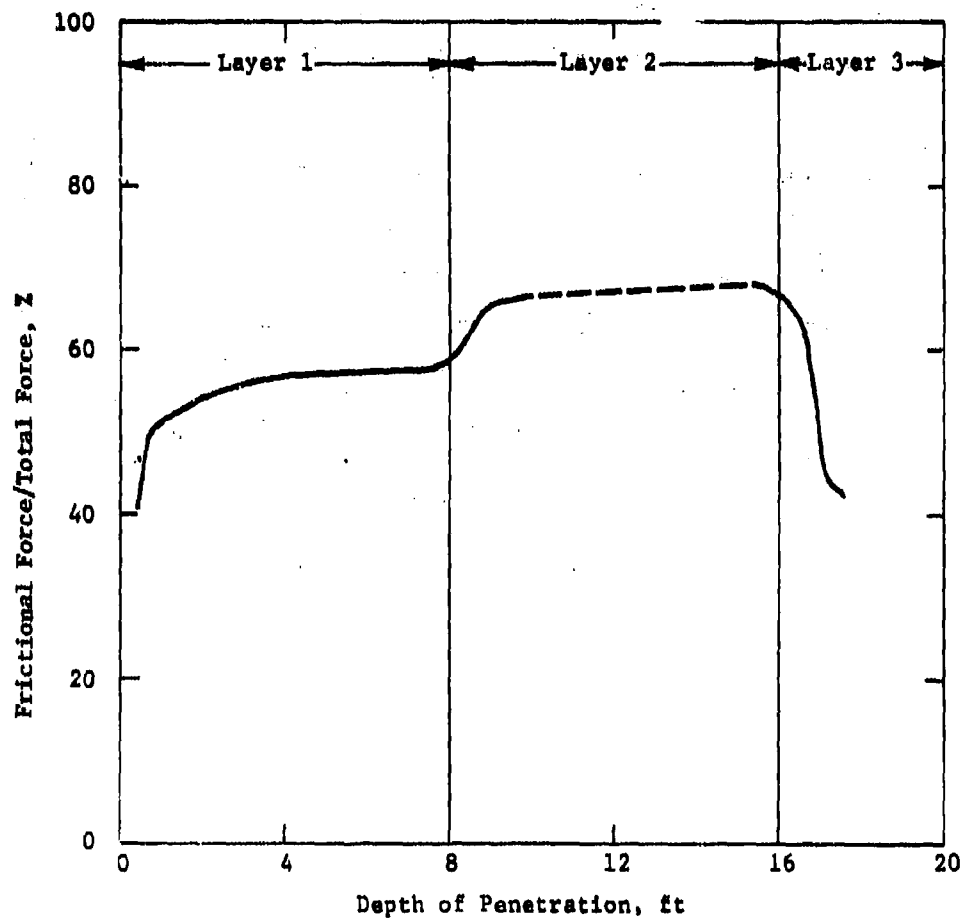


Figure 18. Ratio of Frictional Force to Total Axial Force on Penetrator vs Depth of Penetration

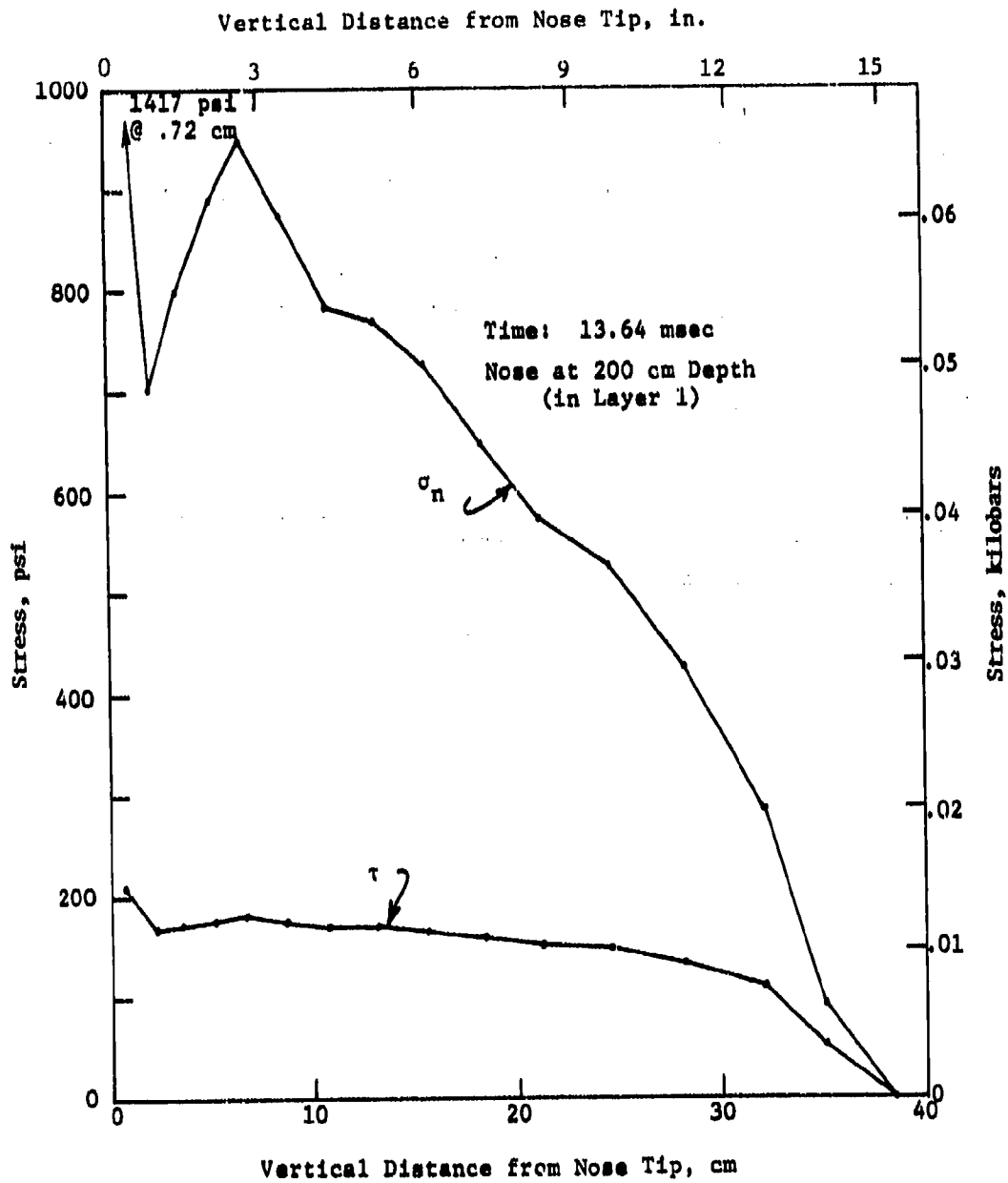


Figure 19. Normal and Tangential Stress (σ_n, τ)
Distributions along Penetrator Nose

When the normal stress, σ_n , drops below zero, the grid can open to represent separation. This occurs as soil material flows around the ogival nose, nearing the tangency point. Tangency with the cylindrical body is at about 18.5 in. In Layers 1 and 2, σ_n became tensile and target material separated from the penetrator at about 38 cm, or 15 in., as seen in the plot in Figure 20. After separation, soil may subsequently rebound against the aft surface of the penetrator. This did not occur in the current calculation (even if the deleted cells are taken into consideration), but it should be expected as the velocity drops further. While normal stresses acting against the body as a result of such rebound will presumably be small, they may be applied over a large area, and can hence lead to significant frictional drag at late times in the penetration.

While frictional stresses are fairly level along the penetrator nose, the frictional force distribution is much different. Figure 21 shows the frictional force per unit length along the penetrator in Layers 1, 2, and 3. In all layers, friction force peaks several inches back from the nose. The frictional force is still quite high near the point where the target soil separates from the penetrator, despite the fact that normal stresses drop sharply. This is due to the increasing surface area of the nose as distance from the tip increases, and to the yield surface limitation on frictional stresses in the region where normal stresses are high (i.e., nearer the tip).

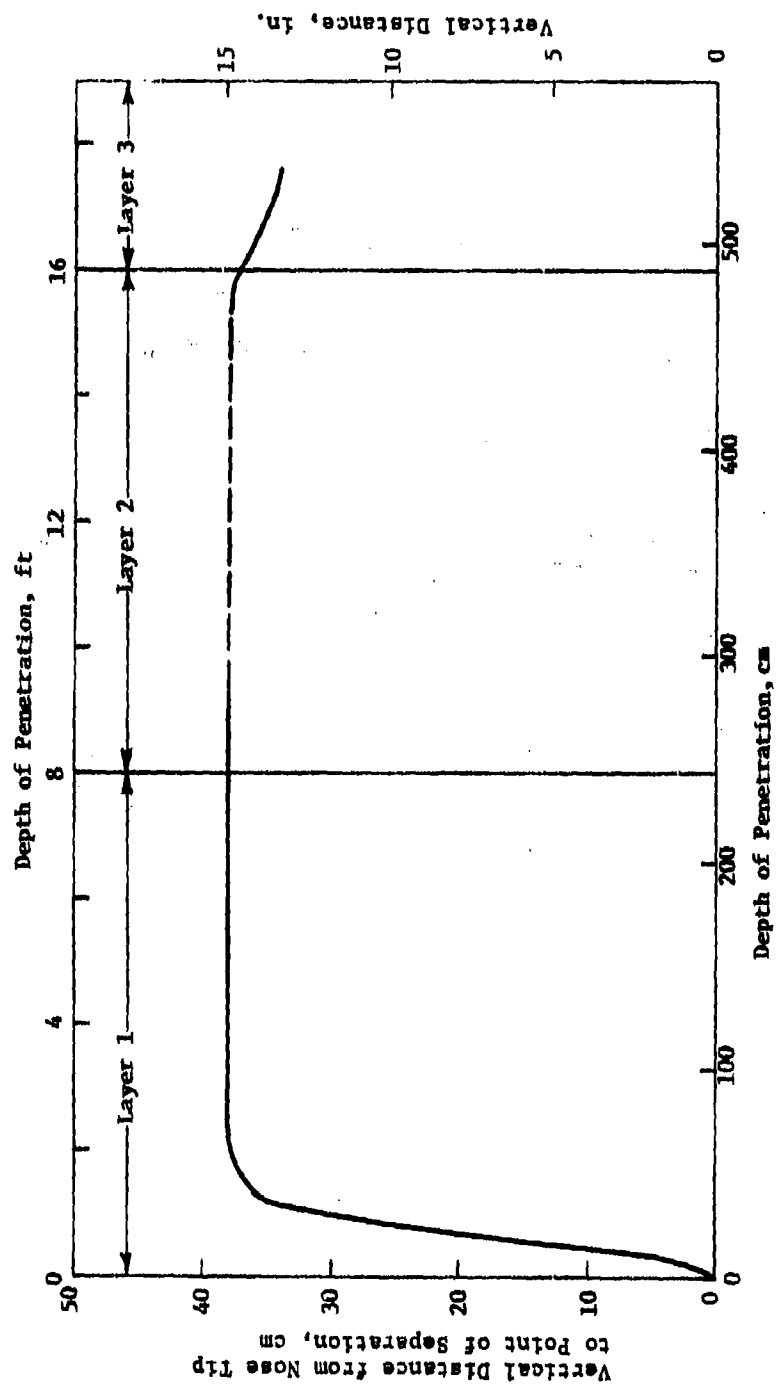


Figure 20. Point of Separation of Target Soil from Penetrator vs Depth of Penetration

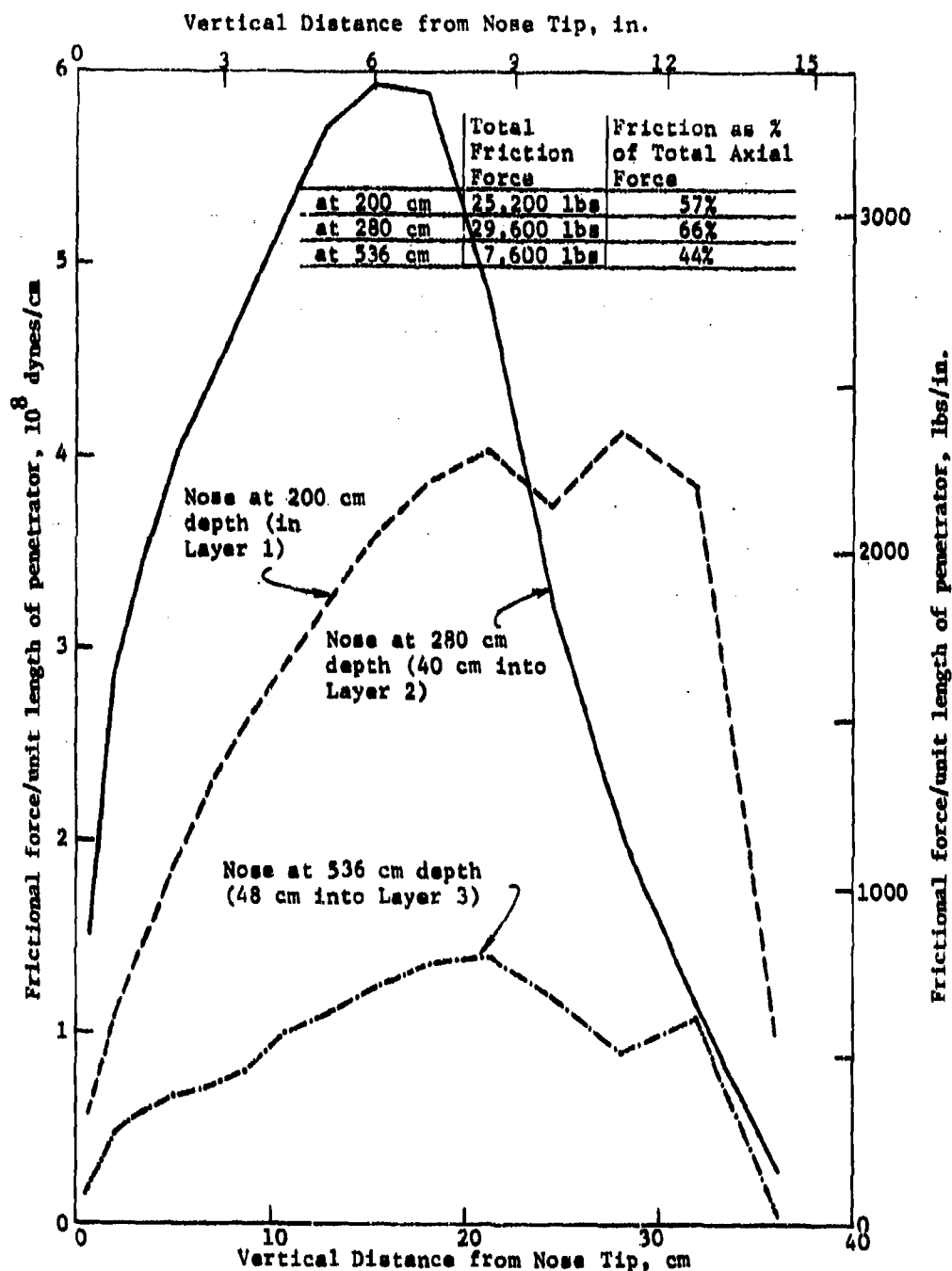


Figure 21. Frictional Force per Unit Length along Penetrator

4.2.3 Pressures and Stresses in Target near Penetrator Nose

Figure 22 contains vertical profiles of pressure in the target soil along the axis and next to the penetrator nose. (The plotted pressures are from the first row of computational cells, which are attached to the axis ahead of the penetrator, and are in contact with the penetrator surface between the nose tip and the separation point.) Three profiles are given, corresponding to representative depths in Layers 1, 2, and 3. Pressures build up relatively slowly ahead of the penetrator, reaching only 100-200 psi 10 cm ahead of the penetrator. Peak values (~1000 psi in Layers 1 and 2) occur near the nose tip. There are large oscillations as unloading starts (probably due to the finite nature of the grid and the sharply hysteretic unloading model), but unloading is otherwise fairly linear to the separation point.

Plots of radial stress profiles in the soil outward from the penetrator are given in Figures 23 and 24 at penetration depths of 127 cm (Layer 1) and 300 cm (Layer 2). This type of plot is useful in assessing the adequacy of the zoning employed. The sharp stress gradient near the nose tip indicates that finer zoning in the radial direction may be needed. The radial zoning employed is probably adequate, however, at the halfway point and beyond. A study to determine the zoning requirements for earth penetrator problems is planned as part of future work.

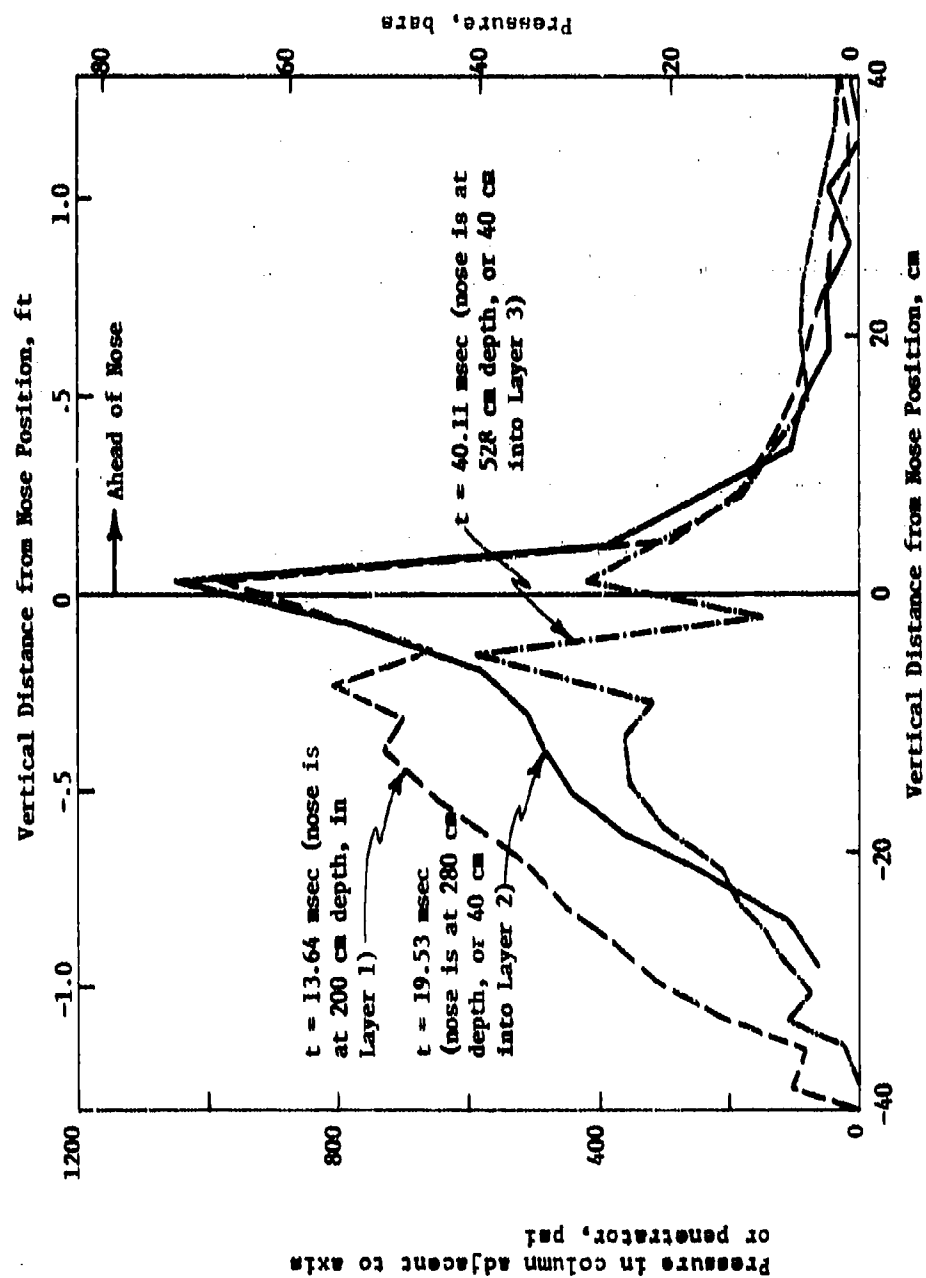


Figure 22. Pressure vs Vertical Distance from Nose Tip

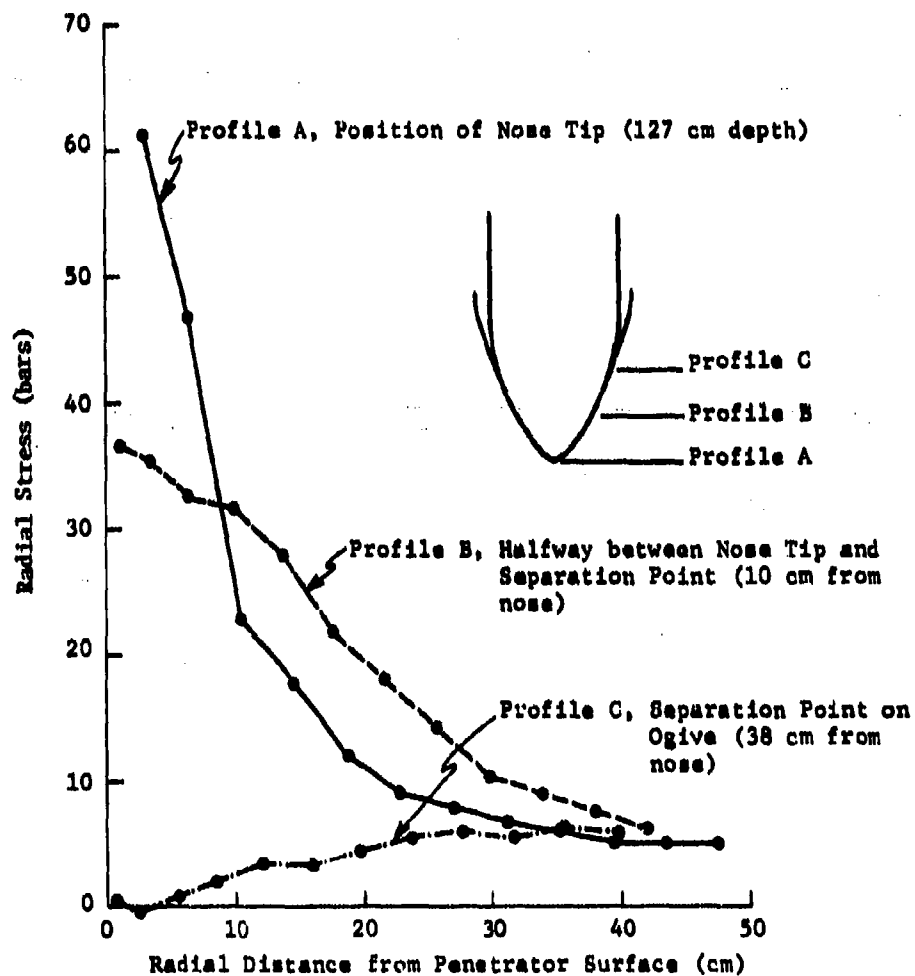


Figure 23. Radial Stress vs Radial Distance from the Penetrator, $t = 8.5$ msec (Layer 1)

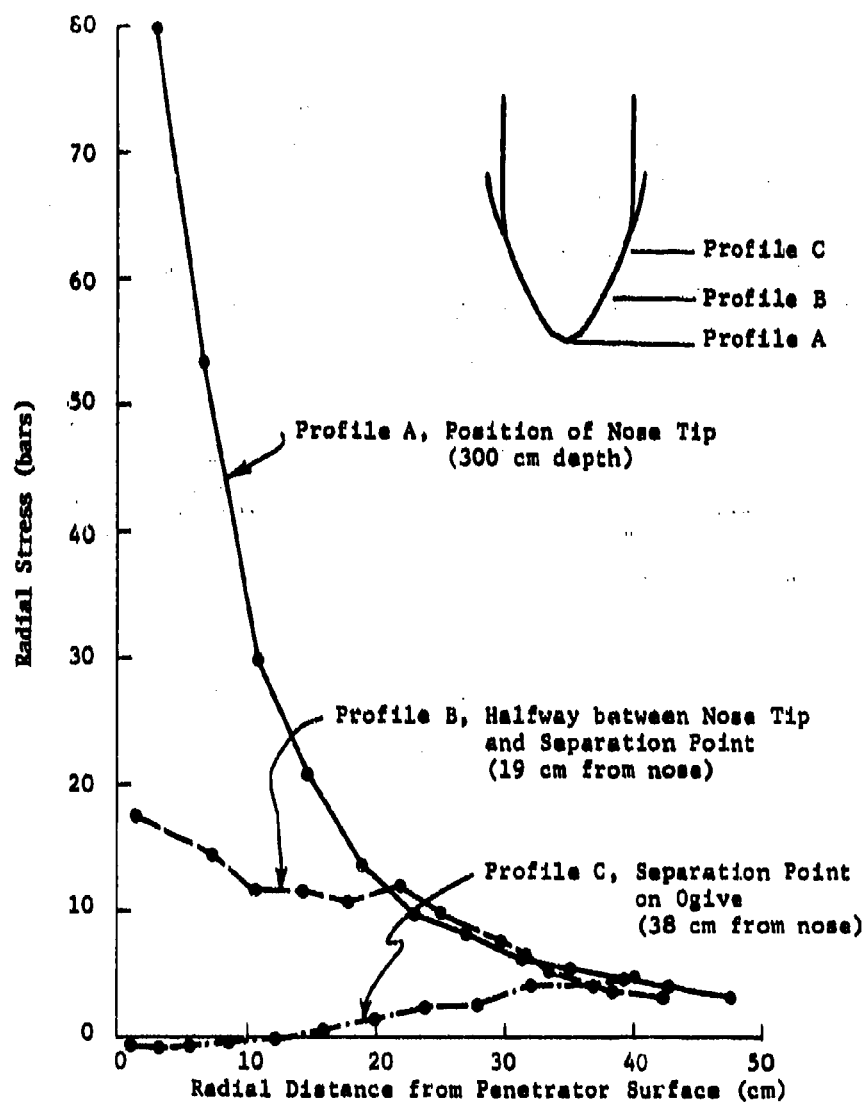


Figure 24. Radial Stress vs Radial Distance from Penetrator, $t = 21.0$ msec (Layer 2)

4.3 COMPARISONS WITH EXPERIMENTS

Preliminary records are available from the field tests. The records which are shown here for comparison with the calculated results are smoothed versions of the uncorrected Sandia traces,⁹ and may differ somewhat from the final filtered and corrected curves to be published by Sandia.²

Figures 25, 26, and 27 compare the measured and computed penetrator deceleration, velocity, and depth histories. The agreement is good. The calculated decelerations are somewhat high, but the ordering of decelerations in the three layers is correct.

There are a number of factors which may have contributed to the observed differences:

- a. Actual site profile vs idealized site profile.
The experimental accelerations show large variations within each of the layers specified in the idealized site profile. This suggests significant property changes within the layers. Also, a preliminary post-test assessment of the site has indicated that the moisture content in the top 4 ft was higher than had been assumed for the idealized site profile, and that this near-surface material consisted of poorly-compacted back-fill rather than undisturbed soil (as had been assumed in the constitutive properties recommended by WES).¹⁰ This would indicate a softer near-surface layer and presumably lower accelerations in that region. Use of softer properties in the calculations would have brought the calculated values into better agreement with the experimental data for the

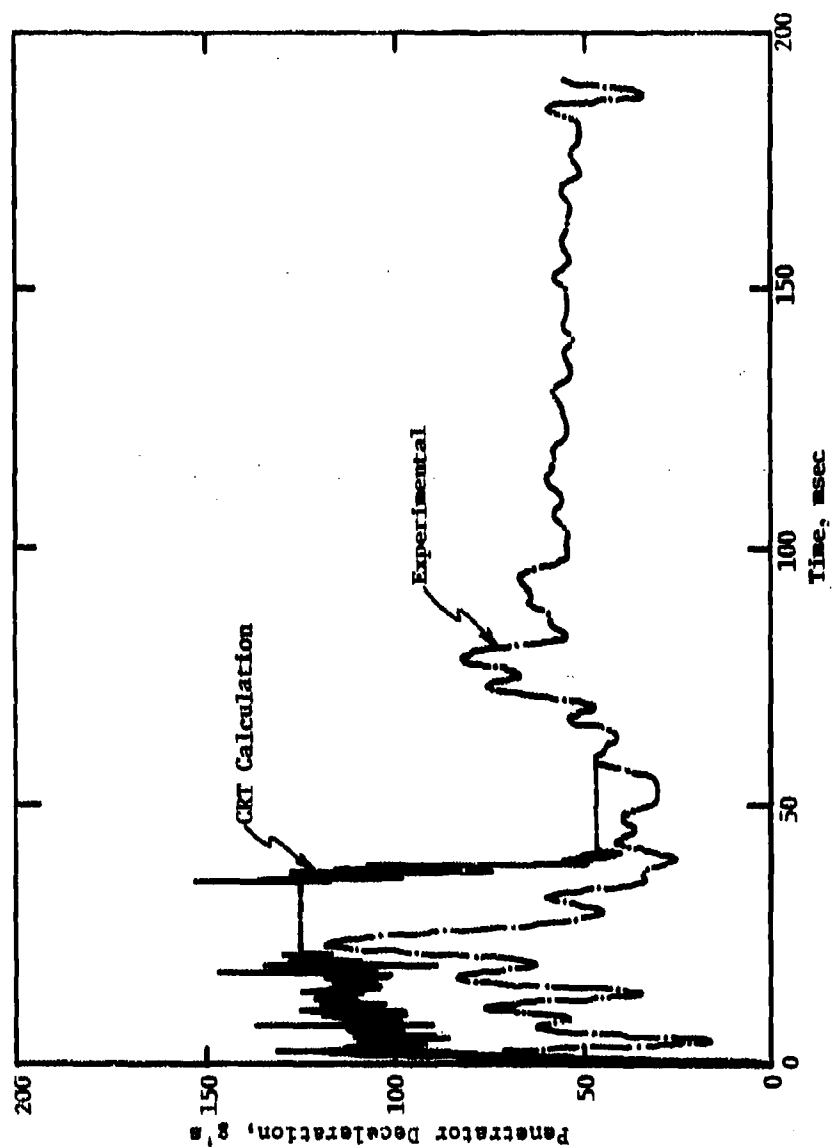


Figure 25. Comparison of Computed and Experimental Time Histories of Penetration Deceleration

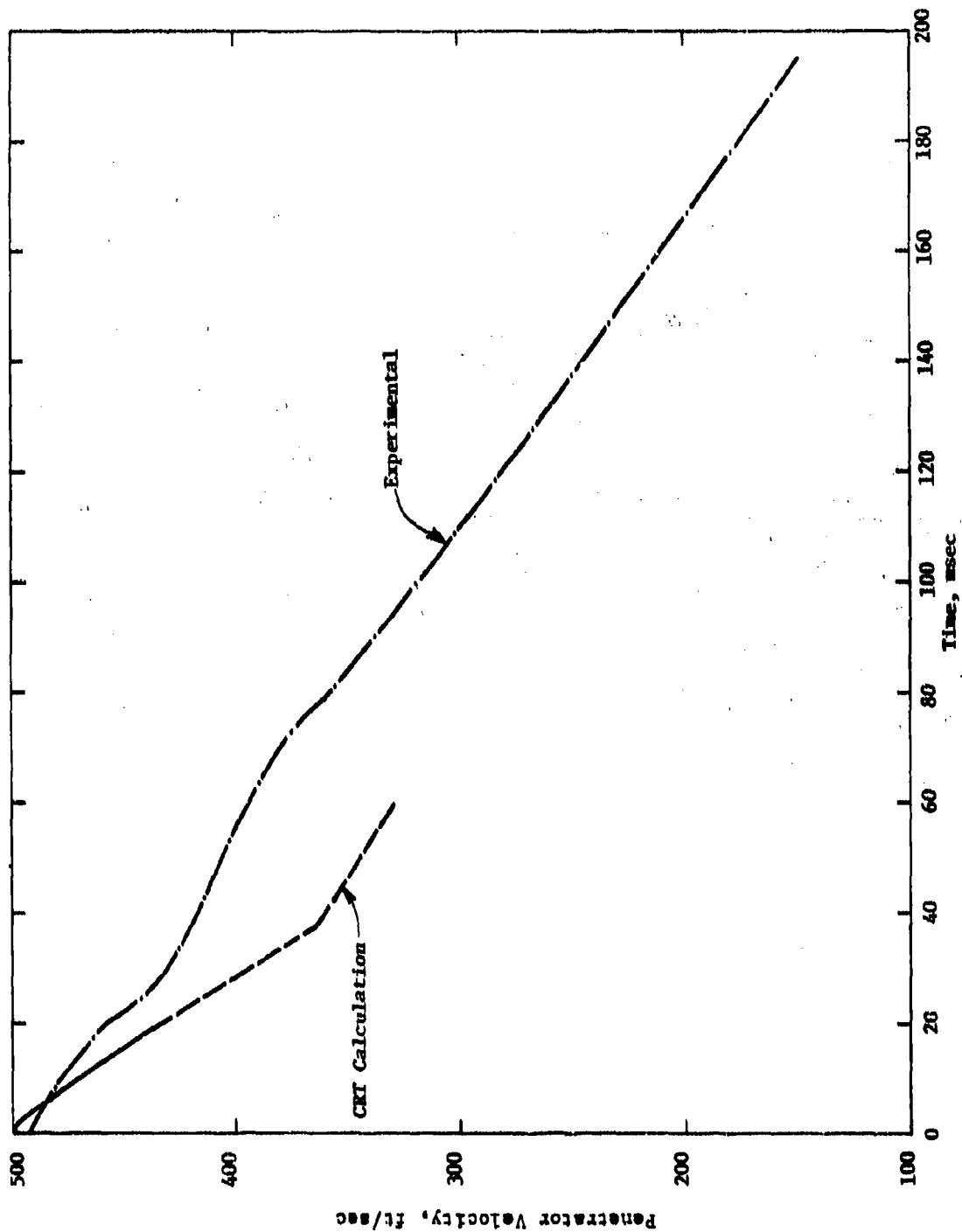


Figure 26. Comparison of Computed and Experimental Time Histories of Penetrator Velocity

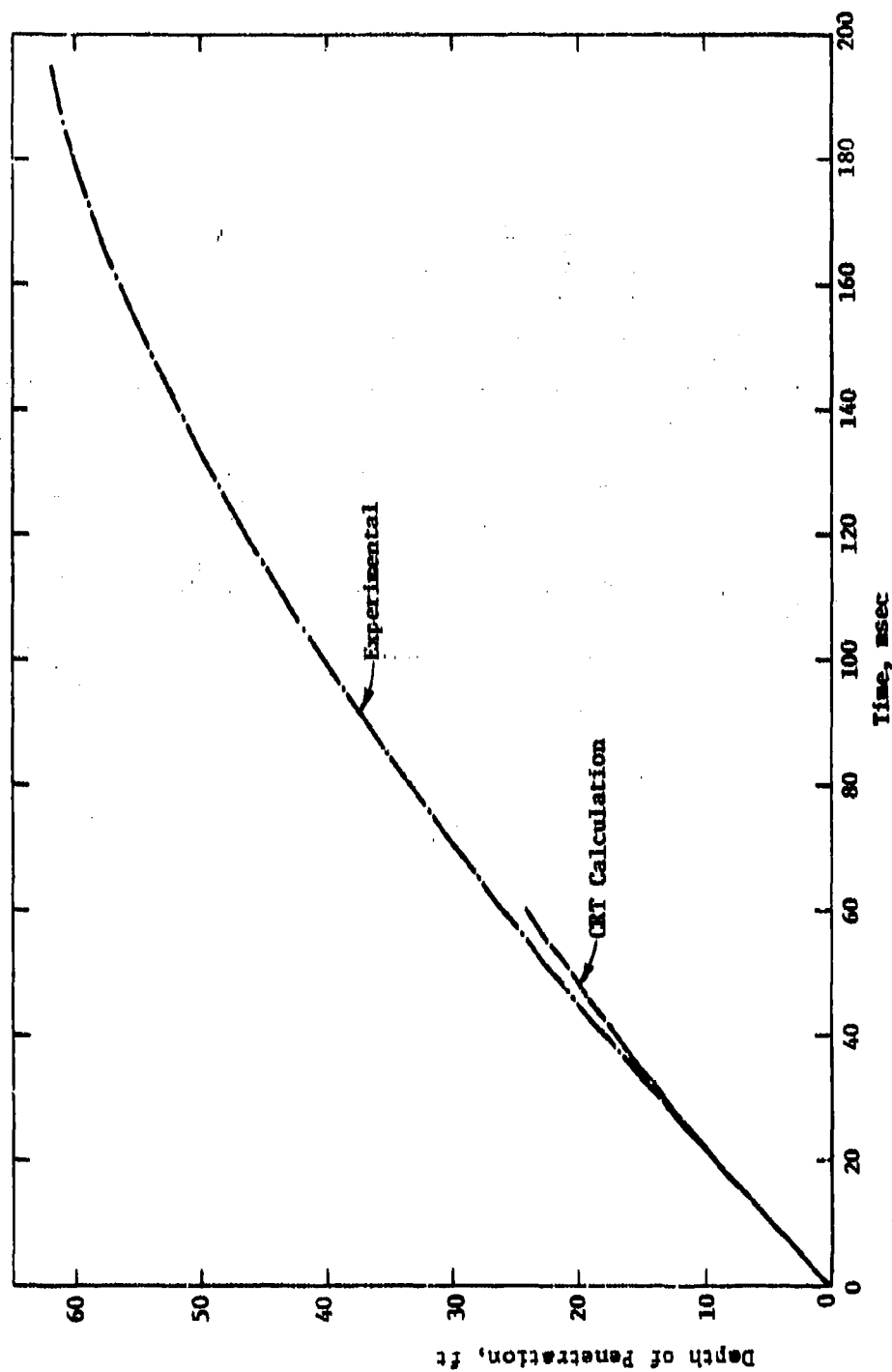


Figure 27. Comparison of Computed and Experimental Time Histories of Depth of Penetration

0-4 ft depth range. Detailed information regarding the actual site profile will be forthcoming from an investigation being carried out by WES.

- b. Friction rule. Friction played a dominant role in the numerical solution, as has been seen in Figure 2. Changing the coefficient in the friction rule from .6 to .4, for example, would have reduced the deceleration level in Layer 1 from 110 g's to 89 g's. Since the solution results (and presumably the physical phenomena) are so sensitive to the friction rule, experiments and more careful modeling are needed to characterize friction under the loading conditions involved in high velocity penetration.
- c. Instrumentation uncertainties. The output from the penetrator instrumentation may be subject to errors or uncertainties from battery excursions, inadequate gauge response, and body vibrations of the non-rigid projectile. The extent of these problems is being assessed by the experimental investigators.

A comparison of the calculated peak pressure vs depth at a radius of .45 m (1.48 ft) from the test centerline with some stress data obtained in the test is shown in Figure 28. The peak pressure vs radius in Layer 2 is compared in Figure 29. Unfortunately, there were significant differences between the calculational conditions (penetrator diameter, mass, and velocity) and the actual test conditions for Sandia tests 2 and 4 (as indicated in the tables on these figures), so direct comparisons cannot be made. However, the general trends appear satisfactory.

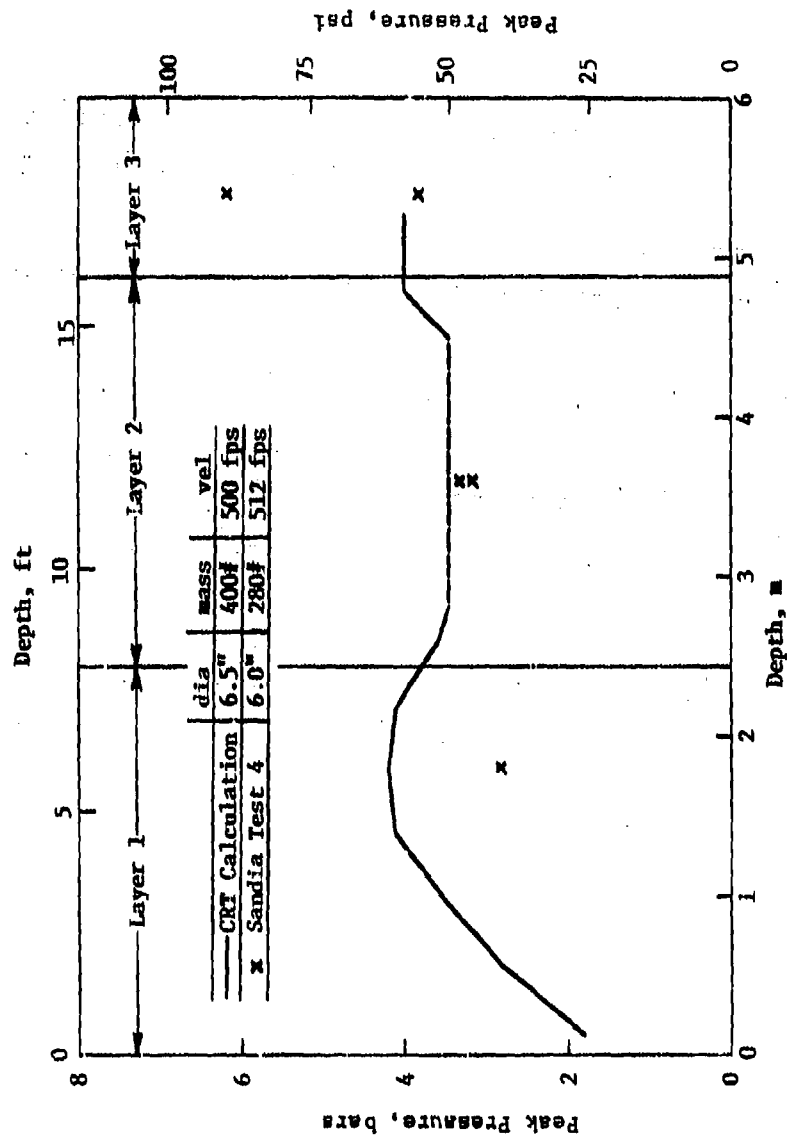


Figure 28. Computed and Experimental Peak Pressures vs Depth at Radius = .45 m

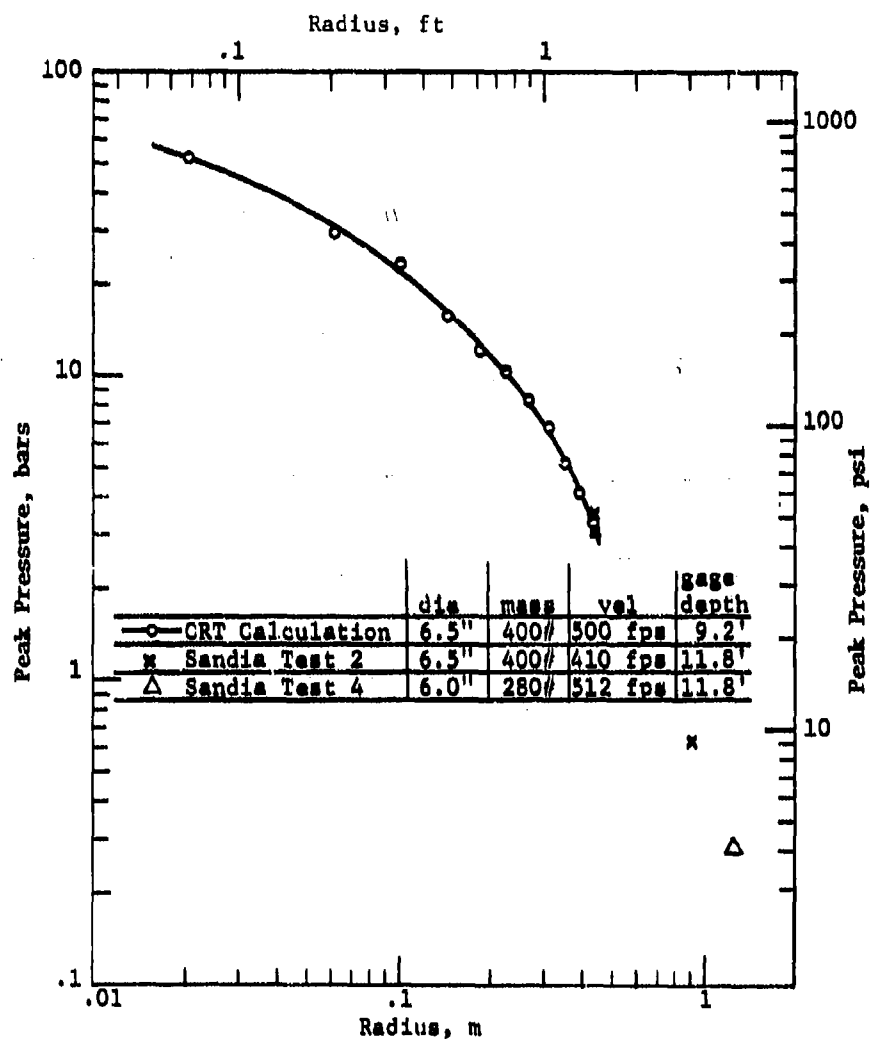


Figure 29. Computed and Experimental Peak Pressures vs Radius in Layer 2

SECTION V

PROBLEM AREAS

In carrying out the finite difference rigid-body calculation of the DNA penetrator problem, a number of problem areas were identified. Where so stated in the following, these areas are being addressed in connection with continuing studies of earth penetrators.

a. Large distortions occur near the penetrator-target medium interface, due to radial flow around the advancing nose and to shear (friction) along the sliding surface. These physical distortions produce corresponding distortions of the Lagrangian computational grid, necessitating periodic realignment of the grid (i.e., local rezoning). If done carefully, such realignments do not significantly degrade a solution, but they are time consuming. Automatic routines are therefore being implemented to efficiently accomplish periodic realignment of the distorted grid near the penetrator. (Grid distortion does not occur in a fixed Eulerian grid, but a separate set of problems is introduced due to radial diffusion of target material properties as damaged target material flows through the fixed grid out and around the penetrator nose.)

b. Stress gradients are affected by the fineness of the computational zoning. In order to determine with reasonable accuracy the stresses in the target medium next to the penetrator (where gradients are steep), relatively fine numerical zoning may be required. Studies to examine the effects of zoning on penetrator predictions, and to establish zoning criteria for reasonable accuracy, are being undertaken.

c. Friction played a very important role in this DNA penetrator calculation, accounting for at least half of the total deceleration. This indicates the necessity for experiments and more careful modeling in order to establish realistic friction relationships for conditions where metal surfaces slide at high velocity and under high stresses through earth media. Such experiments are being undertaken under other DNA programs, and improved friction modeling is being undertaken in future calculational studies.

d. Information regarding the properties of target sites is difficult to obtain. It is reasonable to assume that this will always be the case. And even where extensive subsurface surveys are possible, the property data are uncertain due to local variations and to *in situ* effects. This problem is quite troublesome if one is attempting to validate a numerical method by comparison with a specific test. However, exact knowledge of target properties is not necessary for most of the useful applications of the code; i.e., for studying phenomenology of penetration in different basic types of media, or for examining the effects of target property, penetrator design, and impact parameters upon penetration processes, or for establishing the design environment (stresses and accelerations) within an earth penetrator for representative types of targets and impact conditions.

e. Computer running times for complete penetration solutions are relatively long. Improvements are being made which will substantially reduce these times. Nonetheless, code solutions will probably be primarily useful for

analyzing those portions of penetration events where loading on the penetrator is most severe or is changing rapidly (e.g., while the penetrator nose is burying at the surface, or while the penetrator is passing between different geologic layers, or perhaps just before it comes to rest).

SECTION VI

INTERNAL STRESS RESPONSE OF PENETRATOR

In a deep penetration, target material undergoes large distortions and failure, while a successful penetrator design suffers only elastic strains. (A sacrificial nose section might be an exception). In penetration analyses, the projectile can therefore be assumed to be a rigid body, since projectile deformations are so small that they will not significantly interact with the target response or penetration dynamics.

Rational design of the penetrator interior, however, requires knowledge of the design environment, specifically the accelerations, stress histories, and shock spectra experienced at several relevant stations within the penetrator. Numerical solutions in which the penetrator is treated as a deformable body provide a means for obtaining such information.

This type of solution is illustrated in Figures 30 and 31, performed by CRT under another program.⁷ These figures show the deformation and stress field occurring after 20 in. penetration into soil by a 600 lb projectile fired at 2000 ft/sec.

Finite difference solutions of this type, in which the penetrator deformation and the target deformation are treated *together*, are very time consuming due to the markedly different character of the penetrator and target responses. Good spatial resolution is needed in the penetrator in order to resolve structural details, and the wave

CALIFORNIA JEROME AND TECHNOLOGY REVEALS CODE
 200 IN. 4000-IN PENETRATOR OF STEEL. PENETRATOR 1070 SOIL
 CYCLE 1017

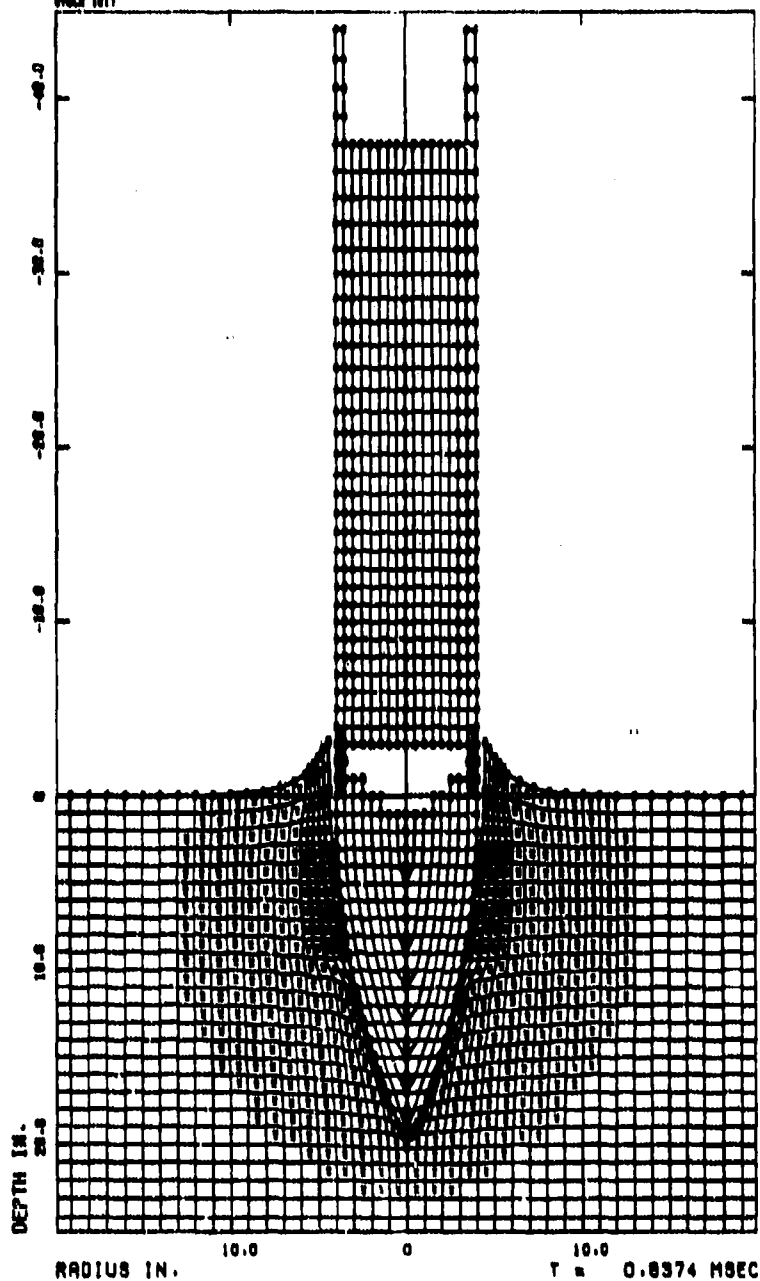


Figure 30. Grid Configuration with Penetrator at
 20 in. Depth from Deformable Body
 Solution

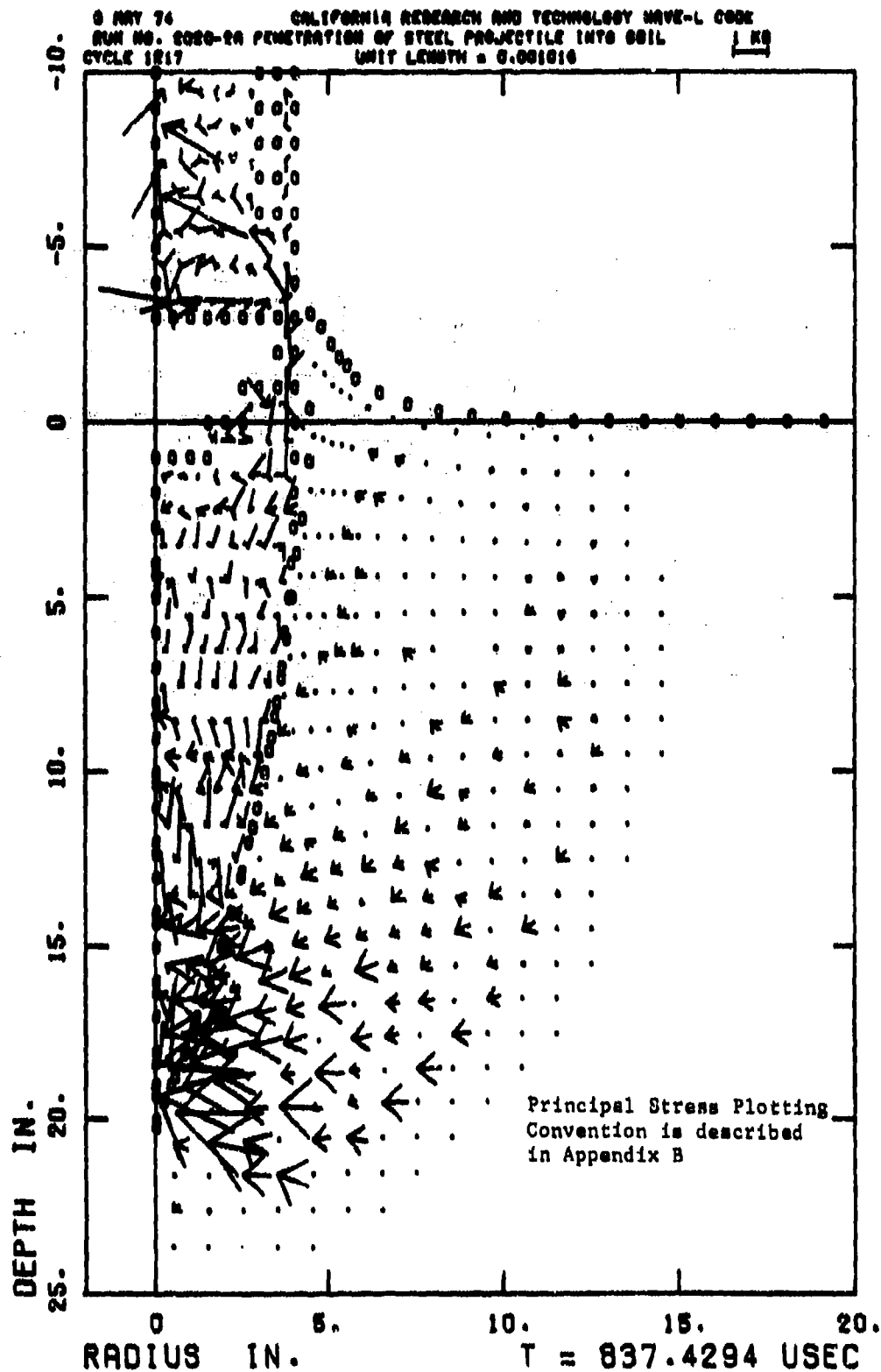


Figure 31. Principal Stress Field with Penetrator at 20 in. Depth from Deformable Body Solution

speeds in typical penetrator materials are relatively high. These factors dictate small integration time steps. On the other hand, coarser spatial resolution and lower wave speeds in the target media would permit much longer time steps.

Because of these large differences in the integration time step and in the magnitudes of the distortions involved, it is efficient to perform separate but coupled analyses of target penetration and of penetrator response. Thus, a rigid-body analysis is first performed of the penetration in the target media. From this rigid-body solution, the penetration history and force loading history imposed on the projectile surface is determined. This information is then used to drive a deformable body analysis of the stress wave response in the penetrator itself.

REFERENCES

1. W. J. Patterson, *Penetration of In-Situ Rock by Air Deliverable Penetrators*, Conference on Rapid Penetration of Terrestrial Materials, Texas A&M University, February 1-3, 1972
2. W. J. Patterson, *DNA/Sandia Soil Penetration Experiment at DRES - Results and Analysis*, SAND-75-0001, Sandia Laboratories, Albuquerque (in publication)
3. J. G. Jackson, Jr., *Physical Property and Dynamic Compressibility Analysis of the Wotahing Hill Blast Range*, Waterways Experiment Station, S-72-4, April 1972
4. Mark L. Wilkins, *Calculation of Elastic-Plastic Flow*, Lawrence Radiation Laboratory, UCRL-7322, Rev. 1, January 1969
5. R. K. Byers, A. J. Chabai, and R. T. Walsh, *Predictions of Projectile Penetration Phenomena and Comparison with Experiments in a Soil Medium*, SAND-75-0174, Sandia Laboratories, Albuquerque (in publication)
6. Report on code calculation of DNA earth penetrator test at DRES, Physics International (to be published)
7. M. H. Wagner, K. N. Kreyenhagen, and W. S. Goerke, *Numerical Analysis of Projectile Impact and Deep Penetration into Earth Media*, CRT 2020-1, California Research & Technology, Inc. (in publication)
8. R. Hill, *Mathematical Theory of Plasticity*, Oxford, (1950)
9. W. J. Patterson, Sandia Laboratories, personal communication
10. P. F. Hadala, Waterways Experiment Station, personal communication

APPENDIX A

MATERIAL MODELS

Material models for each of the four site layers were developed, based on the set of recommended soil properties furnished by WES. Hysteretic elastic-ideally plastic models using a Prandtl-Reuss (non-associated) flow rule were employed. For loading, the bulk and shear moduli were made functions of the volumetric strain (μ). For unloading, the bulk modulus was made a function of μ_{\max} or the maximum pressure (P_{\max}) and the shear modulus was constant, except for Layer 4, where it varied with the unloading bulk modulus. The failure surfaces were fit by making the yield condition a function of pressure.

A.1 LAYER 1

A.1.1 Loading Hydrostat

The following equations were deduced for the loading hydrostat:

$$P = a_1 \mu \quad \mu \leq 0$$

$$P = \sum_{i=1}^7 a_i \mu^i \quad 0 < \mu < \mu_1$$

$$P = P_1 + \gamma(\mu - \mu_1) + \frac{\alpha}{\beta - (\mu - \mu_1)} - \frac{\alpha}{\beta} \quad \mu_1 \leq \mu \leq \mu_c$$

$$P = P_c + K_{\max}(\mu - \mu_c) - (K_{\max} - K_c) \mu^* \left[1 - \exp \frac{\mu_c - \mu}{\mu^*} \right] \quad \mu > \mu_c$$

This model was extended to high pressures and densities (beyond that furnished in the representation) by assuming that the material locked-up, or reached void closure, at a stress of ~12 ksi and a strain of ~38% (V_u was given as ~37%). Beyond void closure, a well-behaved asymptotic form is employed. The values of the constants are:

$$\begin{aligned}
 a_1 &= 7.8933 \times 10^{-4} \text{ Mb} & \gamma &= 5.2546 \times 10^{-4} \text{ Mb} \\
 a_2 &= -.019894 \text{ Mb} & \mu_1 &= .26 \\
 a_3 &= .38493 \text{ Mb} & \mu_c &= .62 \\
 a_4 &= -4.0302 \text{ Mb} & \mu^* &= .25 \\
 a_5 &= 22.519 \text{ Mb} & K_c &= .018319 \text{ Mb} \\
 a_6 &= -62.409 \text{ Mb} & K_{\max} &= .689465 \text{ Mb} \\
 a_7 &= 67.438 \text{ Mb} & P_o &= 1.0191 \times 10^{-4} \text{ Mb} \\
 \alpha &= 1.53904 \times 10^{-5} \text{ Mb} & P_c &= 7.74858 \times 10^{-4} \text{ Mb} \\
 \beta &= .38941 & \rho_o &= 1.4897 \text{ gm/cm}^3 \text{ (93 lb/ft}^3\text{)}
 \end{aligned}$$

A.1.2 Shear Modulus - Loading

The shear modulus function for loading was approximately determined from a graphical assessment of the variation of Poisson's ratio along the uniaxial strain stress path (stress difference vs pressure) and the bulk modulus (as derived from the hydrostat equations). Parametric integration runs were then made to find values of the constants giving a good fit to the stress path. A maximum value equal to the unloading shear modulus was imposed to prevent energy generation.

$$G_{\text{load}} = \text{Min} \left[\frac{3B(1-2\nu)}{2(1+\nu)}, G_{\text{unload}} \right]$$

where $B = (\mu + 1) \frac{dP_{load}}{d\mu} (\mu)$

and $v = .5 - .25 \exp(-6.5\mu^{.83})$

Initial values of Young's modulus, the bulk modulus, the shear modulus, the constrained modulus, Poisson's ratio, and the dilatational sound speed from the model are:

$$E_0 = 17,173 \text{ psi}$$

$$B_0 = 11,448 \text{ psi}$$

$$G_0 = 6,869 \text{ psi}$$

$$M_0 = 20,607 \text{ psi}$$

$$v_0 = .25$$

$$c_0 = 1,013 \text{ ft/sec}$$

A.1.3 Unloading Model

In the hysteretic region, $\mu < \mu_c$, a model giving a fan of constant slope P - μ unloading paths was used (slopes are function of μ_{max}):

$$P = P_{max} + K(\mu - \mu_{max}) \quad \mu_{max} < \mu_c$$

$$P = P_c + K_c(\mu - \mu_c) \quad \mu_{max} \geq \mu_c$$

In this region, the unloading bulk modulus varied from a minimum of 41.7 ksi to a maximum of 430 ksi, equal to the bulk modulus for loading at void closure. The unloading bulk modulus was made a function of the maximum pressure, $P_{max}(\mu_{max})$. A constant value of 25 ksi for the unloading

shear modulus was assumed. The initial Poisson's ratio for unloading was set equal to that for loading ($\nu_0 = .25$), giving an initial value of 41.7 ksi for the unloading bulk modulus. K is a function given by

$$K = \frac{B_0 + B_1 [\exp(bP_{\max}) - 1]}{\mu_{\max} + 1} \quad \mu_{\max} < \mu_c$$

where P_{\max} is obtained from the loading hydrostat equations evaluated at μ_{\max} . The constants are:

$$B_0 = 2.87277 \times 10^{-3} \text{ Mb}$$

$$b = 1000$$

$$B_1 = .0229 \text{ Mb}$$

For $\mu > \mu_c$, unloading is assumed to be reversible (follows the load path).

Hydrostatic tension is limited by imposing a minimum value of pressure: $P_{\min} = -12.26 \text{ psi}$.

A.1.4 Failure Surface

A yield function $Y(P)$ was fit to the failure envelope suggested, where $Y = \sqrt{3J_2}$ at failure. Beyond the data region, an asymptotic form was used to smoothly extend the failure surface to a limit of $Y = 750 \text{ psi}$ at infinity. The functions derived are:

$$Y = 20 + 1.6313 P \quad -12.26 \leq P \leq 0$$

$$Y = 20 + 408.14 \left[\exp(2.4994 \times 10^{-4} P) - \exp(-3.747 \times 10^{-3} P) \right] \quad 0 < P \leq 1420$$

$$Y = 600 + 150 \frac{P-1420}{P-439.29}$$

$$P > 1420$$

Here the units for Y and P are psi.

A.1.5 Comparative Results

Plots of stress vs strain, stress difference vs pressure, and pressure vs volumetric strain for uniaxial strain load-unload paths computed with the model, along with the WES curves, are shown in Figures A-1 to A-6. For each type plot, the first figure is for the low stress region and the second figure is for the entire range up to and somewhat beyond void closure.

A.2 LAYER 2

A.2.1 Loading Hydrostat

The following equations were deduced for the loading hydrostat:

$$P = a_1 \mu \quad \mu \leq 0$$

$$P = \sum_{i=1}^5 a_i \mu^i \quad 0 < \mu < \mu_c$$

$$P = P_c + K_{max}(\mu - \mu_c) - (K_{max} - K_c) \mu^* \left[1 - \exp \frac{\mu_c - \mu}{\mu^*} \right] \quad \mu > \mu_c$$

The equation for the fit in the data region was used to extrapolate the hydrostat up to an approximate void closure point corresponding to a stress of ~48 ksi and a strain of ~41% (V_a was given as ~40%). Beyond void closure, a well-behaved asymptotic form is employed. The values of the constants are:

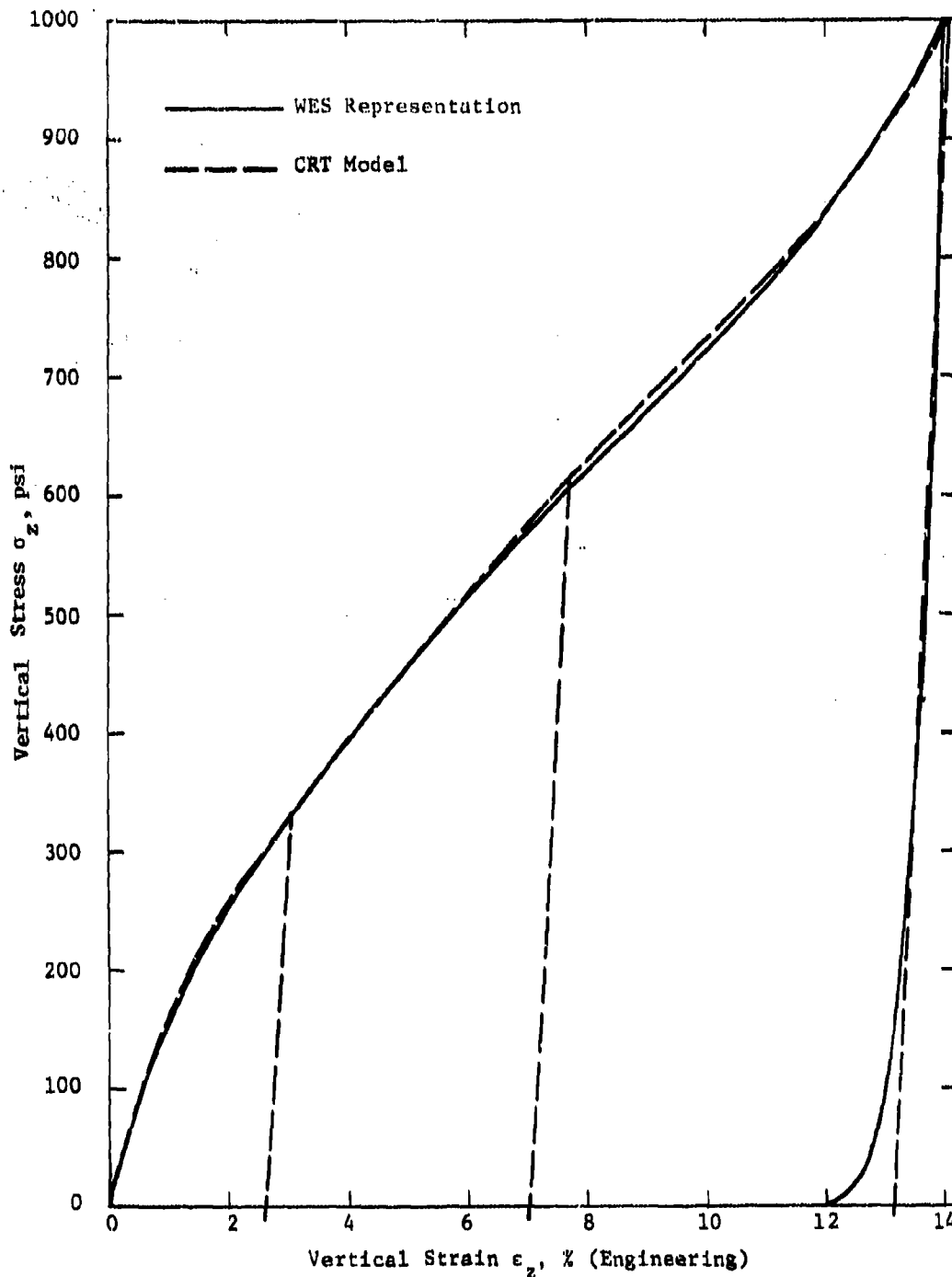


Figure A-1. Uniaxial Strain Load-Unload Paths for Layer 1
(σ_z to 1000 psi)

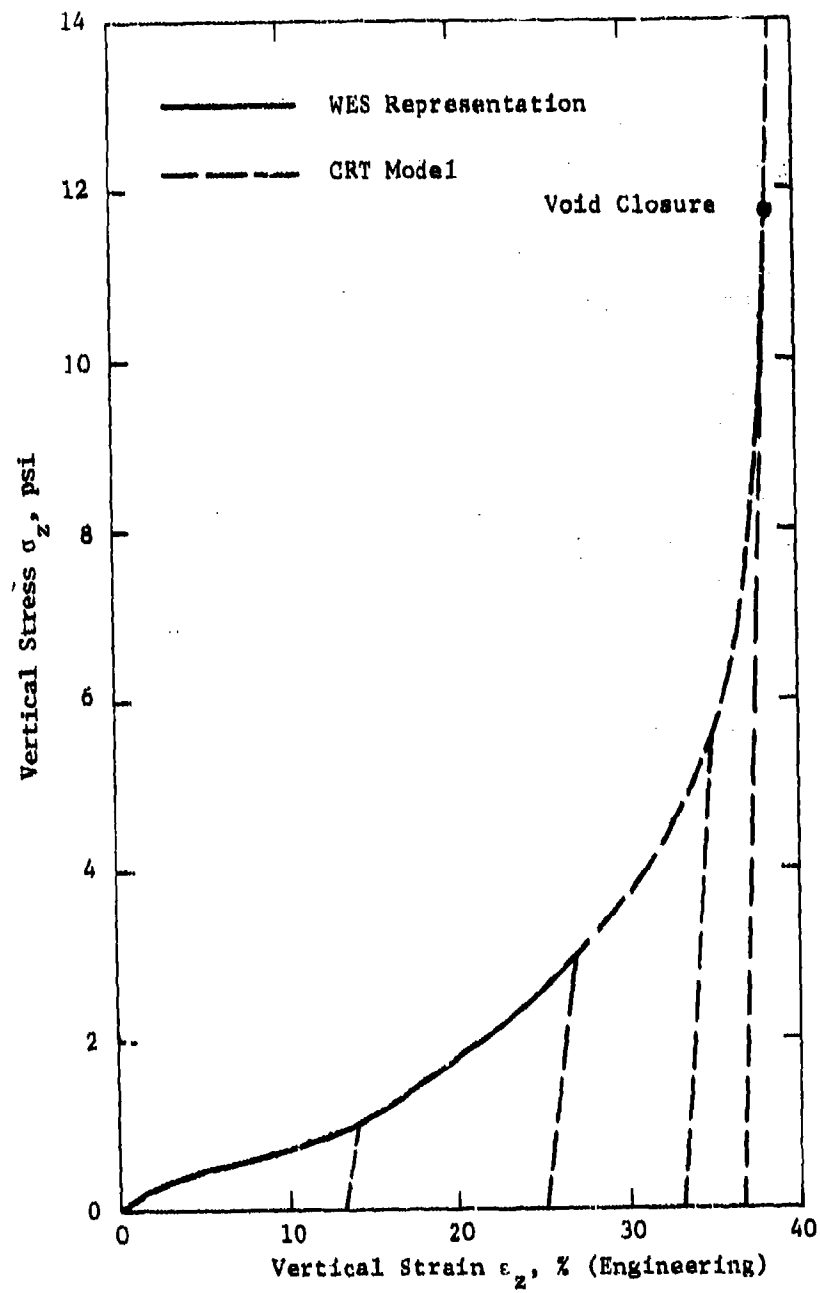


Figure A-2. Uniaxial Strain Load-Unload Paths for Layer 1
(σ_z to 14 ksi)

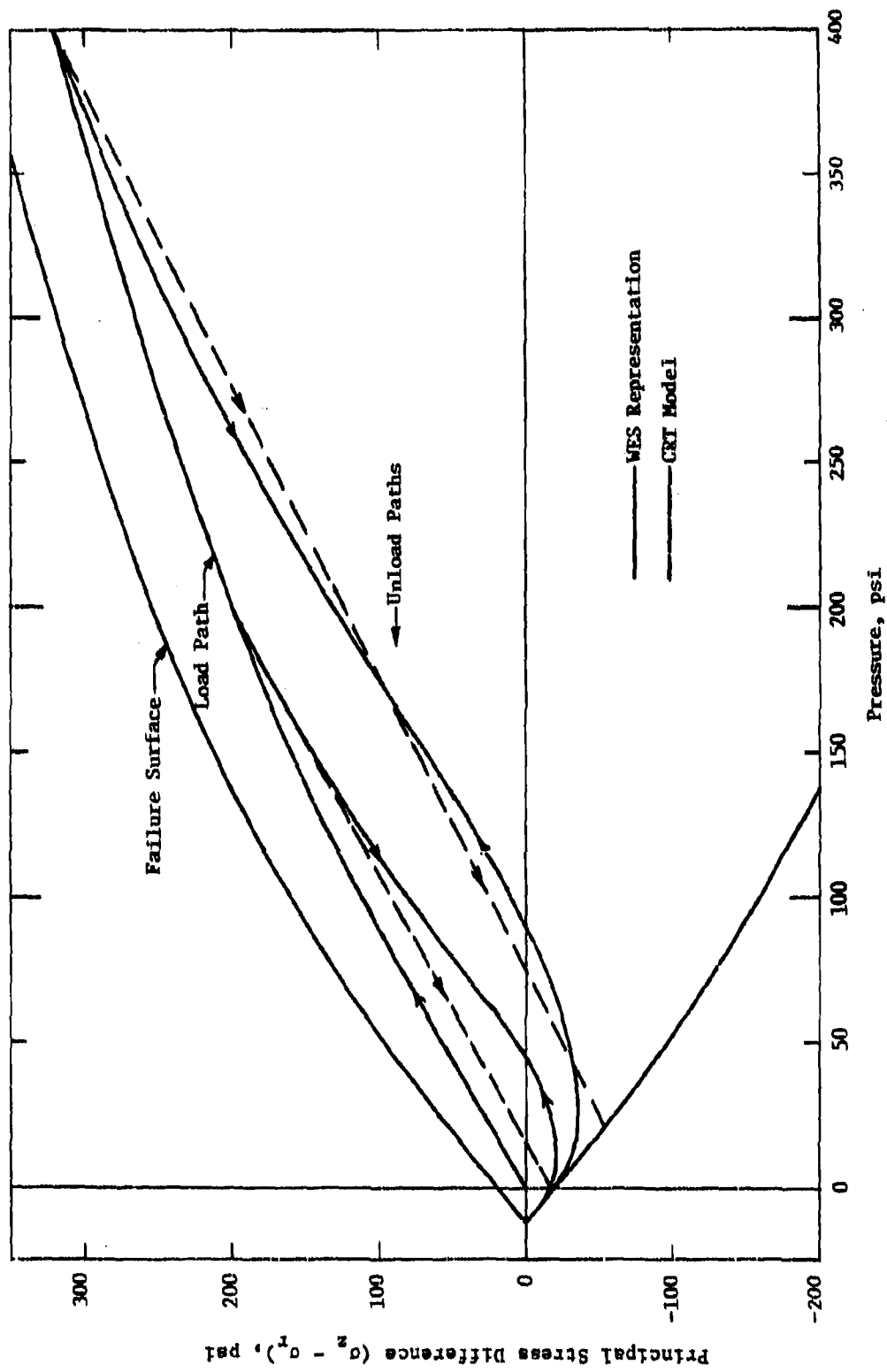


Figure A-3. Uniaxial Strain Stress Paths and Failure Surface for Layer 1 (P to 400 psi)

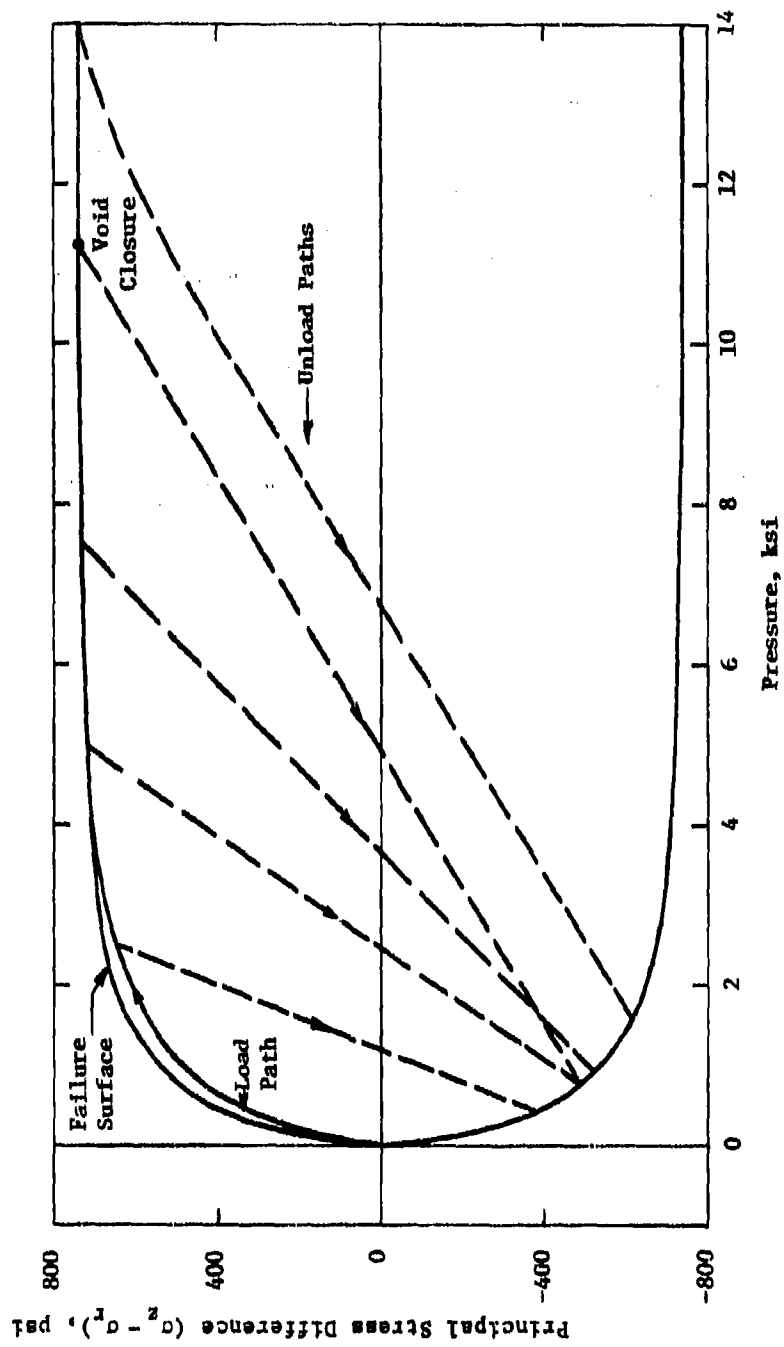


Figure A-4. Uniaxial Strain Stress Paths and Failure Surface in High-Pressure Region for Layer 1 (P to 14 ksi)

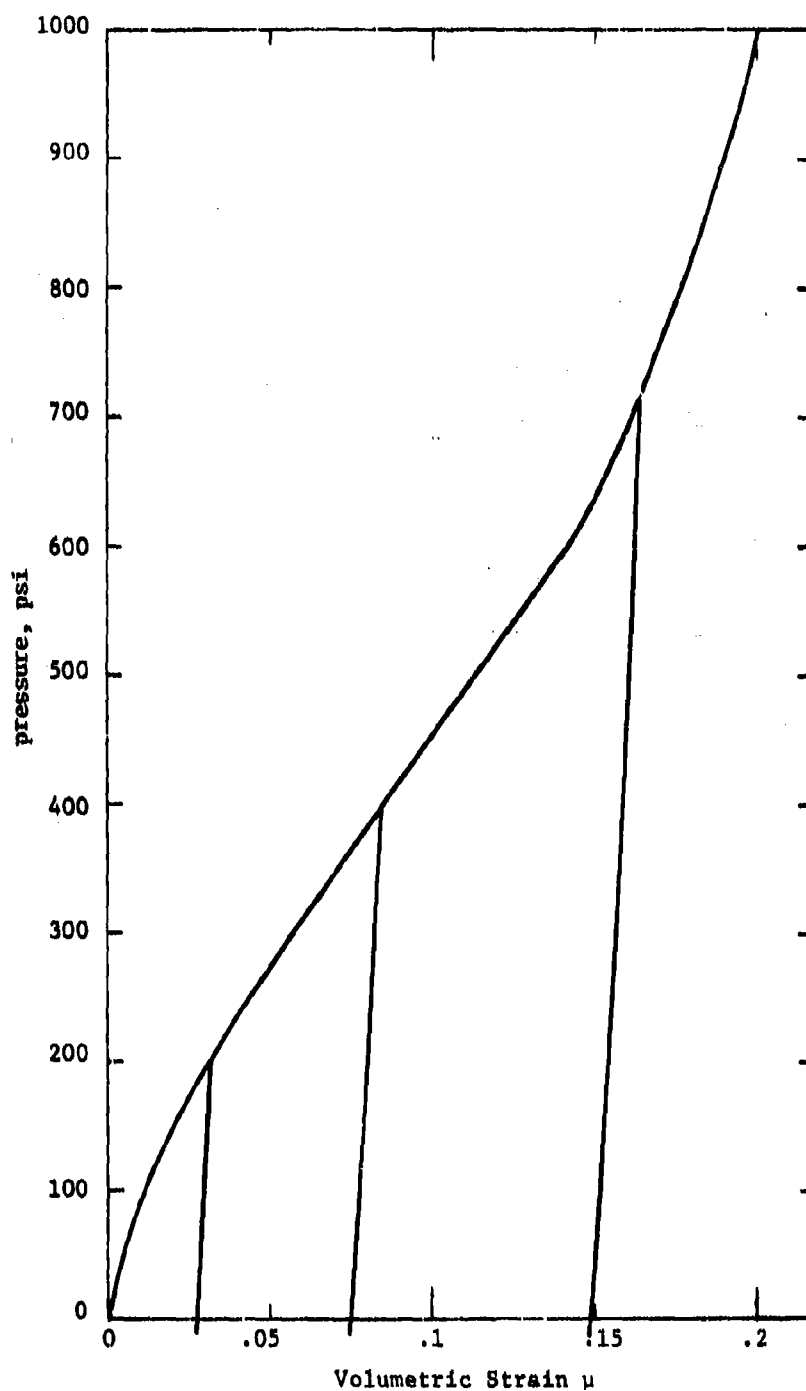


Figure A-5. Hydrostatic Load-Unload Paths for Layer 1
(P to 1000 psi)

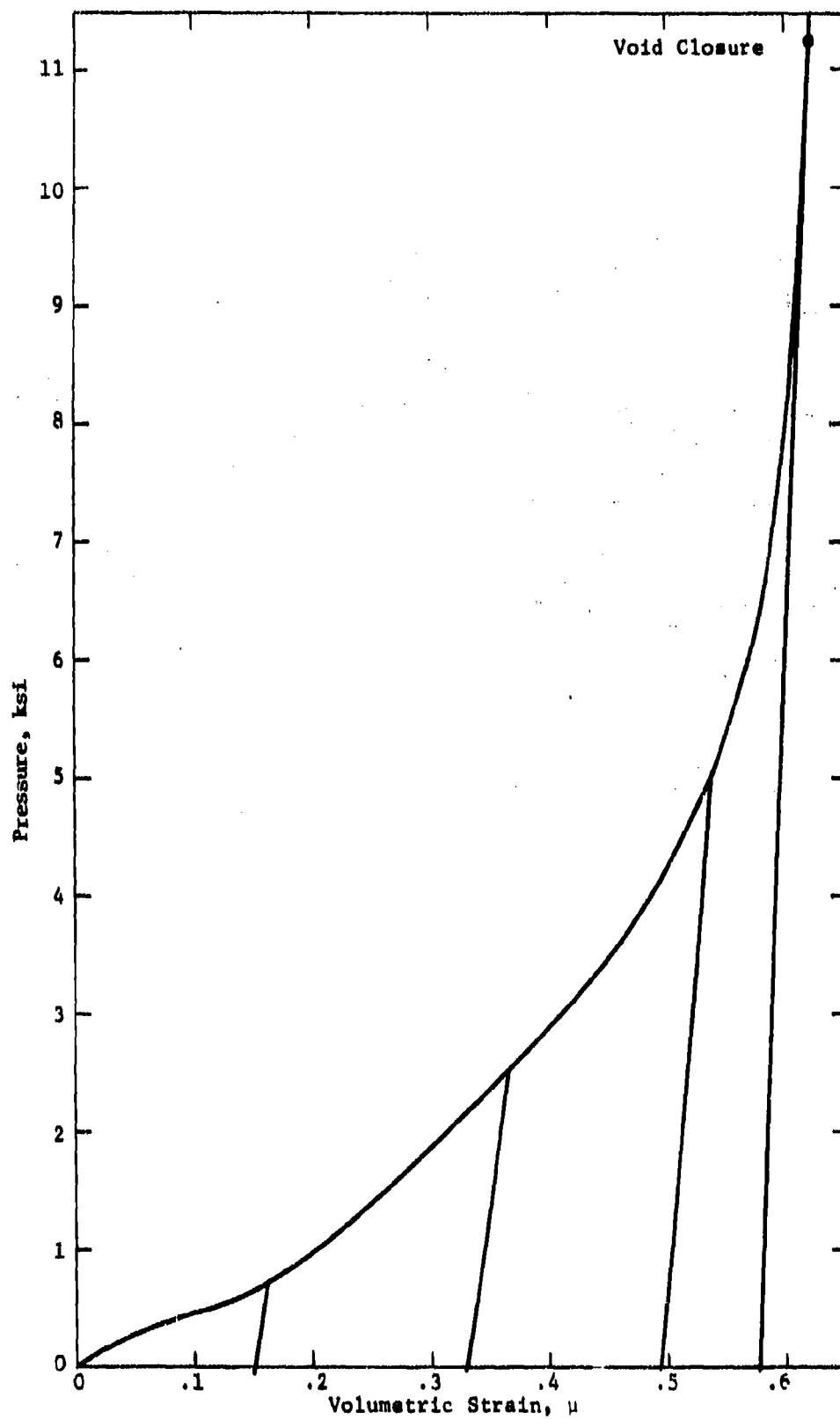


Figure A-6. Hydrostatic Load-Unload Paths for Layer 1
(P to 11.5 ksi)

$$\begin{aligned}
a_1 &= 2.27 \times 10^{-4} \text{ Mb} & \mu_c &= .7 \\
a_2 &= -7.6853 \times 10^{-4} \text{ Mb} & K_c &= .0233697 \text{ Mb} \\
a_3 &= .011947 \text{ Mb} & K_{\max} &= .689465 \text{ Mb} \\
a_4 &= -.034525 \text{ Mb} & P_c &= 3.15417 \times 10^{-3} \text{ Mb} \\
a_5 &= .045002 \text{ Mb} & \rho_o &= 1.4256 \text{ gm/cm}^3 (89 \text{ lb/ft}^3) \\
\mu^* &= .25
\end{aligned}$$

A.2.2 Shear Modulus - Loading

The shear modulus in loading was determined by a method similar to that for Layer 1.

$$G_{\text{load}} = \text{Min} \left[\frac{3B(1-2\nu)}{2(1+\nu)}, G_{\text{unload}} \right]$$

where

$$B = (\mu+1) \frac{dP_{\text{load}}}{d\mu} (\mu)$$

and

$$\nu = .5 - .3 \exp(-.1687\mu^{.319})$$

Initial values of Young's modulus, the bulk modulus, the shear modulus, the constrained modulus, Poisson's ratio, and the dilatational sound speed from the model are:

$$\begin{aligned}
E_o &= 5,926 \text{ psi} & M_o &= 6,585 \text{ psi} \\
B_o &= 3,292 \text{ psi} & \nu_o &= .2 \\
G_o &= 2,469 \text{ psi} & c_o &= 585 \text{ ft/sec}
\end{aligned}$$

A.2.3 Unloading Model

In the hysteretic region, $\mu < \mu_c$, a model giving a fan of constant slope $P-\mu$ unloading paths was used (slopes are a function of μ_{max}):

$$P = P_{max} + K(\mu - \mu_{max}) \quad \mu_{max} < \mu_c$$

$$P = P_c + K_c(\mu - \mu_c) \quad \mu_{max} \geq \mu_c$$

In this region, the unloading bulk modulus varies from a minimum of 74.3 ksi to a maximum of 576 ksi, equal to the bulk modulus for loading at void closure. A constant representative value of 67 ksi for the unloading shear modulus was assumed. This value was determined from the given unload path from $\sigma_z = 1000$ psi and an estimate of the unloading Poisson's ratio at that point. K is a function given by:

$$K = \frac{B_0 + B_1 [\exp(b\mu_{max}) - 1]}{\mu_{max} + 1} \quad \mu_{max} < \mu_c$$

The constants, as determined from the given unload paths, are:

$$B_0 = 5.12073 \times 10^{-3} \text{ Mb}$$

$$B_1 = 7.8964 \times 10^{-4} \text{ Mb}$$

$$b = 5.4326$$

The initial Poisson's ratio for unloading is .1532 from this fit.

For $\mu > \mu_c$, unloading is assumed to be reversible (follows the load path).

Hydrostatic tension is limited by imposing a minimum value of pressure: $P_{\min} = -12$ psi.

A.2.4 Failure Surface

A yield function $Y(P)$ was fit to the failure envelope suggested, where $Y = \sqrt{3}J_2'$ at failure. An asymptotic form was used to smoothly extend the failure surface in the high pressure region. The functions derived are:

$$\begin{aligned} Y &= 16 + \frac{4}{3}P & -12 \leq P < 300 \\ Y &= 416 + \frac{4}{3}(P-300) & & \\ &\quad - 7.7552 \times 10^{-4} (P-300)^{1.9172} & 300 < P \leq 1200 \\ Y &= 1258.3 + 1647.87 \frac{P-1200}{P+1683.71} & P > 1200 \end{aligned}$$

Here the units for Y and P are psi.

A.2.5 Comparative Results

Plots of stress vs strain, stress difference vs pressure, and pressure vs volumetric strain for uniaxial strain load-unload paths computed with the model, along with the WES curves, are shown in Figures A-7 to A-12. For each type plot, the first figure is for the low stress region and the second figure is for the entire range up to and somewhat beyond void closure.

A.3 LAYER 3

A.3.1 Loading Hydrostat

The following equations were deduced for the loading hydrostat:

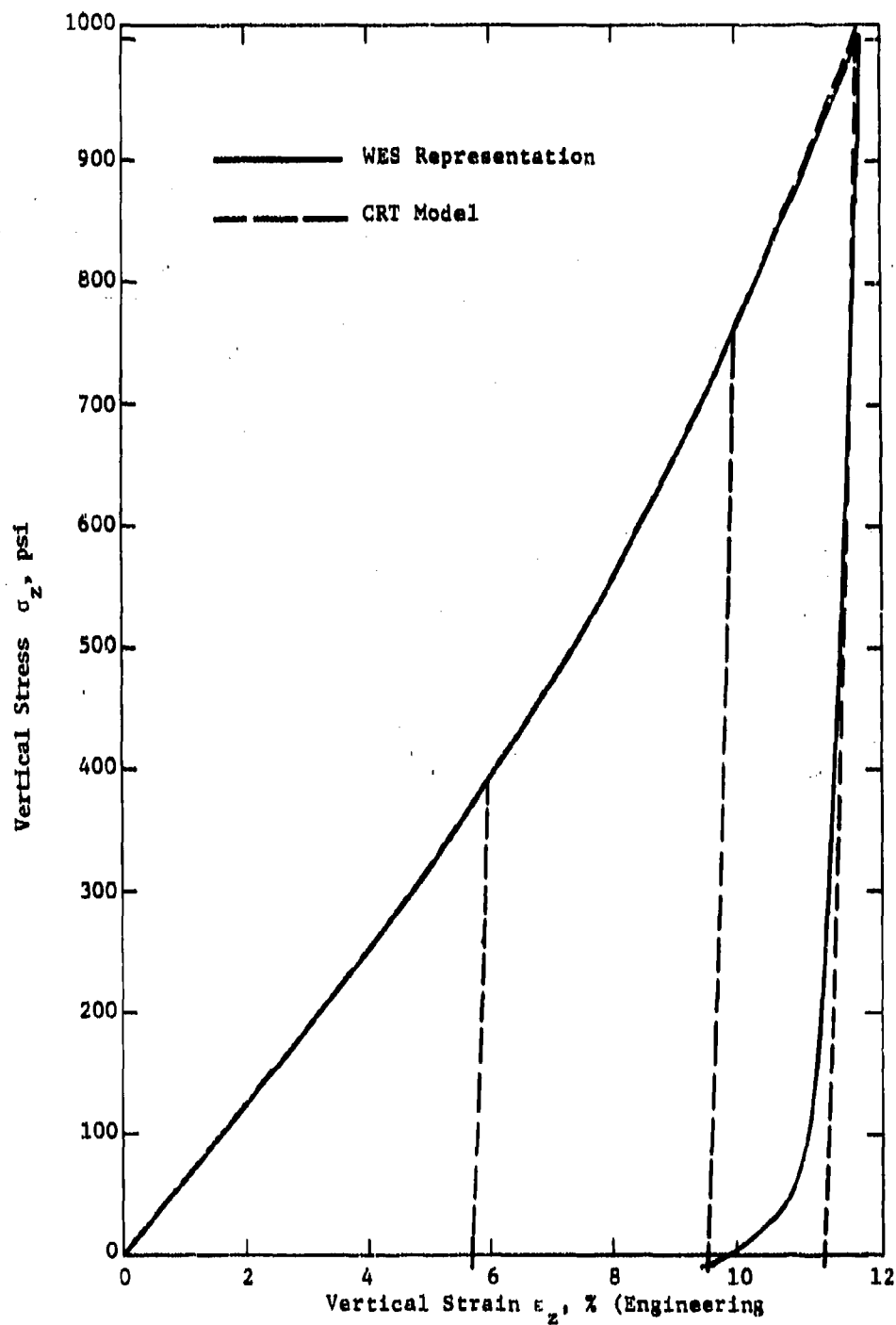


Figure A-7. Uniaxial Strain Load-Unload Paths for Layer 2 (σ_z to 1000 psi)

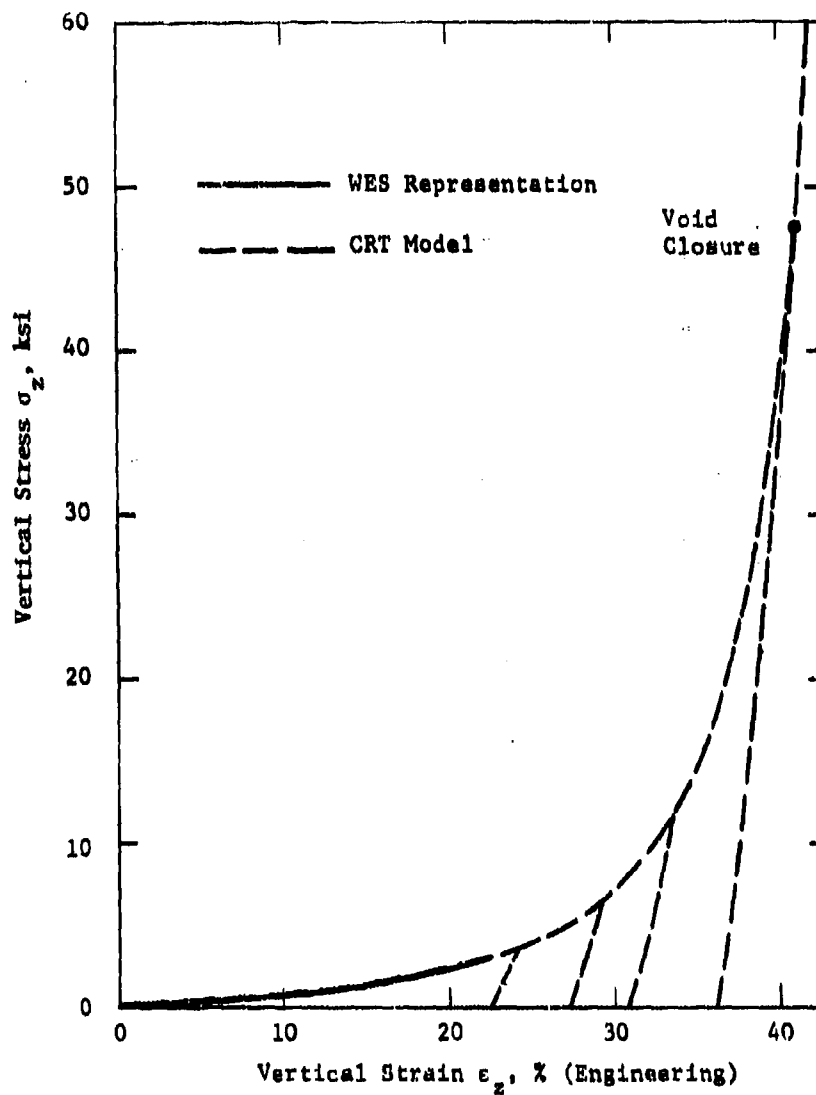


Figure A-8. Uniaxial Strain Load-Unload Paths for Layer 2 (σ_z to 60 ksi)

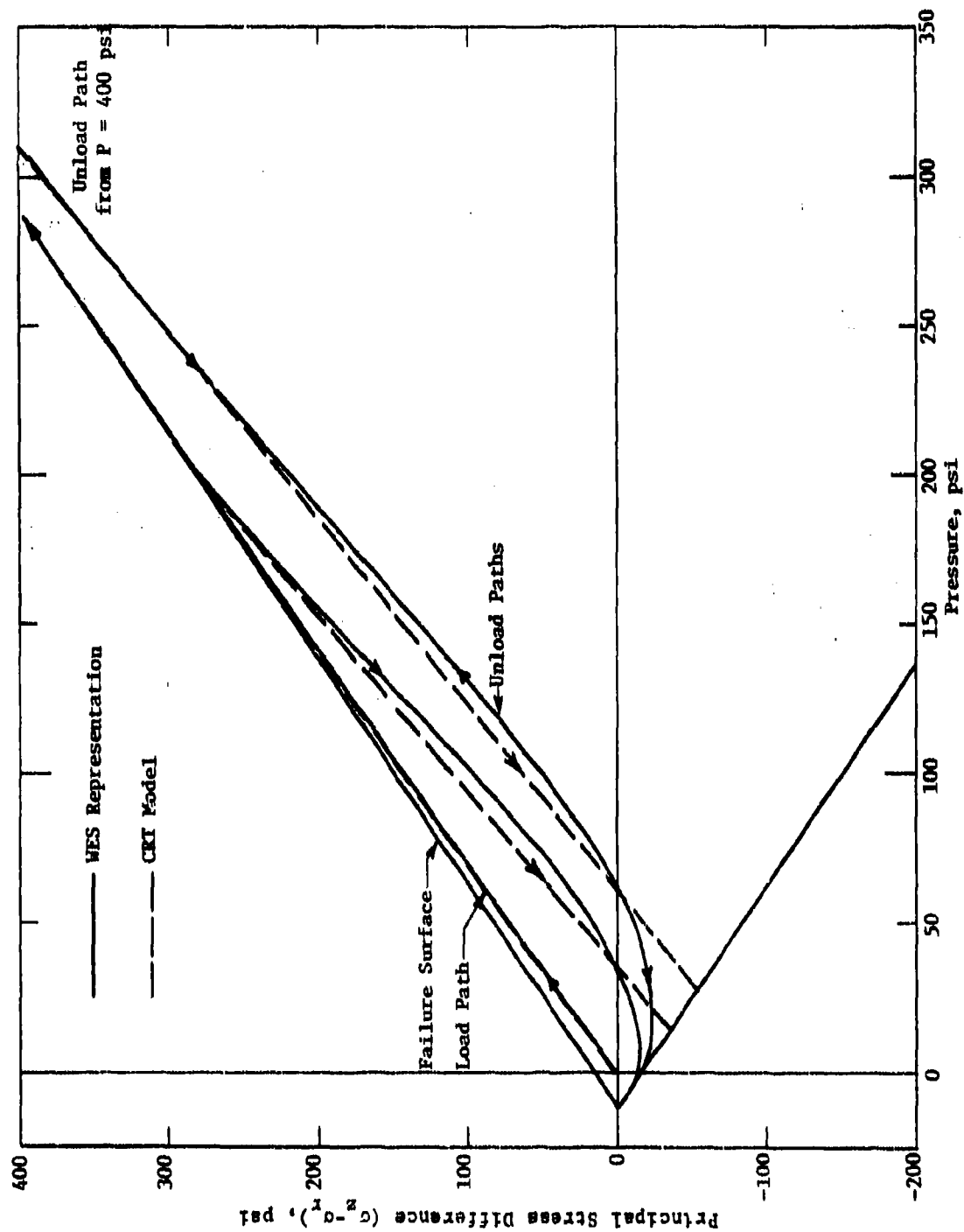


Figure A-9. Uniaxial Strain Stress Paths and Failure Surface for Layer 2 (P to 400 psi)

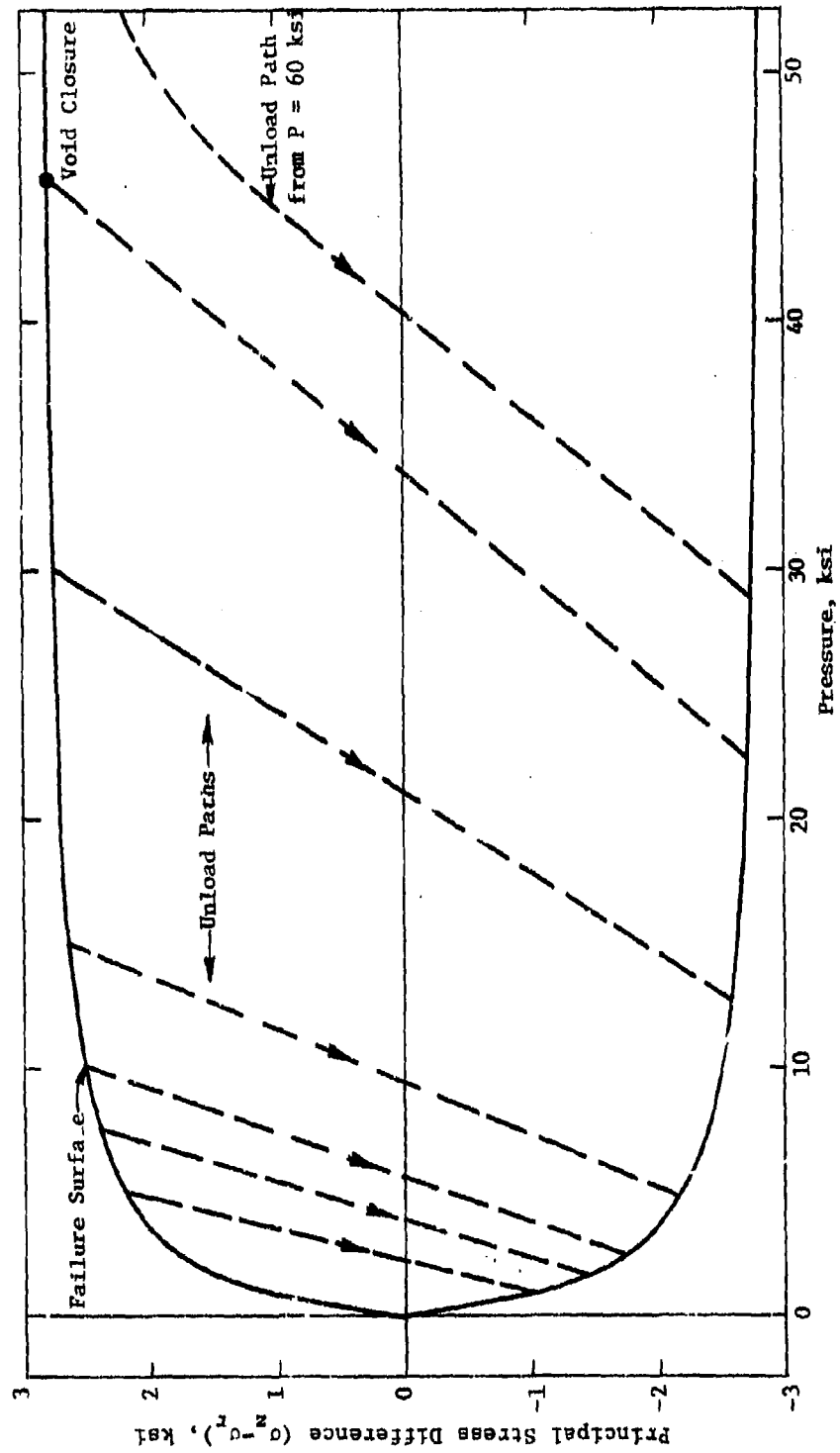


Figure A-10. Uniaxial Strain Stress Paths and Failure Surface in High-Pressure Region for Layer 2 (P to 60 ksi)

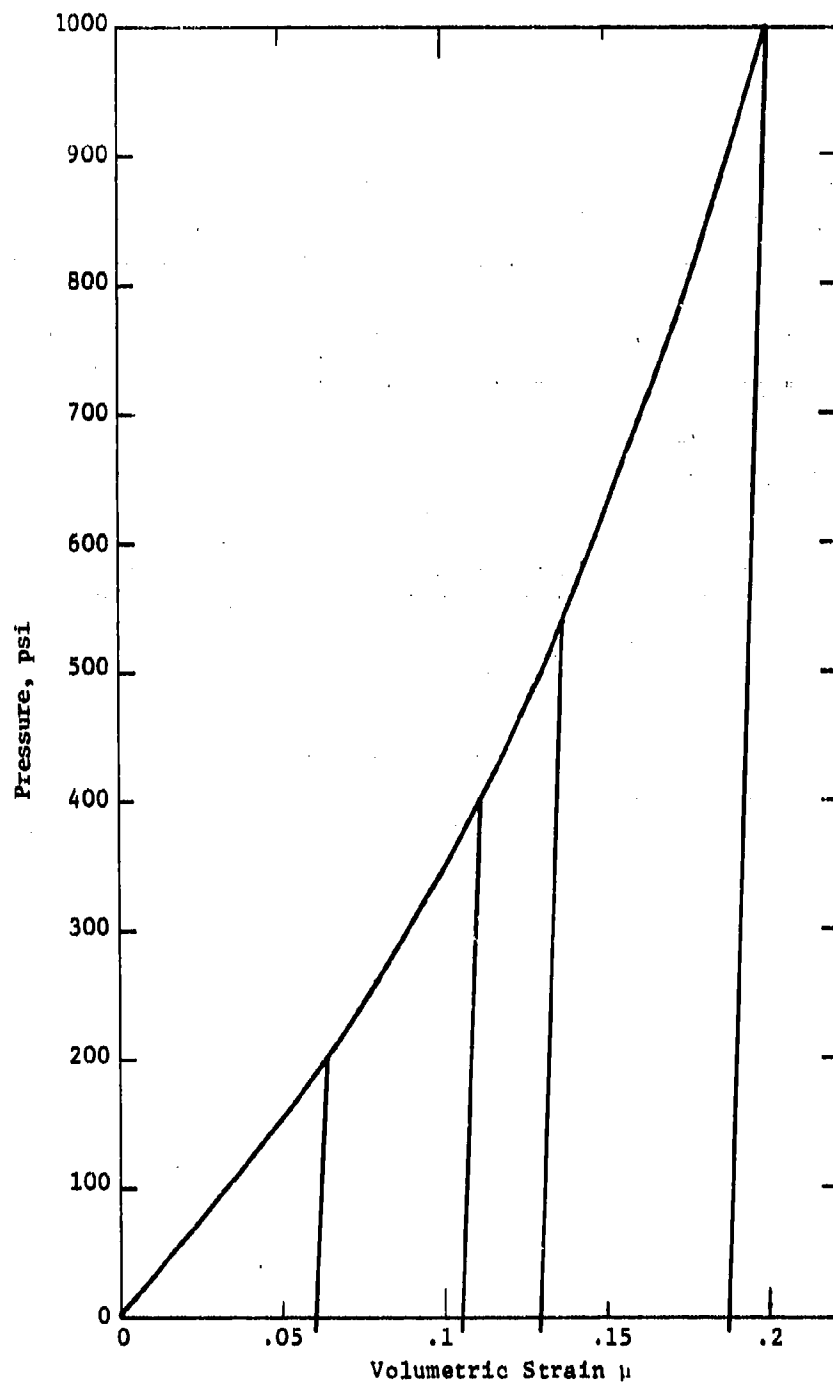


Figure A-11. Hydrostatic Load-Unload Paths for Layer 2
(P to 1000 psi)

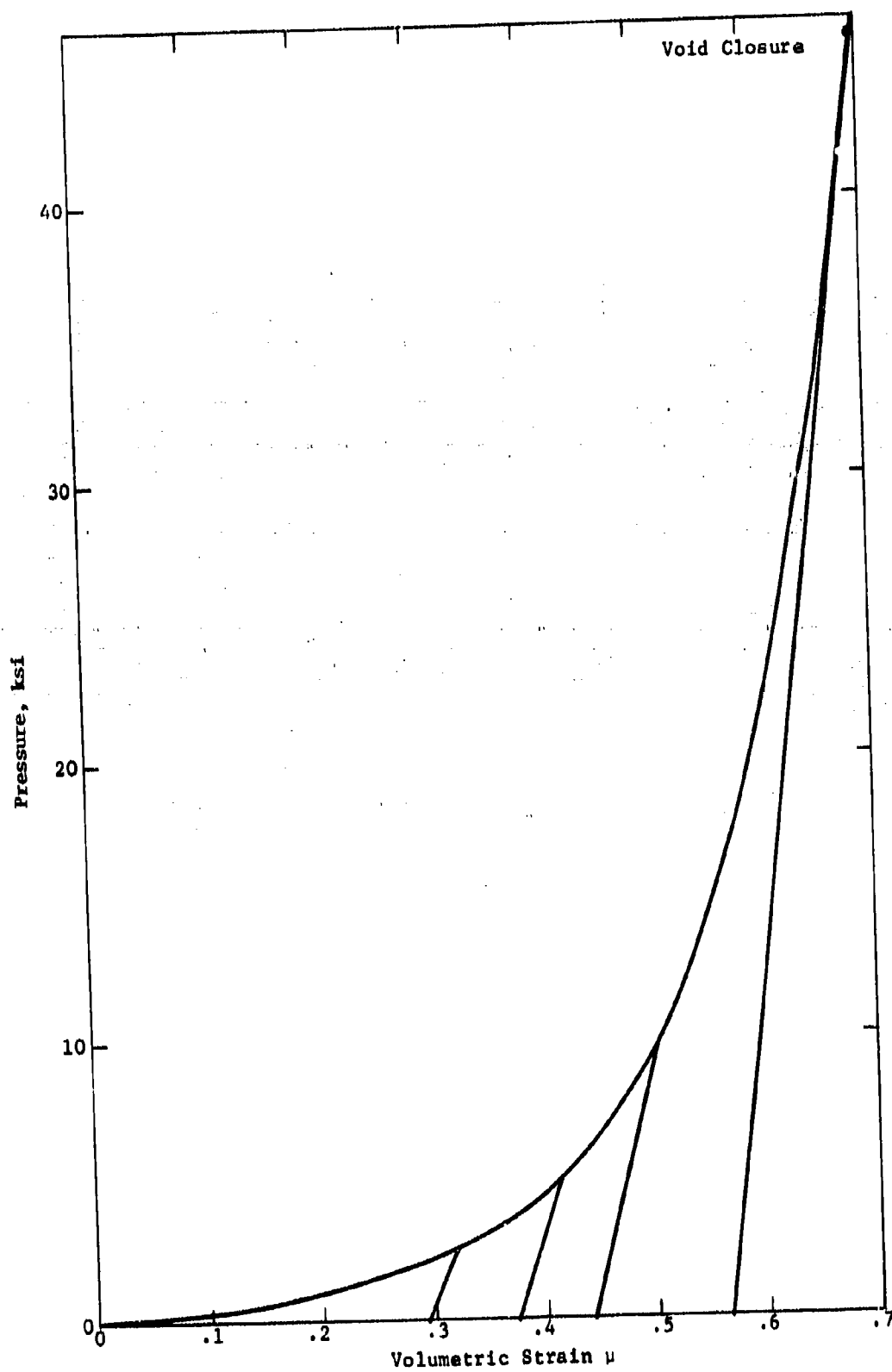


Figure A-12. Hydrostatic Load-Unload Paths for Layer 2
(P to 46 ksi)

$$P = a_1 \mu$$

$$\mu < 0$$

$$P = P_i + a_i(\mu - \mu_i) + b_i(\mu - \mu_i)^2 + c_i(\mu - \mu_i)^3$$

$$\mu_i \leq \mu < \mu_{i+1}$$

$$i = 1, 2, 3$$

$$P = P_c - K_c(\mu_c - \mu) + A(\mu_c - \mu)^\alpha$$

$$\mu_4 \leq \mu \leq \mu_c$$

$$P = P_c + K_{\max}(\mu - \mu_c)$$

$$- (K_{\max} - K_c) \mu^* \left[1 - \exp \frac{\mu_c - \mu}{\mu^*} \right]$$

$$\mu > \mu_c$$

The values of the constants are:

$$a_1 = 2.38661 \times 10^{-4} \text{ Mb}$$

$$\mu_1 = 0$$

$$b_1 = -1.43803 \times 10^{-4} \text{ Mb}$$

$$\mu_2 = .0547$$

$$c_1 = 7.11694 \times 10^{-3} \text{ Mb}$$

$$\mu_3 = .1013$$

$$a_2 = 2.86813 \times 10^{-4} \text{ Mb}$$

$$\mu_4 = .1221$$

$$b_2 = 1.02409 \times 10^{-3} \text{ Mb}$$

$$\mu_c = .14155$$

$$c_2 = 6.39712 \times 10^{-2} \text{ Mb}$$

$$\mu^* = .25$$

$$a_3 = 7.99009 \times 10^{-4} \text{ Mb}$$

$$K_c = .028085 \text{ Mb}$$

$$b_3 = 9.96726 \times 10^{-3} \text{ Mb}$$

$$K_{\max} = .689465 \text{ Mb}$$

$$c_3 = -1.80756 \times 10^{-1} \text{ Mb}$$

$$P_1 = 0$$

$$A = 3.79269 \times 10^{-2} \text{ Mb}$$

$$P_2 = 1.37893 \times 10^{-5} \text{ Mb}$$

$$\alpha = 1.11227$$

$$P_3 = 3.58522 \times 10^{-5} \text{ Mb}$$

$$\rho_0 = 1.8581 \text{ gm/cm}^3 (116 \text{ lb/ft}^3) \quad P_c = 1.27413 \times 10^{-4} \text{ Mb}$$

A.3.2 Shear Modulus - Loading

The shear modulus function for loading was developed from an analytic fit to Poisson's ratio along the loading stress path and the bulk modulus as derived from the

hydrostat equations. A maximum value equal to the unloading shear modulus was imposed to prevent energy generation

$$G_{load} = \text{Min} \left[\frac{3B(1-2\nu)}{2(1+\nu)}, G_{unload} \right]$$

where

$$B = (\mu+1) \frac{dP_{load}(\mu)}{d\mu}$$

and

$$\nu = \frac{3 - \frac{d\Delta}{dP}}{6 + \frac{d\Delta}{dP}}$$

where

$$\Delta = \sigma_z - \sigma_r$$

The following expressions were derived for the derivative

$\frac{d\Delta}{dP}$ along the uniaxial stress loading path:

$$\frac{d\Delta}{dP} = S + B\beta P^{\beta-1} \quad 0 \leq P \leq 300 \text{ psi}$$

$$\frac{d\Delta}{dP} = \frac{DE}{(E+P-300)^2} \quad P > 300 \text{ psi}$$

where

$$S = .66667$$

$$B = -4.69643 \times 10^{-4} \text{ psi}^{-1}$$

$$\beta = 2.07216$$

$$D = 137.925 \text{ psi}$$

$$E = 688.145 \text{ psi}$$

Initial values of Young's modulus, the bulk modulus, the shear modulus, the constrained modulus, Poisson's ratio, and the dilatational sound speed from the model are:

$$\begin{aligned} E_0 &= 3,115 \text{ psi} & M_0 &= 5,000 \text{ psi} \\ B_0 &= 3,462 \text{ psi} & \nu_0 &= .35 \\ G_0 &= 1,154 \text{ psi} & c_0 &= 447 \text{ ft/sec} \end{aligned}$$

A.3.3 Unloading Model

In the hysteretic region, $\mu < \mu_c$, a model giving a fan of constant slope P - μ unloading paths was used (slopes are a function of μ_{\max}):

$$P = P_{\max} + K(\mu - \mu_{\max}) \quad \mu_{\max} < \mu_c$$

$$P = P_c + K_c(\mu - \mu_c) \quad \mu_{\max} \geq \mu_c$$

In this region, the unloading bulk modulus varies from a minimum of 35.8 ksi to a maximum of 465 ksi, equal to the bulk modulus for loading at void closure. A constant representative value of 15 ksi for the unloading shear modulus was assumed. This value was determined from the given unload path from $\sigma_z = 1000$ psi and an estimate of the unloading Poisson's ratio at that point. K is a function given by:

$$K = \frac{B_0 + B_1 [\exp(b\mu_{\max}) - 1]}{\mu_{\max} + 1} \quad \mu_{\max} < \mu_c$$

The constants, as determined from the given unload paths, are:

$$B_0 = 2.47298 \times 10^{-3} \text{ Mb}$$

$$B_1 = 1.02046 \times 10^{-7} \text{ Mb}$$

$$b = 88.855$$

The initial Poisson's ratio for unloading is .3165 from this fit.

For $p > p_c$, unloading is assumed to be reversible (follows the load path).

Hydrostatic tension is limited by imposing a minimum value of pressure: $P_{\min} = -29.5 \text{ psi}$.

A.3.4 Failure Surface

A yield function $Y(P)$ was fit to the failure envelope suggested, where $Y = \sqrt{3J_2}$ at failure. An asymptotic form was used to smoothly extend the failure surface in the high-pressure region. The functions derived are:

$$Y = 22 + \frac{22}{29.5} P \quad -29.5 \leq P \leq 0$$

$$Y = 22 + \frac{22}{29.5} P - 4.0337 \times 10^{-3} P^{1.7663} \quad 0 < P \leq 300$$

$$Y = 150 + \frac{118.77(P-300)}{652.07 + (P-300)} \quad P > 300$$

Here the units for Y and P are psi.

A.3.5 Comparative Results

Plots of stress vs strain, stress difference vs pressure, and pressure vs volumetric strain for uniaxial strain load-

unload paths computed with the model, along with the WES curves, are shown in Figures A-13 to A-16.

A.4 LAYER 4

As suggested by WES, a model using a higher value for Poisson's ratio than that originally recommended was formulated in order to give better agreement with data from tri-axial tests with small constant confining pressures.

A.4.1 Loading Hydrostat

The following equations were deduced for the loading hydrostat:

$$P = K_0 \mu \quad \mu \leq 0$$

$$P = P_c - K_c(\mu_c - \mu) + A[\exp a(\mu_c - \mu)^\alpha - 1] \quad 0 < \mu < \mu_c$$

$$P = P_c + K_c(\mu - \mu_c) \quad \mu > \mu_c$$

The values of the constants are:

$$\begin{aligned} A &= -3.57227 \times 10^{-4} \text{ Mb} & K_c &= 3.75514 \times 10^{-2} \text{ Mb} \\ a &= -509.52 & K_0 &= 1.02597 \times 10^{-2} \text{ Mb} \\ \alpha &= 1.3 & \mu_c &= .0009 \\ P_c &= 1.43636 \times 10^{-5} \text{ Mb} & \rho_0 &= 1.9702 \text{ gm/cm}^3 \\ & & & (123 \text{ lb/ft}^3) \end{aligned}$$

A.4.2 Unloading Model

In the hysteretic region, $\mu < \mu_c$, the P - μ unloading paths were made a function of the hydrostatic load path and the value of μ_{\max} attained:

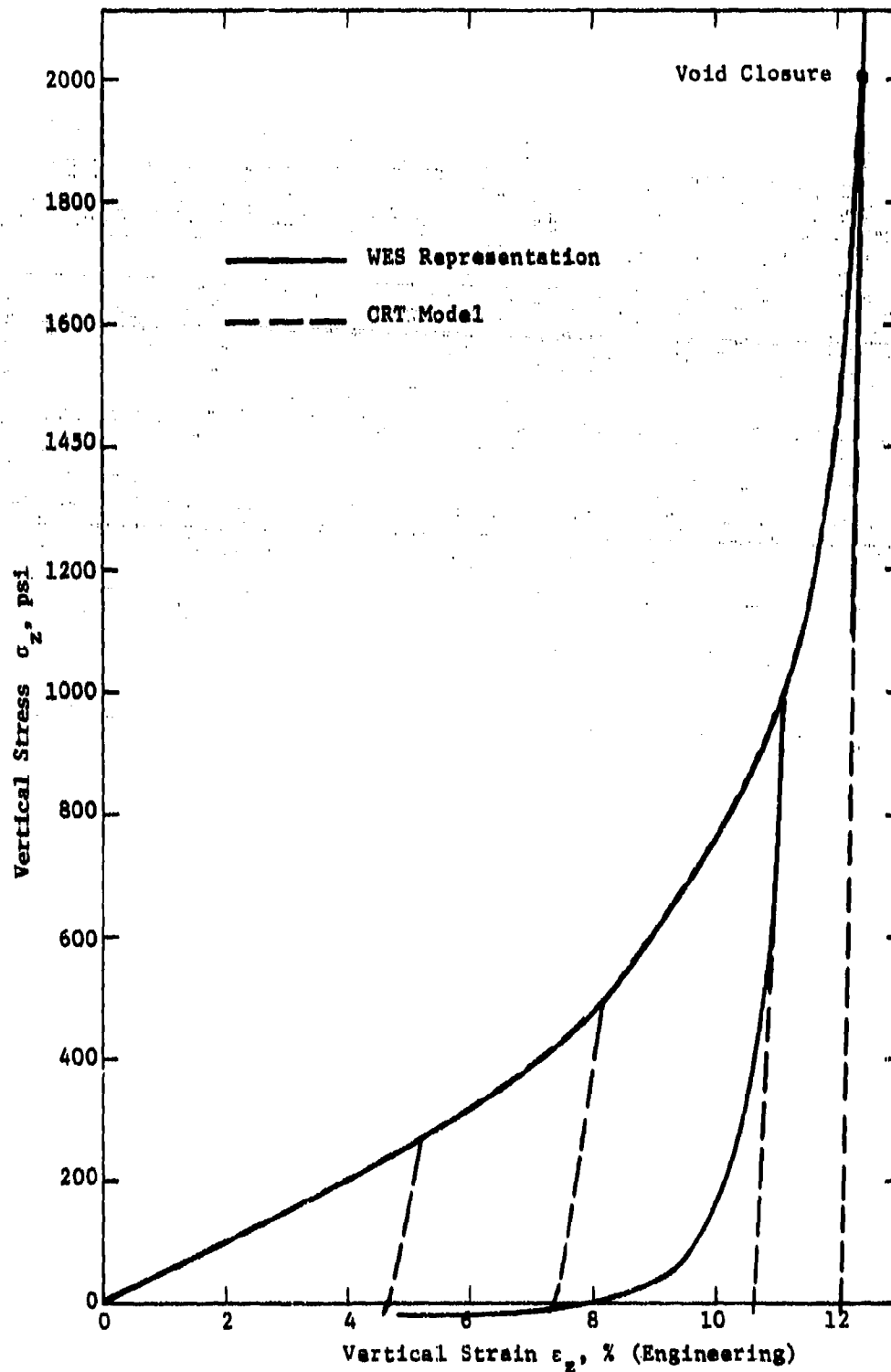


Figure A-13. Uniaxial Strain Load-Unload Paths for Layer 3

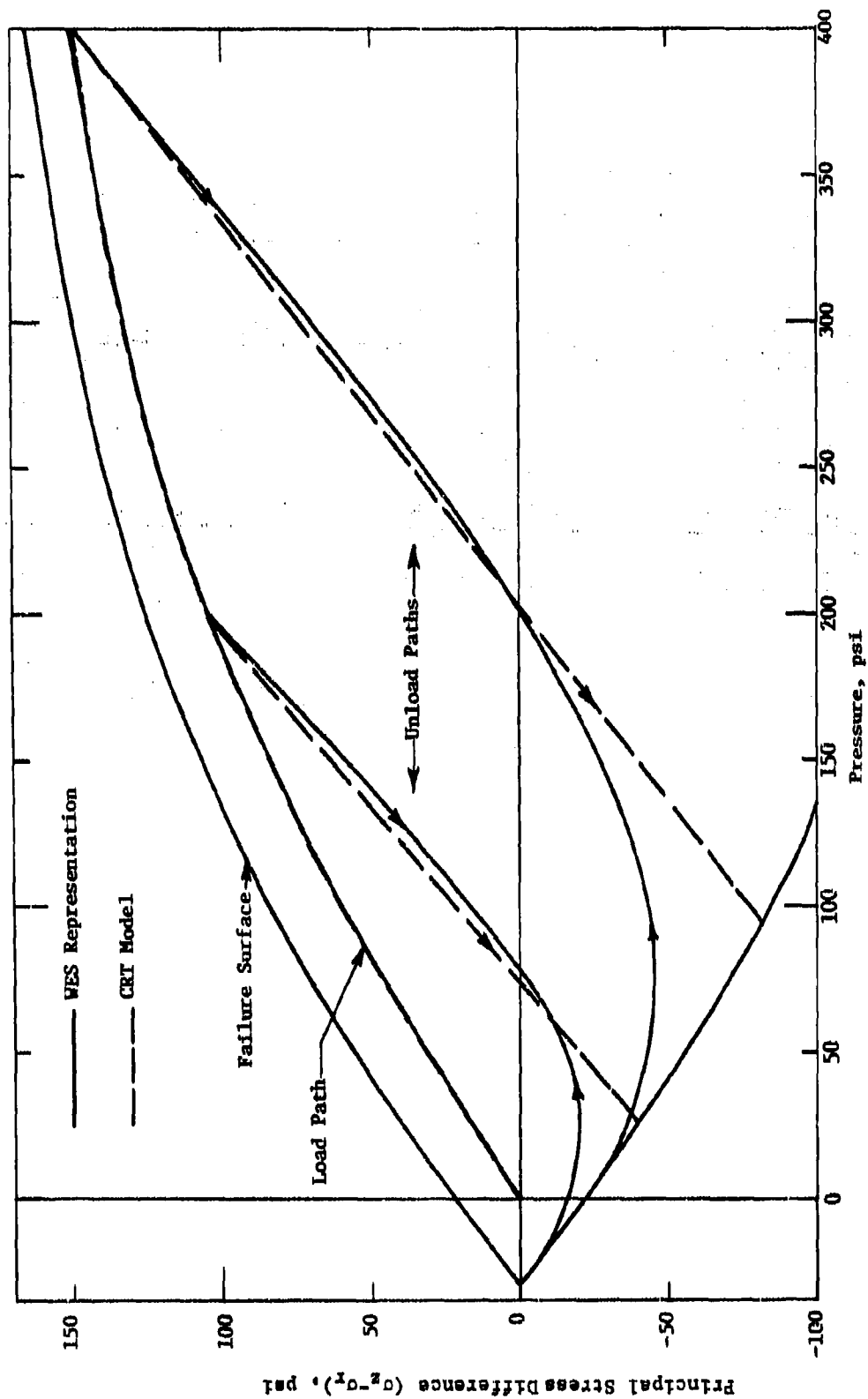


Figure A-14. Uniaxial Strain Stress Paths and Failure Surface for Layer 3

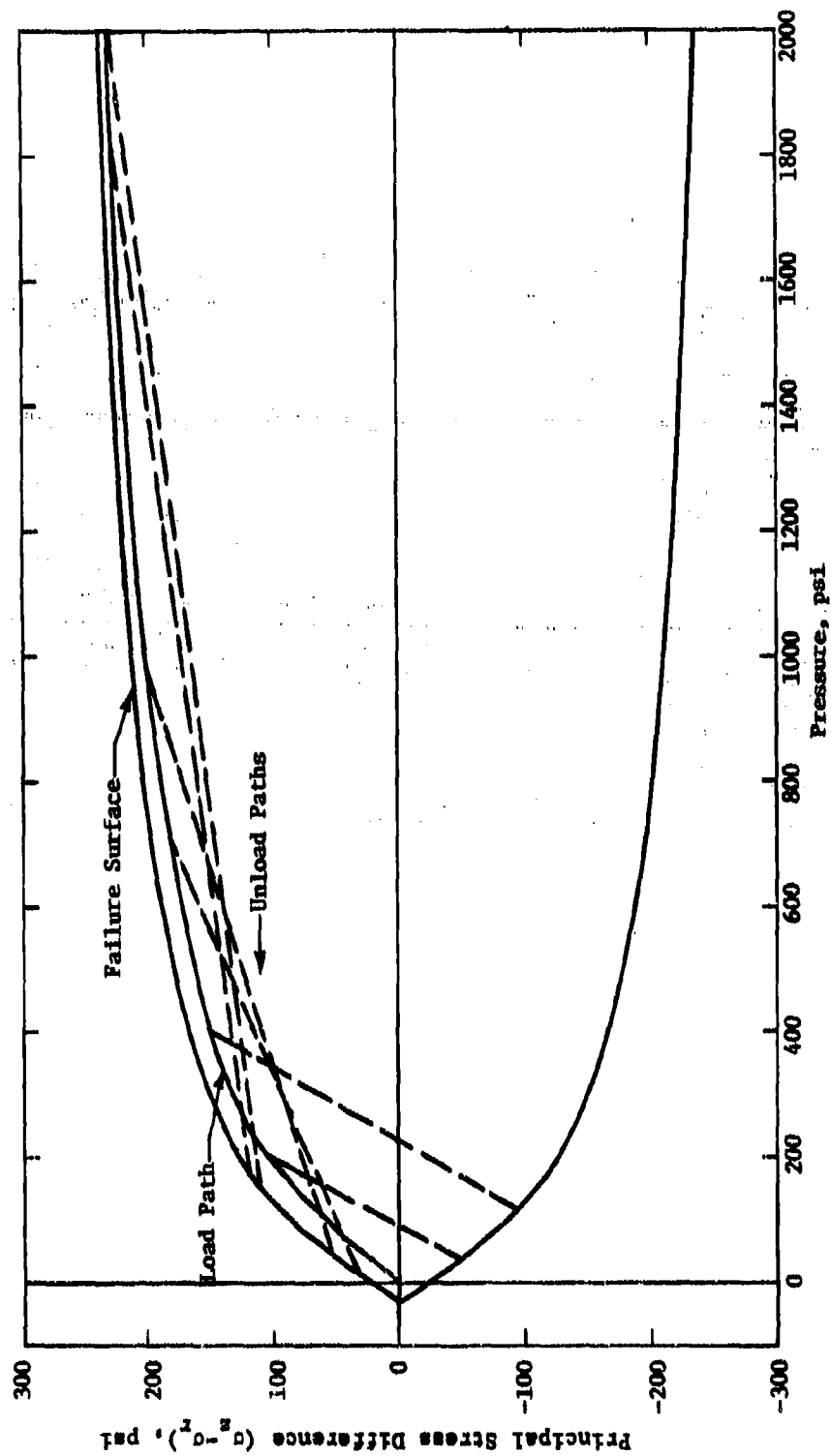


Figure A-15. Uniaxial Strain Stress Paths and Failure Surface in High Pressure Region for Layer 3
(P to 2000 psi)

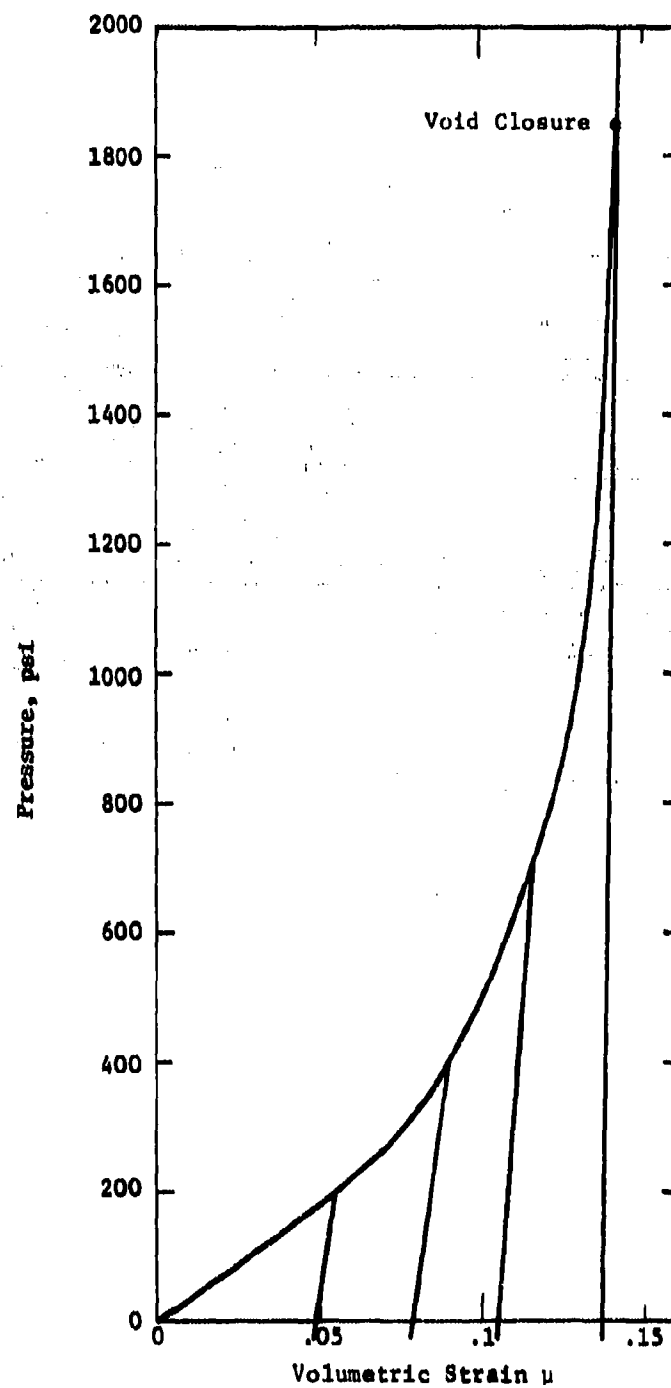


Figure A-16. Hydrostatic Load-Unload Paths for Layer 3

$$P = P_{load} - A_u (\mu_{max} - \mu)^{1/2} \quad \mu_{max} < \mu_c$$

$$P = P_{load} - A_u (\mu_c - \mu)^{1/2} \quad \mu_{max} \geq \mu_c$$

where $P_{load}(\mu)$ is the loading hydrostat and $A_u = 3.7548 \times 10^{-5}$ Mb.

For $\mu > \mu_c$, unloading is assumed to be reversible (follows the load path).

Hydrostatic tension is limited by imposing a minimum value of pressure: $P_{min} = -50$ psi.

A.4.3 Shear Modulus - Loading and Unloading

The shear modulus for both loading and unloading were made variables, depending on the bulk modulus. A constant Poisson's ratio in both loading and unloading was employed.

$$G = \frac{3B(1-2\nu)}{2(1+\nu)}$$

where

$$B = (\mu+1) \frac{dP(\mu)}{d\mu}$$

and

$$\nu = .497$$

$P(\mu)$ is the appropriate loading or unloading hydrostatic equation.

Initial values of Young's modulus, the bulk modulus, the shear modulus, the constrained modulus, and the dilatational sound speed from the model are:

$$E_0 = 2,679 \text{ psi} \quad G_0 = 894.6 \text{ psi} \quad c_0 = 2,377 \text{ ft/sec}$$

$$B_0 = 148.8 \text{ ksi} \quad M_0 = 150 \text{ ksi}$$

A.4.4 Failure Surface

A yield function $Y(P)$ was fit to the failure envelope suggested, where $Y = \sqrt{3J_2}$ at failure. The functions derived are:

$$Y = 25 + .5P \quad -50 \leq P \leq 0$$

$$Y = 50 + A(P_1 - P)^\alpha + B(P_1 - P)^2 \quad 0 < P \leq 150$$

$$Y = 50 \quad P > 150$$

where

$$A = -2.58234 \times 10^{-15} \text{ psi}$$

$$B = -8.89951 \times 10^{-4} \text{ psi}$$

$$\alpha = 7.024$$

$$P_1 = 150 \text{ psi}$$

Here the units for Y and P are psi.

A.4.5 Comparative Results

Plots of stress vs strain, stress difference vs pressure, and pressure vs volumetric strain for uniaxial strain load-unload paths computed with the model, along with the WES curves, are shown in Figures A-17 to A-19.

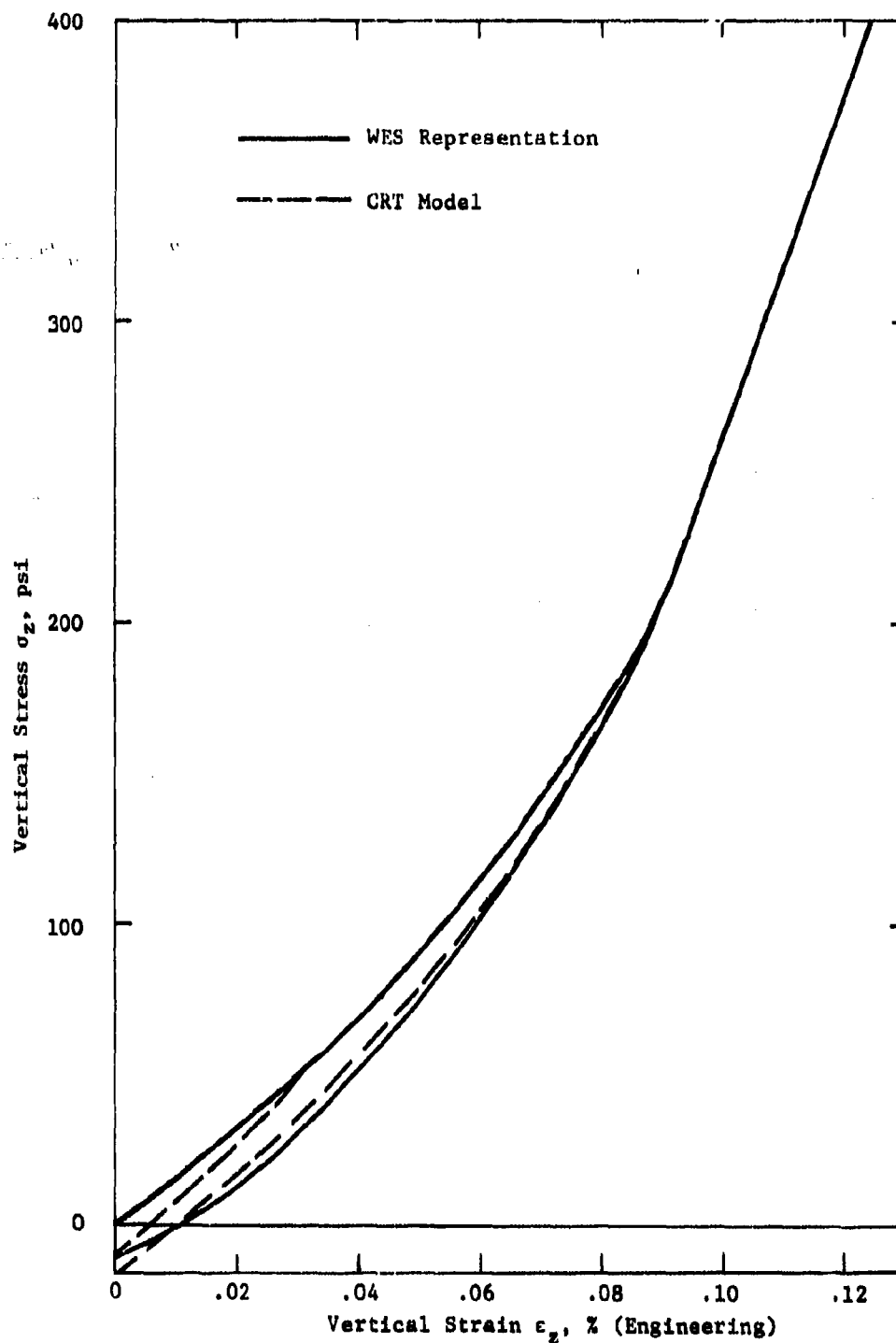


Figure A-17. Uniaxial Strain Load-Unload Paths for Layer 4

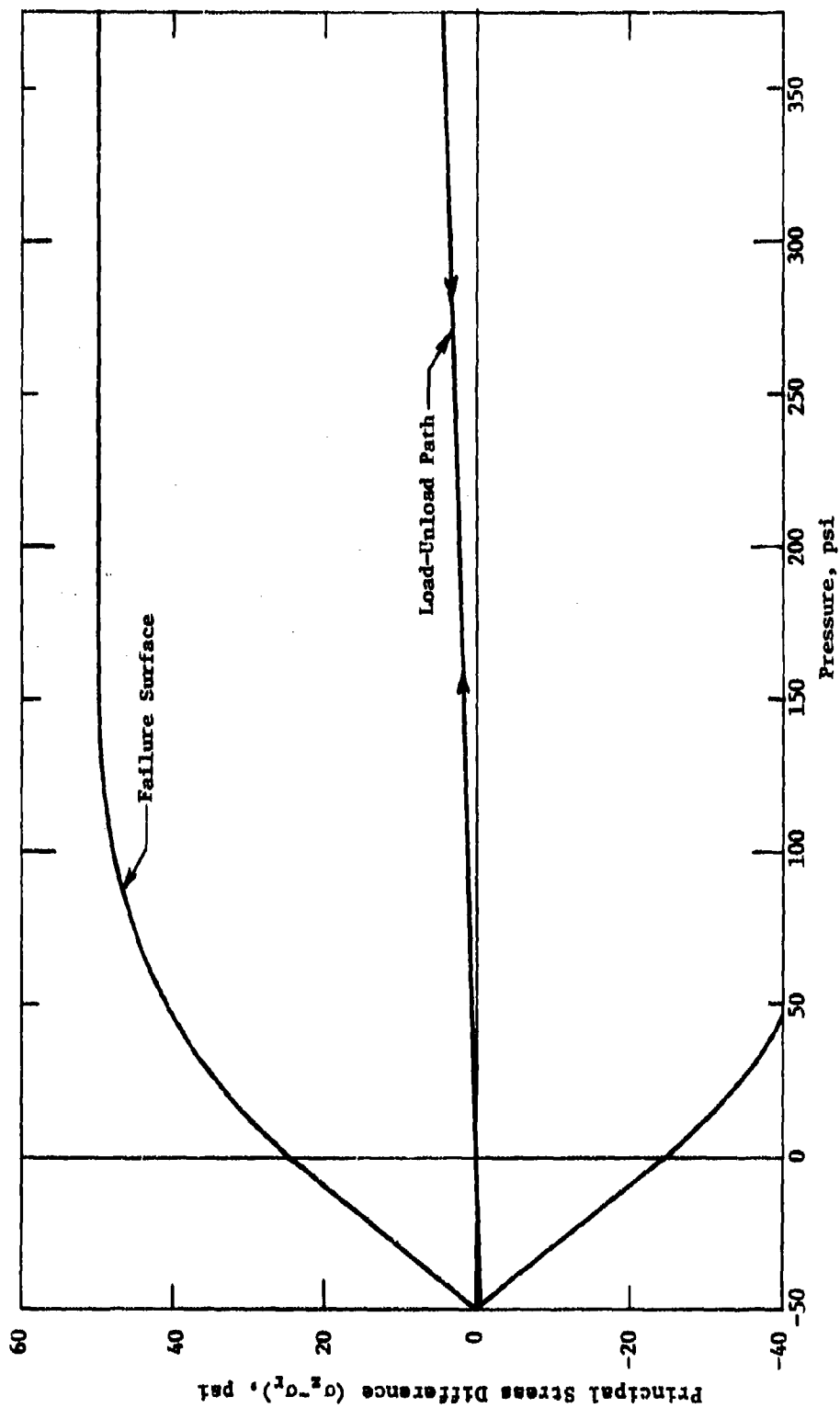


Figure A-18. Uniaxial Strain Stress Path and Failure Surface for Layer 4

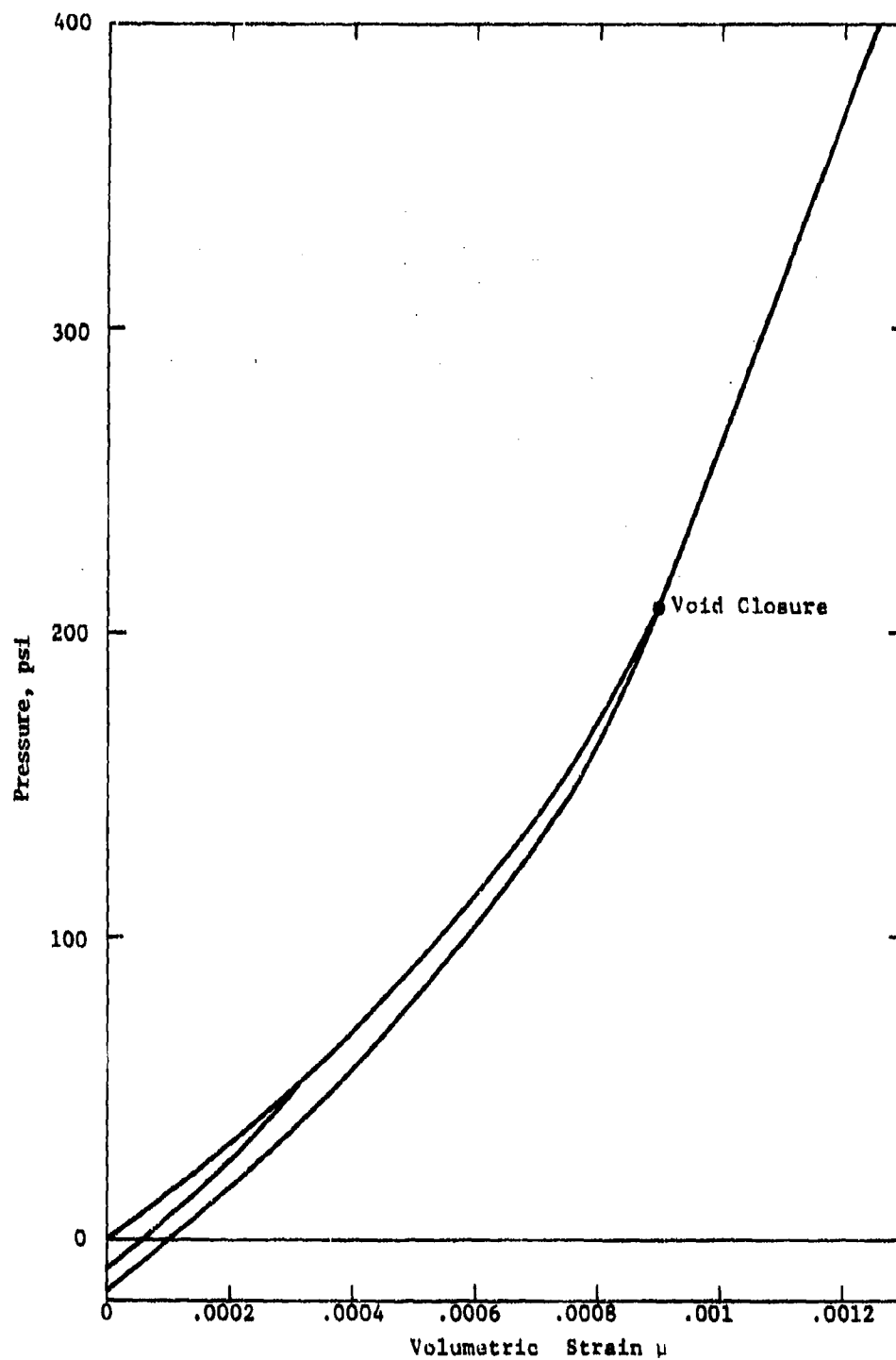


Figure A-19. Hydrostatic Load-Unload Paths for Layer 4

APPENDIX B DISTORTION, VELOCITY, AND PRINCIPAL STRESS FIELD PLOTS

A series of field plots of the computational grid, particle velocities, and principal stresses which illustrate the soil response during the penetration were prepared. These are shown for the following penetration depths and times:

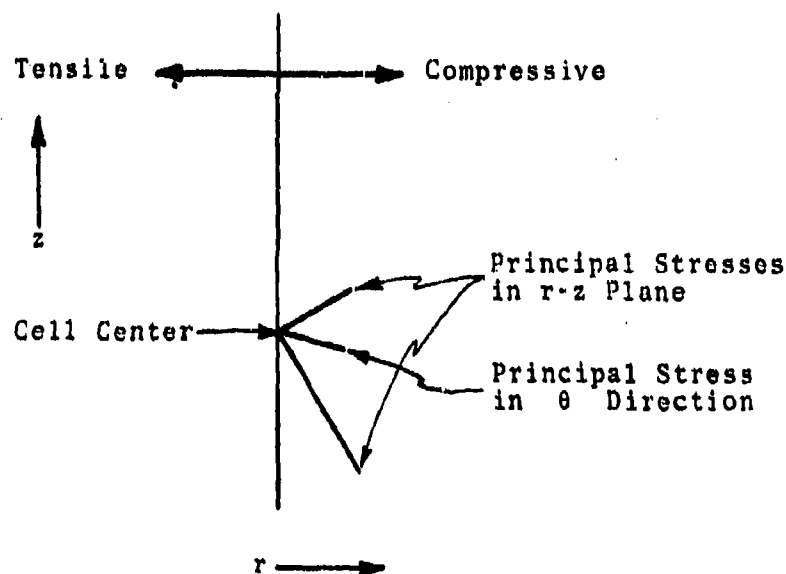
Depth (m) (ft)	Time (msec)	Figure No. of plot for		
		Distortion (Grid)	Velocity	Stress
.10 .33	.66	B-1	B-2	B-3
.40 1.32	2.65	B-4	B-5	B-6
2.00 6.56	13.64	B-7	B-8	B-9
2.80 9.19	19.52	B-10	B-11	B-12
3.00 9.83	21.03	B-13	-	-
5.28 17.31	40.11	B-14	B-15	B-16
5.36 17.58	40.87	B-17	-	-

The plots of the grid also show which material is currently failing; i.e., is on the yield surface. This is denoted by cells containing an x or + , with x indicating a compressive pressure, $P \geq 0$, and + indicating hydrostatic tension, $P < 0$.

The velocity vector field plots show the direction and magnitude of the particle velocity at each lattice

point in the computing grid. (For clarity in viewing the soil response, the velocity vectors of the projectile are not shown.)

In the stress field plots, the principal components of the stress tensor for each cell are shown, as follows: The magnitude of the two principal stresses in the r - z plane are plotted in their corresponding principal directions. The third principal stress (in the azimuthal direction) is plotted along the line bisecting the other two principal directions. Vectors pointing to the right are compressive, to the left, tensile. An example of how a stress tensor is plotted is sketched below:



CALIFORNIA RESEARCH AND TECHNOLOGY HAVE-L CODE
 RUN NO. 2080-2. OMA PENETRATOR TEST AT DRES (RIGID BODY SOL'N)
 CYCLE 91

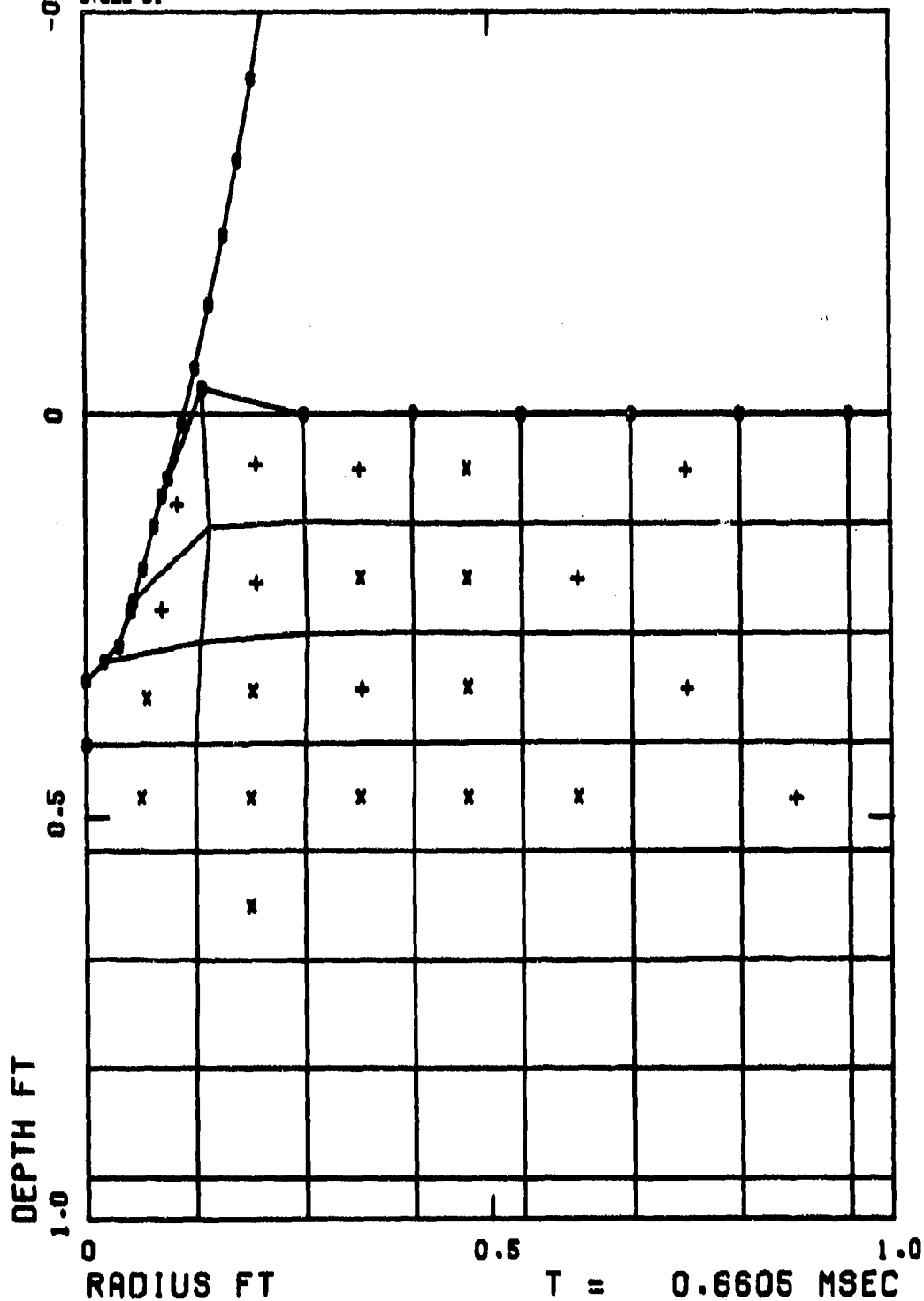


Figure B-1. Grid Configuration with Penetrator at 10 cm Depth

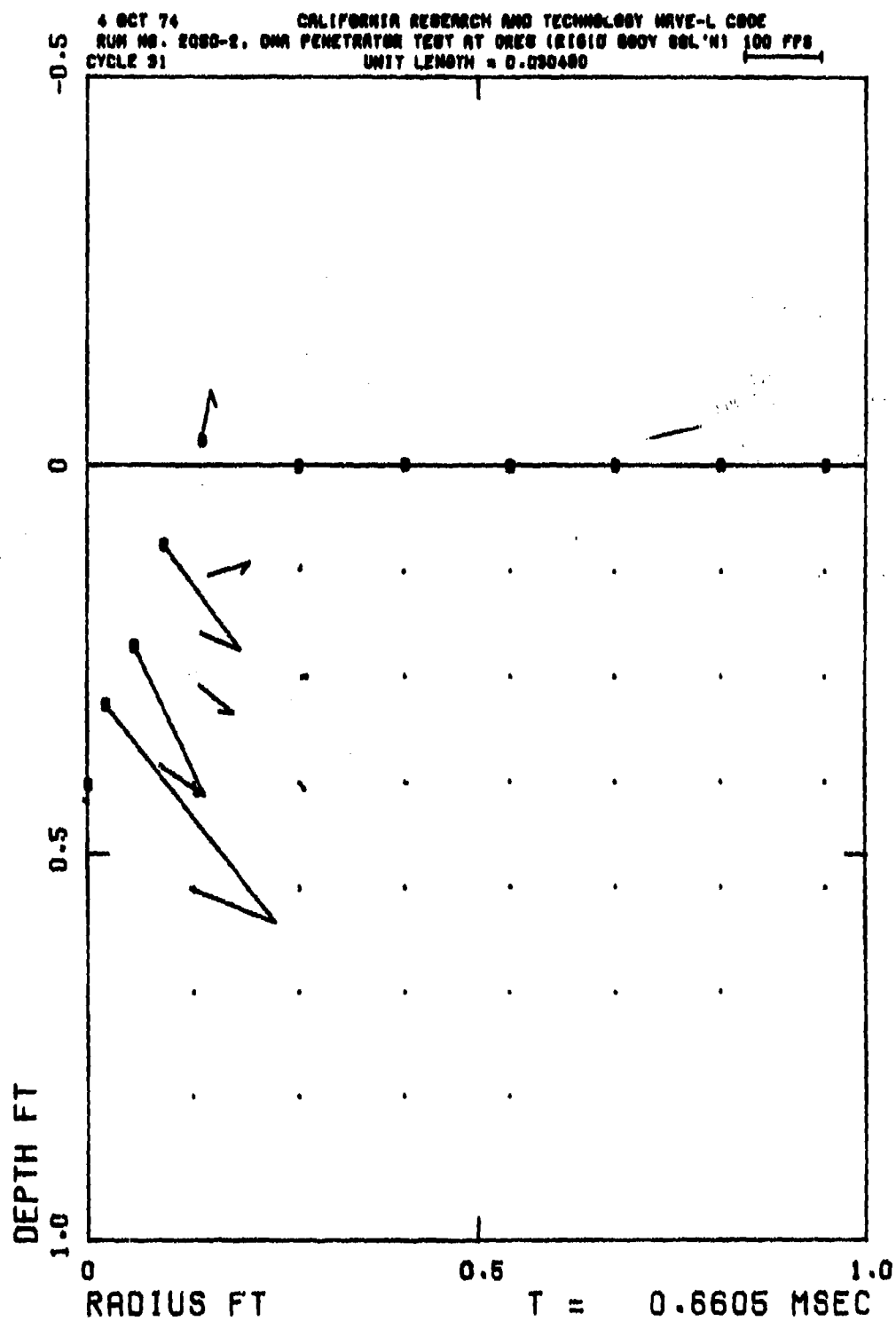


Figure H-2. Particle Velocity Field with Penetrator at 10 cm Depth

4 OCT 74 CALIFORNIA RESEARCH AND TECHNOLOGY WAVE-L CODE
 RUN NO. 2060-2. DWA PENETRATOR TEST AT DRES (RIGID BODY 96L'H) 50 BAR
 CYCLE 91 UNIT LENGTH = 0.000810

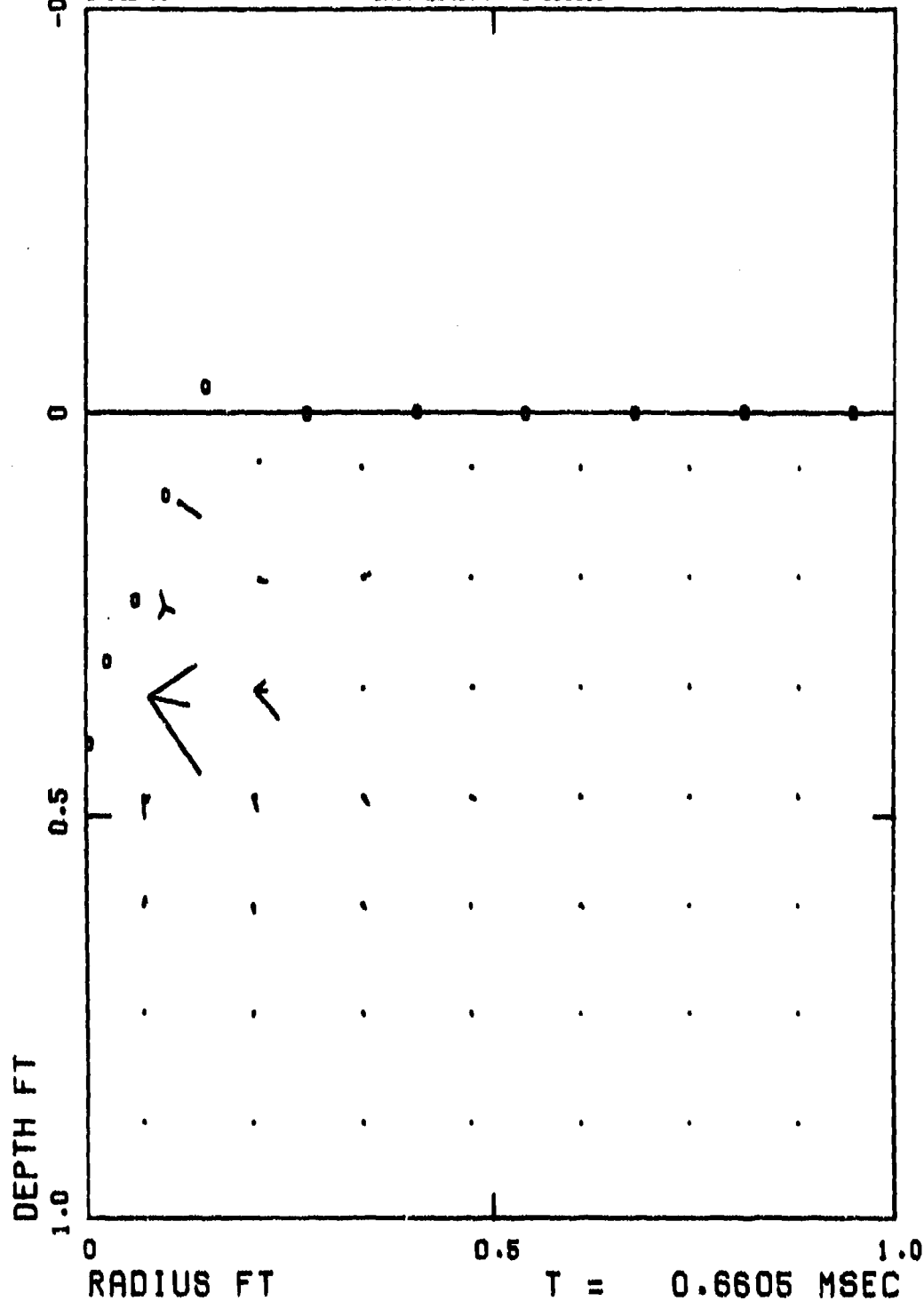


Figure B-3. Principal Stress Field with Penetrator at 10 cm Depth

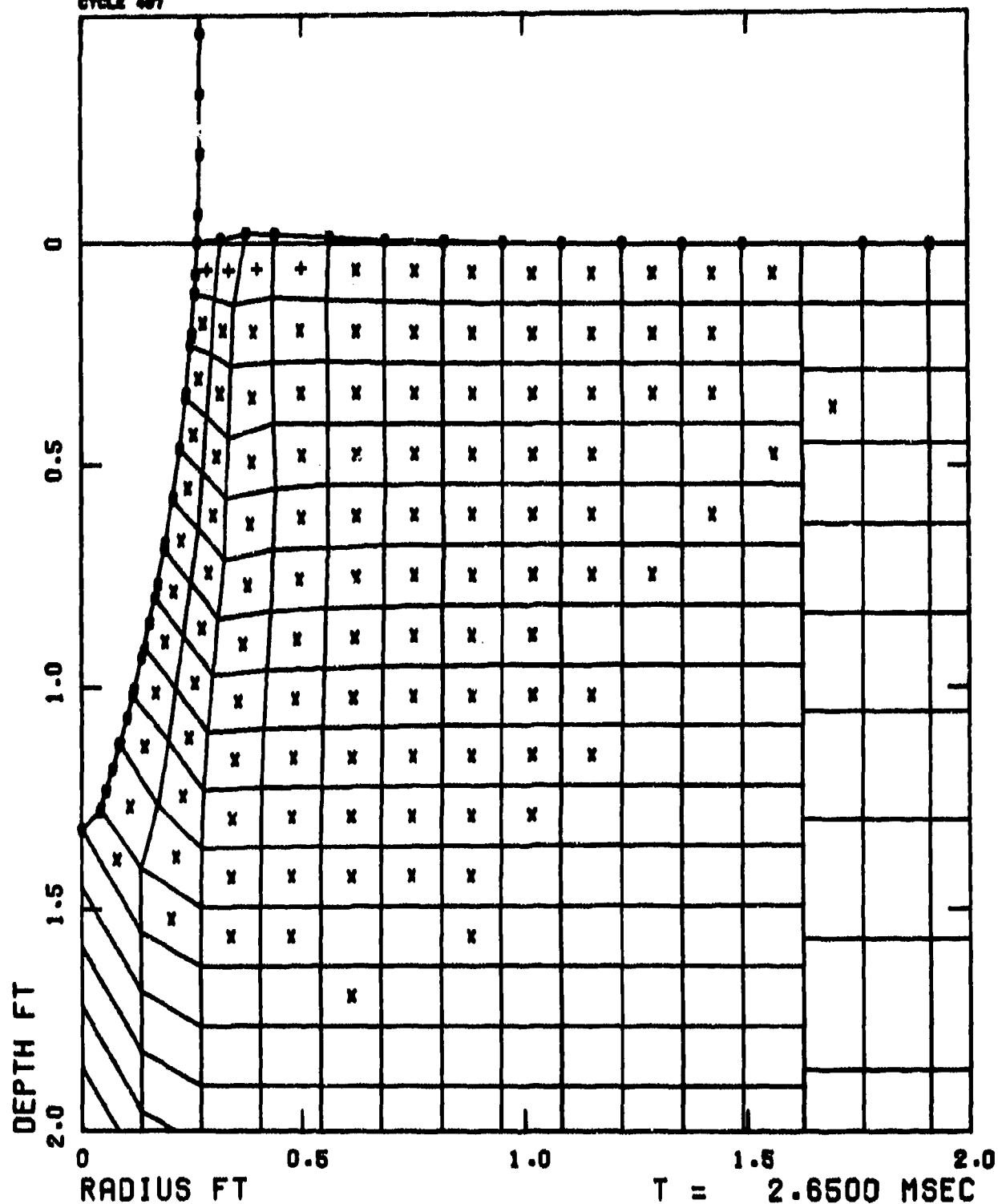


Figure B-4. Grid Configuration with Penetrator at 40 cm Depth

JUL 74 CALIFORNIA RESEARCH AND TECHNOLOGY WAVE-L CODE
 RUN NO. 2000-2. DMM PENETRATOR TEST AT GRES (RIGID BODY SOL'N)
 CYCLE 497 UNIT LENGTH = 0.000400

200 FPS

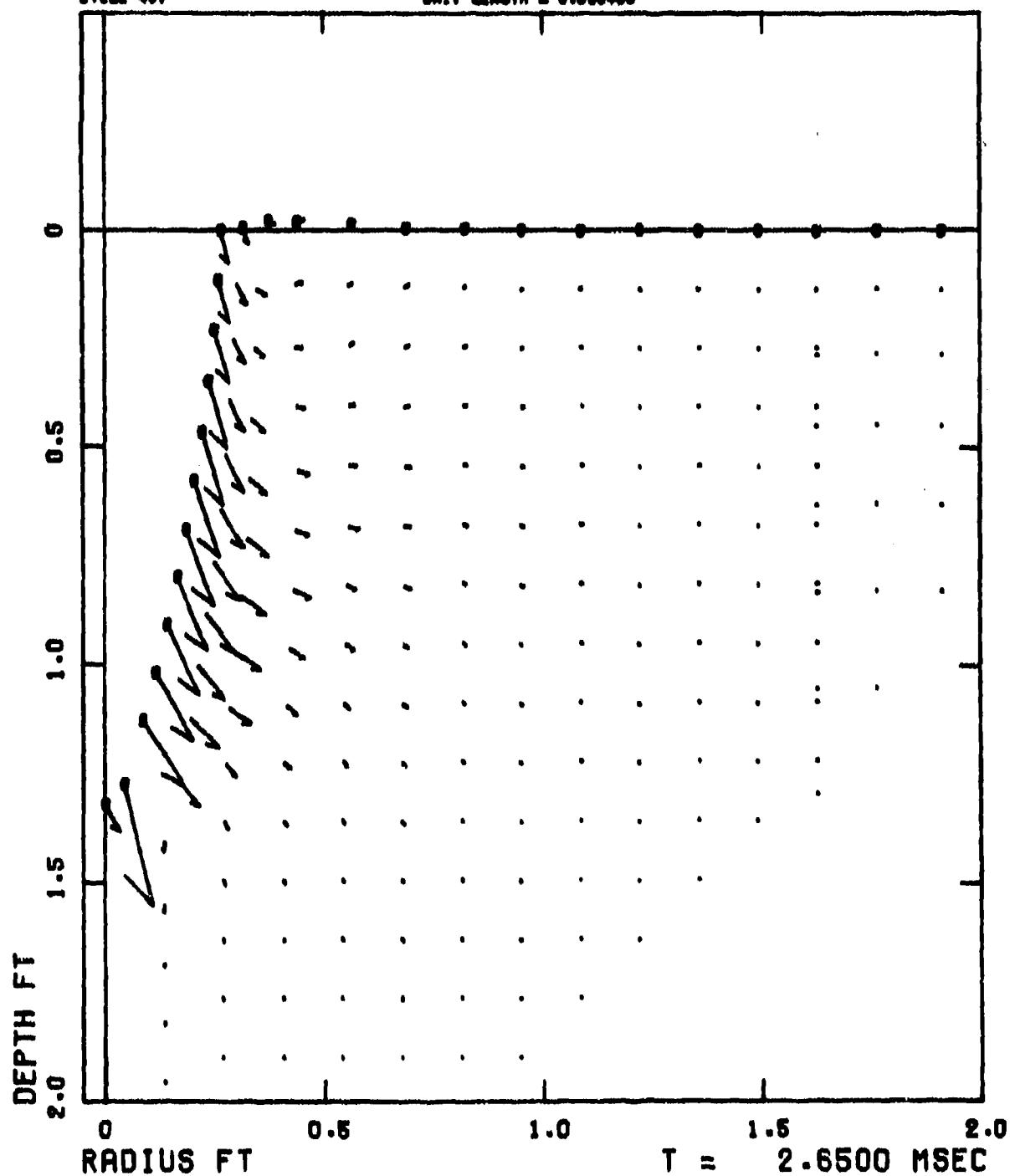


Figure B-5. Particle Velocity Field with Penetrator at 40 cm Depth

JUL 74
 RUN NO. 2050-2. OMA PENETRATOR TEST AT ORES (RIGID BODY SOL'N)
 CYCLE 487

CALIFORNIA RESEARCH AND TECHNOLOGY WAVE-L CODE
 UNIT LENGTH = 0.000010

100 DARS

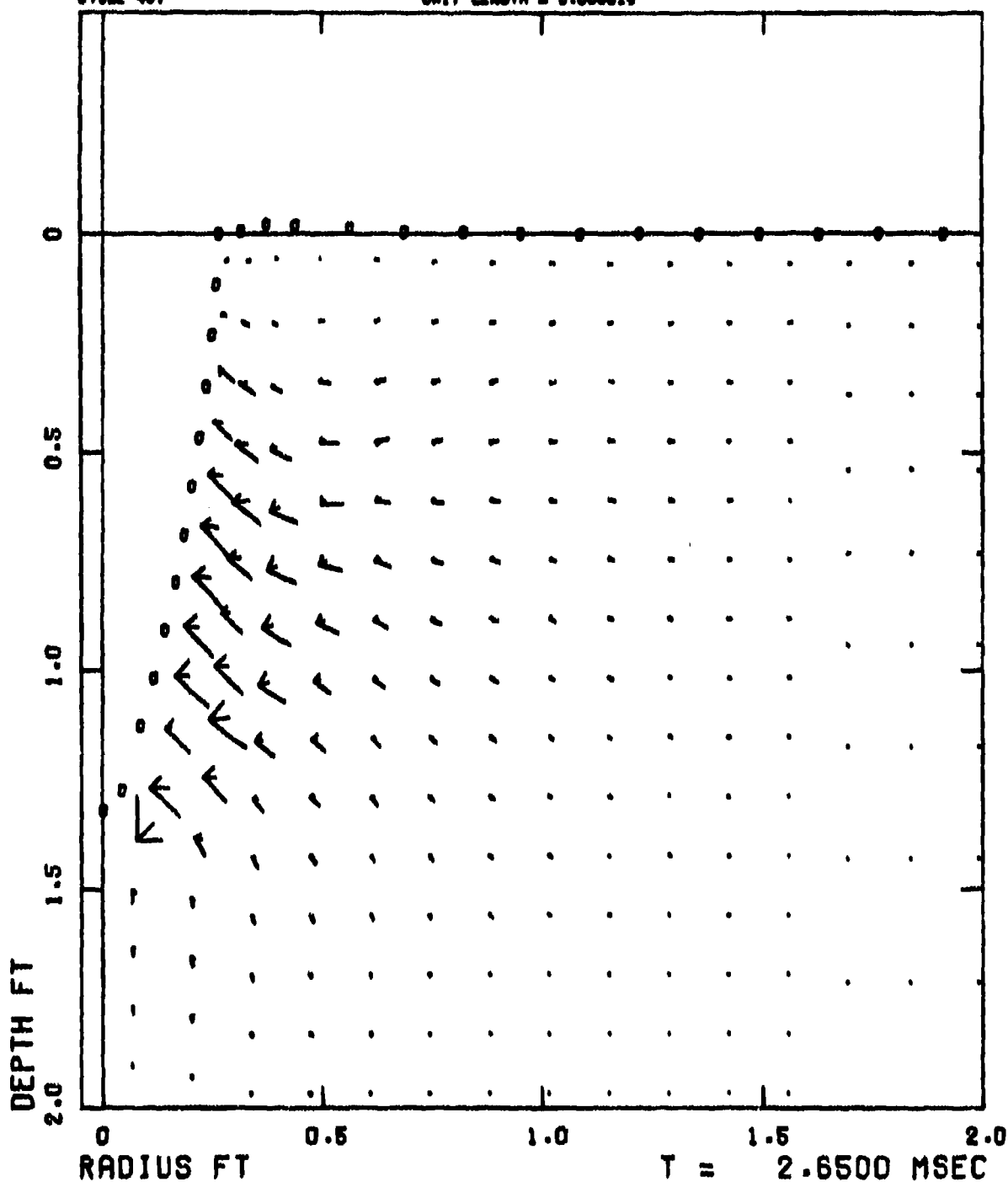


Figure B-6. Principal Stress Field with Penetrator at 40 cm Depth

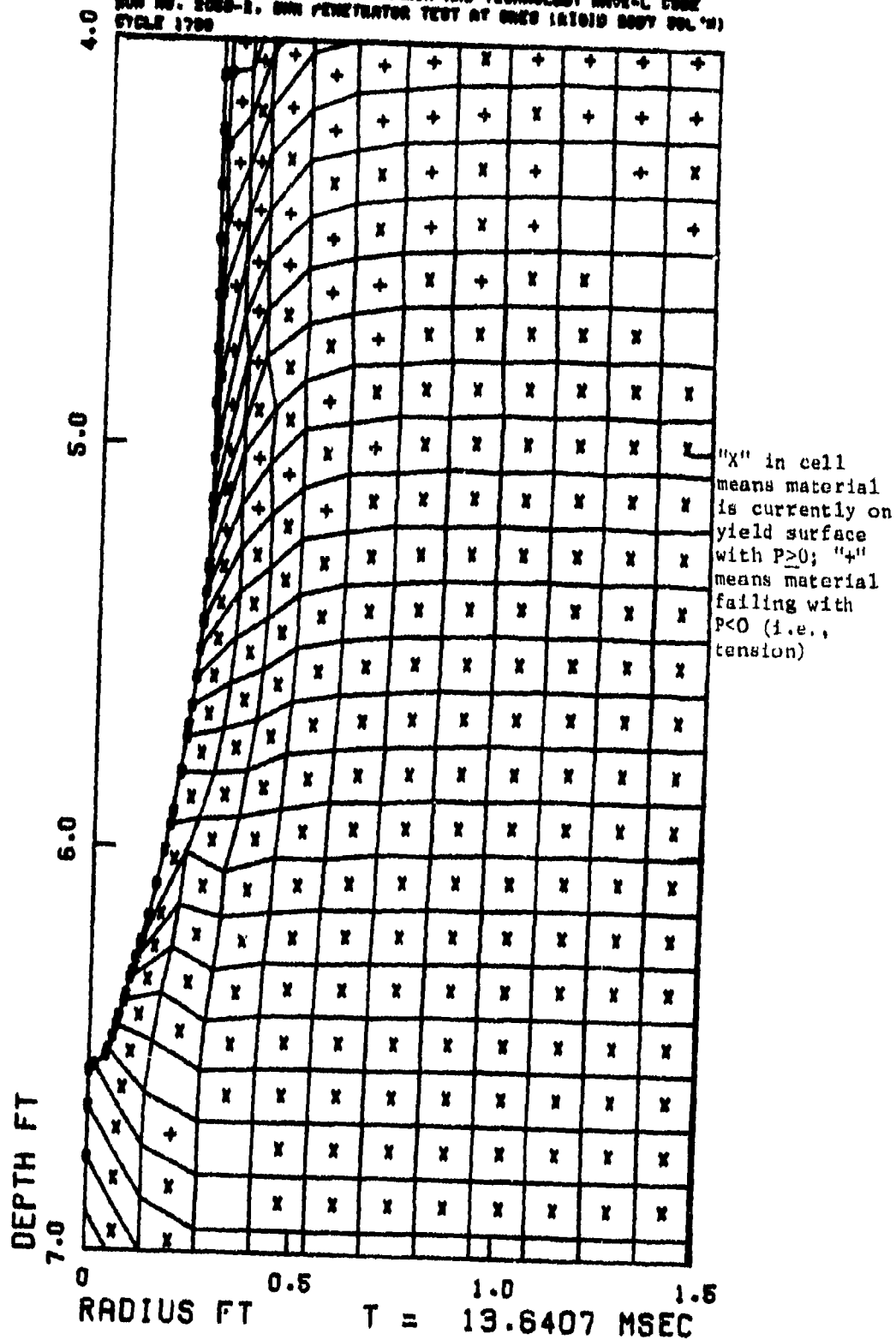


Figure B-7. Grid Configuration with Penetrator at 200 cm Depth

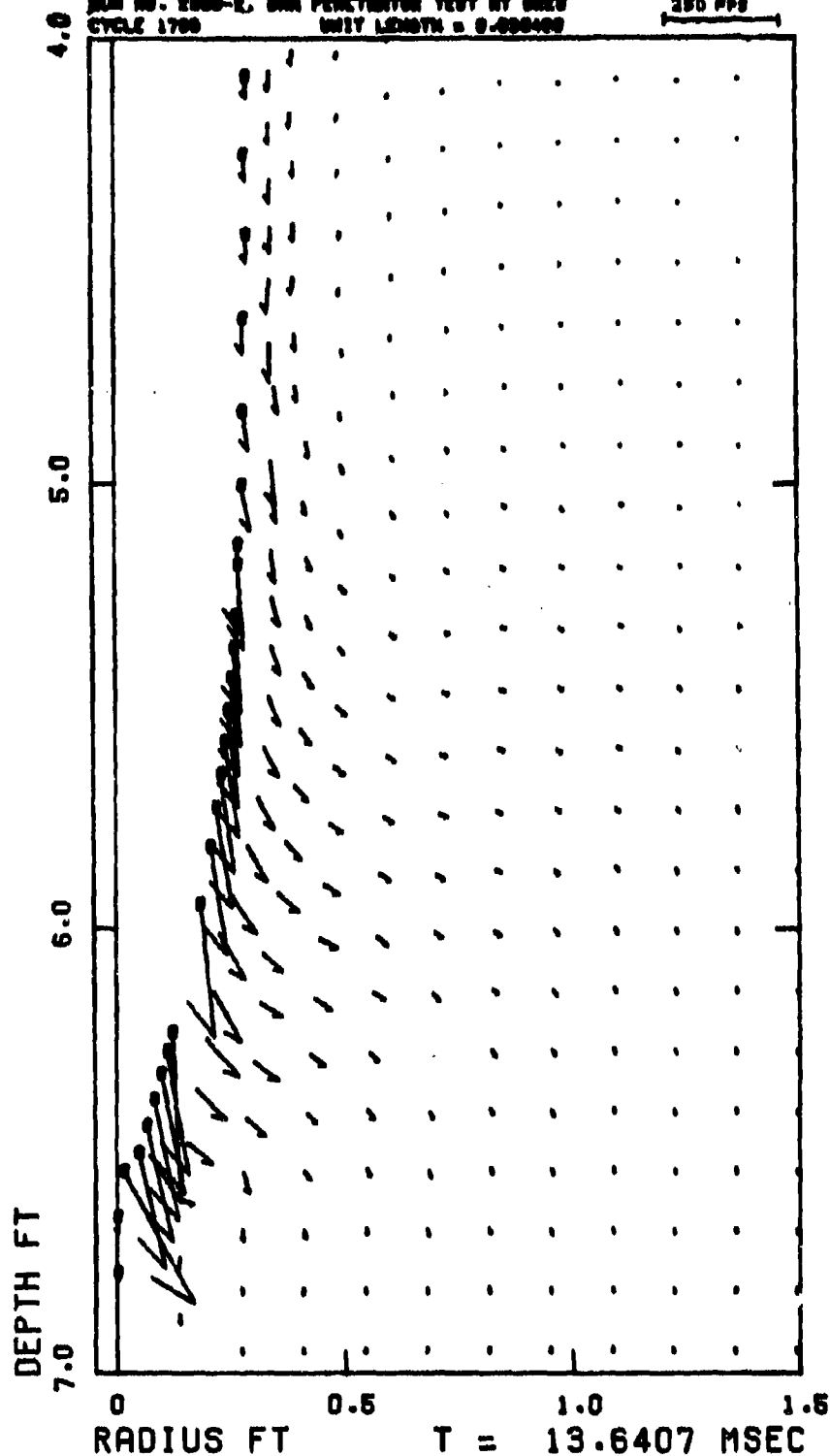


Figure B-8. Particle Velocity Field with Penetrator at 200 cm Depth

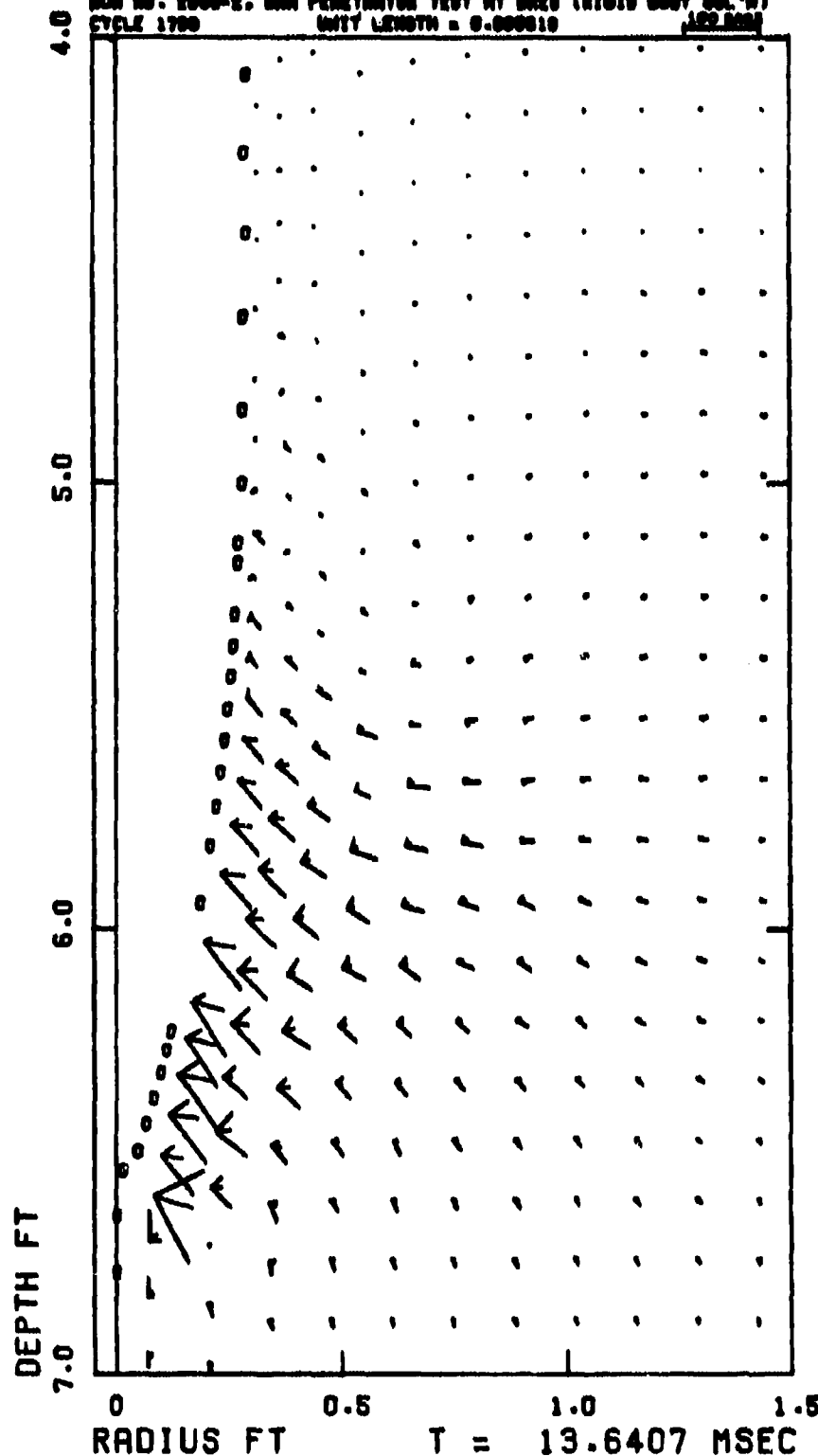


Figure B-9. Principal Stress Field with Penetrator at 200 cm Depth

CALIFORNIA RESEARCH AND TECHNOLOGY WAVE-L CODE
 RUN NO. 2080-E. OMA PENETRATOR TEST AT ORES (RIGID BODY SOL'N)
 CYCLE 2480

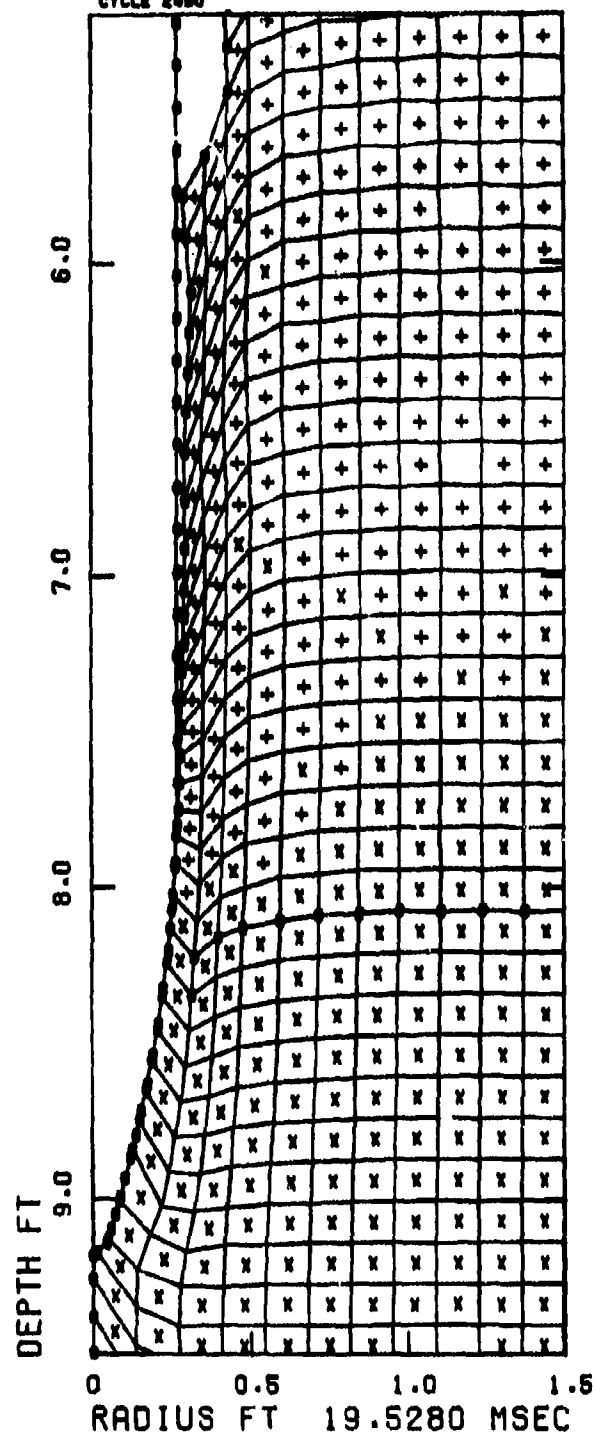


Figure B-10. Grid Configuration with Penetrator at 280 cm Depth

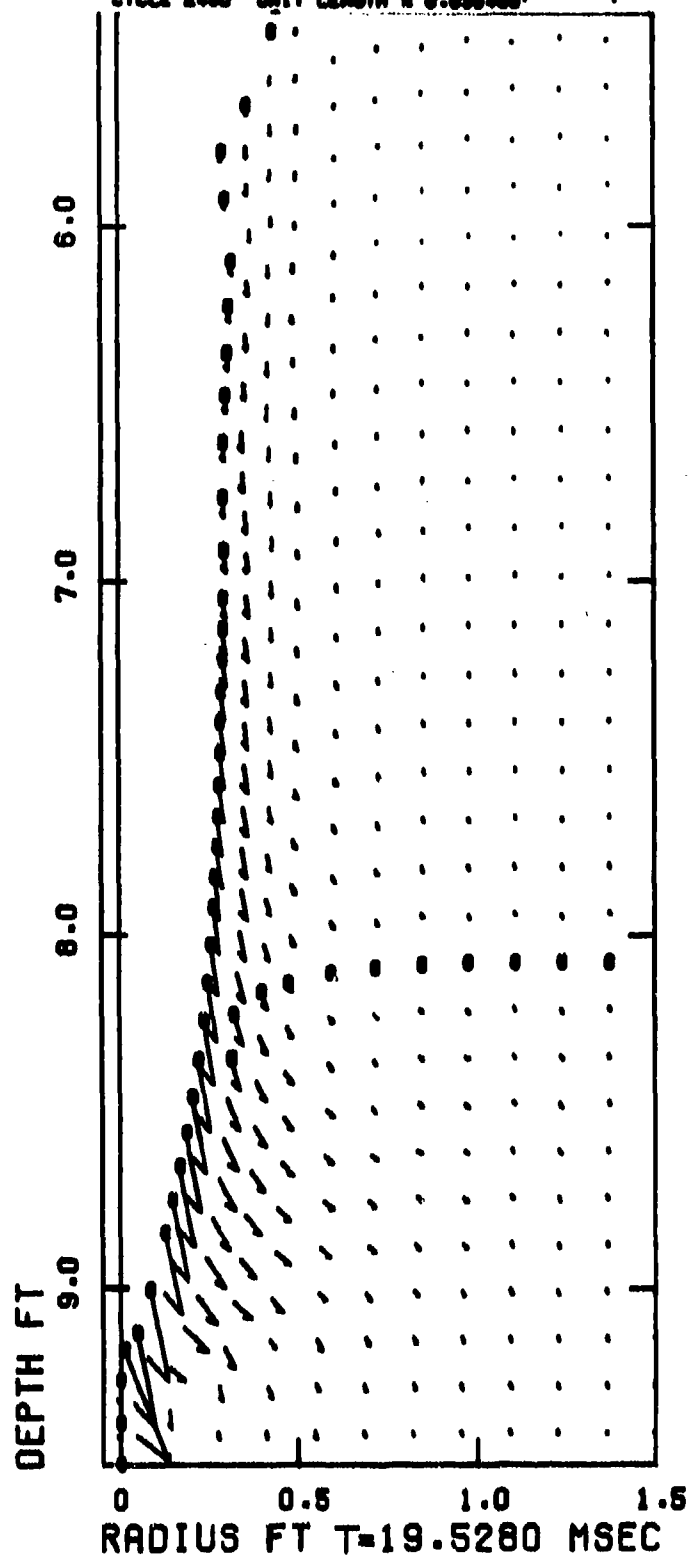


Figure B-11. Particle Velocity Field with Penetrator at 280 cm Depth

CALIFORNIA RESEARCH AND TECHNOLOGY WAVE-L CODE
 RUN NO. 2000-2, 000 PENETRATOR TEST AT 200 CM (RIGID BODY SOL'N)
 CYCLE 2400 UNIT LENGTH = 0.000010

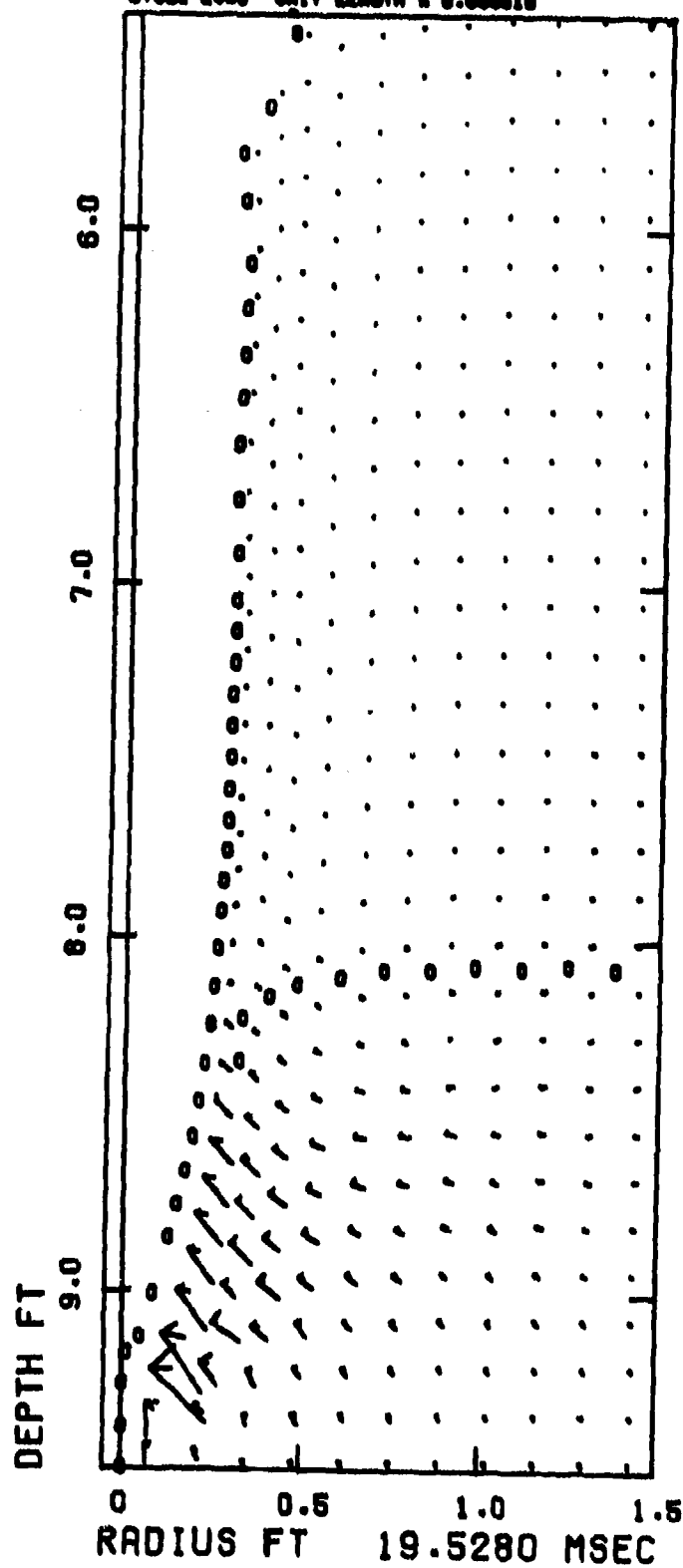


Figure B-12. Principal Stress Field with Penetrator at 280 cm Depth

20 JUL 74 CALIFORNIA RESEARCH AND TECHNOLOGY WAVE-L CODE
 RUN NO. 1000-P. 000 PENETRATOR TEST AT 0000 (0100 0000 00.00)
 CYCLE 0007

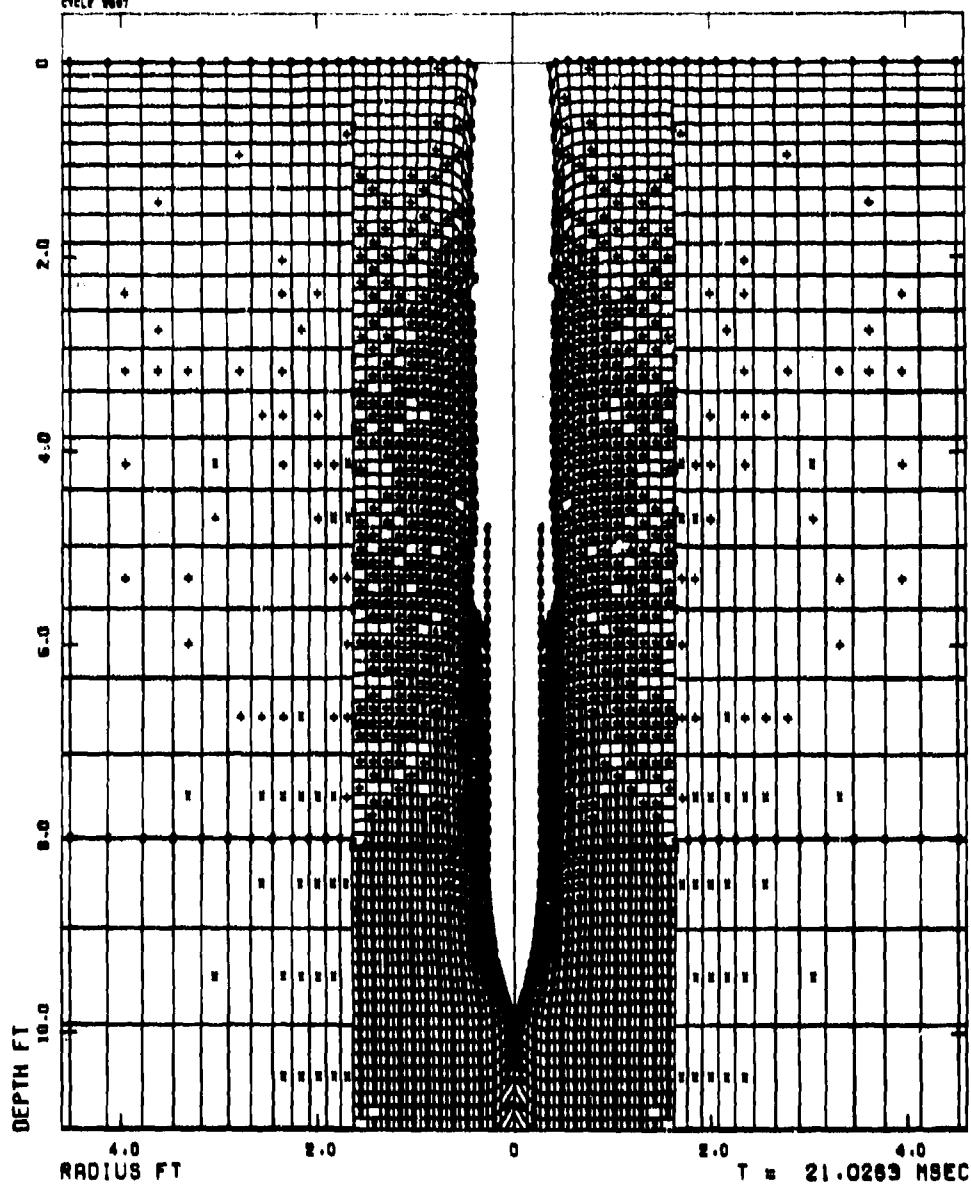


Figure B-13. Grid Configuration with Penetrator at 300 cm Depth

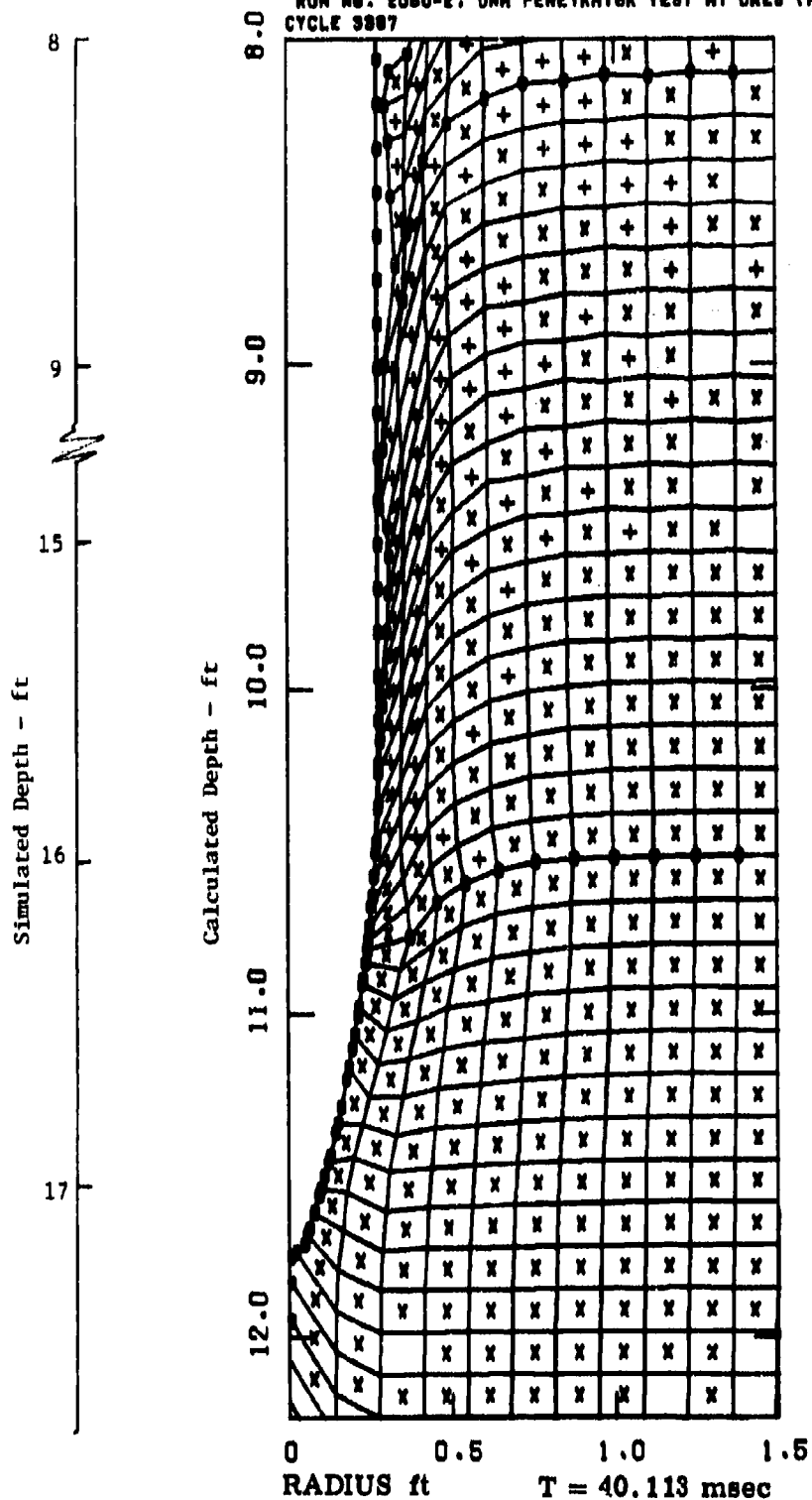


Figure B-14. Grid Configuration with Penetrator at 528 cm Depth

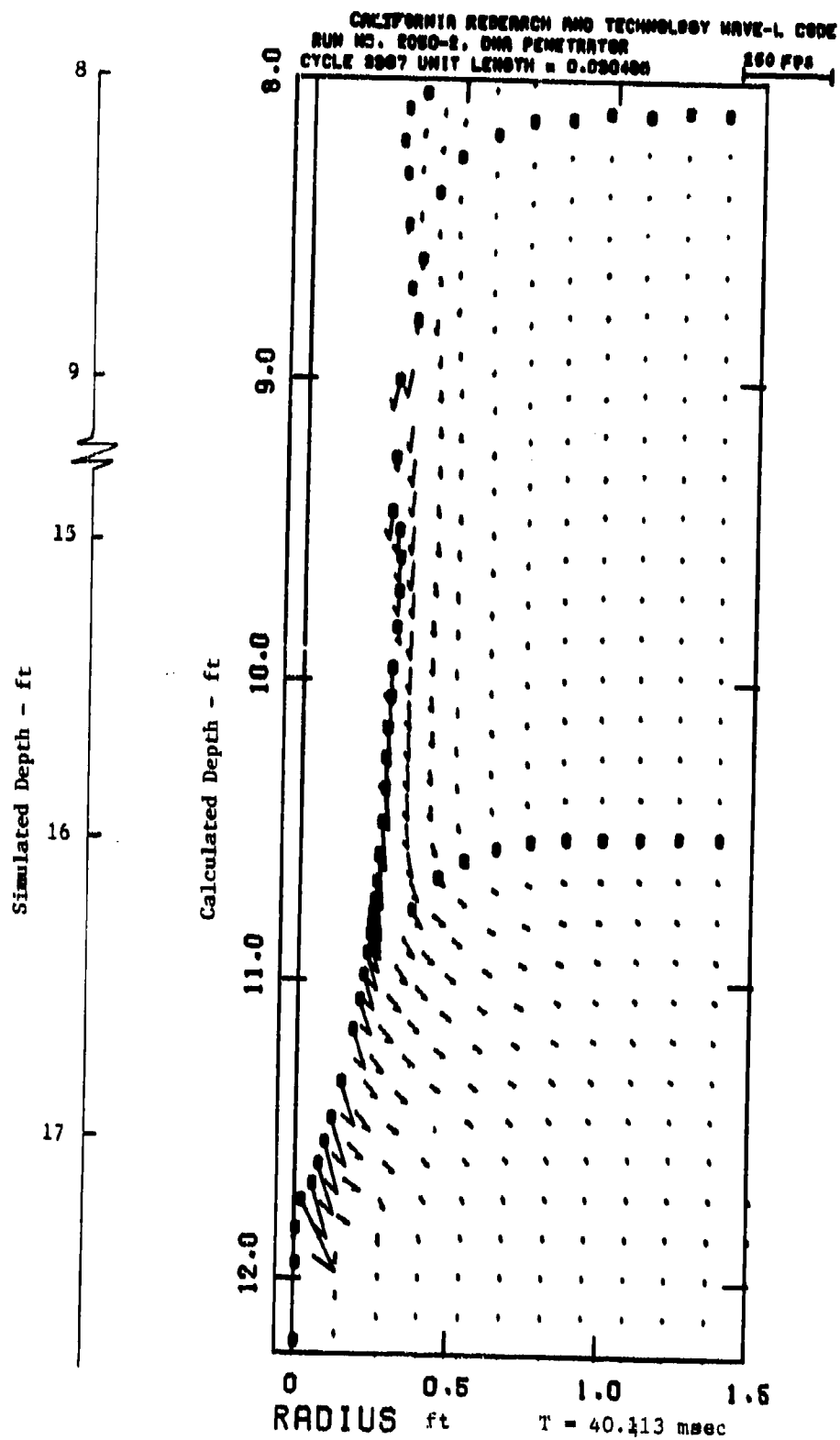


Figure B-15. Particle Velocity Field with Penetrator at 528 cm Depth

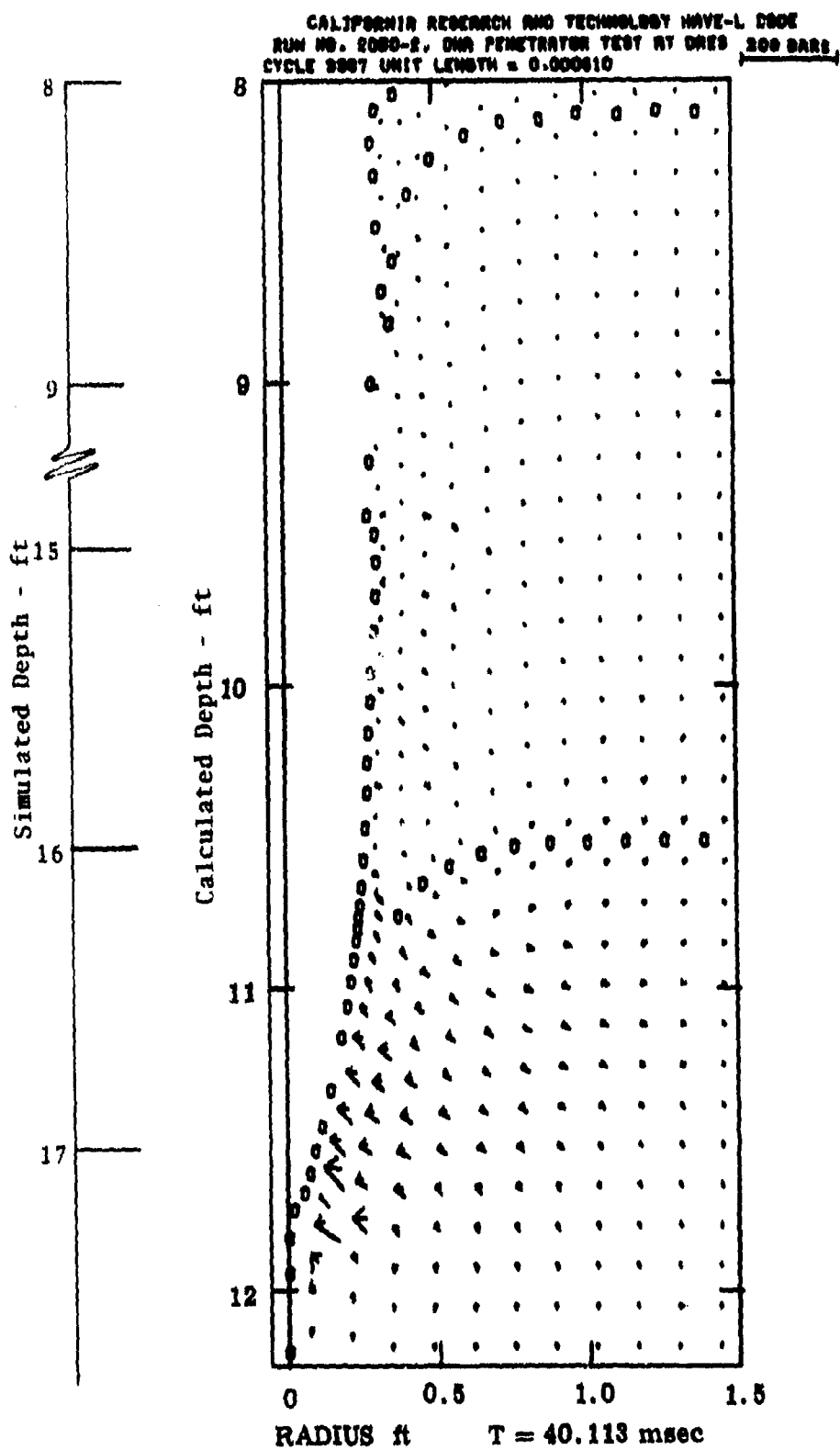


Figure B-16. Principal Stress Field with Penetrator at 528 cm Depth

RUN NO. 2050-2. DVA PENETRATOR TEST AT OREG (RIGID BODY SOL'N)
CYCLE 3525

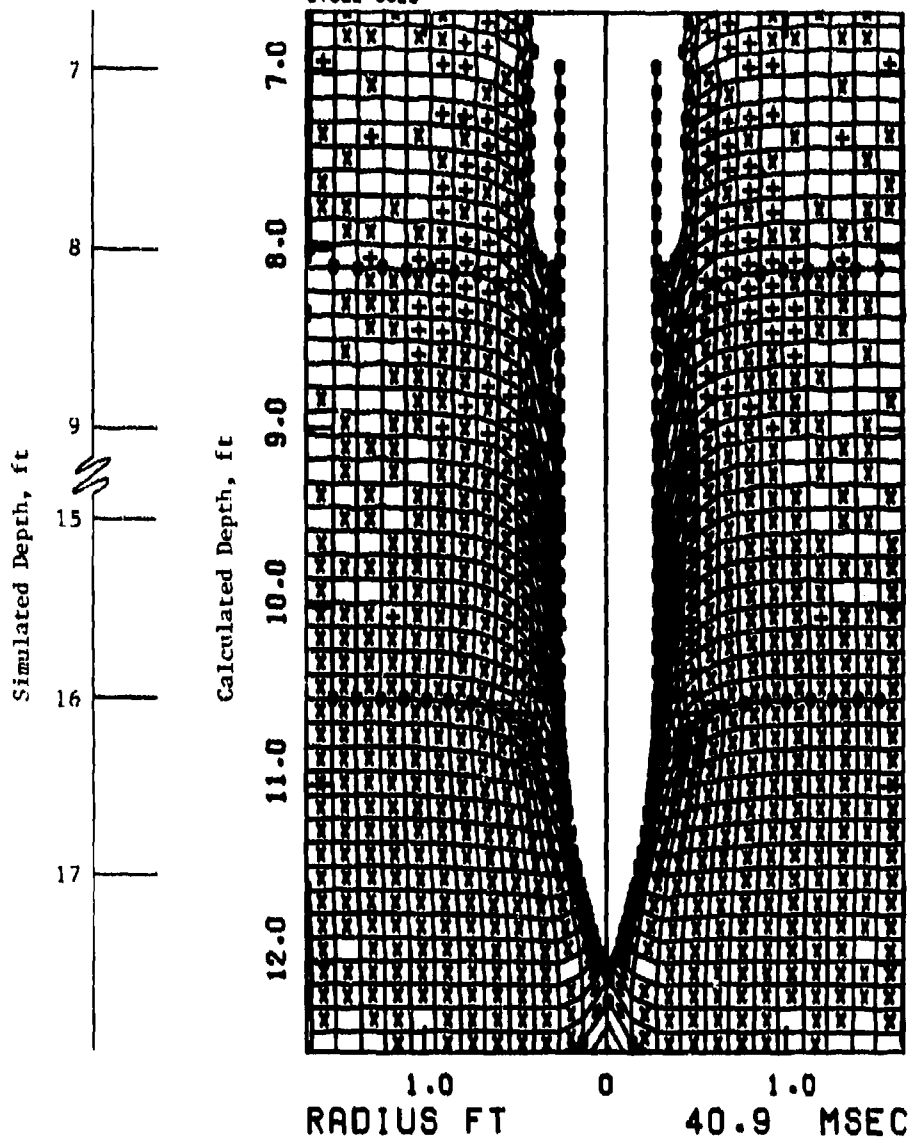


Figure B-17. Grid Configuration at End of Solution, with Penetrator at 536 cm Depth

APPENDIX C

FRICTION STRESSES, TARGET DYNAMICS NEAR PENETRATOR NOSE, AND ENERGY PARTITIONING

Normal and tangential (frictional) stresses applied to the penetrator nose surface are shown in Figures C-1 to C-5 for penetrator depths of 10, 40, and 200 cm (in Layer 1), 280 cm (in Layer 2), and 528 cm (in Layer 3). Generally, these plots show that the normal stress falls sharply with increasing distance from the nose. The frictional stress, on the other hand, is nearly level in Layers 1 and 3 (due to the constraint on friction imposed by the relatively flat yield surface in these layers). The higher yield surface in Layer 2 allows higher frictional stresses.

Velocity components of the target soil points which are in contact with the penetrator nose are shown in Figures C-6 to C-8 at penetration depths of 200 cm (Layer 1), 300 cm (Layer 2), and 536 cm (Layer 3). In these plots, v_n and v_t are the velocity components normal and tangential to the penetrator surface.

Time histories of the kinetic energy of the penetrator and the kinetic and internal energy in the target are shown in Figure C-9.

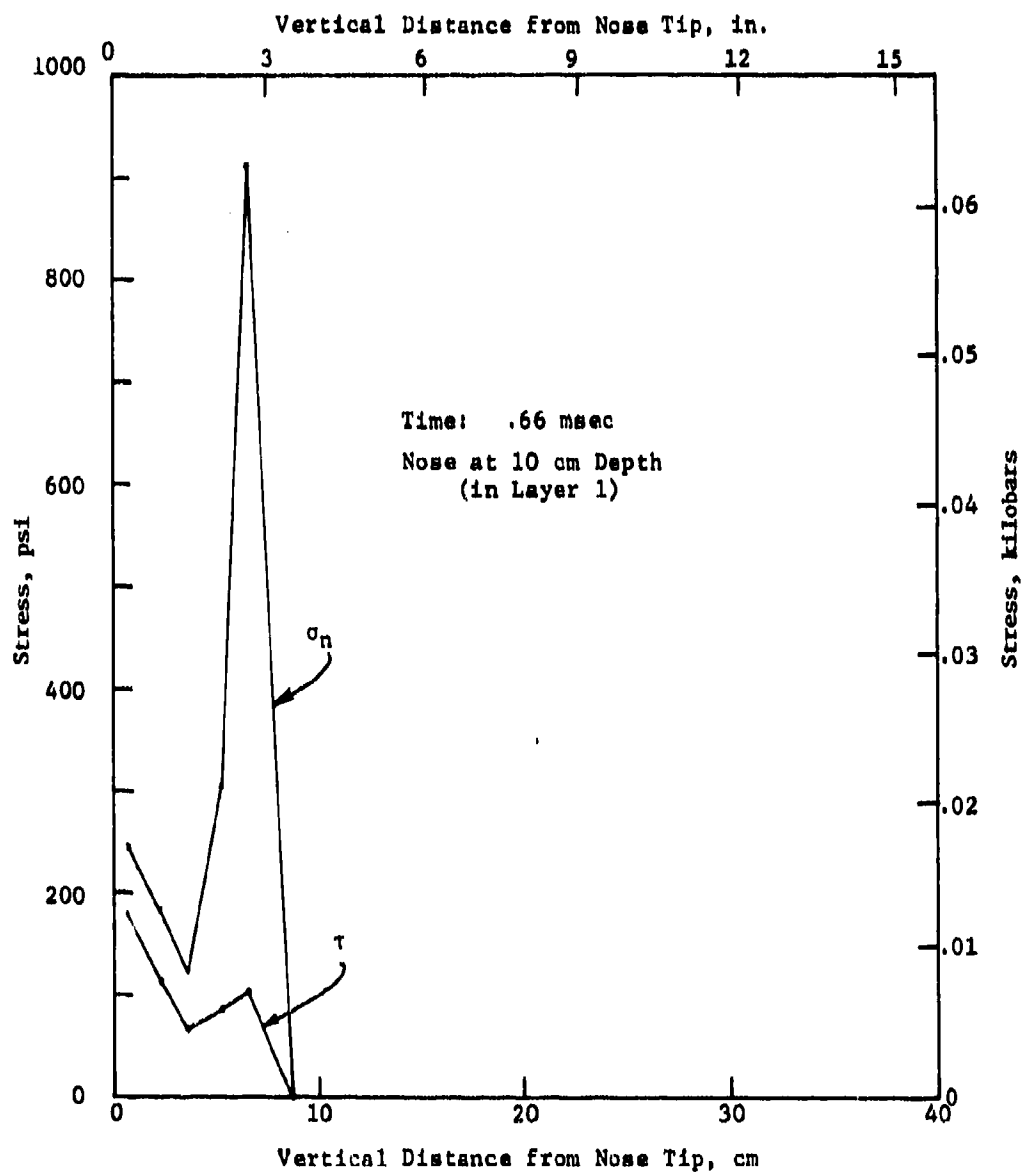


Figure C-1. Normal and Tangential Stress (σ_n, τ)
Distributions along Penetrator Nose

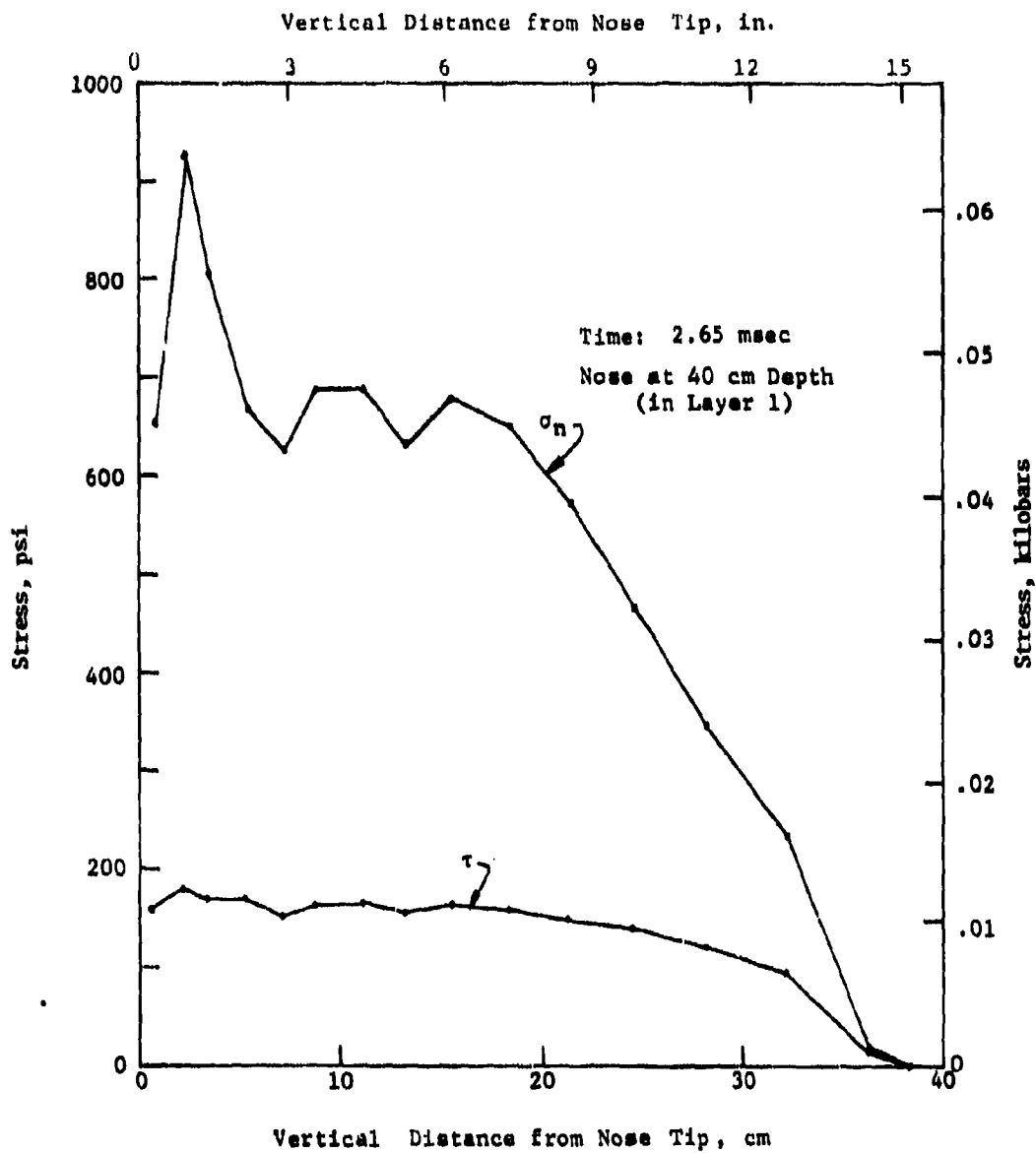


Figure C-2. Normal and Tangential Stress (σ_n, τ) Distributions along Penetrator Nose

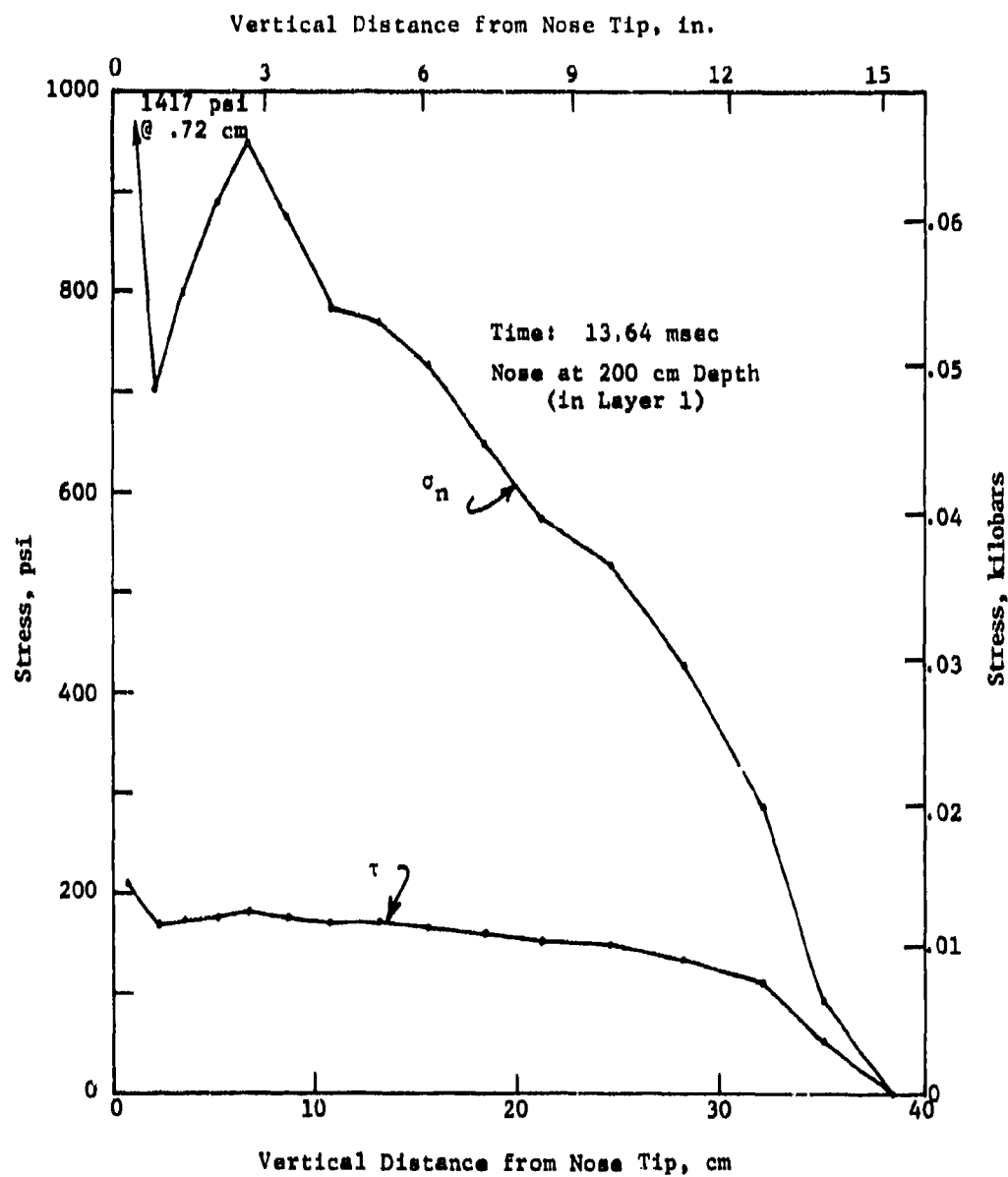


Figure C-3. Normal and Tangential Stress (σ_n, τ)
Distributions Along Penetrator Nose
at 200 cm

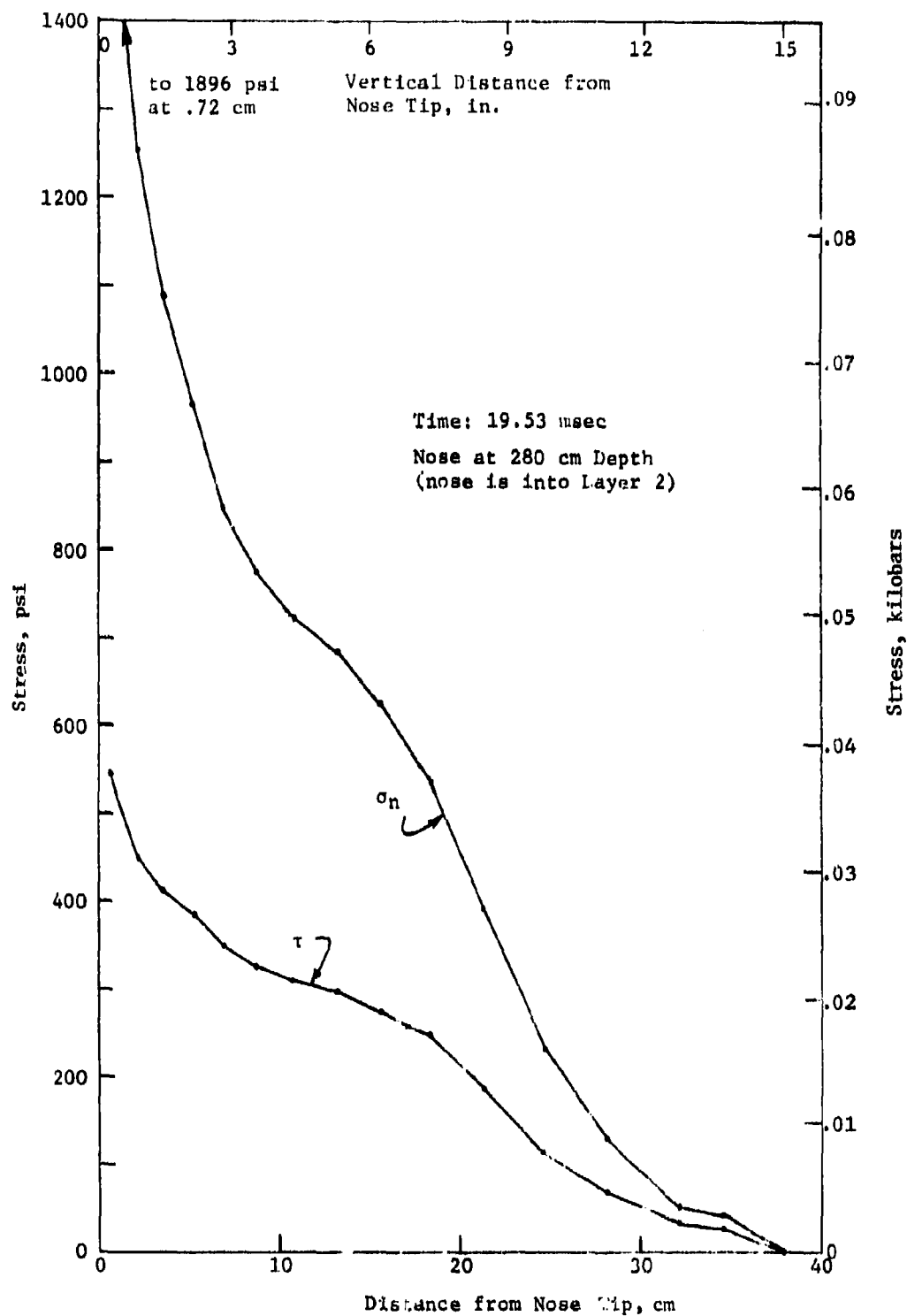


Figure C-4. Normal and Tangential Stress (σ_n, τ) Distributions along Penetrator Nose

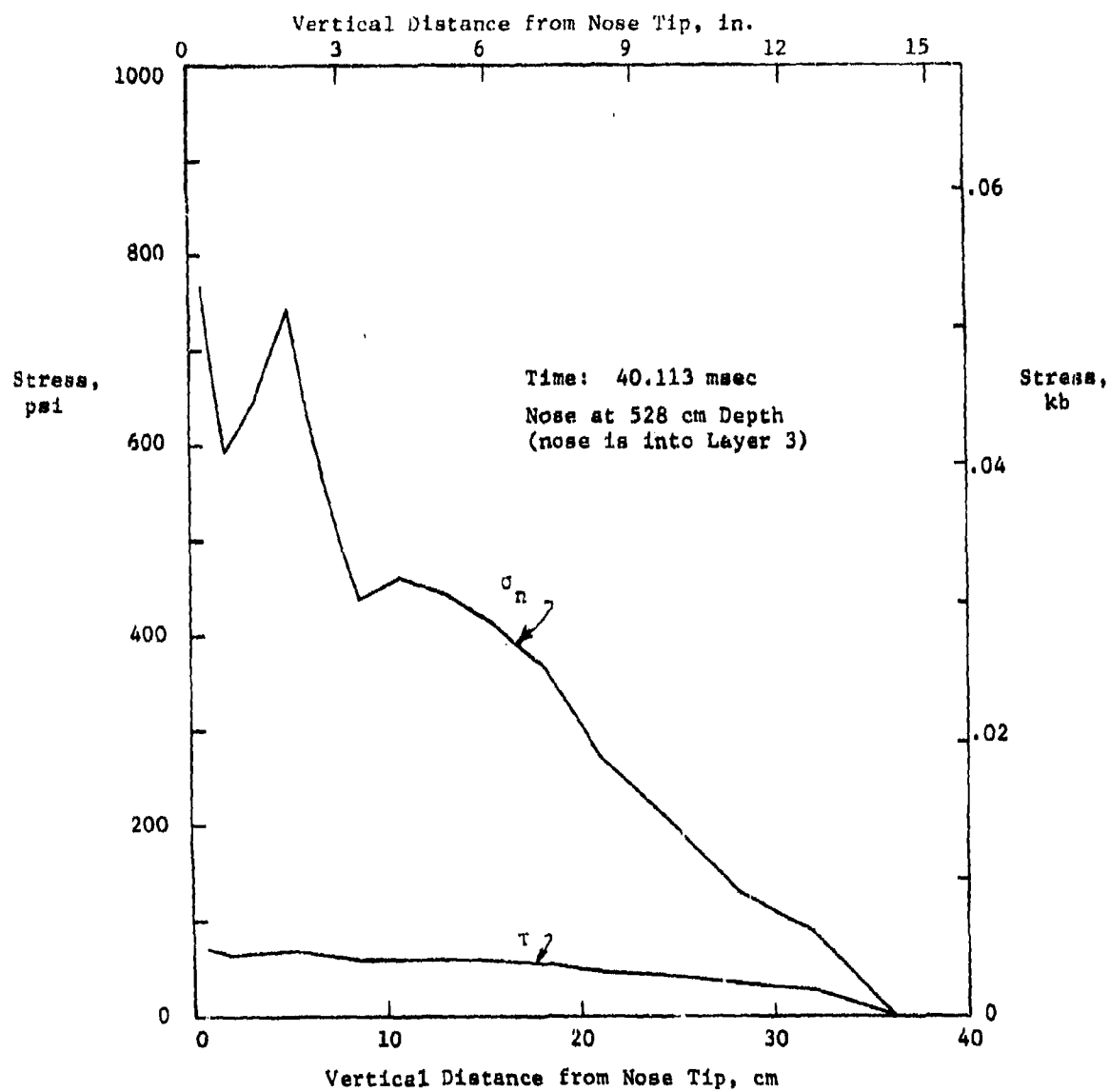


Figure C-5. Normal and Tangential Stress (σ_n, τ) Distributions Along Penetrator Nose

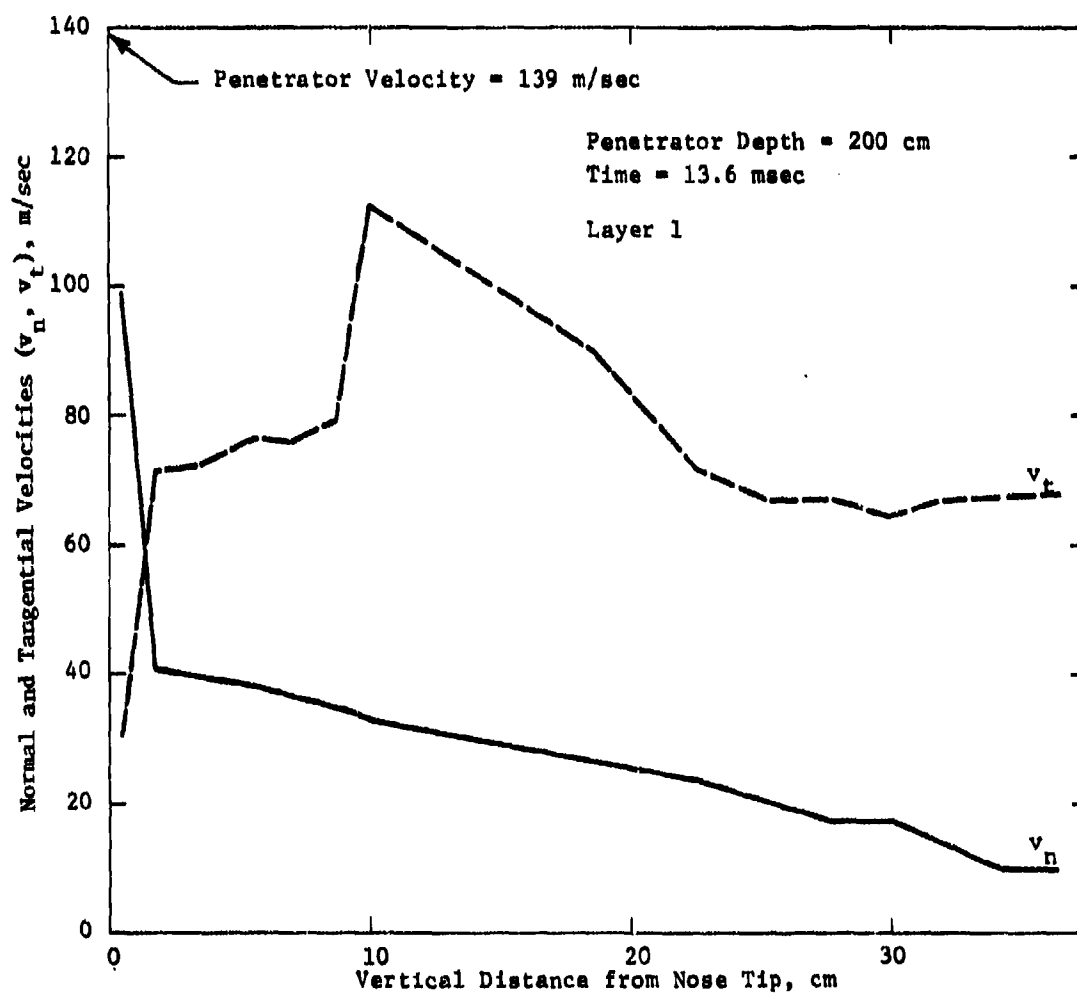


Figure C-6. Velocity Components of Soil in Contact with Projectile Nose

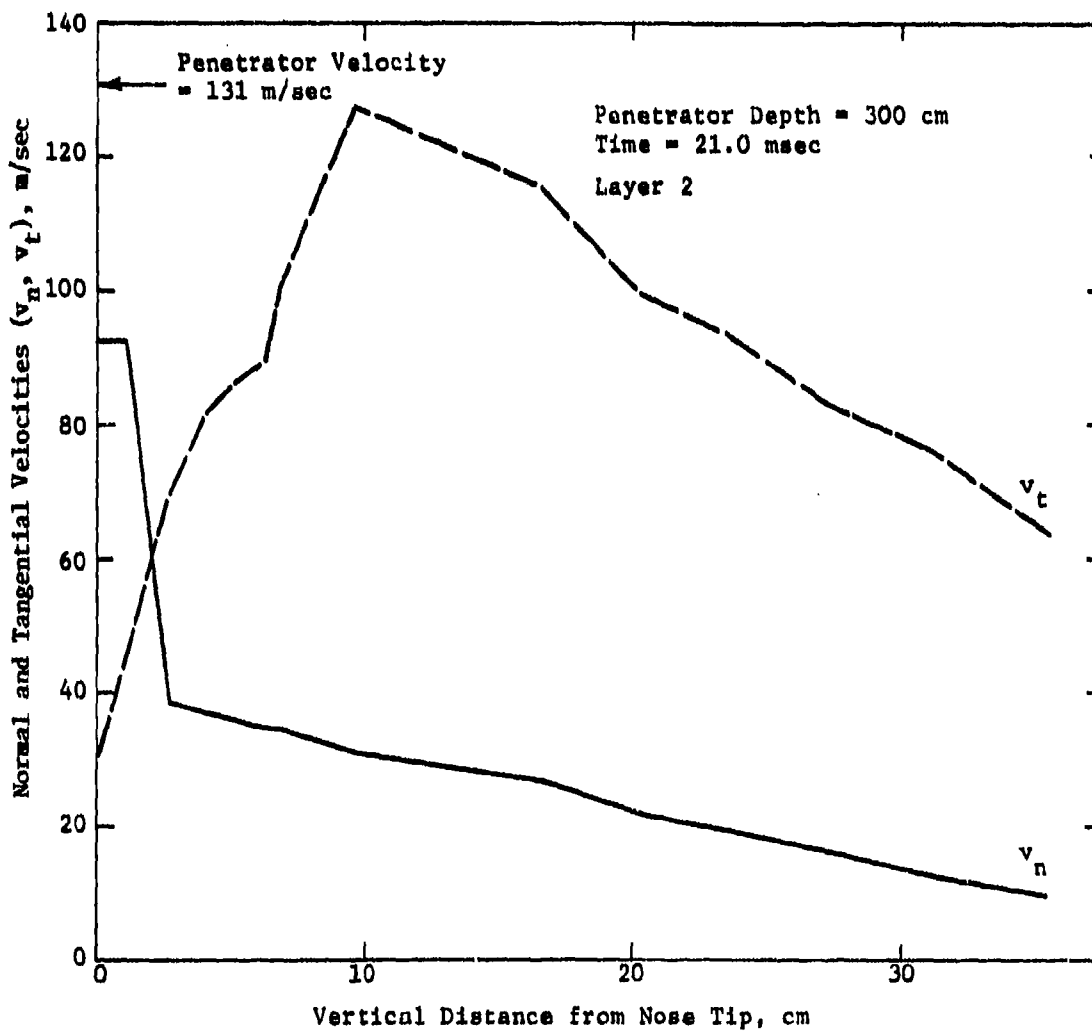


Figure C-7. Velocity Components of Soil in Contact with Projectile Nose

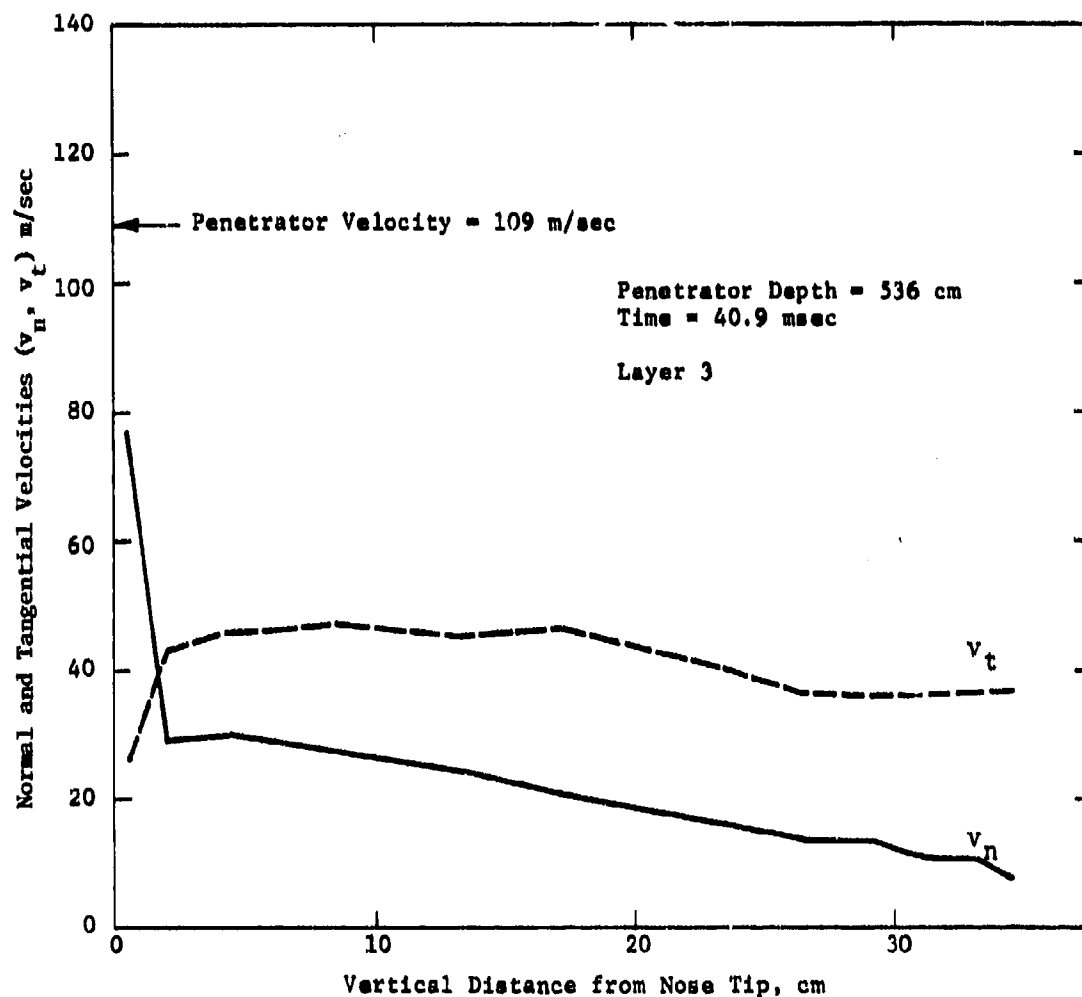


Figure C-8. Velocity Components of Soil in Contact with Projectile Nose

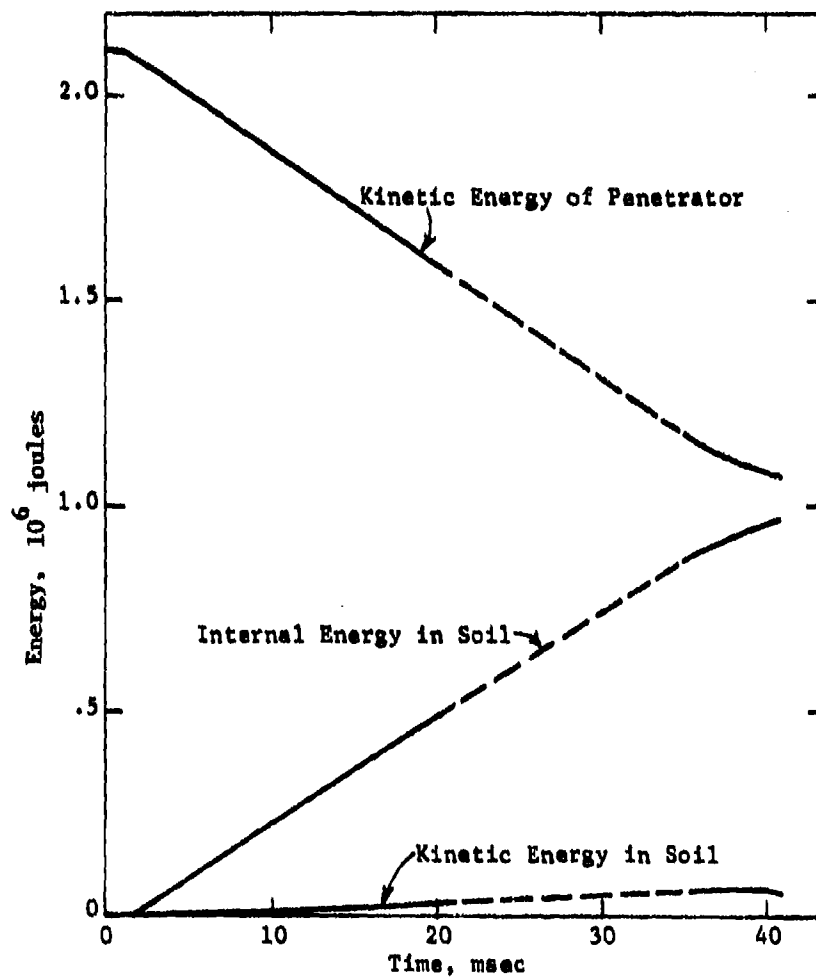


Figure C-9. Energy Partition during Penetrator Calculation

APPENDIX D

TIME HISTORIES OF STRESS, VELOCITY, AND DISPLACEMENT OF TARGET STATIONS

Time histories of stress, velocity, and displacement were obtained at a number of locations in the soil medium. The stations selected for the code output correspond to grid points nearest to the layout of stations suggested by WES. The following parameters are plotted:

- | | |
|-----------------------------|-----------------|
| a. Radial stress | σ_r |
| Vertical stress | σ_z |
| Hoop stress | σ_θ |
| Shear stress | σ_{rz} |
| b. Radial particle velocity | \dot{u} |
| Vertical particle velocity | \dot{w} |
| c. Radial displacement | u |
| Vertical displacement | w |

Positive stresses are compressive. Positive u , \dot{u} is radially outward. Positive w , \dot{w} is vertically down.

The locations of the time-history stations in Layer 1 are shown in the following sketch. No meaningful time histories were recorded in Layer 2, due to the limited penetration of that layer by actual code integration. Partial stress and velocity time histories are included for one station (#12) in Layer 3, located at a radius of ~.5 ft and a depth of ~17.5 ft.

As an aid in interpreting the graphs, the time of arrival of the projectile tip at the same depth as the station depth is indicated on the graphs by a vertical dashed line labelled t_a .

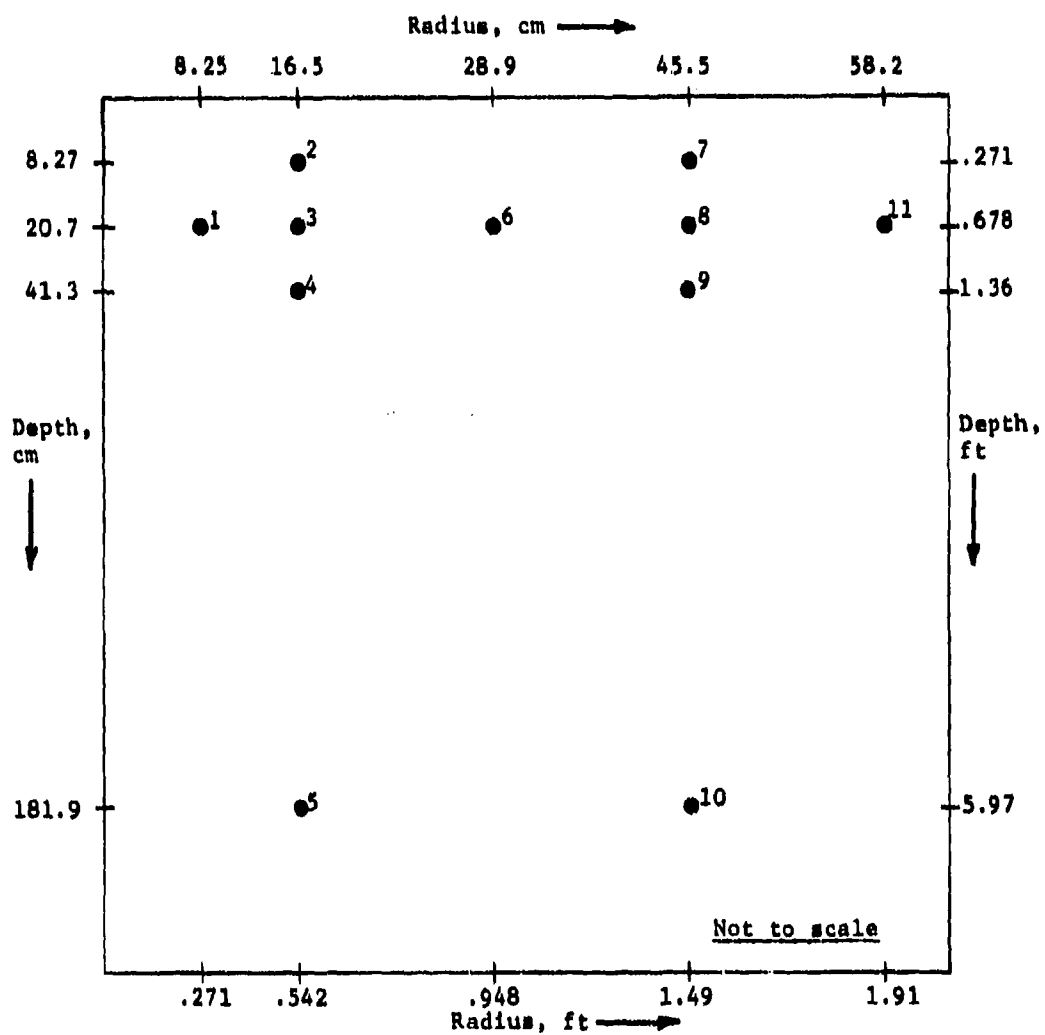


Figure D-1. Locations of Time-History Stations in Layer 1

19 SEP 74

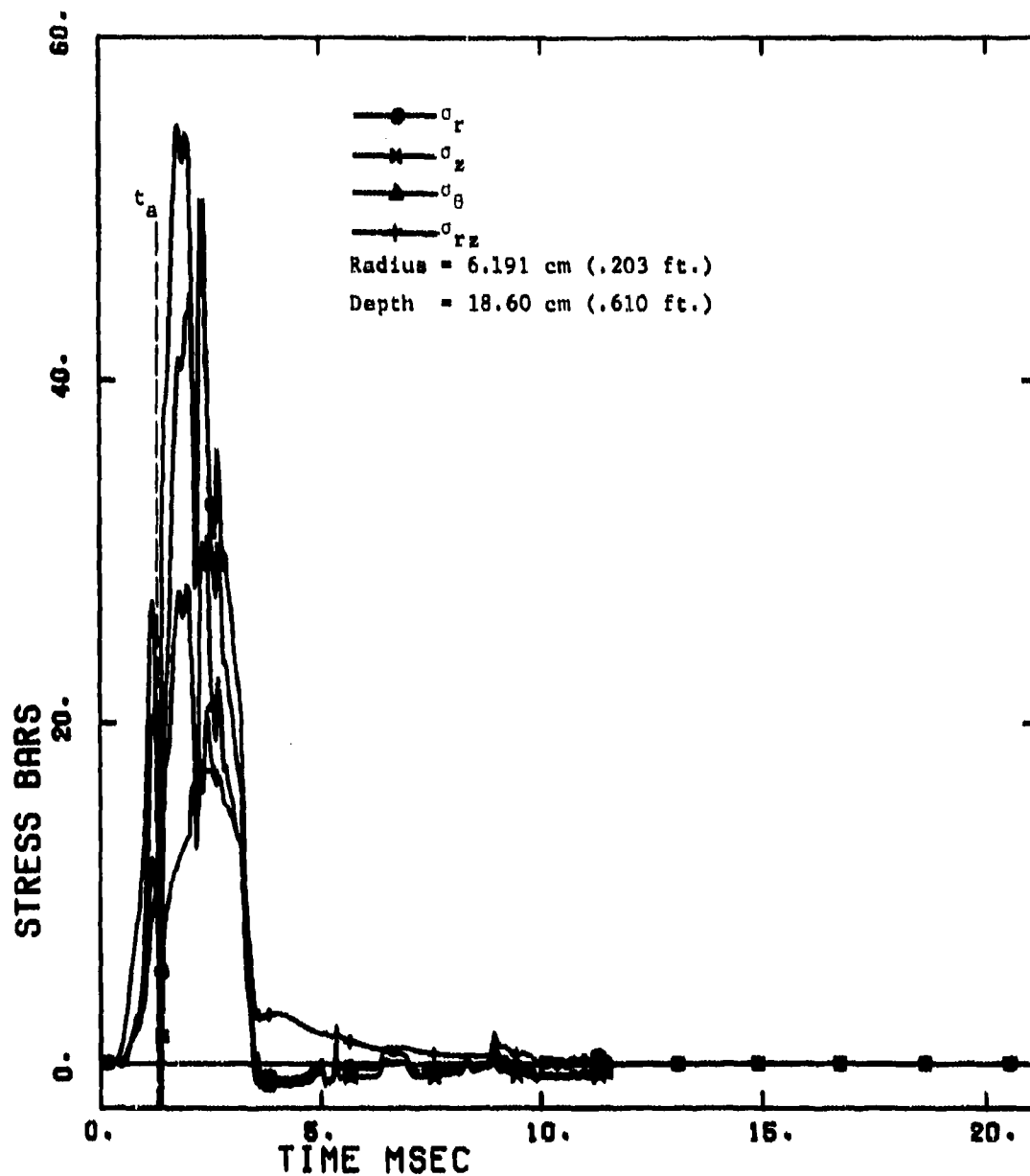


Figure D-2. Stress Components at Station 1

18 SEP 74

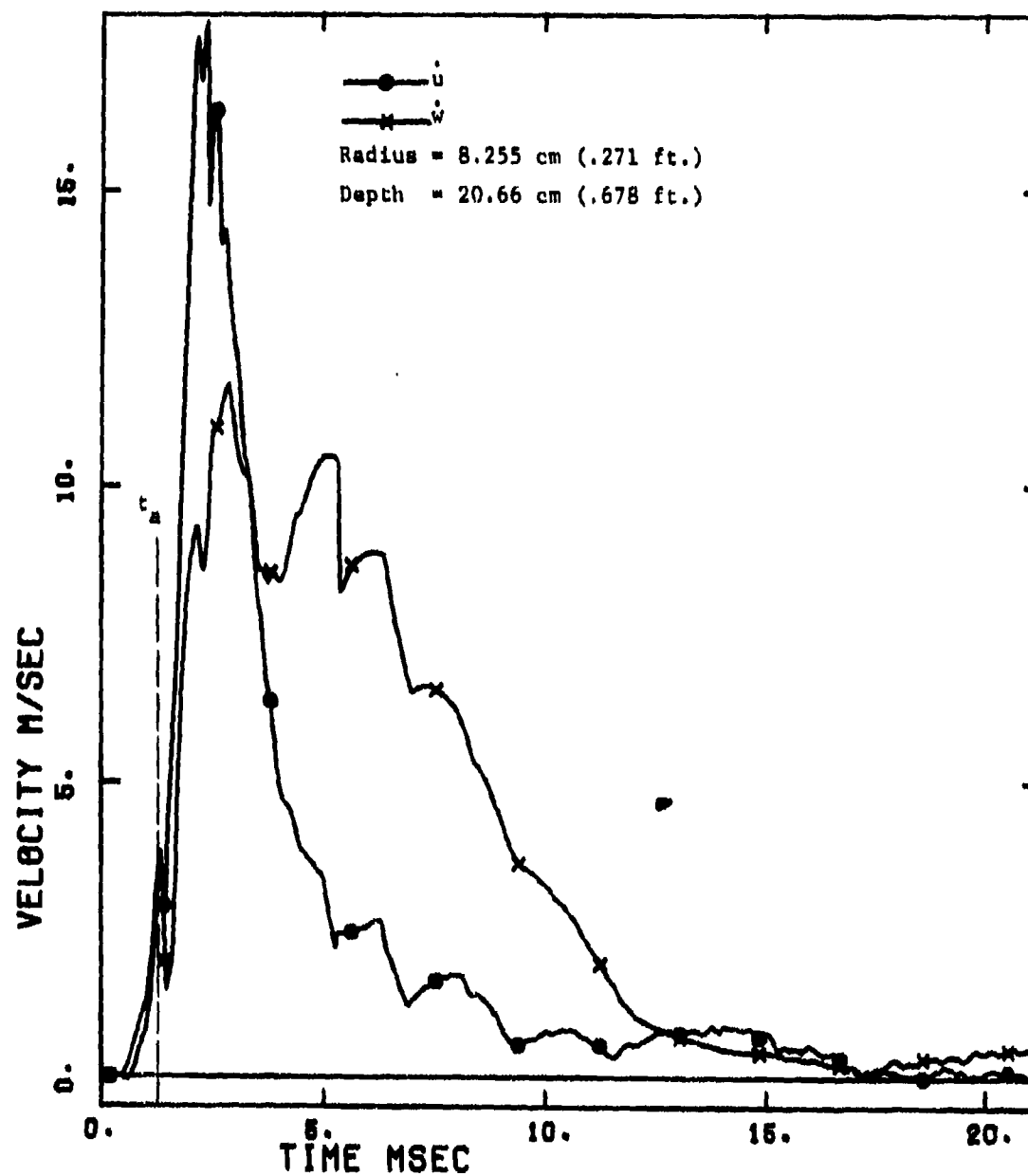


Figure D-3. Velocity Components at Station 1

13 SEP 74

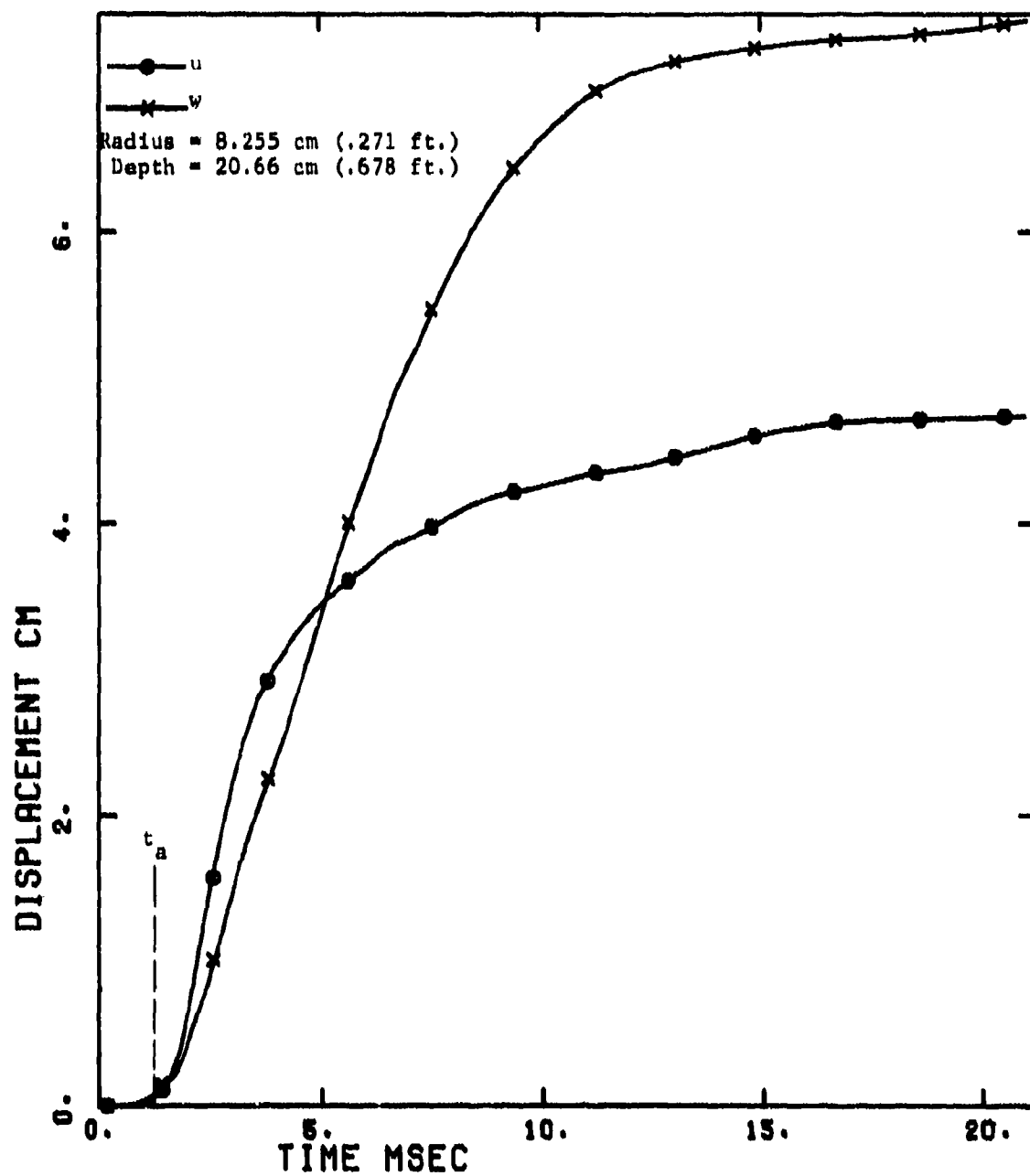


Figure D-4. Displacement Components at Station 1

19 SEP 74

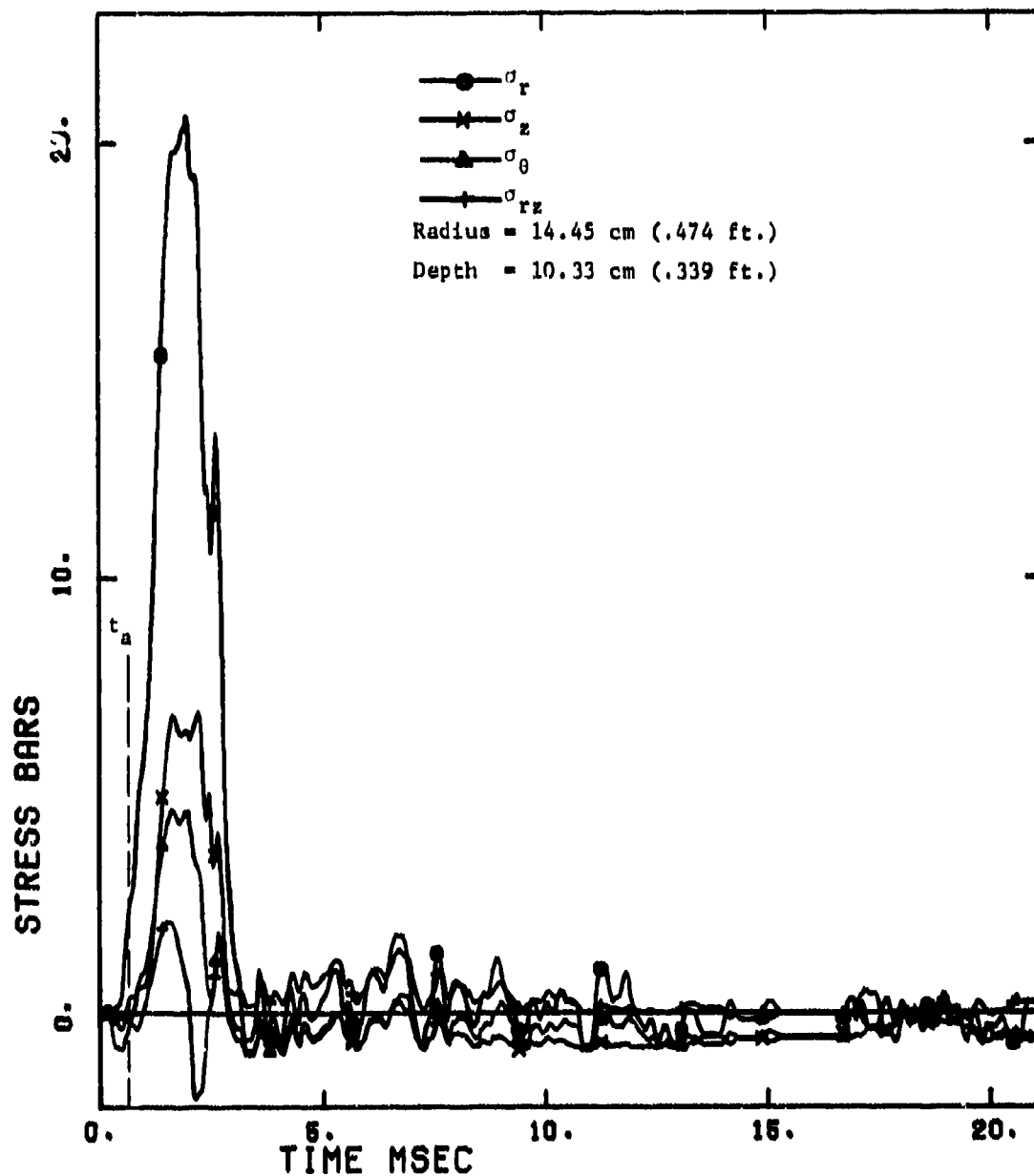


Figure D-5. Stress Components at Station 2

19 SEP 74

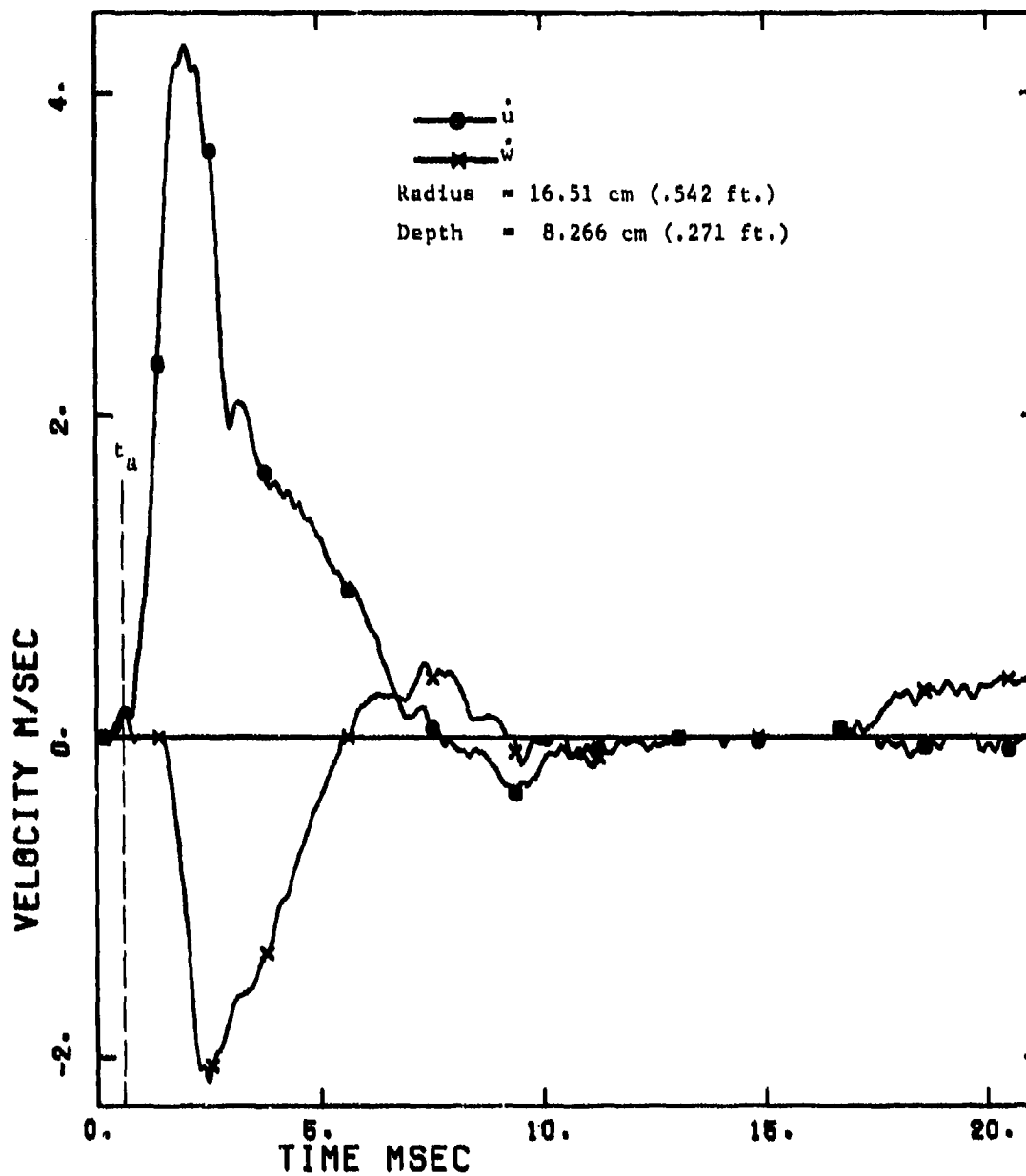


Figure D-6. Velocity Components at Station 2

19 SEP 74

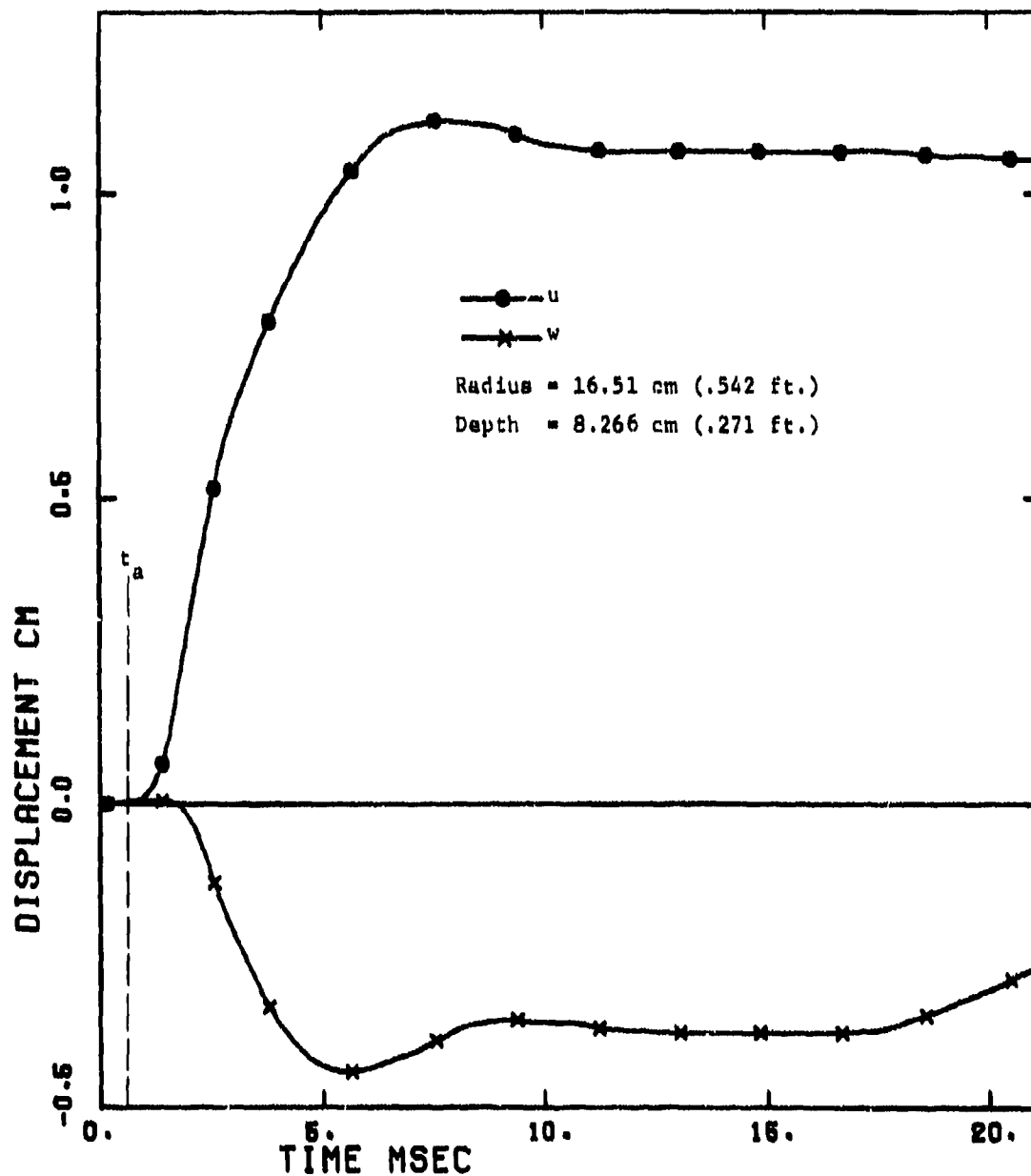


Figure D-7. Displacement Components at Station 2

18 SEP 74

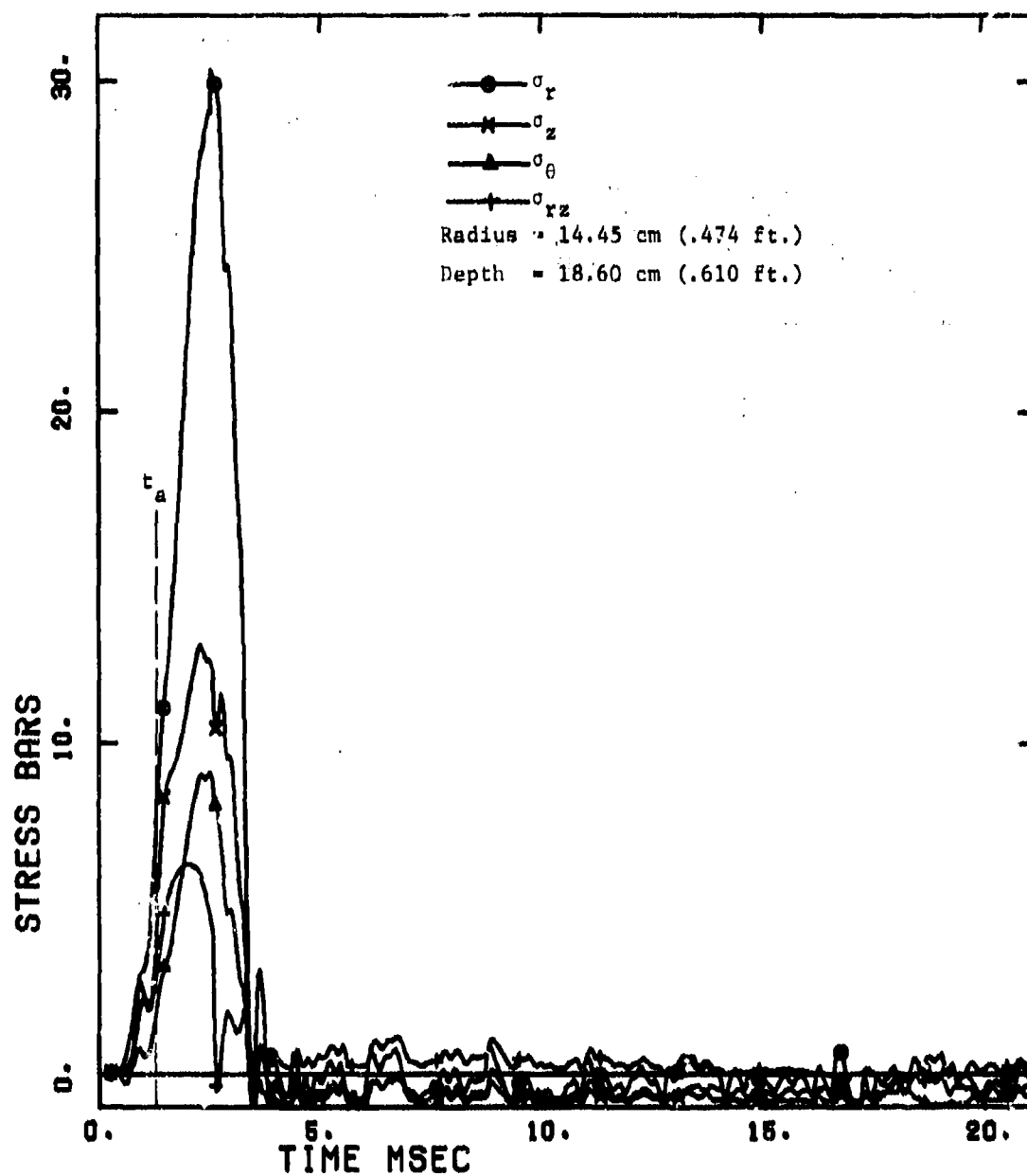


Figure D-8. Stress Components at Station 3

13 SEP 74

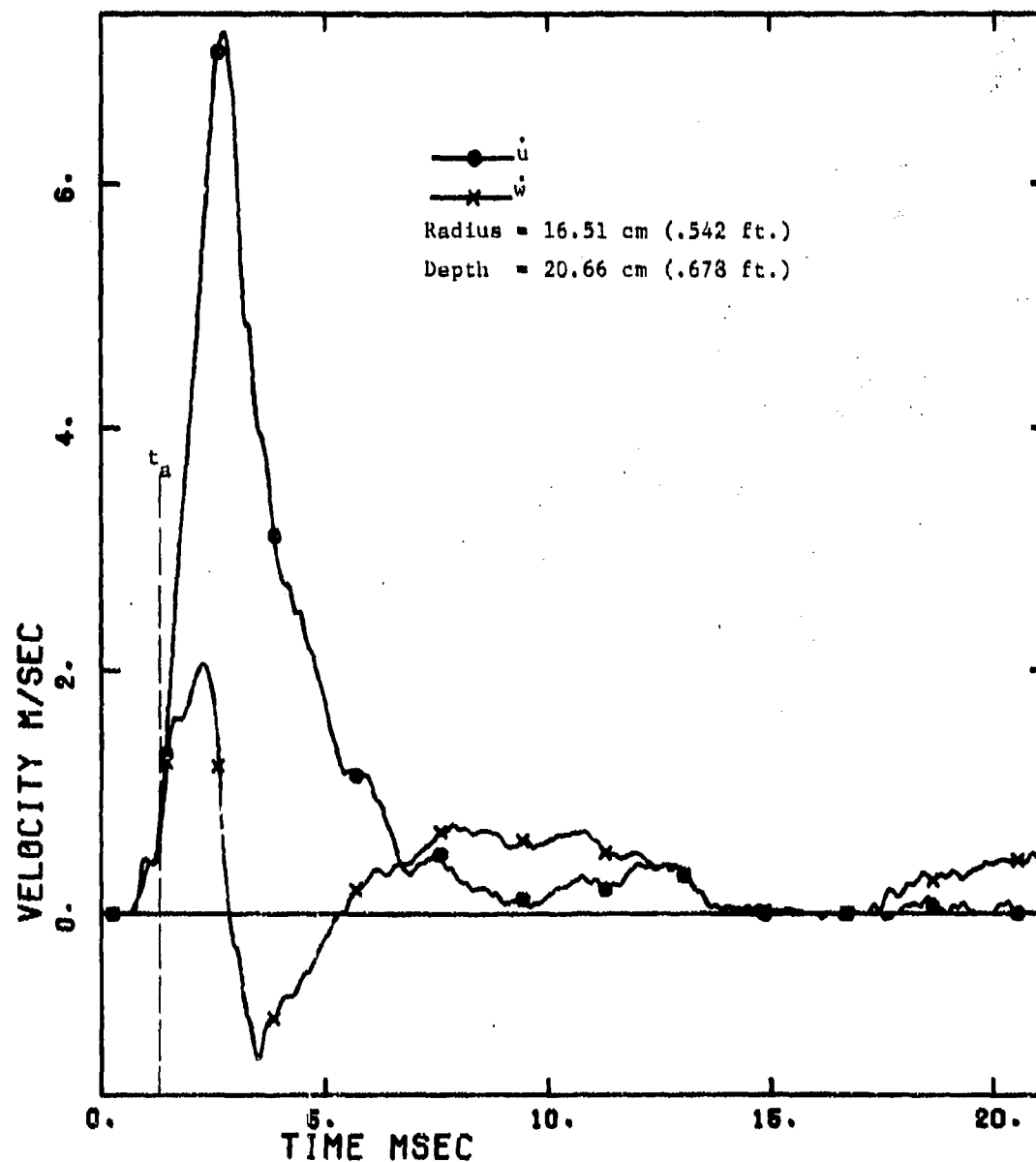


Figure D-9 Velocity Components at Station 3

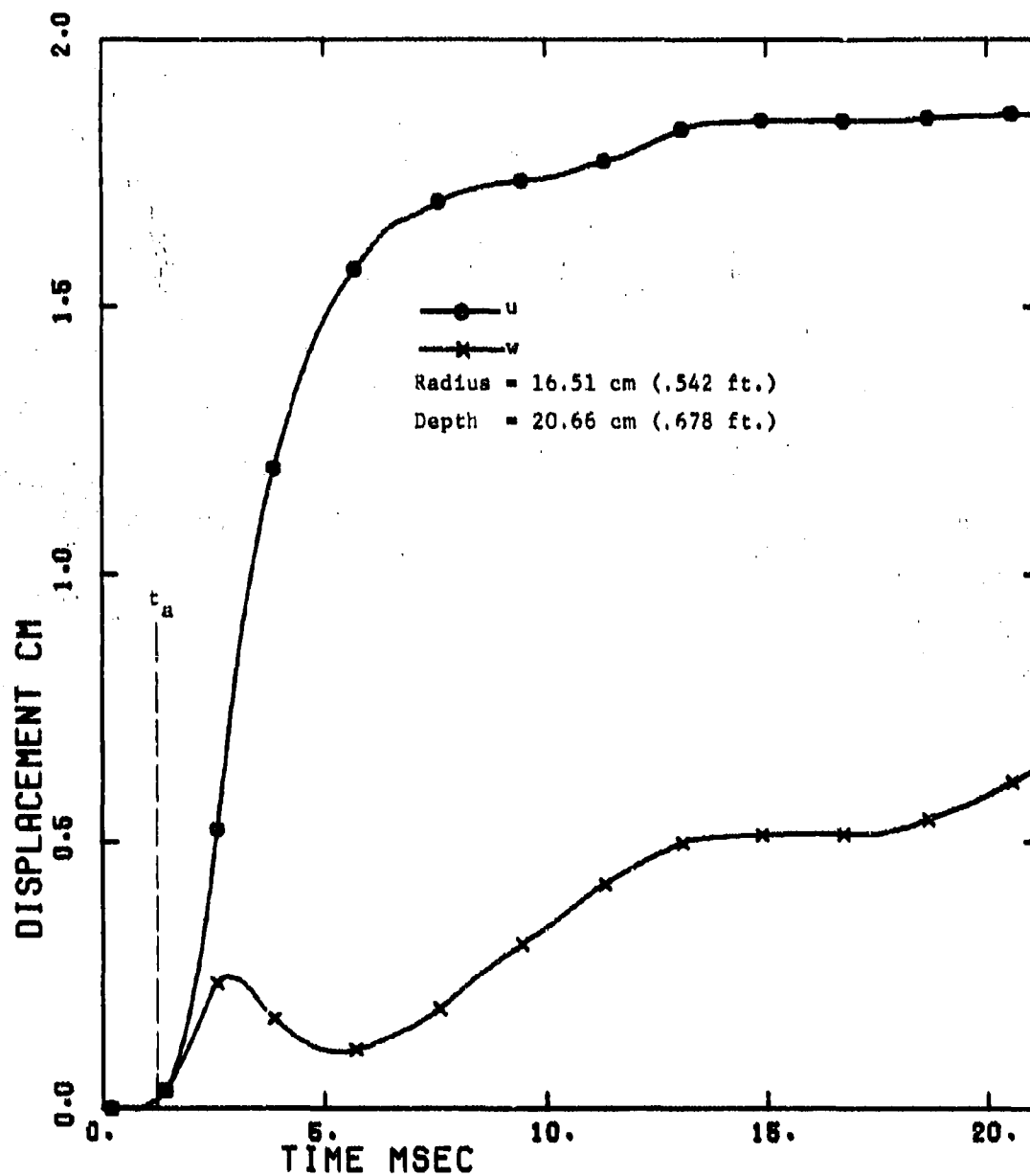


Figure D-10. Displacement Components at Station 3

16 SEP 74

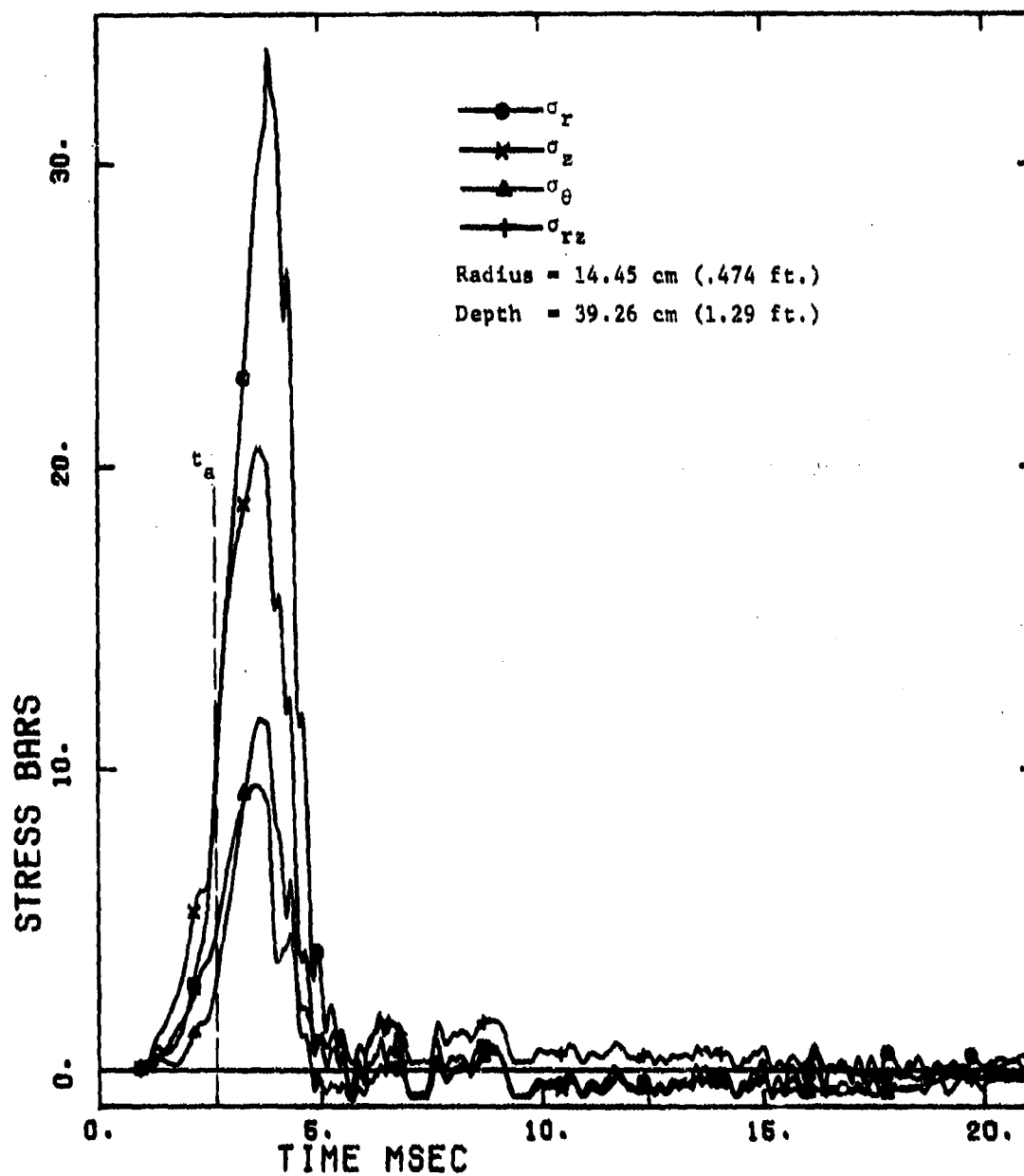


Figure D-11. Stress Components at Station 4

18 SEP 74

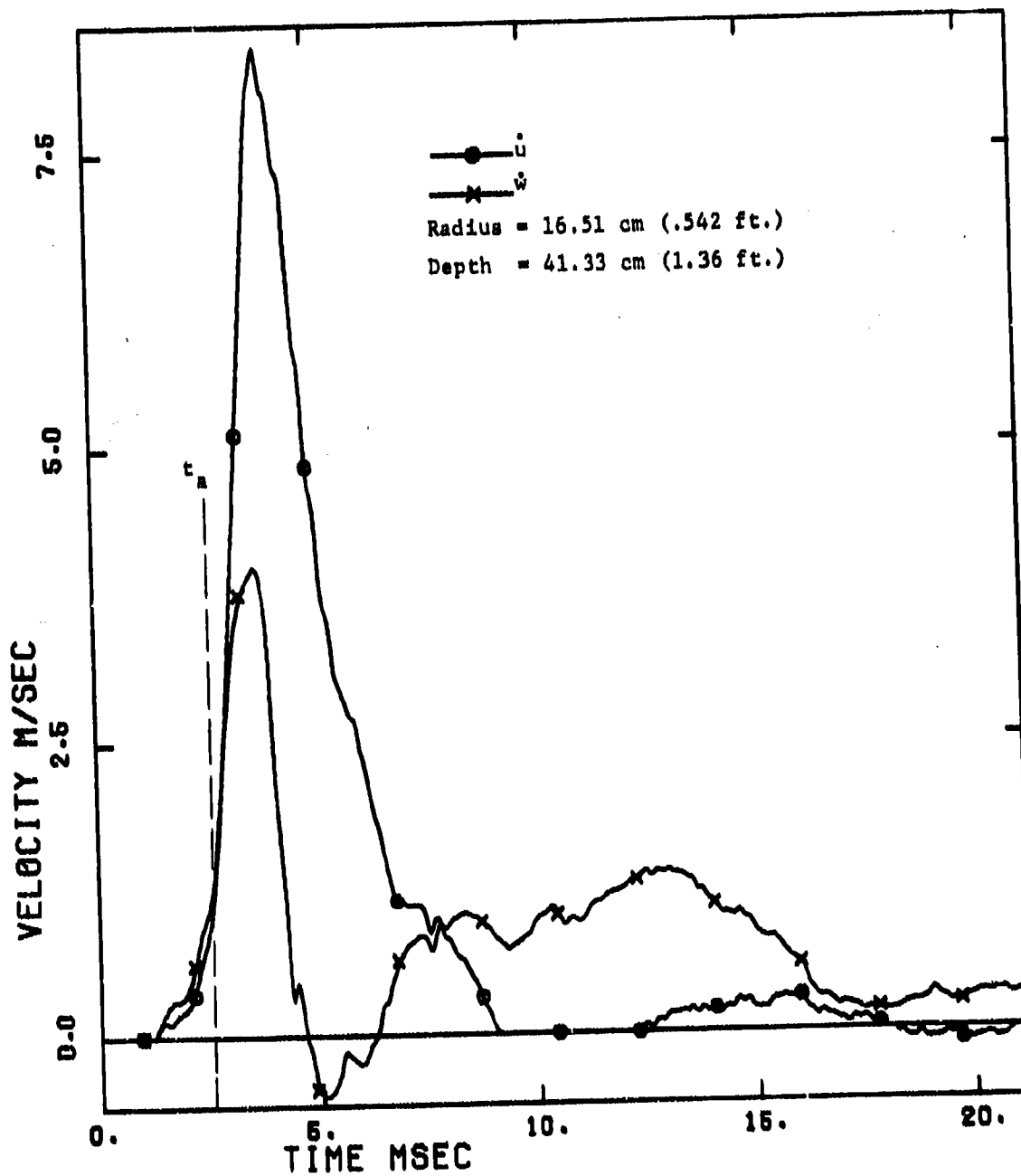


Figure D-12. Velocity Components at Station 4

18 SEP 74

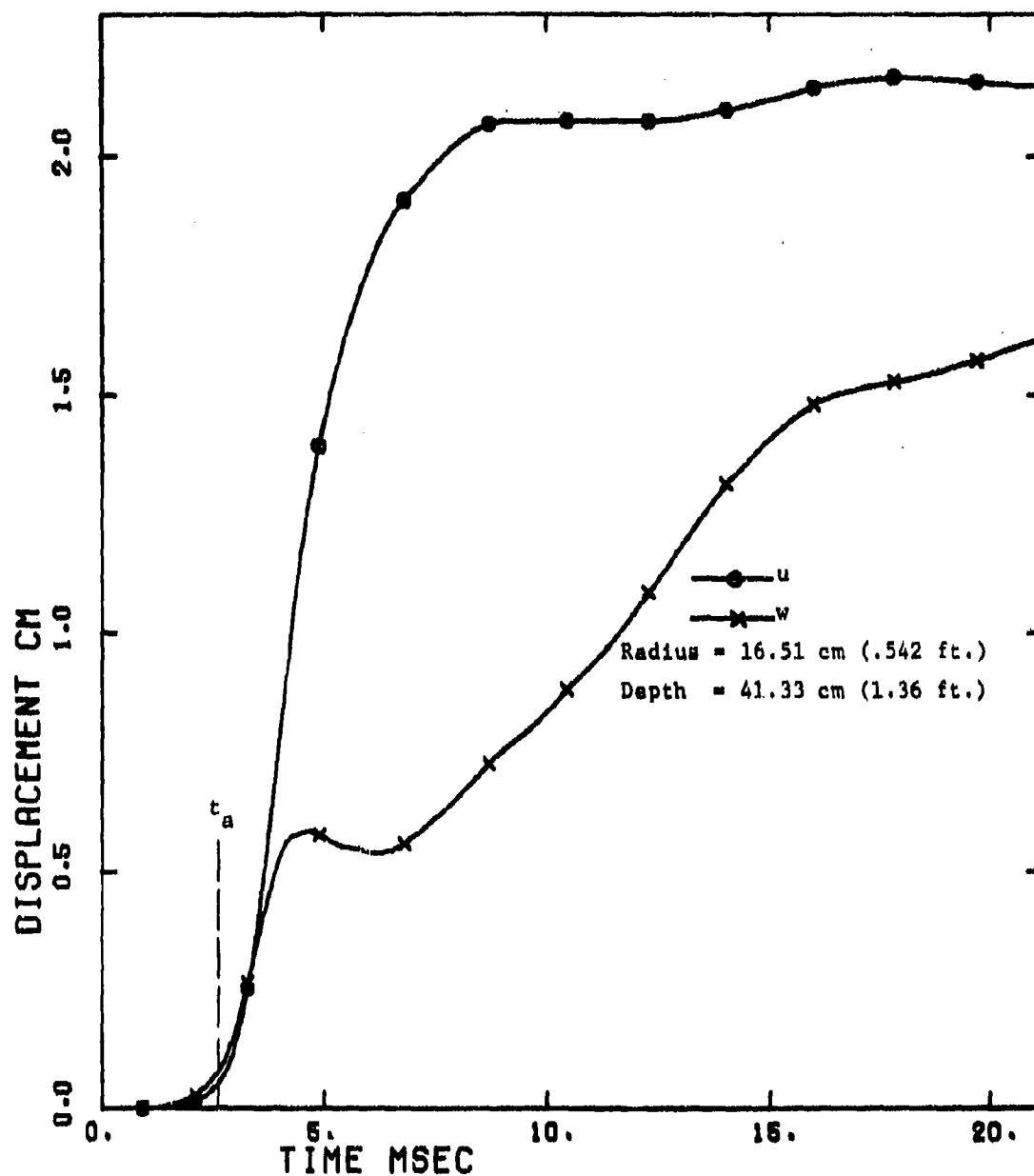


Figure D-13. Displacement Components at Station 4

18 SEP 74

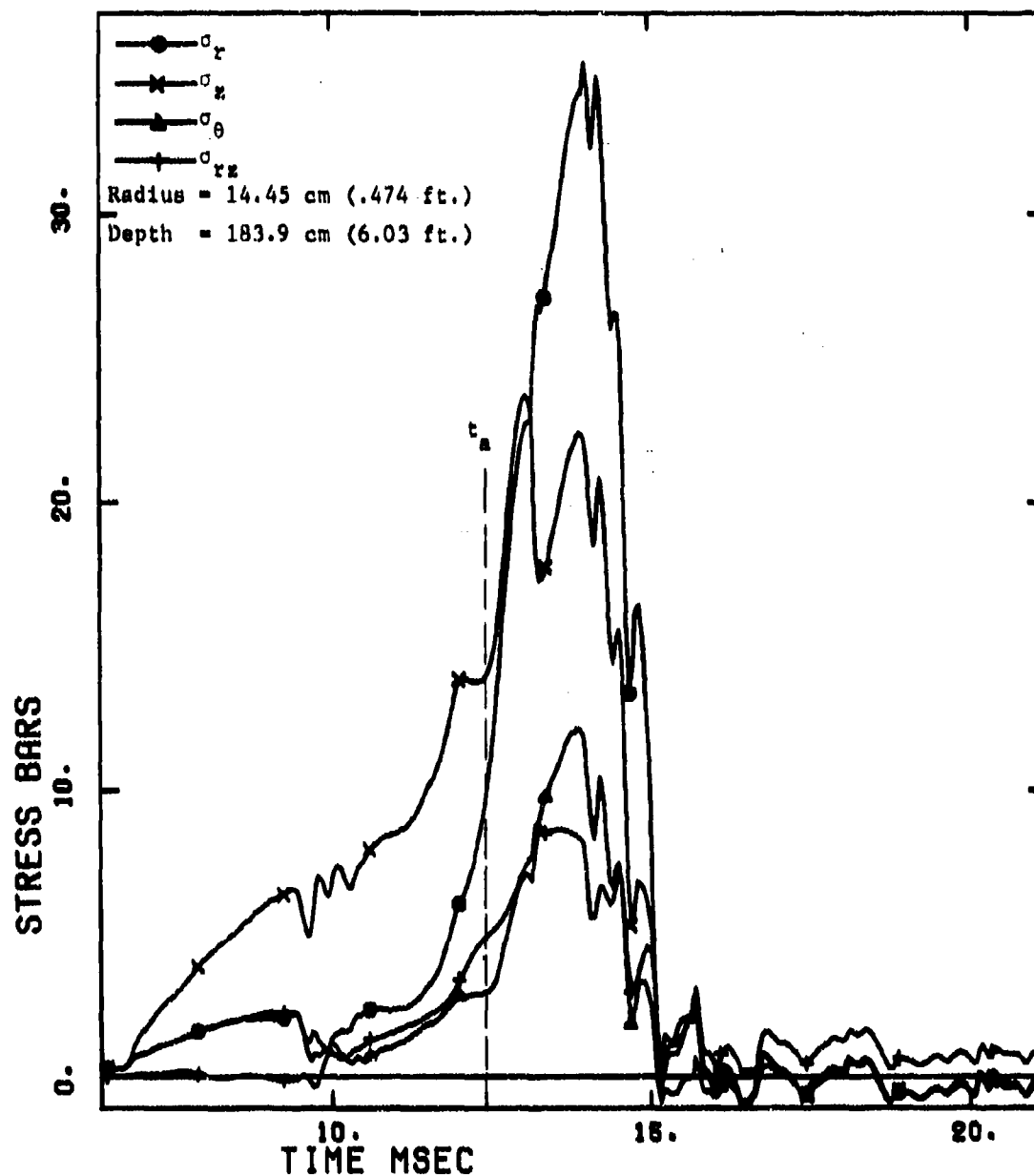


Figure D-14. Stress Components at Station 5

18 SEP 74

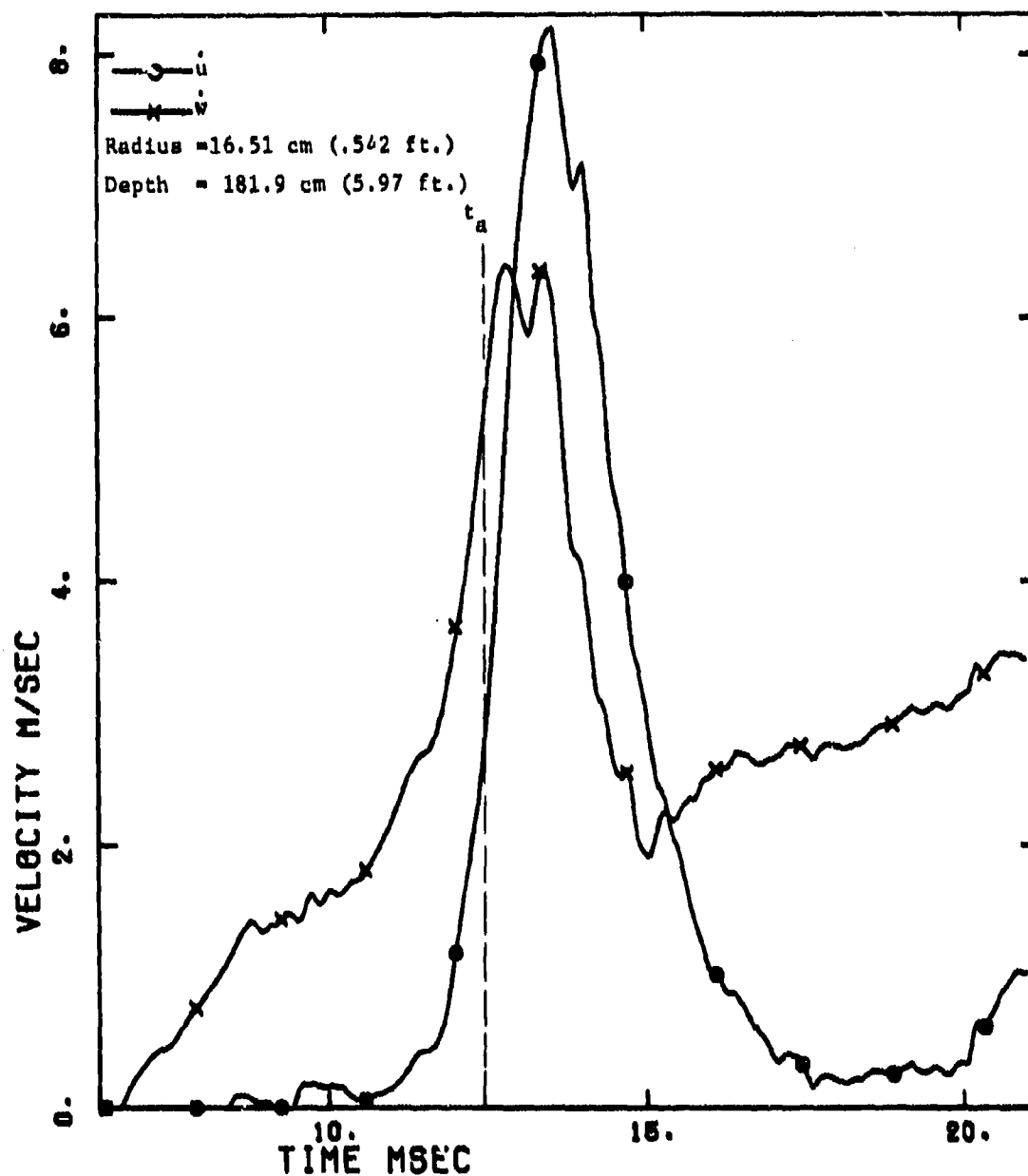


Figure D-15. Velocity Components at Station 5

18 SEP 74

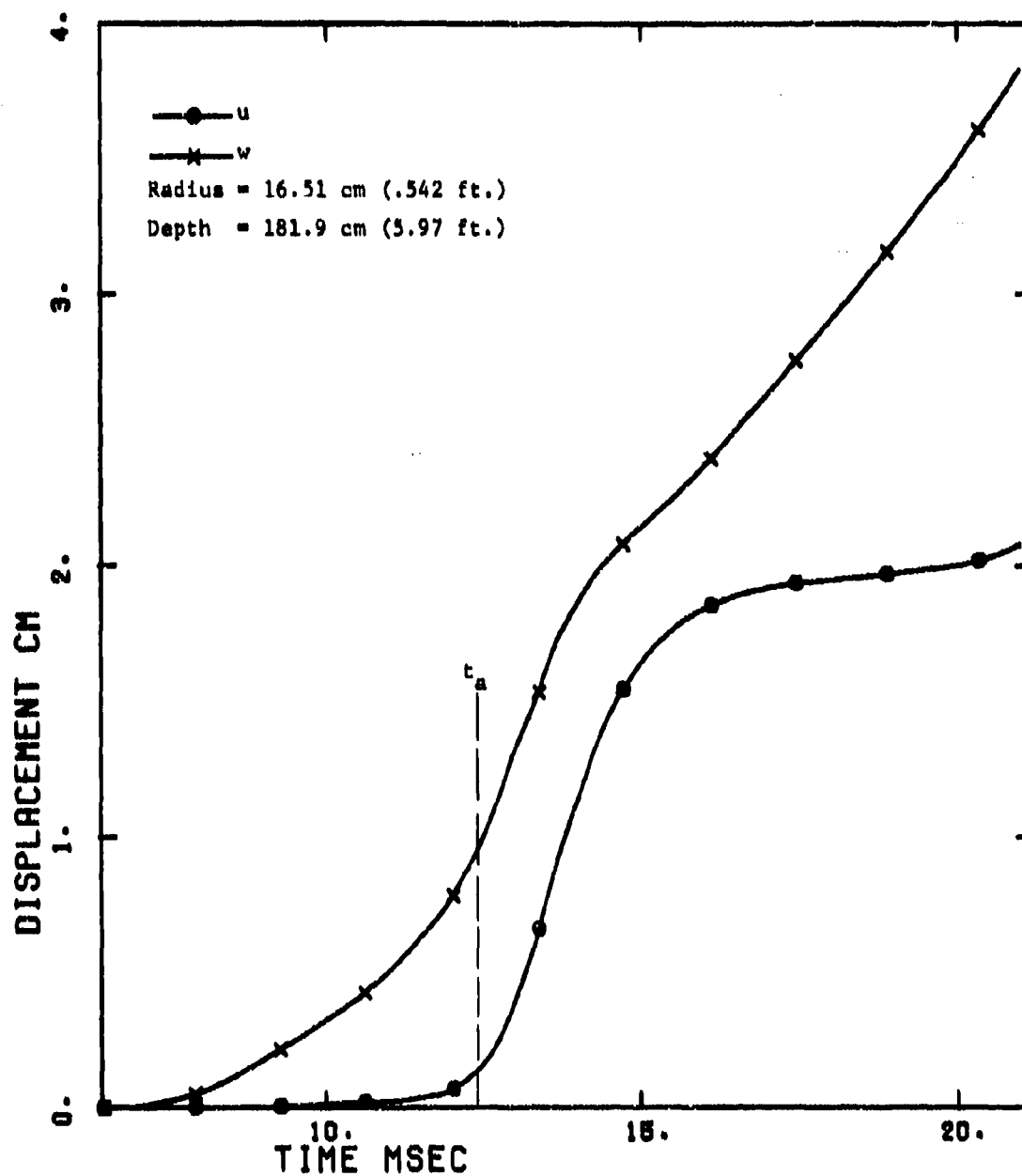


Figure D-16. Displacement Components at Station 5

18 SEP 74

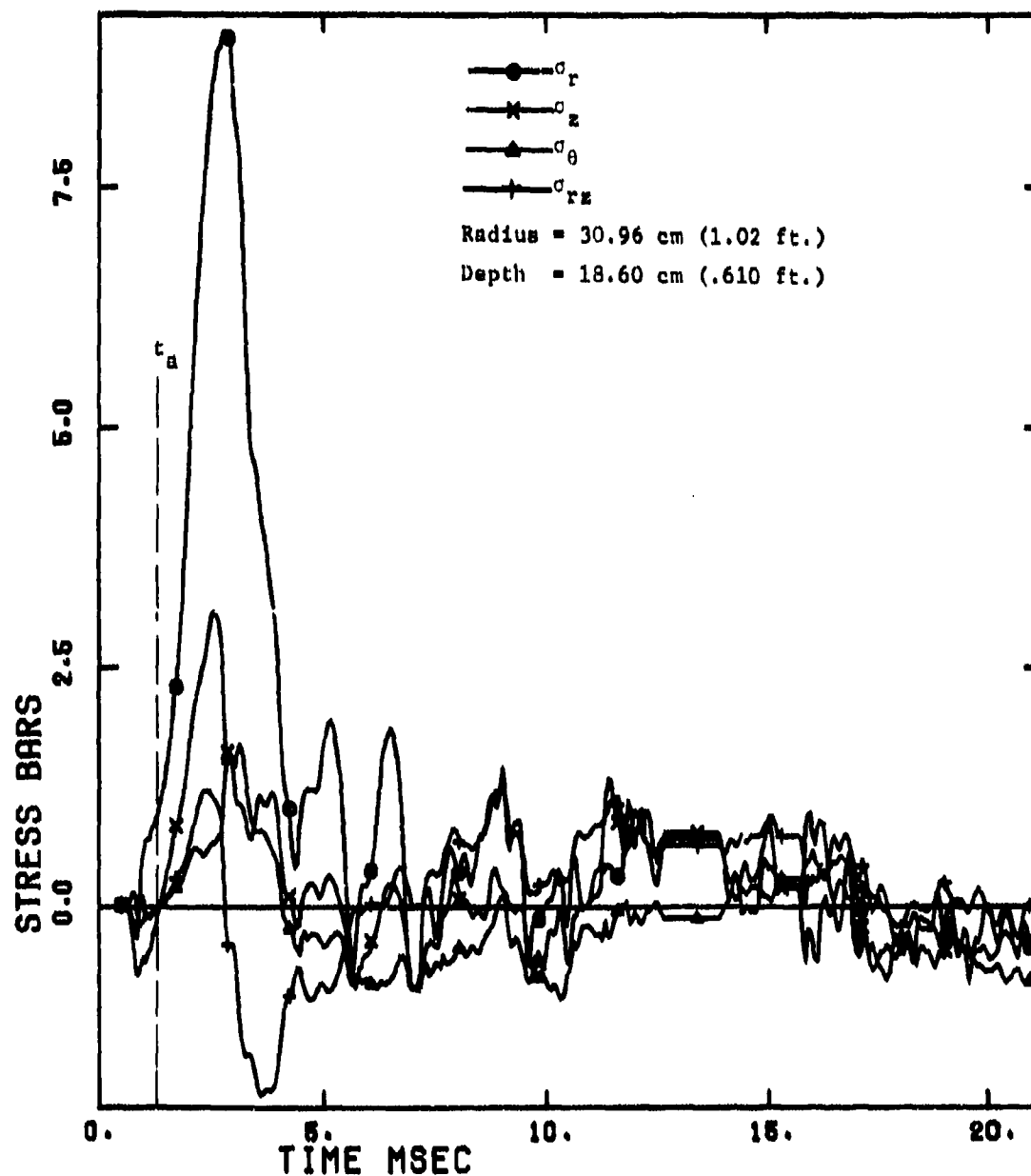


Figure D-17. Stress Components at Station 6

10 SEP 74

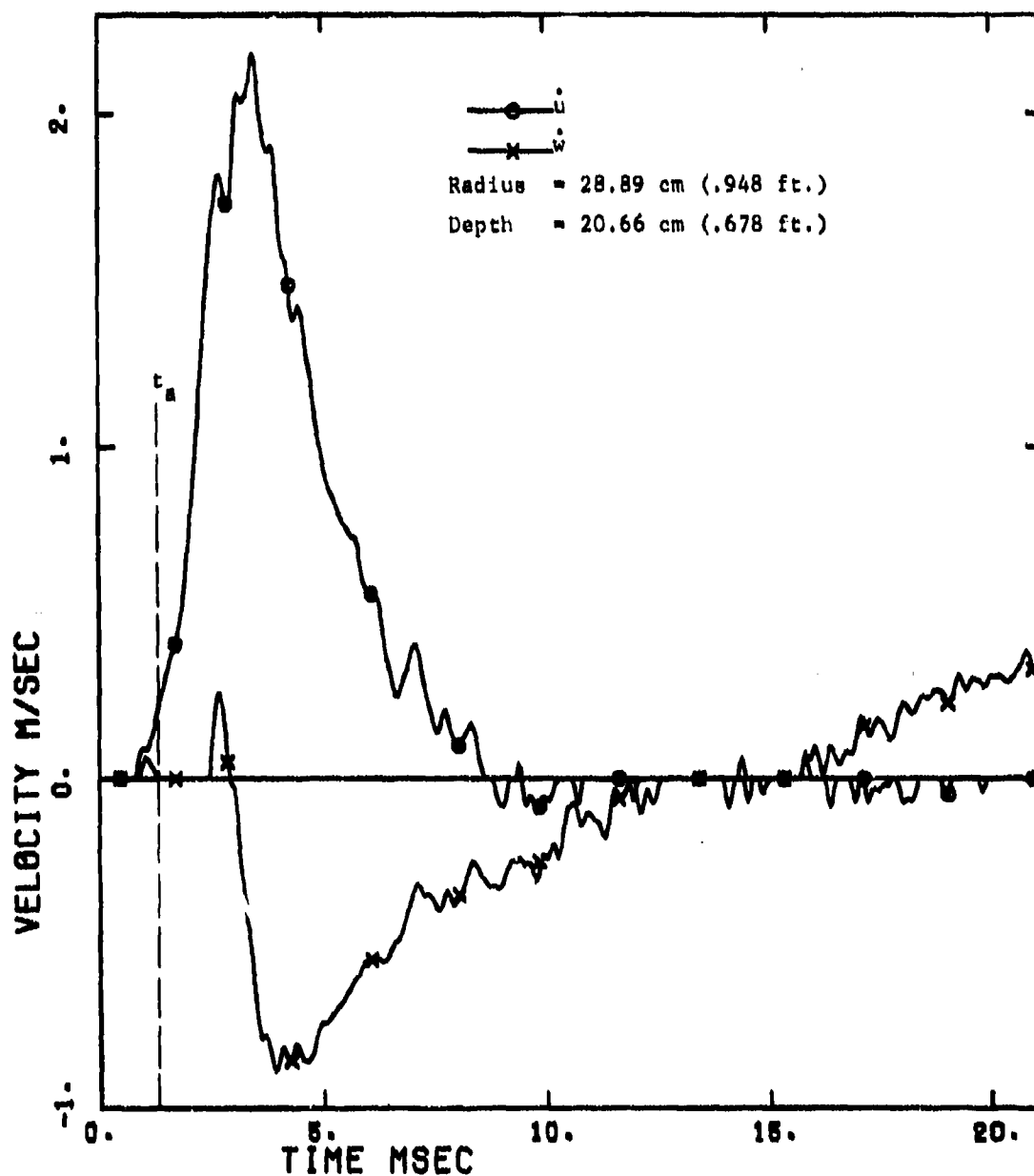


Figure D-18. Velocity Components at Station 6

18 SEP 74

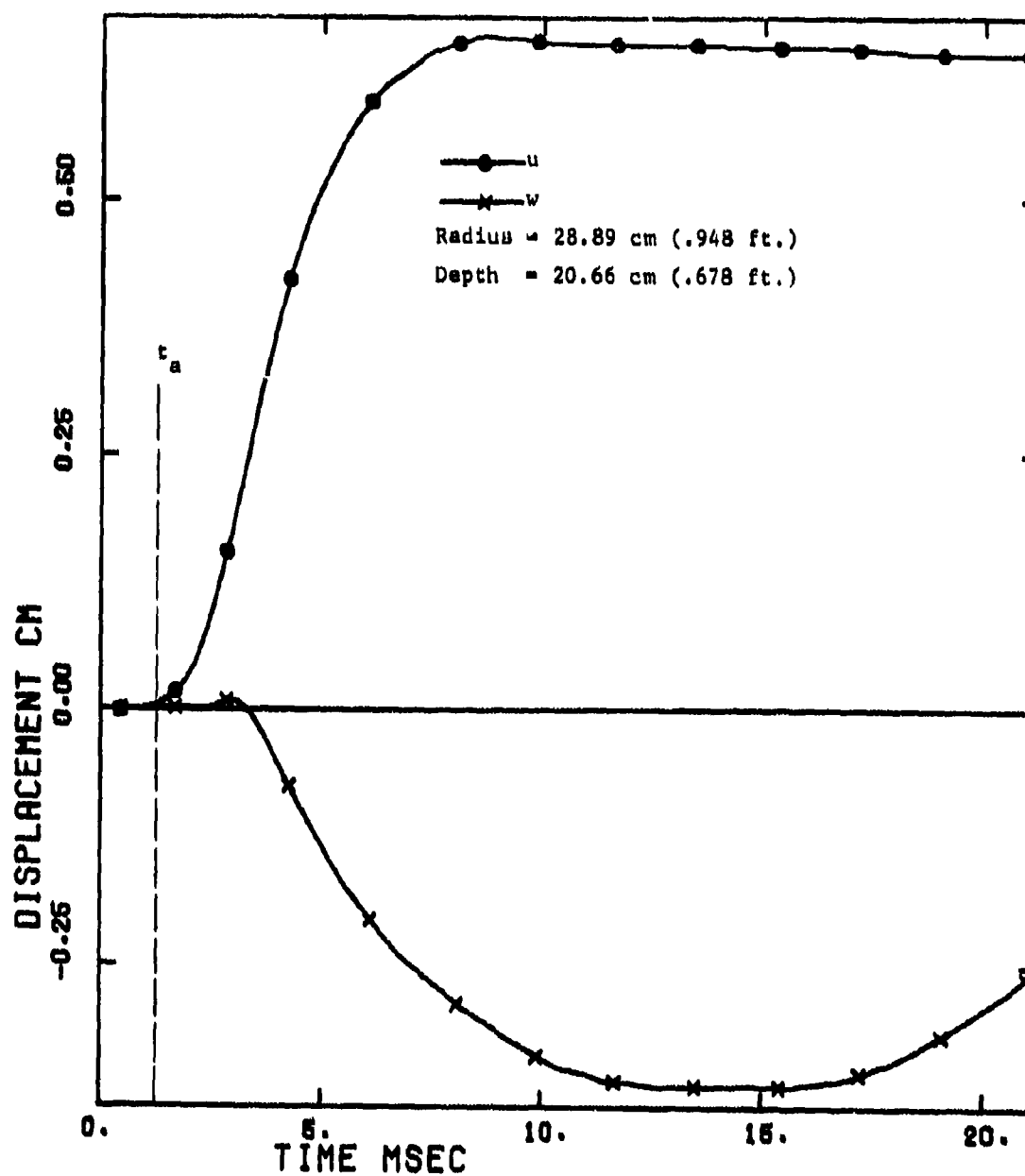


Figure D-19. Displacement Components at Station 6

18 SEP 74

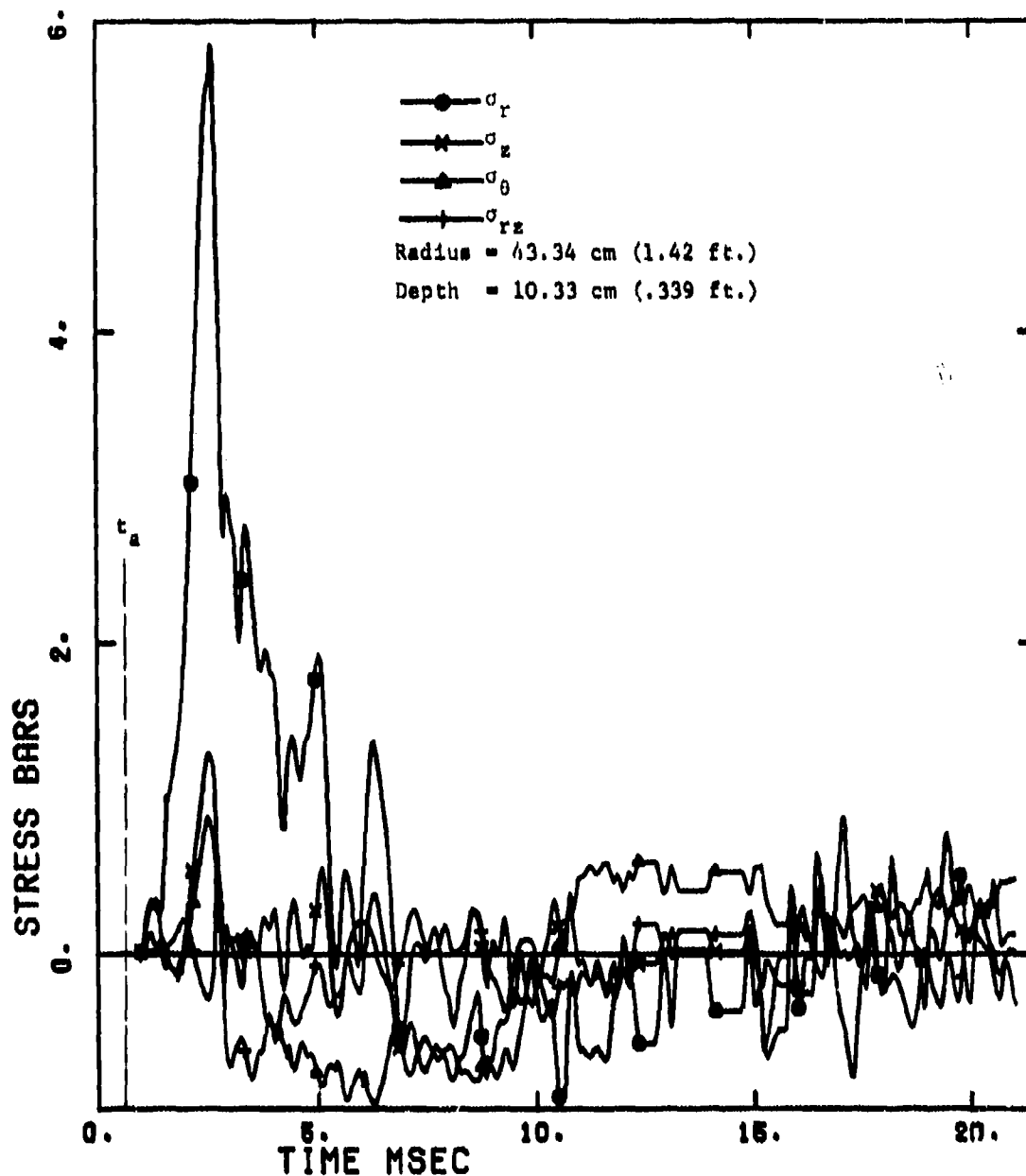


Figure D-20. Stress Components at Station 7

10 SEP 74

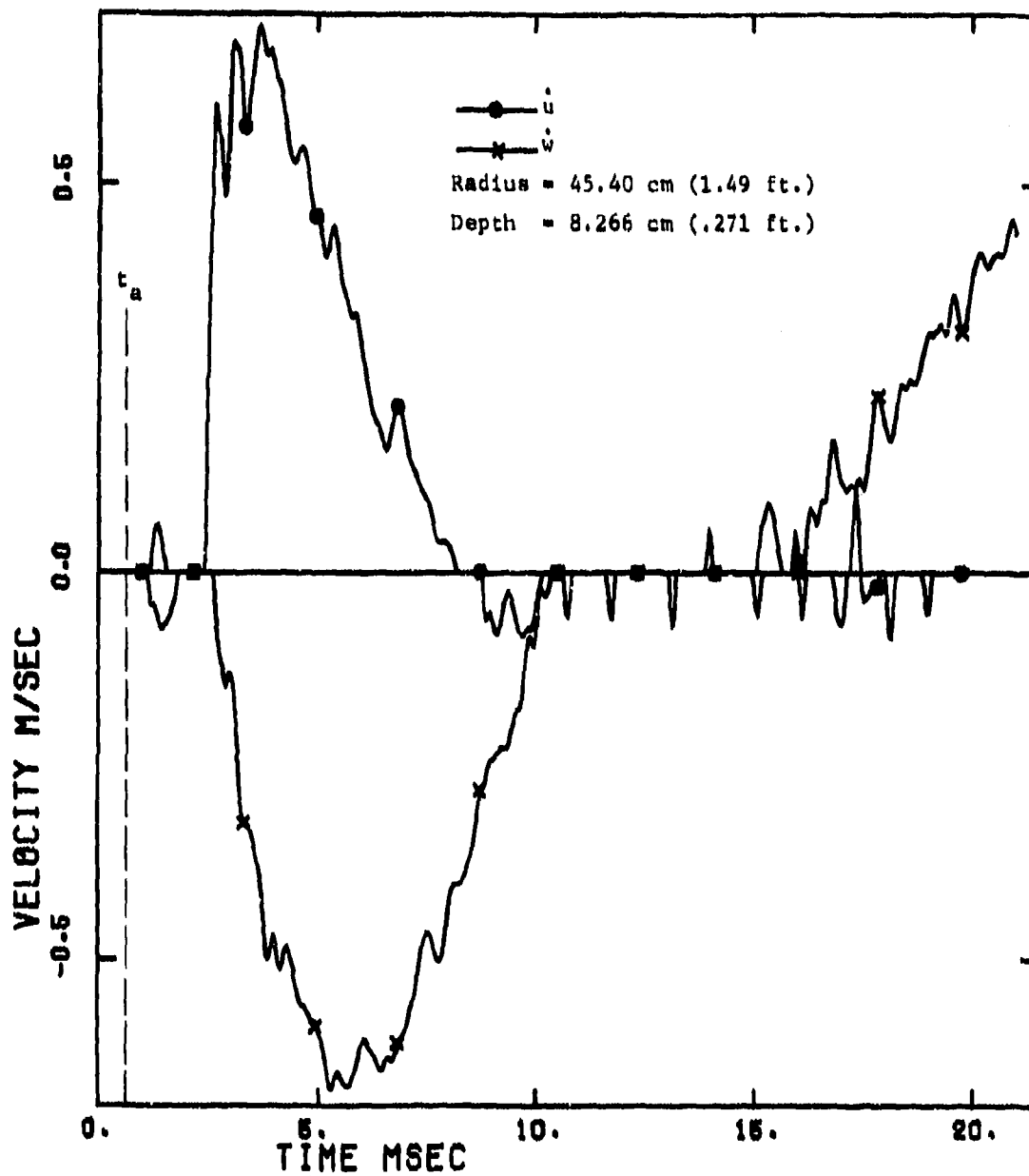


Figure D-21. Velocity Components at Station 7

10 SEP 74

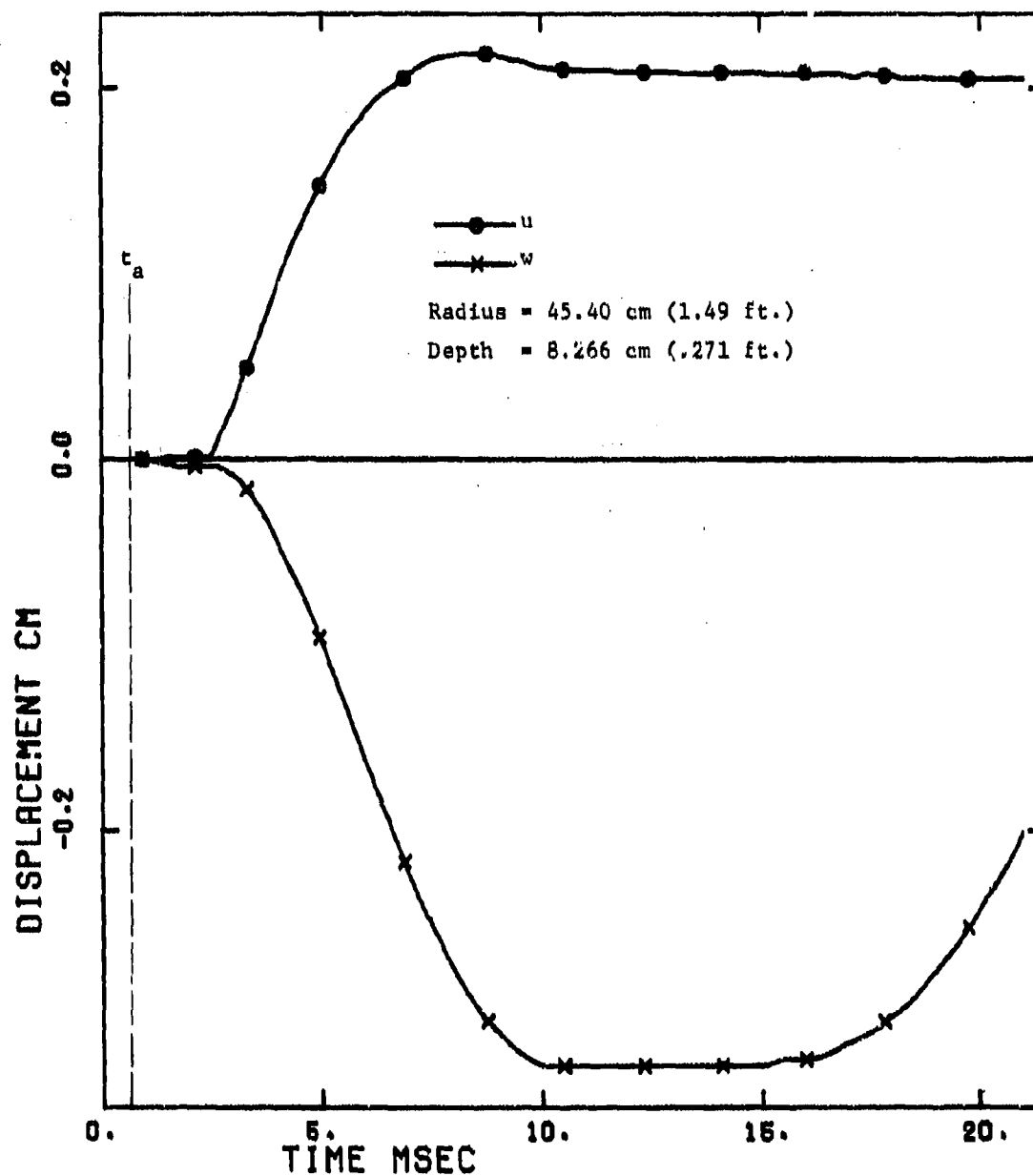


Figure D-22. Displacement Components at Station 7

18 SEP 74

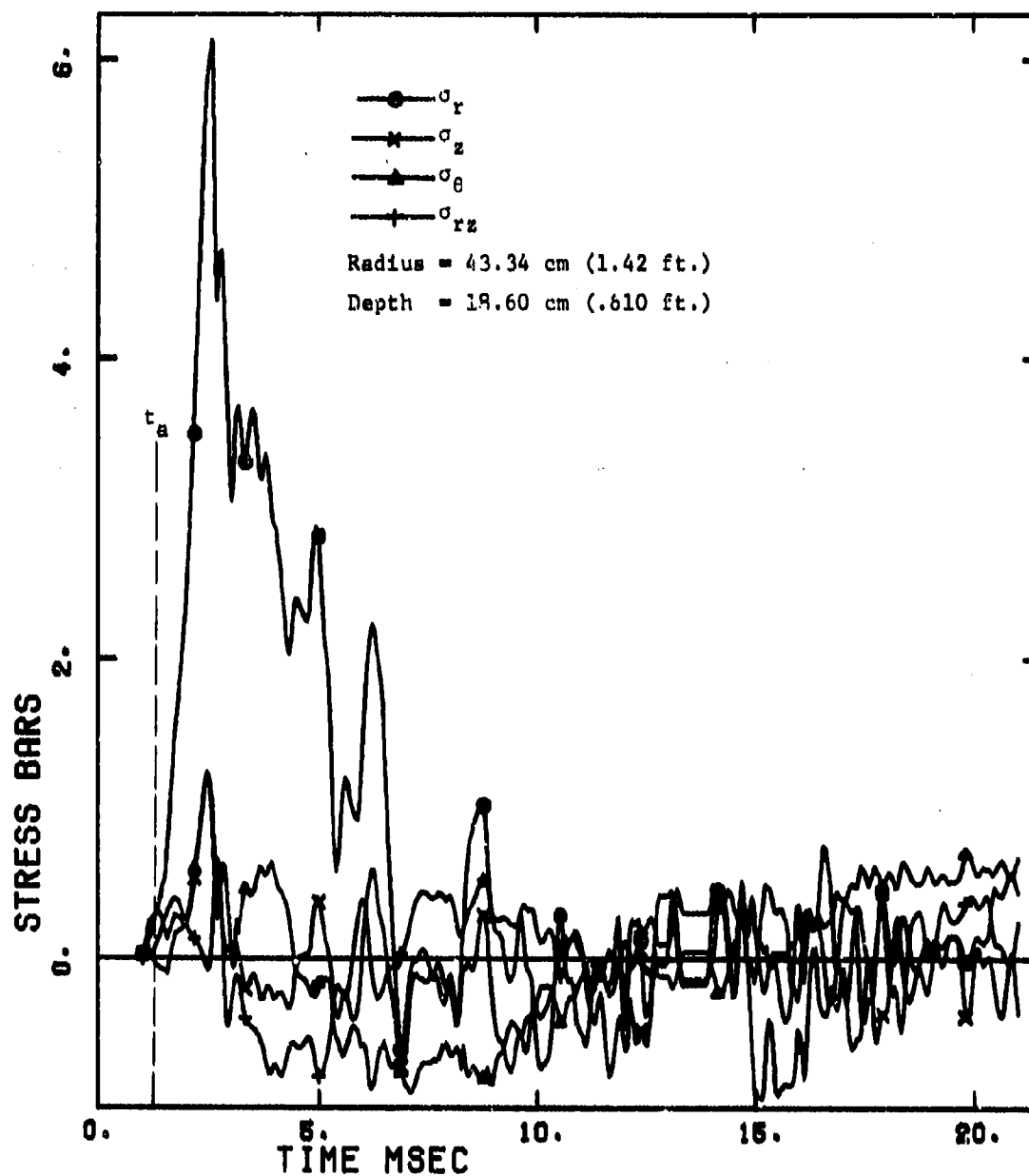


Figure D-23. Stress Components at Station 8

16 SEP 74

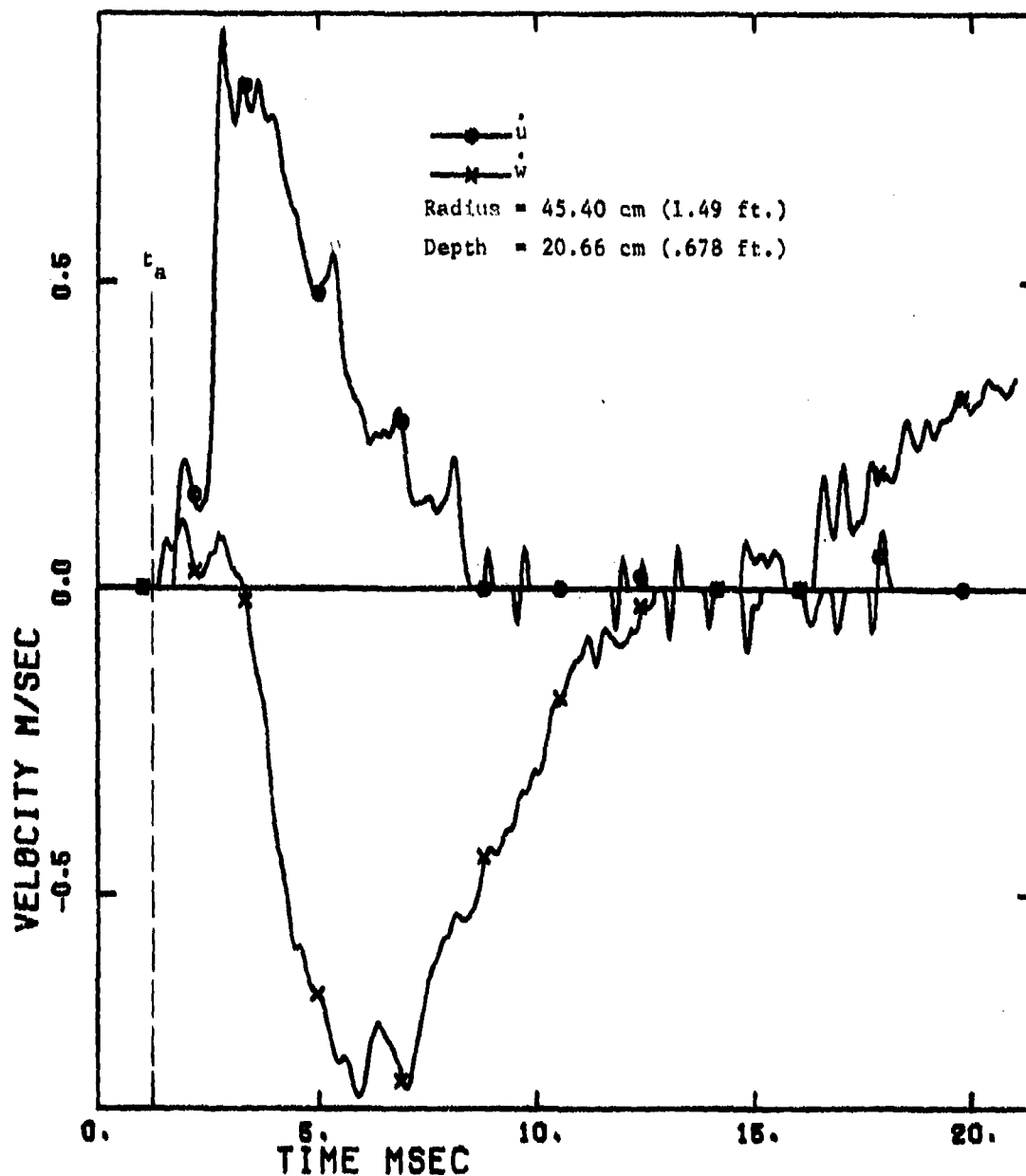


Figure D-24. Velocity Components at Station 8

18 SEP 74

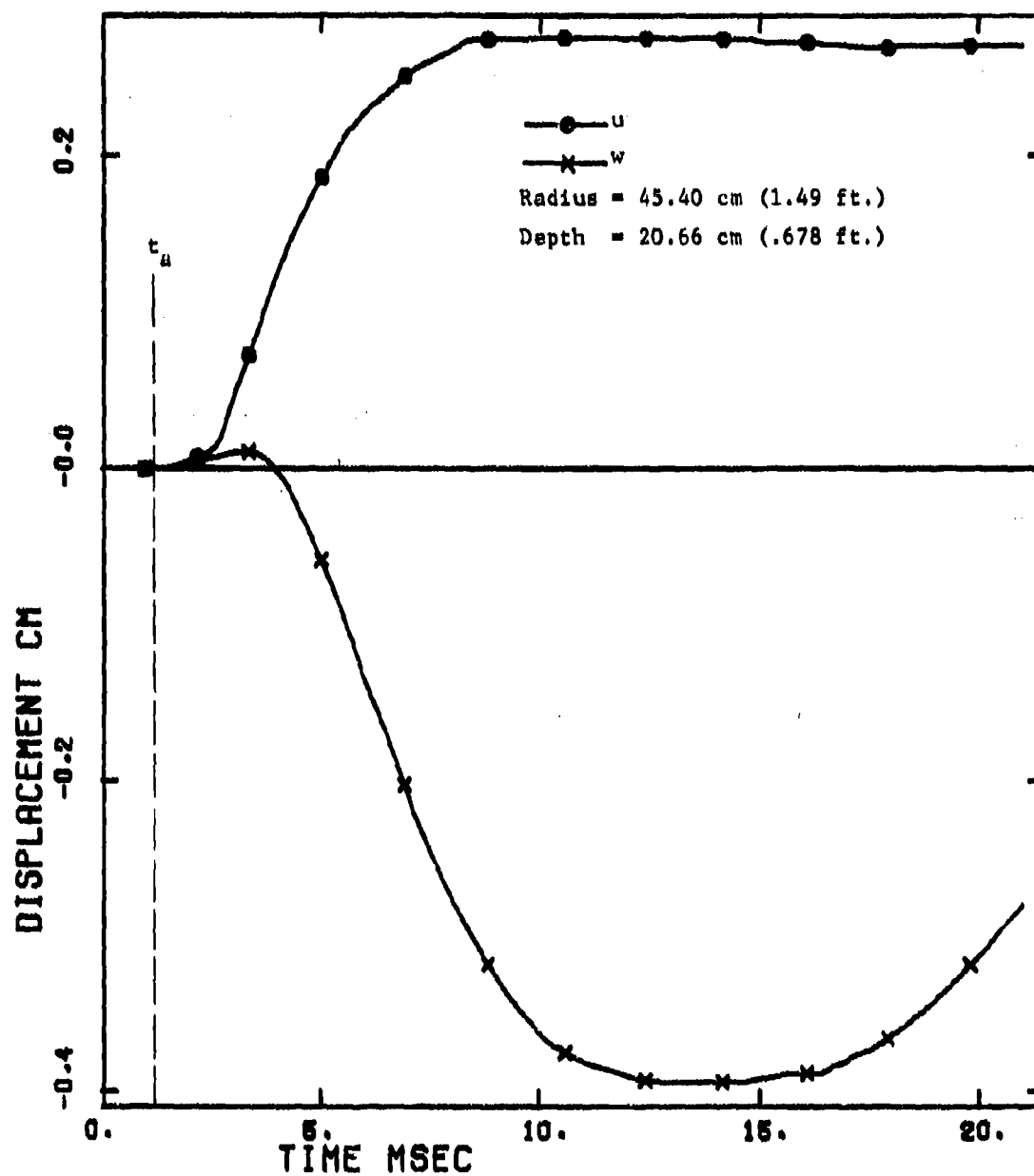


Figure D-25. Displacement Components at Station 8

18 SEP 74

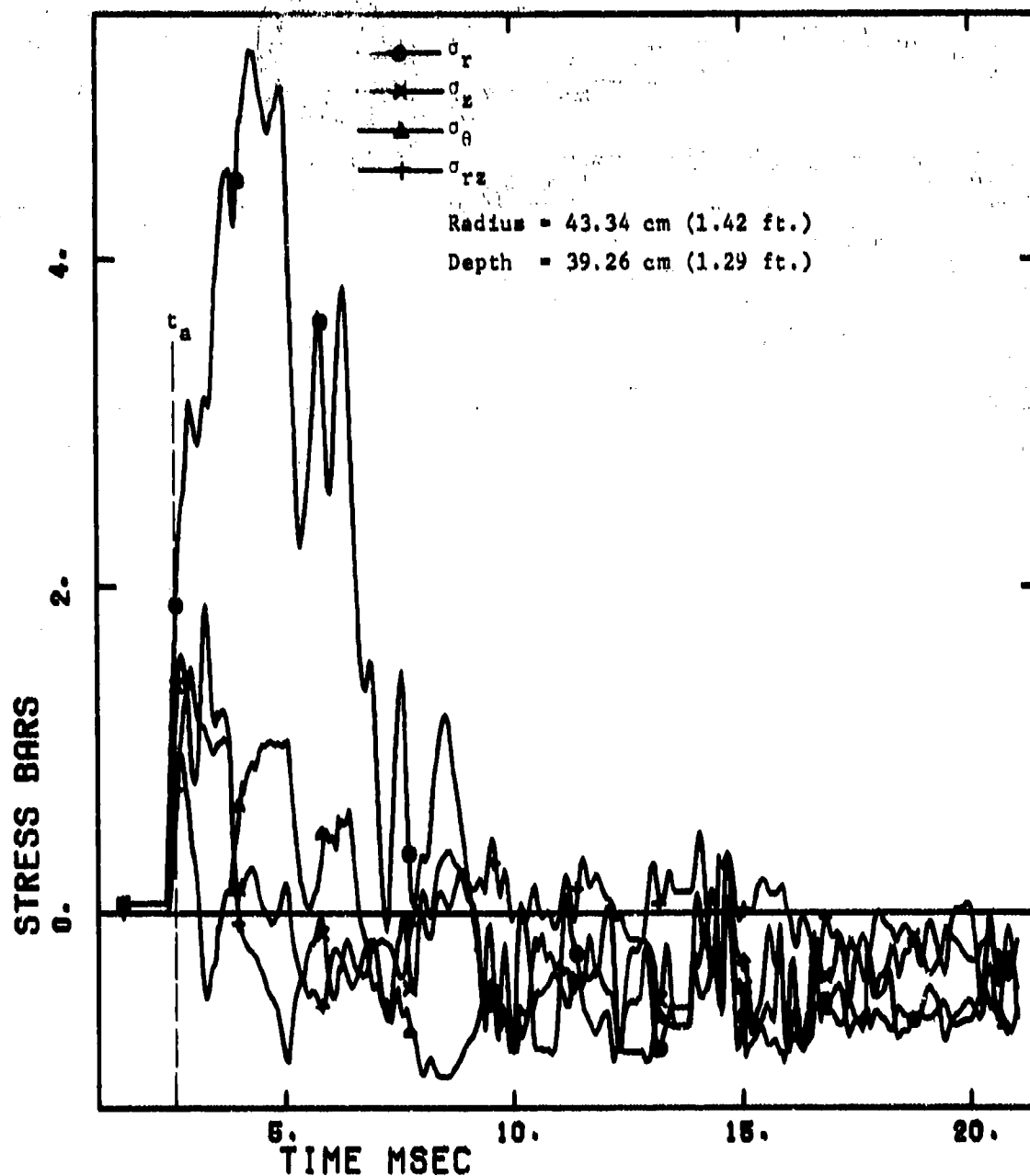


Figure D-26. Stress Components at Station 9

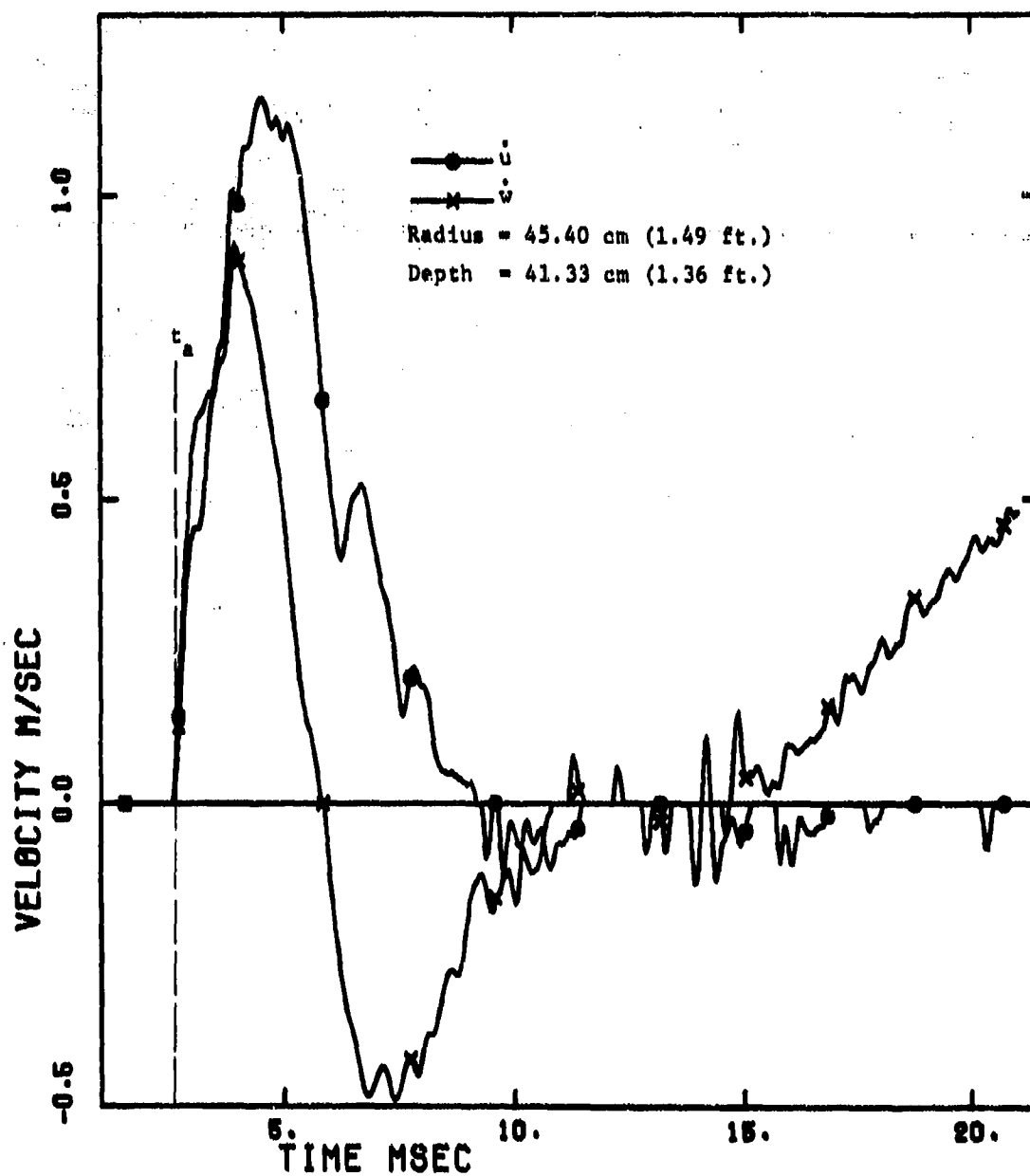


Figure D-27. Velocity Components at Station 9

10 SEP 74

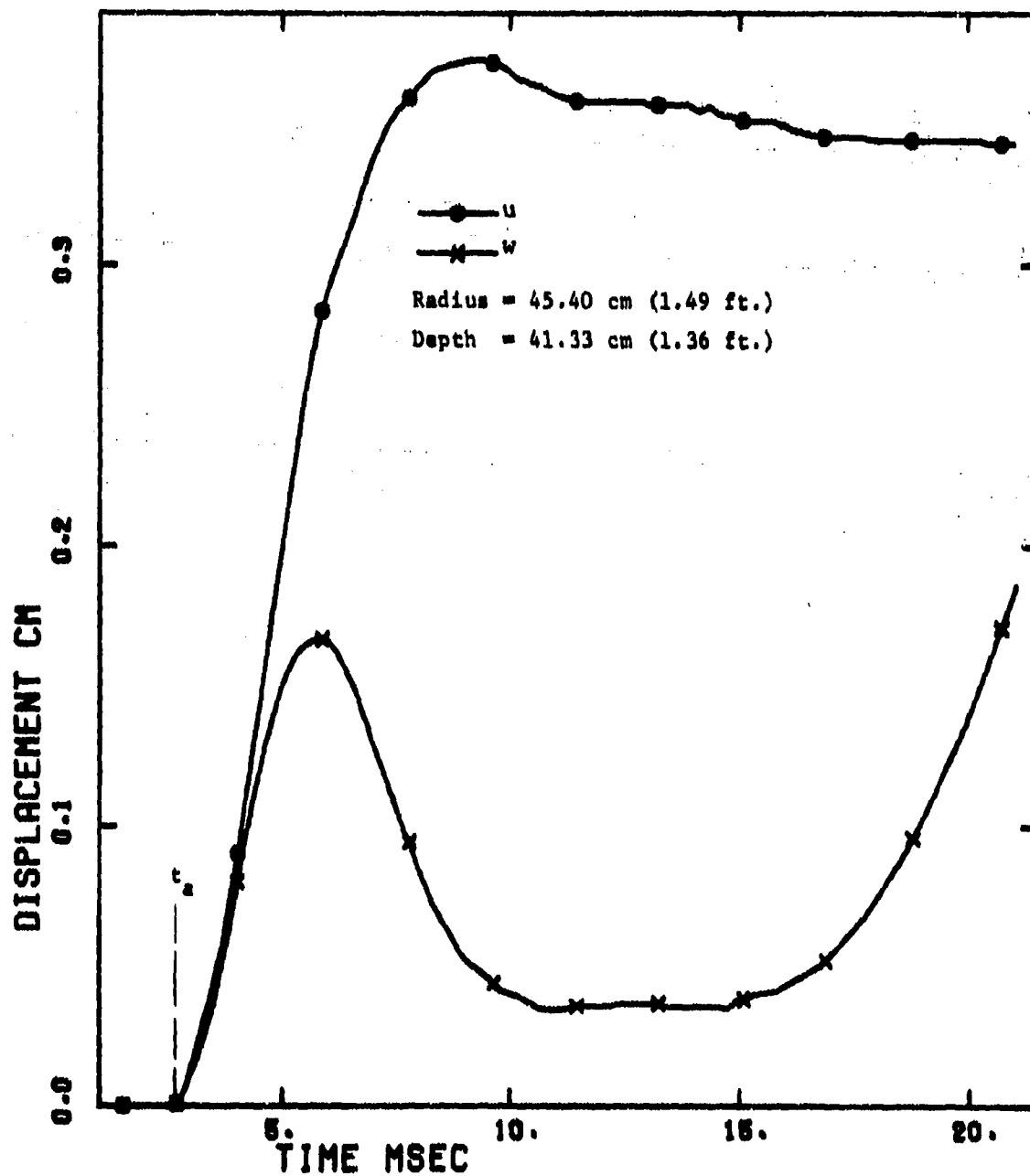


Figure D-28. Displacement Components at Station 9

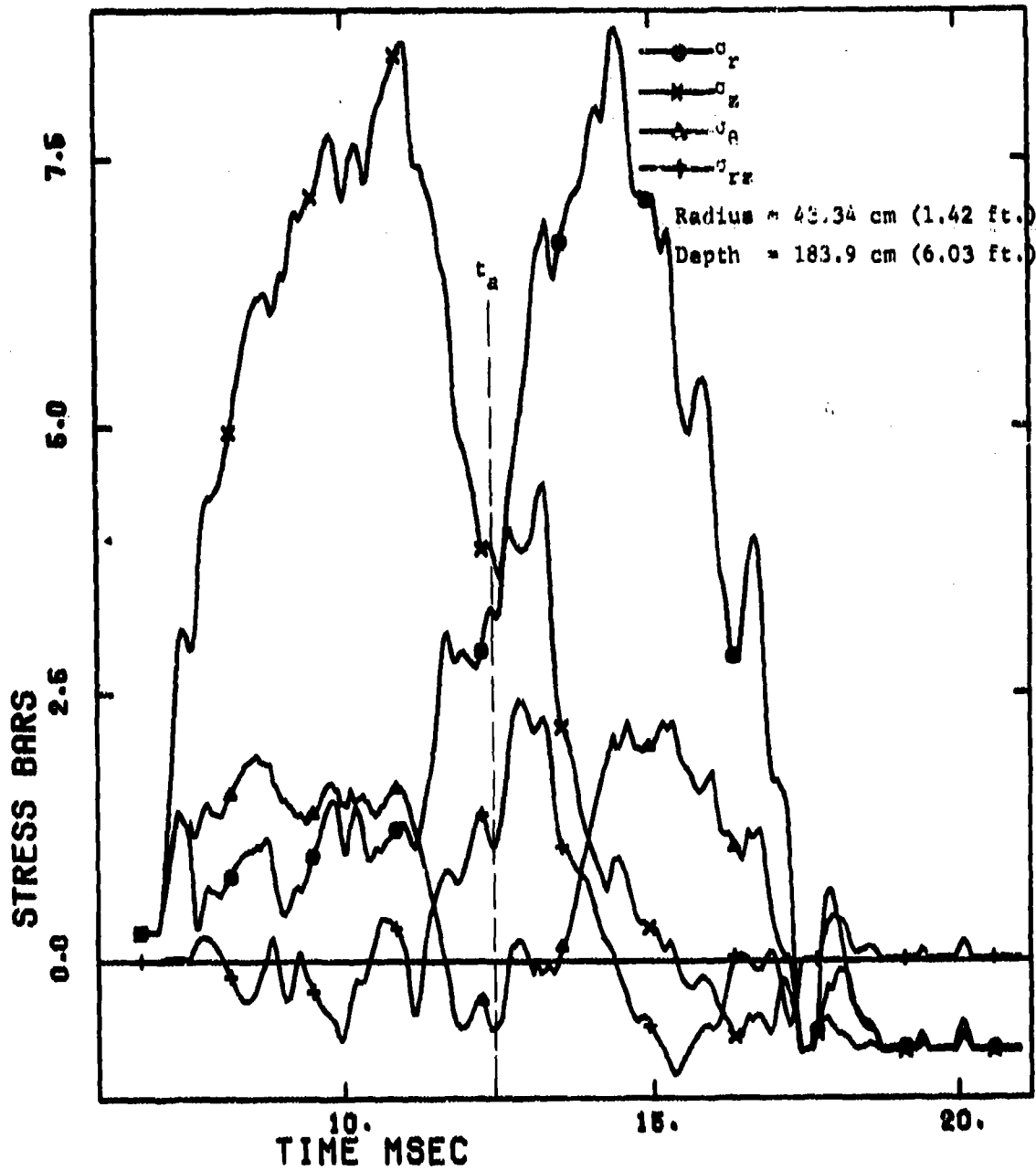


Figure D-29. Stress Components at Station 10

10 SEP 74

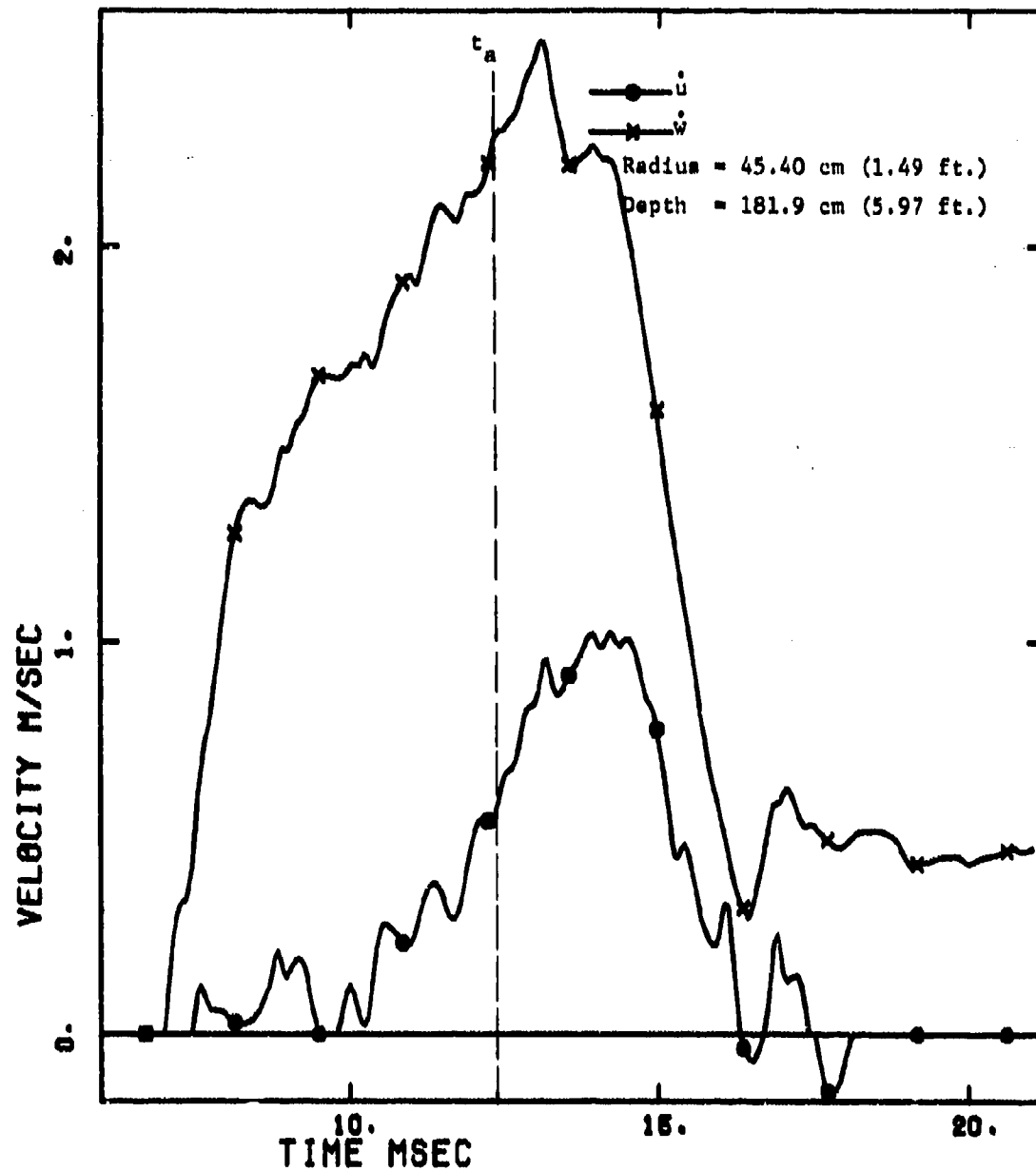


Figure D-30. Velocity Components at Station 10

18 SEP 74

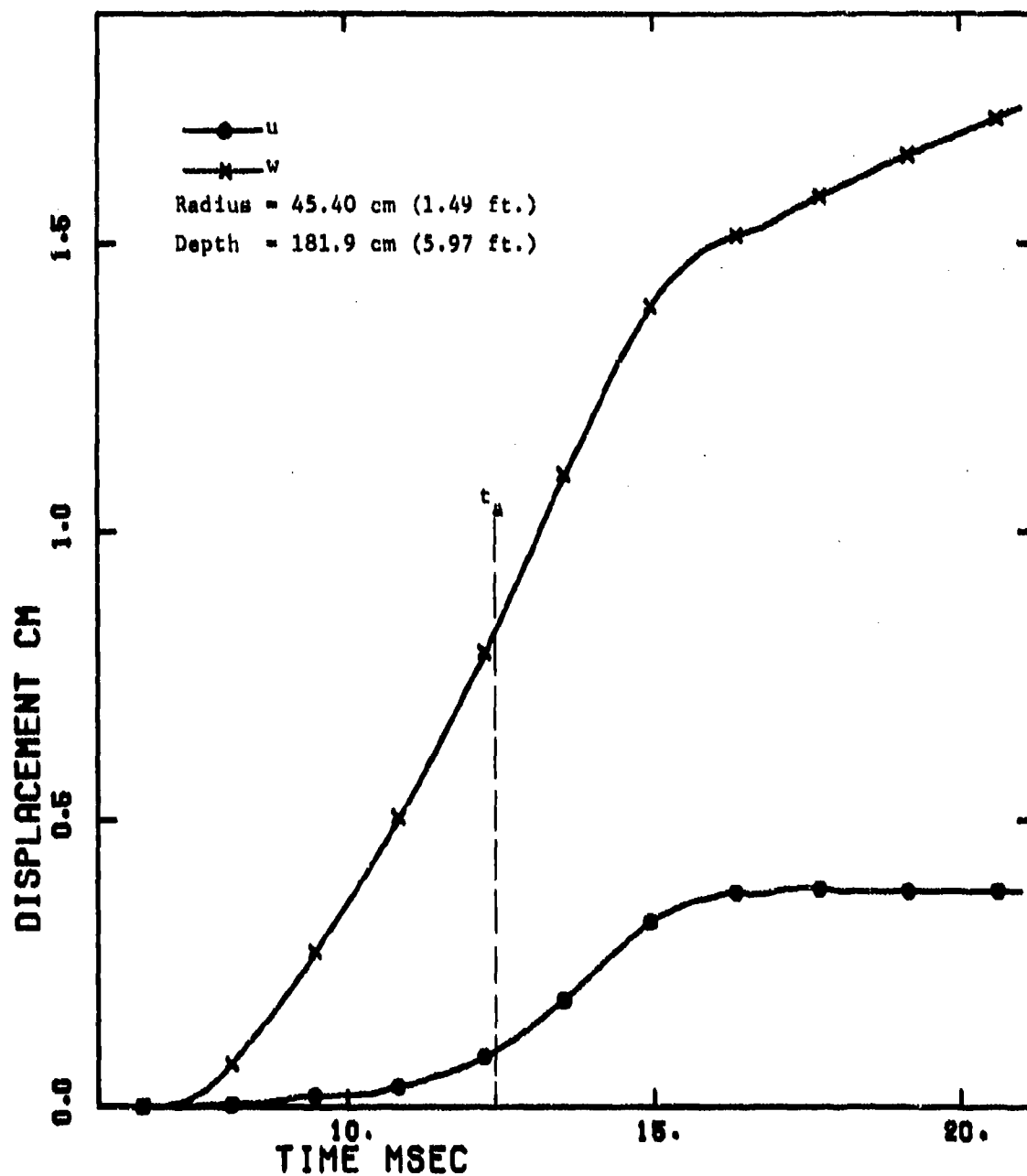


Figure D-31. Displacement Components at Station 10

18 SEP 74

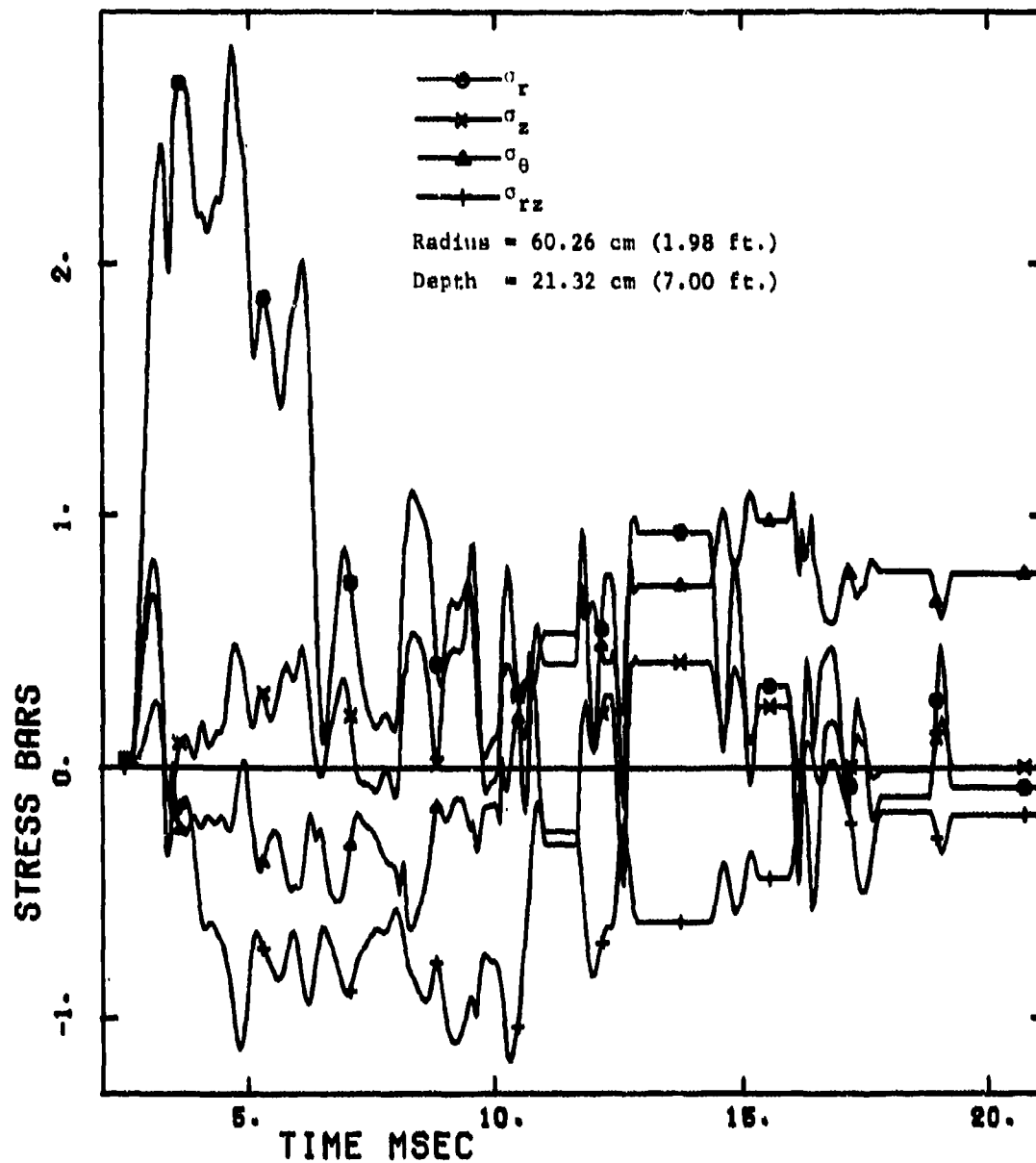


Figure D-32. Stress Components at Station 11

18 SEP 74

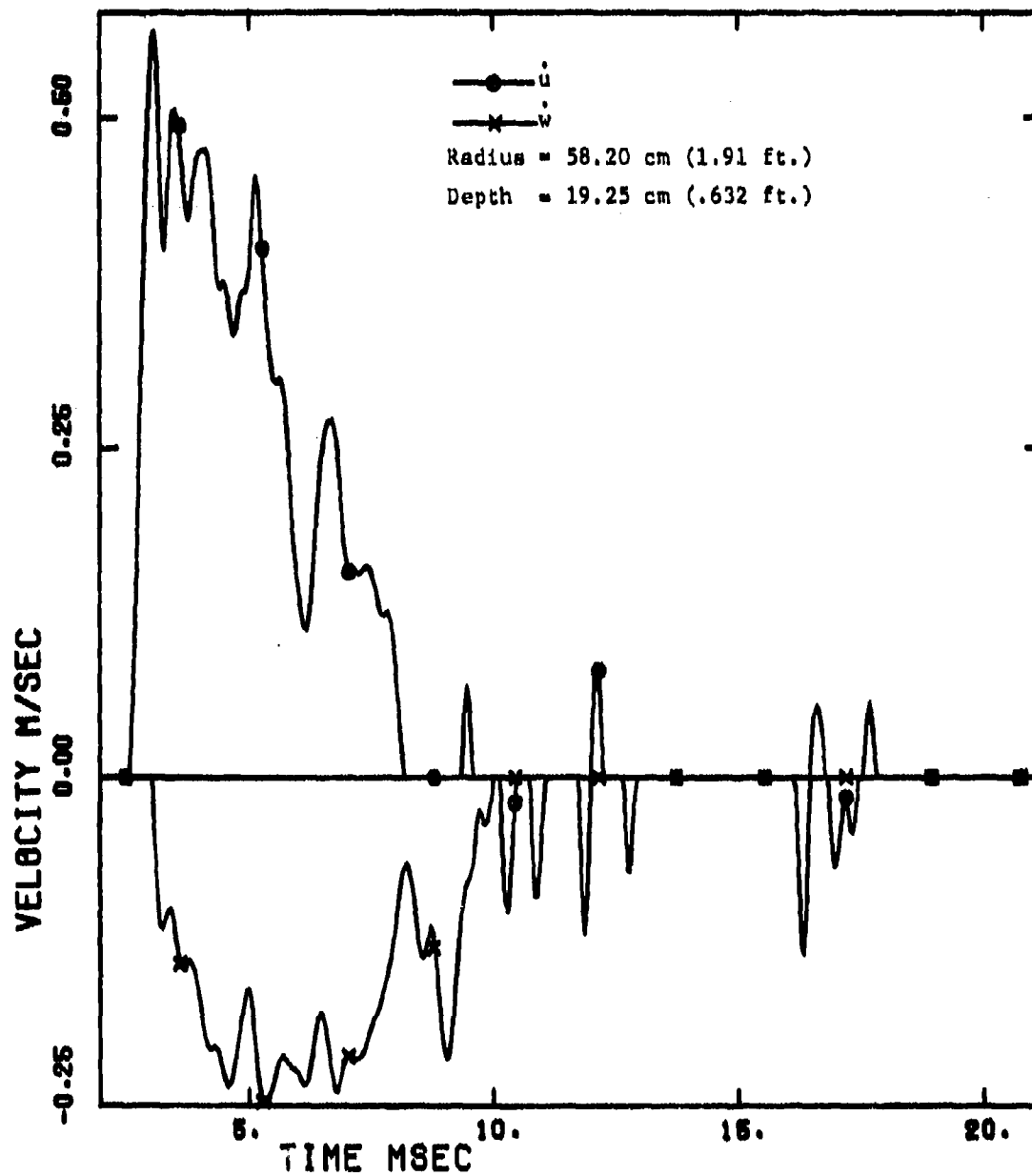


Figure D-33. Velocity Components at Station 11

16 SEP 74

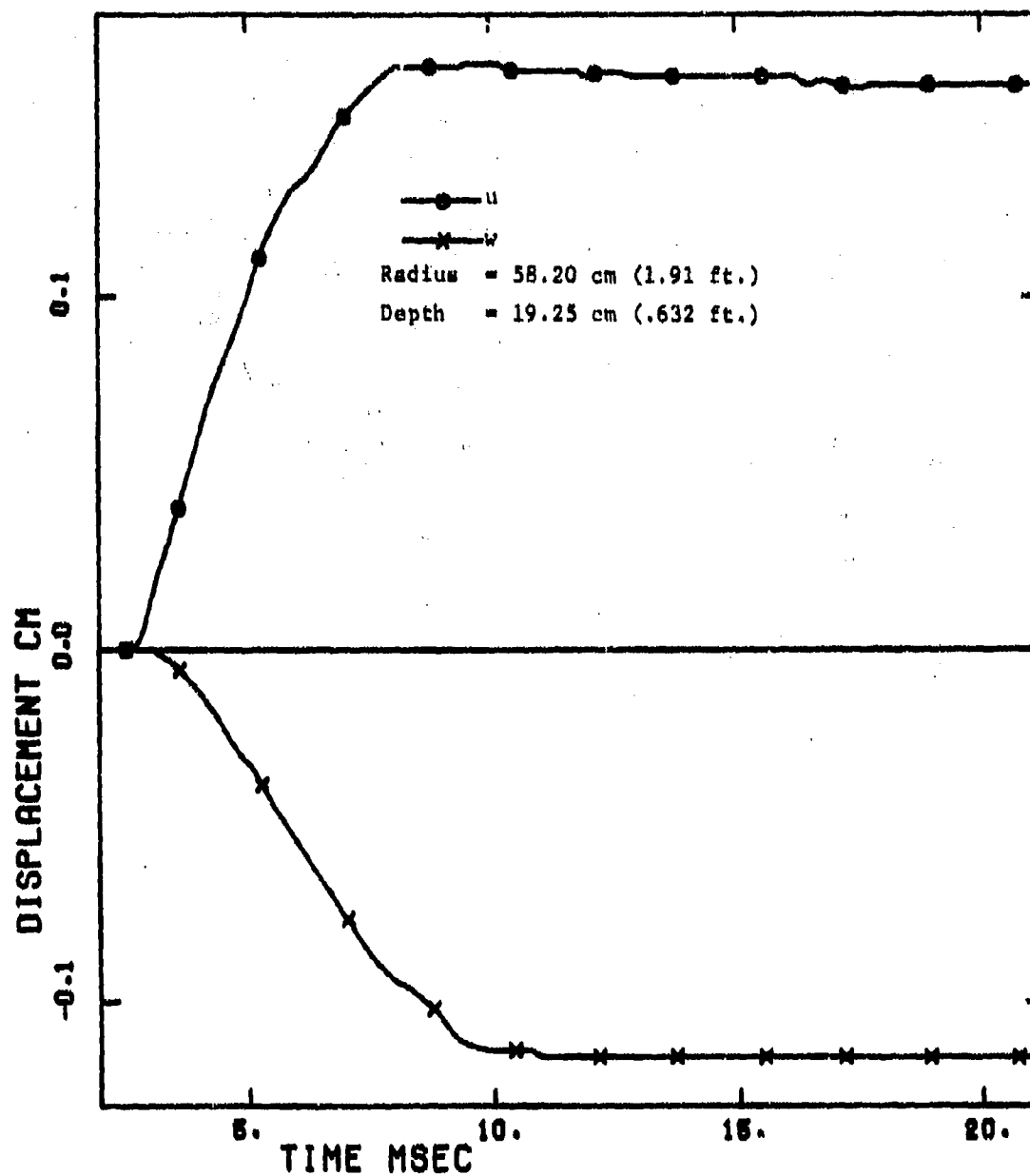


Figure D-34. Displacement Components at Station 11

18 SEP 74

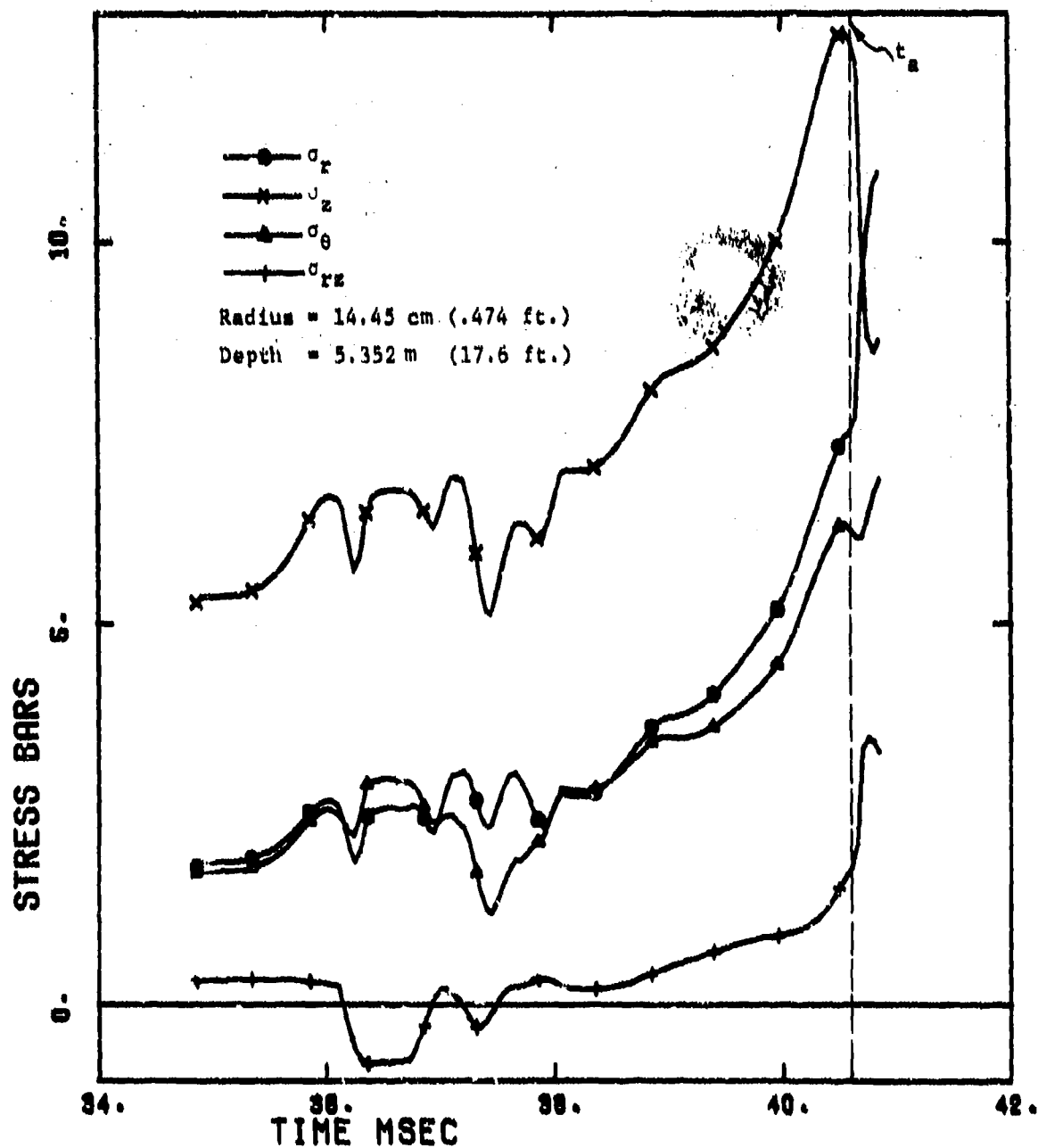


Figure D-35. Stress Components at Station 12

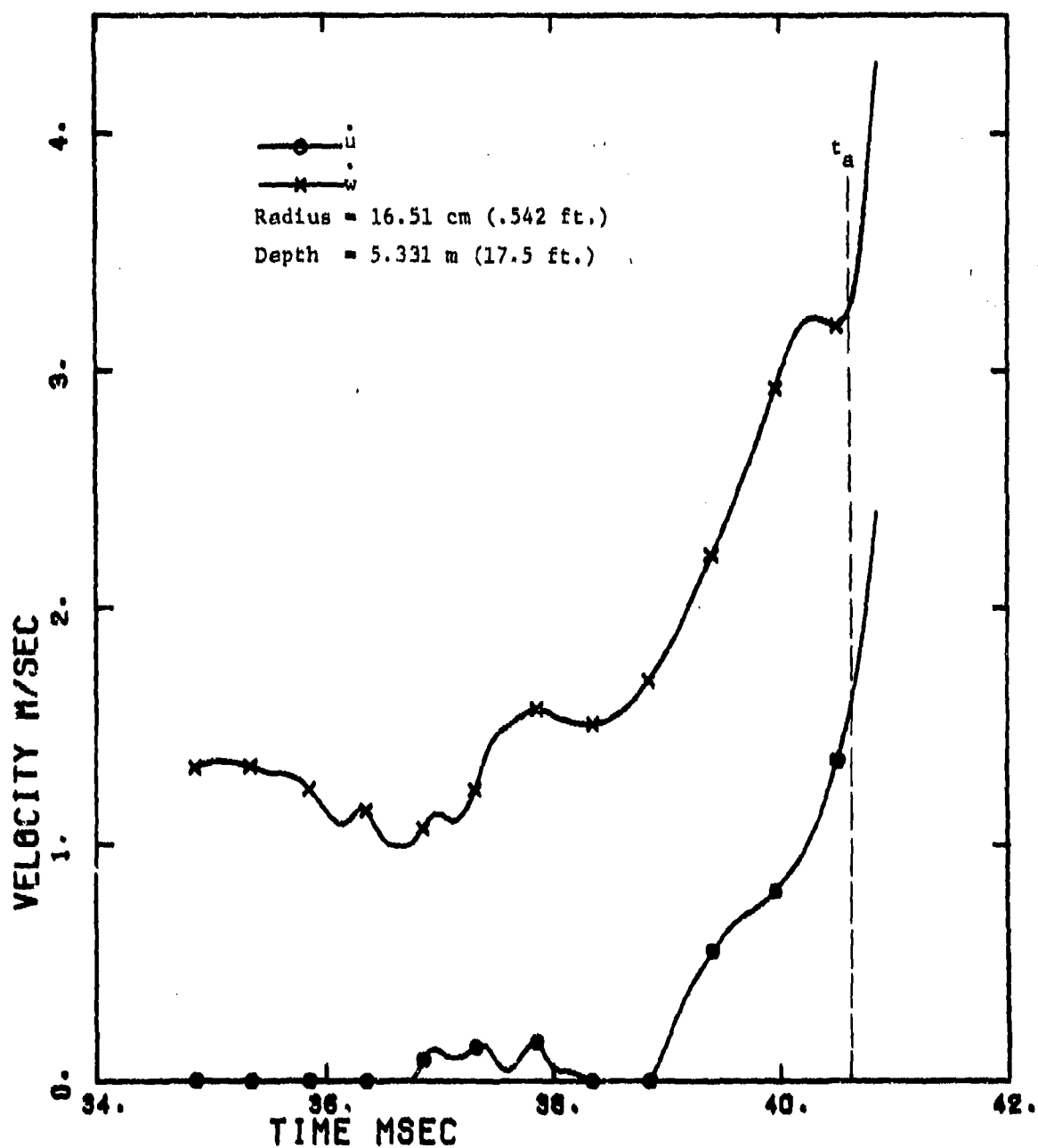


Figure D-36. Velocity Components at Station 12

DISTRIBUTION LIST

DEPARTMENT OF DEFENSE

Assistant to the Secretary of Defense
Atomic Energy
ATTN: Honorable Donald R. Cotter

Director
Defense Civil Preparedness Agency
ATTN: Technical Library

Defense Documentation Center
2 cy ATTN: TO

Director
Defense Intelligence Agency
ATTN: Technical Library
ATTN: DI-7D, Edward O'Farrell
ATTN: DT-2, Wpns. & Sys. Div.
ATTN: DI-7E

Defense Mapping Agency
ATTN: H. Lindsey

Director
Defense Nuclear Agency
15 cy ATTN: SP88
ATTN: DDST
ATTN: BTBI, Archives
2 cy ATTN: STTL, Tech. Library

Dir. of Defense Resch. & Engineering
ATTN: R. Thorkildsen
ATTN: George R. Barse
ATTN: AD/SW
ATTN: DD/S&SS
ATTN: DD/TWP
ATTN: Milton J. Minneman

Commander
Field Command
Defense Nuclear Agency
ATTN: FCPR

Interservice Nuclear Weapons School
ATTN: Tech. Lib.

Director
Joint Strat. Tgt. Planning Staff, JCS
ATTN: STINFO Library

Chief
Livermore Division Field Command DNA
Lawrence Livermore Laboratory
ATTN: FCPRL

Weapons Systems Evaluation Group
ATTN: Document Control

DEPARTMENT OF THE ARMY

Asst. Chief of Staff for Force Development
Department of the Army
ATTN: Technical Library
ATTN: Dir. of Chem. & Nuc. Ops.

DEPARTMENT OF THE ARMY (Continued)

Director
BMD Advanced Tech. Center
ATTN: 1CRDABH-X
ATTN: CRDABH-S

Manager
BMD Program Office
ATTN: John Shea

Headquarters, Central Army Group
ATTN: CENEN, LTC J. L. Spruill

Chief of Res. Dev. & Acquisition
Department of the Army
ATTN: DAMA-CBM-N, LTC E. V. DeBoesser, Jr.
ATTN: Technical Library

Commander
Frankford Arsenal
ATTN: L. Baldini

Commander
Harry Diamond Laboratories
ATTN: Frank J. Vralerio
ATTN: AMXDO-NP
ATTN: AMXDO-RBH, James H. Gwaltney
ATTN: Allen Holmes

Department of the Army
Office Chief of Engineers
2 cy ATTN: DAEN-RDM
2 cy ATTN: DAEN-MCE-D

Commander
Picatinny Arsenal
ATTN: Ray Goldstein
ATTN: Jerry Pental
ATTN: Marty Margolin
ATTN: Ray Mooser
ATTN: William Meyer
ATTN: Technical Library
ATTN: P. Angellotti
ATTN: Paul Harris
ATTN: Ernie Zimpo

Director
U. S. Army Ballistic Research Laboratories
ATTN: J. W. Apgar
ATTN: D. Dunn
ATTN: G. Grabarek
ATTN: B. Roter
ATTN: G. Roecker
ATTN: Norris J. Huffington, Jr.
ATTN: J. H. Keeser
ATTN: AMXBR-X, Julius J. Messaros
ATTN: AMXBR-TB, J. T. Frasier
2 cy ATTN: Tech. Library, Edward Bailey
ATTN: W. Taylor

Commander and Director
U.S. Army Cold Region Res. Engr. Lab
ATTN: G. Swinnow

DEPARTMENT OF THE ARMY (Continued)

Commander
U.S. Army Comm. Command
ATTN: Technical Library

Commander
U.S. Army Engineer Center
ATTN: ATSEN-SY-L

Project Engineer
U.S. Army Engineer Dist., Huntsville
ATTN: HNDSE-R, Michael M. Dembo

Division Engineer
U.S. Army Engineer Dist., Ohio River
ATTN: Technical Library

Commandant
U.S. Army Engineer School
ATTN: S. Grasier

Director
U.S. Army Engr. Waterways Exper. Sta.
ATTN: John N. Strange
ATTN: Guy Jackson
ATTN: Behzad Rohani
ATTN: Leo Ingram
ATTN: Technical Library
ATTN: William Flathau
ATTN: Kim Davis
ATTN: A. Rooke
ATTN: P. Hadala

Commander
U.S. Army Mat. & Mechanics Resh. Ctr.
ATTN: Richard Shea
ATTN: Technical Library
ATTN: John Mewall

Director
U.S. Army Material Sys. Analysis Agcy.
ATTN: M. Roches
ATTN: J. Speranza

Commander
U.S. Army Materiel Command
ATTN: Technical Library
2 cy ATTN: AMCRD-WN
2 cy ATTN: AMCRD-BN

Commander
U.S. Army Materiel Command
ATTN: Research & Concepts Branch

Commander
U.S. Army Missile Command
ATTN: Technical Library
ATTN: F. Fleming
ATTN: W. Jann

Commander
U.S. Army Mobility Equip. R & D Center
ATTN: Technical Library

Commander
U.S. Army Nuclear Agency
ATTN: Tech. Library
ATTN: COL Quinn
ATTN: MAJ F. P. Weichel

DEPARTMENT OF THE ARMY (Continued)

Commandant
U.S. Army War College
ATTN: Library

Commander
U.S. Army Weapons Command
ATTN: Technical Library
ATTN: COL C. Treat
ATTN: Frank Black

DEPARTMENT OF THE NAVY

Chief of Naval Research
Department of the Navy
ATTN: Technical Library

Officer-in-Charge
Civil Engineering Laboratory
ATTN: Technical Library
ATTN: R. J. Odello

Commander
Naval Electronic Systems Command
ATTN: PME 117-21A

Commander
Naval Facilities Engineering Command
ATTN: Technical Library

Superintendent
Naval Postgraduate School
ATTN: Code 2124, Tech. Rpts. Librarian

Director
Naval Research Laboratory
ATTN: Code 2027, Tech. Lib.

Commander
Naval Surface Weapons Center
ATTN: Mary P. King
ATTN: Robert D. Haldenreich
ATTN: Code 730, Tech. Library
ATTN: Jules Enig
ATTN: Code 1224, Navy Nuc. Prgms. Off.
ATTN: Mr. Kasdorf
ATTN: G. Briggs

Commander
Naval Surface Weapons Center
ATTN: M. Welland
ATTN: Technical Library
ATTN: William Wisherd
ATTN: Ted Williams

Commander
Naval Weapons Center
ATTN: Carl Austin
ATTN: Code 533, Tech. Lib.
ATTN: Paul Cordle

Commanding Officer
Naval Weapons Evaluation Facility
ATTN: Technical Library

Director
Strategic Systems Project Office
ATTN: NSP-43, Tech. Library

DEPARTMENT OF THE AIR FORCE

AF Armament Laboratory, AFSC

ATTN: Massey Valentine
ATTN: Dr. Kulp
ATTN: Capt Larry Looney
ATTN: DLOSL-Library
ATTN: William Cramer
ATTN: Leonard Wilson
ATTN: John Collins
ATTN: Maj Thomas Tomasetti

AF Institute of Technology, AU

ATTN: Library, AFIT, Bldg. 640, Area B

AF Weapons Laboratory, AFSC

ATTN: SUL
ATTN: Robert Port
ATTN: DEV, M. A. Plamondon

Headquarters

Air Force Systems Command
ATTN: Technical Library

Commander

Armament Development & Test Center
ATTN: Technical Library

Commander

Foreign Technology Division, AFSC
ATTN: TD-BTA, Library

HQ USAF/IN

ATTN: INATA

Commander

Rome Air Development Center, AFSC
ATTN: EMTLD, Document Library

SAMSO/DE

ATTN: DEB

HQ USAF/HD

ATTN: RDPM, Col J. E. McCormick

ENERGY RESEARCH & DEVELOPMENT ADMINISTRATION

Division of Military Application

ATTN: Document Control for Test Office

Los Alamos Scientific Laboratory

ATTN: Doc. Con. for G. Dials
ATTN: Doc. Con. for C. Cremer
ATTN: Doc. Con. for Tom Dowler
ATTN: Doc. Con. for Reports Library

Sandia Laboratories

ATTN: Doc. Con. for Tech. Library
ATTN: Doc. Con. for T. Gold

Sandia Laboratories

ATTN: Doc. Con. for John Colp
ATTN: Doc. Con. for John Kelgas
ATTN: Doc. Con. for William Patterson
ATTN: Doc. Con. for Walter Herrmann
ATTN: Doc. Con. for 3141, Sandia Rpt. Coll.
ATTN: Doc. Con. for William Caudle
ATTN: Doc. Con. for Luke J. Vortman

ENERGY RESEARCH & DEVELOPMENT ADMINISTRATION

(Continued)

U.S. Energy Resch. & Dev. Administration

Albuquerque Operations Office
ATTN: Doc. Con. for Tech. Library

U.S. Energy Resch. & Dev. Administration

Library Branch G-043
ATTN: Doc. Con. for Class. Tech. Lib.

U.S. Energy Resch. & Dev. Administration

Nevada Operations Office
ATTN: Doc. Con. for Tech. Library

University of California

Lawrence Livermore Laboratory
ATTN: Doc. Con. for W. Scanlin
ATTN: Doc. Con. for R. L. Walker
ATTN: Larry W. Woodruff, L-125
ATTN: Frank Walker
ATTN: Technical Library
ATTN: Mark Wilkins

OTHER GOVERNMENT

Bureau of Mines

Twin Cities Research Center
ATTN: R. E. Thill

DEPARTMENT OF DEFENSE CONTRACTORS

Aerospace Corporation

ATTN: R. Strickler
ATTN: George Young
ATTN: Tech. Info. Services

Agbabian Associates

ATTN: M. Agbabian

Applied Theory, Inc.

2 cy ATTN: John G. Trullo

Avco

Government Products Group

ATTN: Frank Lasher
ATTN: John Atanasoff
ATTN: David Henderson
ATTN: Research Lib., A830, Rm. 7201

Battelle Memorial Institute

ATTN: Technical Library

Bell Telephone Laboratories, Inc.

ATTN: Tech. Rpt. Ctr.

The Boeing Company

ATTN: Aerospace Library
ATTN: Reynold Atlas

California Research & Technology, Inc.

ATTN: Ken Kreyenhagen
ATTN: M. H. Wagner
ATTN: W. S. Goerke
10 cy ATTN: Technical Library

Civil/Nuclear Systems Corp.

ATTN: Robert Crawford

DEPARTMENT OF DEFENSE CONTRACTORS (Continued)

EG&G, Inc.
Albuquerque Division
ATTN: Technical Library

General Dynamics Corp.
Pomona Operation
ATTN: Keith Anderson

General Electric Company
TEMPO-Center for Advanced Studies
ATTN: DASIAC

IIT Research Institute
ATTN: Technical Library

Institute for Defense Analysis
ATTN: IDA, Ruth S. Smith, Librarian

J. L. Merritt
Consulting & Special Engr. Svs. Inc.,
ATTN: Technical Library
ATTN: J. L. Merritt

Kaman Avidyne
Division of Kaman Sciences Corp
ATTN: E. S. Crisalone
ATTN: Norman F. Hobbs
ATTN: Technical Library

Kaman Sciences Corporation
ATTN: Library

Lockheed Missiles & Space Co., Inc.
ATTN: Technical Library

Lockheed Missiles & Space Company
ATTN: Technical Info. Ctr. D/Coll.

Martin Marietta Aerospace
Orlando Division
ATTN: Al Cowan
ATTN: M. Anthony

Nathan M. Newmark
Consulting Engineering Services
ATTN: Nathan M. Newmark

University of New Mexico
ATTN: H. D. Southward
ATTN: G. E. Triandafalidis

Physics International Company
ATTN: Doc. Con. for Fred M. Sauer
ATTN: Doc. Con. for Robert Swift
ATTN: Doc. Con. for Dennis Orphal
ATTN: Doc. Con. for Larry A. Behrmann
ATTN: Doc. Con. for Tech. Library
ATTN: Doc. Con. for Charles Godfrey

R & D Associates
ATTN: J. G. Lewis
ATTN: Cyrus P. Knowles
ATTN: Technical Library
ATTN: Henry Cooper
ATTN: William B. Wright, Jr.
ATTN: Harold L. Brode

DEPARTMENT OF DEFENSE CONTRACTORS (Continued)

Science Applications, Inc.
ATTN: D. E. Maxwell
ATTN: David Bernstein

Science Applications, Inc.
ATTN: William M. Layson

Science Applications, Inc.
ATTN: Technical Library
ATTN: C. Hudson

Stanford Research Institute
ATTN: SRI, Library, Rm. G021
ATTN: Lynn Seamans
ATTN: Burt R. Gasten
ATTN: George R. Abrahamson
ATTN: Carl Peterson

Systems, Science and Software, Inc.
ATTN: Technical Library
ATTN: Robert T. Allen
ATTN: Donald R. Grine

Terra Tek, Inc.
ATTN: Technical Library
ATTN: A. H. Jones
ATTN: Sidney Green

Texas A & M University System
C/O Texas A & M Research Foundation
ATTN: Harry Coyle

The BDM Corporation
ATTN: Technical Library

The BDM Corporation
ATTN: Hank Ponsford

TRW Systems Group
ATTN: Tech. Info. Center/S-1930

University of Oklahoma
Research Institute
ATTN: John Thompson

Weidinger Associates, Consulting Engineers
ATTN: J. W. Wright
ATTN: Melvin L. Baron

Weidinger Associates, Consulting Engineers
ATTN: J. Isenberg